

Effects of Oxide Incorporation into Sulfide Solid Electrolytes and
Development of All-Solid-State Lithium-Ion Batteries
(硫化物系固体電解質への酸化物導入の効果と
全固体電池の開発)

July, 2023

Doctor of Philosophy (Engineering)

Radian Febi Indrawan

ラディアン フェビ インドラワン

Toyohashi University of Technology

Date of Submission (month day, year) : July 7th, 2023

Department of Electrical and Electronic Information Engineering	Student ID Number	D209204	Supervisors	Atsunori Matsuda
Applicant's name	Radian Febi Indrawan			

Abstract (Doctor)

Title of Thesis	Effects of Oxide Incorporation into Sulfide Solid Electrolytes and Development of All-Solid-State Lithium-Ion Batteries.
-----------------	--

Approx. 800 words

Solid electrolytes (SEs) play a critical role in all-solid-state lithium-ion batteries (ASSLIBs) by acting as both electron separators and ion conductors. One promising method for SE synthesis is liquid-phase synthesis, which offers scalability and energy efficiency. However, impurities and the complexity of SEs prepared through this method have posed challenges, making liquid electrolytes indispensable in many cases.

In a study aimed at addressing these challenges, highly conducting lithium-ion solid electrolytes based on a $100\text{Li}_3\text{PS}_4\text{-}50\text{LiI-xLi}_3\text{PO}_4$ composition ($0 \leq x \leq 20$ mol%) were successfully synthesized using liquid-phase synthesis with ethyl propionate as the reaction medium. Interestingly, the addition of Li_3PO_4 into the $\text{Li}_3\text{PS}_4\text{-LiI}$ structure, up to $x = 20$, did not result in noticeable segregated peaks in the X-ray diffraction patterns.

Further analysis using ^{31}P NMR revealed the formation of PO_2S_2^- and POS_3^{3-} units, indicating that Li_3PO_4 reacted with the $\text{Li}_2\text{S-P}_2\text{S}_5$ system to form $\text{Li}_3\text{PO}_4\text{-xSx}$. Among the synthesized electrolytes, the one with $x = 10$ exhibited the highest room temperature conductivity of approximately $8.5 \times 10^{-4} \text{ Scm}^{-1}$.

Moreover, the study also addressed the issue of Li_3PO_4 impurity formation during the synthesis of $\text{Li}_6\text{PS}_5\text{Cl}$ argyrodite SEs using liquid-phase synthesis. By replacing hydroxide-based solvents with thiol-based solvents, Li_3PO_4 was successfully eliminated from the $\text{Li}_6\text{PS}_5\text{Cl}$ SEs. This modification resulted in the $\text{Li}_6\text{PS}_5\text{Cl}$ SEs achieving the highest ionic conductivity value ($>2 \text{ mS}\cdot\text{cm}^{-1}$) ever reported through liquid-phase synthesis. Importantly, the absence of Li_3PO_4 in the argyrodite SE led to significantly increased capacity and remarkable stability.

To further enhance the stability of the $\text{Li}_6\text{PS}_5\text{Cl}$ argyrodite SE, the study explored oxygen doping by synthesizing $\text{Li}_6\text{PS}_{5-2.5x}\text{O}_{2.5x}\text{Cl}$ ($x = 0, 0.05, \text{ and } 0.10$) solid electrolytes using liquid-phase synthesis. The solid electrolyte with $x = 0.05$ exhibited high ionic conductivity along with improved electrochemical stability against lithium metal and oxide cathodes. Argyrodites with $x = 0.05$ and $x = 0.10$ demonstrated superior capacity retention and higher Coulomb efficiency compared to $x = 0$. Moreover, the solid electrolytes exhibited enhanced stability during Li symmetrical cell measurements.

Overall, this work provides valuable insights into achieving high-performance ASSLIBs through liquid-phase synthesis. By carefully controlling the composition and synthesis conditions, such as introducing Li_3PO_4 or oxygen doping, it is possible to optimize the conductivity and stability of the solid electrolyte systems, paving the way for the development of advanced all-solid-state lithium-ion batteries.

In addition to addressing stability challenges in sulfide-based solid electrolytes, oxygen substitution offers several notable advantages for the performance and functionality of these materials in ASSLIBs.

The incorporation of Li_3PO_4 into the $\text{Li}_3\text{PS}_4\text{-LiI}$ system and P_2O_5 into $\text{Li}_6\text{PS}_5\text{Cl}$ lead to the formation of oxysulfide units. These oxysulfide compounds play a crucial role in enhancing the electrochemical stability of the solid electrolyte, particularly at the interface. The presence of the oxysulfide units helps to minimize unwanted reactions and side effects, improving the overall stability and performance of the solid electrolyte. This finding highlights the potential of incorporating Li_3PO_4 and P_2O_5 as strategies to enhance the electrochemical stability of solid electrolytes, making them promising candidates for advanced energy storage applications.

In summary, oxygen substitution in sulfide-based solid electrolytes provides numerous benefits for all-solid-state lithium-ion batteries. It enhances Li-ion conductivity, improves electrochemical stability, expands the electrochemical window, promotes compatibility with oxide cathodes, and allows for precise control over doping levels. These advantages contribute to the development of high-performance ASSLIBs with improved energy storage capacity, longer cycle life, and enhanced overall battery performance.

Table of Contents

Abstract	i
Table of Contents	iii
Figure List	v
Table List	x
Nomenclature	xi
1. General Introduction	1
1.1 Background.....	1
1.2 Lithium-ion Batteries	1
1.3 All-Solid-State Lithium-Ion Batteries	6
1.4 Solid Electrolytes.....	9
1.4.1 Defect Chemistry in Solid Electrolyte	10
1.4.2 Electronic Conductivity.....	12
1.4.3 Ionic Conductivity.....	13
1.4.4 Ions Movement Within the Crystal Lattice	15
1.5 Oxide-based Solid Electrolytes.....	19
1.6 Sulfide-based Solid Electrolytes.....	21
1.7 Oxysulfide-based Solid Electrolyte	26
1.8 Synthesize of Sulfide-based Solid Electrolyte.....	27
1.8.1 Melt Quench.....	27
1.8.2 Ball Milling	28
1.8.3 Liquid Phase Synthesis or Wet Chemical Reactions.....	28
1.9 Objectives	31
1.10 Outline	32
References.....	34
2. Preparation of 100Li₃PS₄-50LiI-xLi₃PO₄ Solid Electrolytes by Liquid Phase Shaking	42
2.1 Background.....	42
2.2 Introduction.....	42
2.3 Experimental Method	44
2.4 Experimental Results and Discussion.....	52
2.5 Conclusions.....	69
References.....	70
3. Liquid Phase Synthesis of Pure Argyrodite Solid Electrolyte	72
3.1 Background.....	72
3.2 Introduction.....	73
3.3 Experimental Method	76
3.3.1 Liquid Phase Synthesis.....	76
3.3.2 Mechanical Ball Milling Synthesis	76
3.3.3 Material Characterization.....	77

3.3.4	Electrochemical Performance Measurement.....	77
3.4	Result and Discussions	80
3.4.1	Characterization and ionic conductivity measurement	80
3.4.2	Heat Treatment Optimization	93
3.4.3	Lithium Metal Stability and Battery Performance Measurement	112
3.5	Conclusions.....	123
	References.....	124
4.	Oxygen-doped Argyrodite Solid Electrolyte by Liquid Phase Synthesis.....	130
4.1	Background.....	130
4.2	Introduction.....	131
4.3	Experimental Method	134
4.3.1	Sample Preparation	134
4.3.2	Material Characterization.....	135
4.3.3	Electrochemical Performance Measurement.....	135
4.4	Result and Discussions	137
4.4.1	Structure Analysis of $\text{Li}_6\text{PS}_{5-2.5x}\text{O}_{2.5x}\text{Cl}$	137
4.4.2	Electrochemical Performance of $\text{Li}_6\text{PS}_{5-2.5x}\text{O}_{2.5x}\text{Cl}$	142
4.4.3	Battery Cycle Performance of $\text{Li}_6\text{PS}_{5-2.5x}\text{O}_{2.5x}\text{Cl}$	153
4.5	Conclusions.....	166
	References.....	167
5.	General Conclusion and Future Works Possibility.....	174
	List of Publications	177
	Acknowledgements	178

Figure List

Figure 1.1	The schematic illustration of Li-ion batteries using liquid electrolyte.....	5
Figure 1.2	Schematic illustration of an all-solid-state lithium-ion battery	8
Figure 1.3	Idealized representations of intrinsic point defects in an ionic crystal; (a) Schottky defect, (b) Frenkel defect.	17
Figure 1.4	Proposed ion migration mechanism of (a) traditional vacancy Li ion diffusion and (b) concerted Li ion migration with a flatter energy landscape induced by the Coulombic interactions between the mobile ions.....	18
Figure 2.1	Flow chart of the preparation of $100\text{Li}_3\text{PS}_4\text{-}50\text{LiI-xLi}_3\text{PO}_4$ ($x=\text{mol}\%$) solid electrolyte with liquid phase shaking method.....	48
Figure 2.2	Photograph of the as-retrieved $100\text{Li}_3\text{PS}_4\text{-}50\text{LiI-xLi}_3\text{PO}_4$ ($x=\text{mol}\%$) precursor prepared after shaking process for 3 h.....	49
Figure 2.3	Photograph of the as-retrieved powder of $100\text{Li}_3\text{PS}_4\text{-}50\text{LiI-xLi}_3\text{PO}_4$ ($x=\text{mol}\%$) solid electrolyte	49
Figure 2.4	Schematic illustration of MAS-NMR measurement	50
Figure 2.5	Schematic diagram of cell for ionic conductivity measurement	50
Figure 2.6	Schematic diagram of cell for cyclic voltammogram test	51
Figure 2.7	Schematic diagram of cell for DC polarization test	51
Figure 2.8	XRD patterns of $100\text{Li}_3\text{PS}_4\text{-}50\text{LiI-xLi}_3\text{PO}_4$ ($x=\text{mol}\%$) solid electrolytes heat treated at $130\text{ }^\circ\text{C}$ for 2 h	56
Figure 2.9	XRD patterns of $100\text{Li}_3\text{PS}_4\text{-}50\text{LiI-xLi}_3\text{PO}_4$ ($x=\text{mol}\%$) solid electrolytes heat treated at $150\text{ }^\circ\text{C}$ for 2 h.	57
Figure 2.10	XRD patterns of $100\text{Li}_3\text{PS}_4\text{-}50\text{LiI-xLi}_3\text{PO}_4$ ($x=\text{mol}\%$) solid electrolytes heat treated at $170\text{ }^\circ\text{C}$ for 2 h.	58
Figure 2.11	Raman spectra of $100\text{Li}_3\text{PS}_4\text{-}50\text{LiI-xLi}_3\text{PO}_4$ ($x=\text{mol}\%$) solid electrolytes after heat treated at $170\text{ }^\circ\text{C}$ for 2 h	59
Figure 2.12	Temperature dependence of ionic conductivity of $100\text{Li}_3\text{PS}_4\text{-}50\text{LiI-}$ $x\text{Li}_3\text{PO}_4$ ($x=\text{mol}\%$) heat treated at $130\text{ }^\circ\text{C}$	60
Figure 2.13	Temperature dependence of ionic conductivity of $100\text{Li}_3\text{PS}_4\text{-}50\text{LiI-}$ $x\text{Li}_3\text{PO}_4$ ($x=\text{mol}\%$) heat treated at $150\text{ }^\circ\text{C}$	61
Figure 2.14	Temperature dependence of ionic conductivity of $100\text{Li}_3\text{PS}_4\text{-}50\text{LiI-}$ $x\text{Li}_3\text{PO}_4$ ($x=\text{mol}\%$) heat treated at $170\text{ }^\circ\text{C}$	62
Figure 2.15	Composition dependence of ionic conductivity at room temperature of $100\text{Li}_3\text{PS}_4\text{-}50\text{LiI-xLi}_3\text{PO}_4$ ($x=\text{mol}\%$) with different heat treatment conditions.....	63
Figure 2.16	^{31}P MAS-NMR of $100\text{Li}_3\text{PS}_4\text{-}50\text{LiI-xLi}_3\text{PO}_4$ ($x=\text{mol}\%$) solid electrolytes heat treated at $130\text{ }^\circ\text{C}$	65
Figure 2.17	(a) Cyclic voltammogram of $\text{Li} 100\text{Li}_3\text{PS}_4\text{-}50\text{LiI-}0\text{Li}_3\text{PO}_4$ heat treated at $130\text{ }^\circ\text{C} \text{SUS}$ at a scan rate of 5 mV s^{-1} (b) magnified voltage scale	66

Figure 2.18	(a) Cyclic voltammogram of Li 100Li ₃ PS ₄ -50LiI-10Li ₃ PO ₄ heat treated at 130 °C SUS at a scan rate of 5 mV s ⁻¹ (b) magnified voltage scale	67
Figure 2.19	DC Polarization curves of Li 100Li ₃ PS ₄ -50Li-xLi ₃ PO ₄ (x=mol%) heat treated at 130 °C Li with a current density of 0.3 mA cm ⁻² , 1 h of charge and discharge time.	68
Figure 3.1	Stoichiometry of Li ₆ PS ₅ Cl. The illustration comparison reaction between Li ₆ PS ₅ Cl by liquid-phase synthesis using a Tetrahydrofuran (THF) with Ethanol (EtOH) and b Acetonitrile (ACN) with 1-Propanethiol (PTH).....	75
Figure 3.2	Schematic illustration of the liquid-phase synthesis with acetonitrile and 1-propanethiol as the solvents to synthesize Li ₆ PS ₅ Cl argyrodite solid electrolyte.....	79
Figure 3.3	The illustration schematic mechanism of the elimination of Li ₃ PO ₄ oxide formation by using acetonitrile (ACN) and 1-propanethiol (PTH) as the solvents.....	83
Figure 3.4	XRD patterns of Li ₆ PS ₅ Cl prepared by liquid-phase synthesis with THF + EtOH, THF + PTH, and ACN + PTH as the solvent. All the samples were dried at 80 °C for overnight then heat treated at 600 °C for 2 h.....	84
Figure 3.5	TG-DTA curves of Li ₆ PS ₅ Cl prepared by liquid phase synthesis using EtOH and THF solvents after evaporated at 80 °C for 12 hours.....	85
Figure 3.6	¹ H NMR spectra of Li ₆ PS ₅ Cl and Li ₂ S-LiCl with THF + EtOH	86
Figure 3.7	¹ H NMR spectra of Li ₆ PS ₅ Cl and Li ₂ S-LiCl with ACN + PTH	87
Figure 3.8	Morphology of Li ₆ PS ₅ Cl _{EtOH+THF} and Li ₆ PS ₅ Cl _{ACN+PTH} . SEM images of Li ₆ PS ₅ Cl with THF + EtOH and ACN + PTH as the solvents after the heat treatment process.....	88
Figure 3.9	Raman spectra patterns of Li ₆ PS ₅ Cl with THF + EtOH and ACN + PTH as the solvents and Li ₆ PS ₅ Cl prepared by ball milling.....	89
Figure 3.10	Nyquist plots of electrochemical impedance from Li ₆ PS ₅ Cl _{EtOH+THF} and Li ₆ PS ₅ Cl _{ACN+PTH} after heat treated at 600 °C for 2 h.	90
Figure 3.11	Temperature dependence of ionic conductivity from Li ₆ PS ₅ Cl _{EtOH+THF} and Li ₆ PS ₅ Cl _{ACN+PTH} after heat treated at 600 °C for 2 h	91
Figure 3.12	Ionic conductivity and activation energy at 25 °C of Li ₆ PS ₅ Cl _{EtOH+THF} and Li ₆ PS ₅ Cl _{ACN+PTH} after heat treated at 600 °C for 2 h	92
Figure 3.13	TG-DTA curves of Li ₆ PS ₅ Cl prepared by liquid phase synthesis using ACN and PTH solvents after evaporated at 80 °C for 12 hours.....	97
Figure 3.14	TG-DTA curves of Li ₆ PS ₅ Cl prepared by mechanical ball milling at 600 rpm for 20 h without the heat treatment process	98
Figure 3.15	XRD patterns of Li ₆ PS ₅ Cl prepared by liquid-phase synthesis with THF + EtOH and ACN + PTH solvents. All the samples were dried at 80 °C overnight then heat-treated at 550 °C and 600 °C for 10 h	99
Figure 3.16	XRD patterns of Li ₆ PS ₅ Cl prepared using mechanical ball milling at 600 rpm for 20 h	100

Figure 3.17	^{31}P MAS-NMR results from $\text{Li}_6\text{PS}_5\text{Cl}$ prepared by ball milling and liquid-phase methods with different types of solvent from THF + EtOH and ACN + PTH after the heat treatment processes.	101
Figure 3.18	Nyquist plots of electrochemical impedance at room temperature from $\text{Li}_6\text{PS}_5\text{Cl}$ with THF + EtOH and ACN + PTH as the solvents after dried and heat-treated at 550 °C and 600 °C for 10 h.....	102
Figure 3.19	Ionic conductivity for $\text{Li}_6\text{PS}_5\text{Cl}$ by liquid phase synthesis. a Temperature dependence of ionic conductivity and b heat treatment dependence of ionic conductivity with activation energy from $\text{Li}_6\text{PS}_5\text{Cl}$ prepared using liquid phase synthesis using ACN+PTH and THF+EtOH after heat-treated at 550 °C and 600 °C for 10 h.....	103
Figure 3.20	Nyquist plots of electrochemical impedance at room temperature from $\text{Li}_6\text{PS}_5\text{Cl}/\text{SE}_{\text{BM}}$ after heat treated for 10 h.....	104
Figure 3.21	Temperature dependence of ionic conductivity from $\text{Li}_6\text{PS}_5\text{Cl}/\text{SE}_{\text{BM}}$ after heat treated for 10 h.....	105
Figure 3.22	Heat treatment temperature dependence of ionic conductivity with activation energy from $\text{Li}_6\text{PS}_5\text{Cl}/\text{SE}_{\text{BM}}$ after heat treated for 10 h.....	106
Figure 3.23	Nyquist plots of electrochemical impedance at room temperature from $\text{Li}_6\text{PS}_5\text{Cl}_{\text{BM}}$ and $\text{Li}_6\text{PS}_5\text{Cl}_{\text{ACN+PTH}}$ after heat treated at 550 °C for 10 h.....	107
Figure 3.24	Temperature dependence of ionic conductivity from $\text{Li}_6\text{PS}_5\text{Cl}_{\text{BM}}$ and $\text{Li}_6\text{PS}_5\text{Cl}_{\text{ACN+PTH}}$ after heat treated at 550 °C for 10 h.....	108
Figure 3.25	Heat treatment temperature dependence of ionic conductivity with activation energy from $\text{Li}_6\text{PS}_5\text{Cl}_{\text{BM}}$ and $\text{Li}_6\text{PS}_5\text{Cl}_{\text{ACN+PTH}}$ after heat treated at 550 °C for 10 h.....	109
Figure 3.26	SEM image of $\text{Li}_6\text{PS}_5\text{Cl}$ prepared using ball milling method at 600 rpm for 20 h then heat treated at 550 °C for 10 h.....	110
Figure 3.27	Galvanostatic DC polarization of symmetrical cell from $\text{Li} \text{Li}_6\text{PS}_5\text{Cl} \text{Li}$ ($m = \text{BM}, \text{THF} + \text{EtOH}, \text{ACN} + \text{PTH}$) at room temperature with 1 h for each charge and discharge.....	116
Figure 3.28	Electronic conductivity of $\text{Li}_6\text{PS}_5\text{Cl}$ SEs. Current versus applied voltage of a $\text{Li}_6\text{PS}_5\text{Cl}/\text{SE}_{\text{BM}}$, b $\text{Li}_6\text{PS}_5\text{Cl}/\text{SE}_{\text{ACN+PTH}}$, and c $\text{Li}_6\text{PS}_5\text{Cl}/\text{SE}_{\text{THF+EtOH}}$ after heat treated at 550 °C for 10h.....	117
Figure 3.29	Charge and discharge capacity curve for $\text{Li-In} \text{Li}_6\text{PS}_5\text{Cl}_{\text{ACN} + \text{PTH}} \text{TiS}_2\text{-Li}_6\text{PS}_5\text{Cl}$ ($m = \text{THF} + \text{EtOH}, \text{ACN} + \text{PTH}$) at room temperature with 0.1C rate.....	118
Figure 3.30	Cycling performance of half cells of $\text{Li-In} \text{Li}_6\text{PS}_5\text{Cl}_{\text{ACN} + \text{PTH}} \text{TiS}_2\text{-Li}_6\text{PS}_5\text{Cl}$ THF + EtOH cycled at 30 °C under 0.1C cycle rate in the voltage range of 3.0–2.4 V vs. Li–In.....	119
Figure 3.31	Cycling performance of half cells of $\text{Li-In} \text{Li}_6\text{PS}_5\text{Cl}_{\text{ACN} + \text{PTH}} \text{TiS}_2\text{-Li}_6\text{PS}_5\text{Cl}_{\text{ACN} + \text{PTH}}$ cycled at 30 °C under 0.1C cycle rate in the voltage range of 3.0–2.4 V vs. Li–In.....	120
Figure 3.32	SEM-EDX mappings from (a) $\text{TiS}_2\text{-Li}_6\text{PS}_5\text{Cl}$ THF + EtOH composite of (b)Ti, (c)Cl, (d)S, and (e)P elements for the selected regions.....	121

Figure 3.33	SEM-EDX mappings from (a)TiS ₂ -Li ₆ PS ₅ Cl ACN + PTH composite of (b)Ti, (c)Cl, (d)S, and (e)P elements for the selected region.....	122
Figure 4.1	XRD patterns of Li ₆ PS _{5-2.5x} O _{2.5x} Cl SEs prepared by liquid phase synthesis using ACN+PTH as the solvents heat treated at 550 °C for 10 h	139
Figure 4.2	Raman Spectroscopy of Li ₆ PS _{5-2.5x} O _{2.5x} Cl SEs prepared by liquid phase synthesis using ACN+PTH as the solvents heat treated at 550 °C for 10 h.....	140
Figure 4.3	³¹ P MAS-NMR patterns of Li ₆ PS _{5-2.5x} O _{2.5x} Cl SEs prepared by liquid phase synthesis using ACN+PTH as the solvents heat treated at 550 °C for 10 h.....	141
Figure 4.4	Temperature dependence of ionic conductivity from Li ₆ PS _{5-2.5x} O _{2.5x} Cl SEs prepared by liquid phase synthesis using ACN+PTH as the solvent then heat treated at 550 °C for 10 h	145
Figure 4.5	Graph of ionic conductivity and activation energy at room temperature of Li ₆ PS _{5-2.5x} O _{2.5x} Cl SEs prepared by liquid phase synthesis using ACN+PTH as the solvent then heat treated at 550 °C for 10 h correspond to Figure 4.4.....	146
Figure 4.6	Cyclic voltammogram of Li Li ₆ PS _{5-2.5x} O _{2.5x} Cl x=0 SUS at room temperature with a scan rate of 5 mV s ⁻¹	147
Figure 4.7	Cyclic voltammogram of Li Li ₆ PS _{5-2.5x} O _{2.5x} Cl x=0.05 SUS at room temperature with a scan rate of 5 mV s ⁻¹	148
Figure 4.8	Cyclic voltammogram of Li Li ₆ PS _{5-2.5x} O _{2.5x} Cl x=0.10 SUS at room temperature with a scan rate of 5 mV s ⁻¹	149
Figure 4.9	Galvanostatic DC polarization of a symmetrical cell from Li Li ₆ PS _{5-2.5x} O _{2.5x} Cl (x=0, 0.05, 0.10) Li at room temperature, with 1 h for each charge and discharge.....	150
Figure 4.10	XRD patterns of Li ₆ PS _{5-2.5x} O _{2.5x} Cl (x=0, 0.05, 0.10) after being exposed to air atmosphere for 10 min with the humidity level approximately at 35%.....	151
Figure 4.11	XRD patterns of Li ₆ PS _{5-2.5x} O _{2.5x} Cl (x=0, 0.05, 0.10) after being exposed to air atmosphere for 30 min with the humidity level approximately at 35%.....	152
Figure 4.12	Charge and discharge capacity curves for Li-In Li ₆ PS _{5-2.5x} O _{2.5x} Cl (x=0) NMC ₁₁₁ with at room temperature with 0.1C rate.....	157
Figure 4.13	Charge and discharge capacity curves for Li-In Li ₆ PS _{5-2.5x} O _{2.5x} Cl (x=0.05) NMC ₁₁₁ with at room temperature with 0.1C rate.....	158
Figure 4.14	Charge and discharge capacity curves for Li-In Li ₆ PS _{5-2.5x} O _{2.5x} Cl (x=0.10) NMC ₁₁₁ with at room temperature with 0.1C rate.....	159
Figure 4.15	Discharge capacity and coulombic efficiency curves for Li-In Li ₆ PS _{5-2.5x} O _{2.5x} Cl (x=0, 0.05, 0.10) NMC ₁₁₁ with at room temperature with 0.1C rate	160

Figure 4.16	SEM – EDX mappings from the $\text{Li}_6\text{PS}_5\text{Cl}$ ($x=0$) + NMC_{111} + AB composite of Ni, Mn, Co, O, P, S, and Cl elements for the selected regions	161
Figure 4.17	SEM – EDX mappings from the $\text{Li}_6\text{PS}_5\text{Cl}$ ($x=0.05$) + NMC_{111} + AB composite of Ni, Mn, Co, O, P, S, and Cl elements for the selected regions	162
Figure 4.18	SEM – EDX mappings from the $\text{Li}_6\text{PS}_5\text{Cl}$ ($x=0.10$) + NMC_{111} + AB composite of Ni, Mn, Co, O, P, S, and Cl elements for the selected regions	163
Figure 4.19	Cycle and rate performance of $\text{Li-In} \mid \text{Li}_6\text{PS}_{5-2.5x}\text{O}_{2.5x}\text{Cl}$ ($x=0, 0.05, x=0.10$) $\mid \text{NMC}_{111}$ at room temperature	165

Table List

Table 2.1. Ionic conductivity at room temperature of $100\text{Li}_3\text{PS}_4\text{-}50\text{LiI-xLi}_3\text{PO}_4$ ($x=\text{mol}\%$) with different kind of Li_3PO_4 concentration and heat treatment temperature.	64
Table 3.1. Crystallite size obtained from XRD data analysis and calculated using Debye-Scherrer equation, ionic conductivity, and electronic conductivity at room temperature from $\text{Li}_6\text{PS}_5\text{Cl/SEs}$	111
Table 4.1. Molecular weight ratio corresponding of $\text{Li}_6\text{PS}_{5-2.5x}\text{O}_{2.5x}\text{Cl}$ ($x=0, 0.05, 0.10$) + NMC111 + AB composites corresponding to SEM-EDX measurements from Figure 4.16, 4.17, and 4.18.....	164

Nomenclature

Abbreviations

EP	Ethyl propionate
THF	Tetrahydrofuran
ACN	Acetonitrile
1-Propanethiol	PTH
EtOH	Ethanol
ASSLiBs	All-solid-state lithium-ion batteries
BM	Ball milling method
CV	Cyclic voltammetry
DC	Direct current
AC	Alternating Current
EIS	Electrochemical impedance spectroscopy
EV	Electric vehicle
AB	Acetylene black
LiB	Lithium-ion battery
LISICON	Lithium superionic conductor
LPS	Li_3PS_4
LPS	Liquid phase shaking
NASICON	Sodium superionic conductor
NMR	Nuclear magnetic resonance
MAS-NMR	Magic-angle spinning-nuclear magnetic resonance
PEEK	Polyether ether ketone
SE	Solid electrolyte
SEs	Solid Electrolytes
LPSI	$\text{Li}_7\text{P}_2\text{S}_8\text{I}$

Chapter 1

General Introduction

1.1 Background

Electricity plays a vital role in sustaining the modern human lifestyle, driven by advancements in science, technology, and population growth. Currently, the majority of electrical energy is generated from fossil fuels, predominantly coal, which emits approximately 1000 g of lifecycle CO₂ per unit.[1] This emission contributes to environmental pollution and global warming concerns. To combat greenhouse gas emissions, there is a global need to transition to a sustainable energy system that promotes the use of renewable energy technologies.[2] One proposed solution is the implementation of a smart grid, which integrates a significant amount of renewable energy resources. Renewable energy sources such as solar, wind, hydroelectric power, geothermal energy, solar heat, and biomass offer great potential due to their abundance and availability.[3] In 2016, these renewable sources accounted for approximately 5% of global electricity production, and it is projected to increase to over 10% by 2040.[4] However, one of the challenges associated with renewable energy sources is their intermittent nature, necessitating advanced electrical energy storage technologies. Over the past decade, advancements in hybrid electric vehicles, plug-in hybrid electric vehicles, and purely electric vehicles have contributed to a reduced reliance on fossil fuels.[5] Lithium-ion batteries (LIBs) have emerged as the preferred choice for the next generation of hybrid electric vehicles and plug-in hybrids. The widespread adoption of LIBs in electric vehicles has the potential to significantly reduce greenhouse gas emissions and dependence on fossil fuels.

1.2 Lithium-Ion Batteries

LIBs have garnered significant attention as a key technology for energy storage in various applications. They have witnessed remarkable advancements and are considered the battery of choice for powering the next generation of hybrid electric

vehicles (HEVs), plug-in hybrid electric vehicles (PHEVs), and purely electric vehicles (EVs).[6, 7] LIBs offer several advantages that make them highly desirable. Firstly, they exhibit a high energy density, allowing for a greater storage capacity of electrical energy compared to other battery technologies. This is crucial for maximizing the driving range and overall performance of electric vehicles. Additionally, LIBs have a relatively long cycle life, meaning they can endure numerous charge and discharge cycles without significant degradation.[8] This durability is essential for ensuring the longevity and reliability of the batteries, especially in demanding automotive applications. Moreover, LIBs have a high power density, enabling them to deliver rapid bursts of energy when needed, such as during acceleration or regenerative braking in electric vehicles.[8] This characteristic contributes to the overall responsiveness and performance of the vehicle. The development and commercialization of LIBs have been driven by continuous research and technological advancements. Efforts have focused on improving their energy density, safety features, charging times, and cost-effectiveness. Researchers are constantly exploring new electrode materials, electrolyte compositions, and battery designs to enhance the performance and sustainability of LIBs. As the demand for electric vehicles continues to grow, the development of efficient, safe, and affordable LIBs remains a crucial area of research and innovation.[9] Overall, lithium-ion batteries have revolutionized the field of energy storage and play a vital role in advancing sustainable transportation and clean energy initiatives.

In general, Li-ion batteries can be described as energy storage systems that depend on the insertion reactions occurring at both electrodes, with lithium ions serving as the charge carriers.[10] Within the Li-ion battery family, various cell chemistries exist, each with its own characteristics. The majority of Li-ion batteries utilize a negative electrode primarily composed of carbon (e.g., graphite) or lithium titanate ($\text{Li}_4\text{Ti}_5\text{O}_{12}$). However, there are ongoing developments with novel materials such as Li metal and Li(Si) alloys. The choice of electrode materials determines the composition of the electrolyte, which typically consists of a combination of lithium salts (e.g., LiPF_6) and an organic solvent (e.g., diethyl carbonate) to facilitate ion transfer. To enable the passage of lithium ions between the electrodes while preventing internal short circuits, a separating membrane is utilized. [11] The kinetics of redox processes in Li-ion batteries are influenced by the nature of the electrodes and their surface area. Furthermore, the cell voltage is determined

by the difference between the equilibrium potential of the cathode and anode. This cell voltage, denoted as ΔE , can be expressed using the equation (1.2.1) as follows:

$$\Delta E = \Delta\phi_{\text{cathode}} - \Delta\phi_{\text{anode}} \quad (1.2.1)$$

The potentials at equilibrium of the cathode and anode are denoted as $\Delta\phi_{\text{cathode}}$ and $\Delta\phi_{\text{anode}}$, respectively. The resulting equation (1.2.1) can be expressed in the form of equation (1.2.2) using the Nernst equation.

$$\Delta E = \Delta\phi_{\text{cathode}} - \Delta\phi_{\text{anode}} = \Delta E^{\circ} - \frac{RT}{nF} \ln \frac{a_{\text{Red}_1}^s a_{\text{Ox}_2}^t}{a_{\text{Red}_2}^q a_{\text{Ox}_1}^p} \quad (1.2.2)$$

$$(p\text{Ox}_1 + q\text{Red}_1 \rightarrow s\text{Red}_2 + t\text{Ox}_2)$$

The Faraday constant, denoted as F , represents the charge carried by one mole of electrons and is equal to 96485 C mol^{-1} . The standard potential is represented by E° . R corresponds to the gas constant, while T represents the temperature. The variable n indicates the number of electrons involved in the redox reaction between the electrodes, and a represents the activity of the redox couples. The redox couples are categorized into two pairs: Ox_1 and Red_1 , which belong to the stronger couple with a higher potential, and Ox_2 and Red_2 , which belong to the weaker couple with a lower potential. The electrolyte facilitates ion conduction between the electrodes in Li-ion batteries. In the case of LIBs, Li ions, as mobile species, move towards regions of opposite charge under the influence of the electric field generated between the cathode and anode. Commonly, the electrolyte in LIBs is composed of a solution of a Li^+ salt in a mixture of polar aprotic organic solvents. The schematic illustration of Li-ion batteries using liquid electrolyte is shown in Figure 1.1. A separating membrane is used to allow lithium ions to pass between the electrodes while preventing an internal short circuit. As depicted, electrons flow from the negative electrode to the positive electrode, while simultaneously Li^+ ions migrate from the negative electrode through the electrolyte to the positive electrode. This movement of Li^+ ions ensures the maintenance of electroneutrality within the battery system. When the

system is operated in charge mode, which refers to its functioning as an electrolytic device, the direction of both electron current and Li^+ ion flow is reversed. In this mode, electrons flow from the positive electrode to the negative electrode, and Li^+ ions move from the positive electrode through the electrolyte to the negative electrode. This reversal of electron current and Li^+ ion flow allows for the recharging or replenishing of the battery's energy storage capacity. The wide range of materials available for the positive and negative electrode materials, electrolyte, and separator in Li-ion batteries offers numerous choices for battery design. However, the selection of these materials is influenced by the technological limitations imposed by their specific functions within the battery system. For the positive and negative electrode materials, factors such as energy storage capacity, stability, cycling performance, and cost are crucial considerations. Different materials offer varying trade-offs in these properties, requiring careful evaluation and selection based on the specific requirements of the battery application. Similarly, the electrolyte composition is critical for efficient ion conduction, safety, and stability. The choice of electrolyte materials must strike a balance between these factors to ensure optimal battery performance and longevity. The separator, which physically separates the electrodes to prevent short circuits, must exhibit appropriate mechanical strength, ionic conductivity, and resistance to degradation. The selection of separator materials is vital for maintaining the overall safety and reliability of the battery system. Ultimately, the technological limitations associated with the different materials used in Li-ion batteries arise from the need to fulfill specific functions while considering factors such as performance, cost, safety, and environmental impact. Extensive research and development efforts continue to address these limitations and advance the performance and capabilities of Li-ion battery materials. [12-14] Nevertheless, the safety concerns related to the utilization of flammable organic liquid electrolytes in conventional LIBs pose significant challenges. Issues such as leakage and the risk of ignition are prevalent, raising concerns about the reliability of these batteries. These safety concerns continue to impede the widespread adoption of LIBs in the market for both electronic devices and EVs.

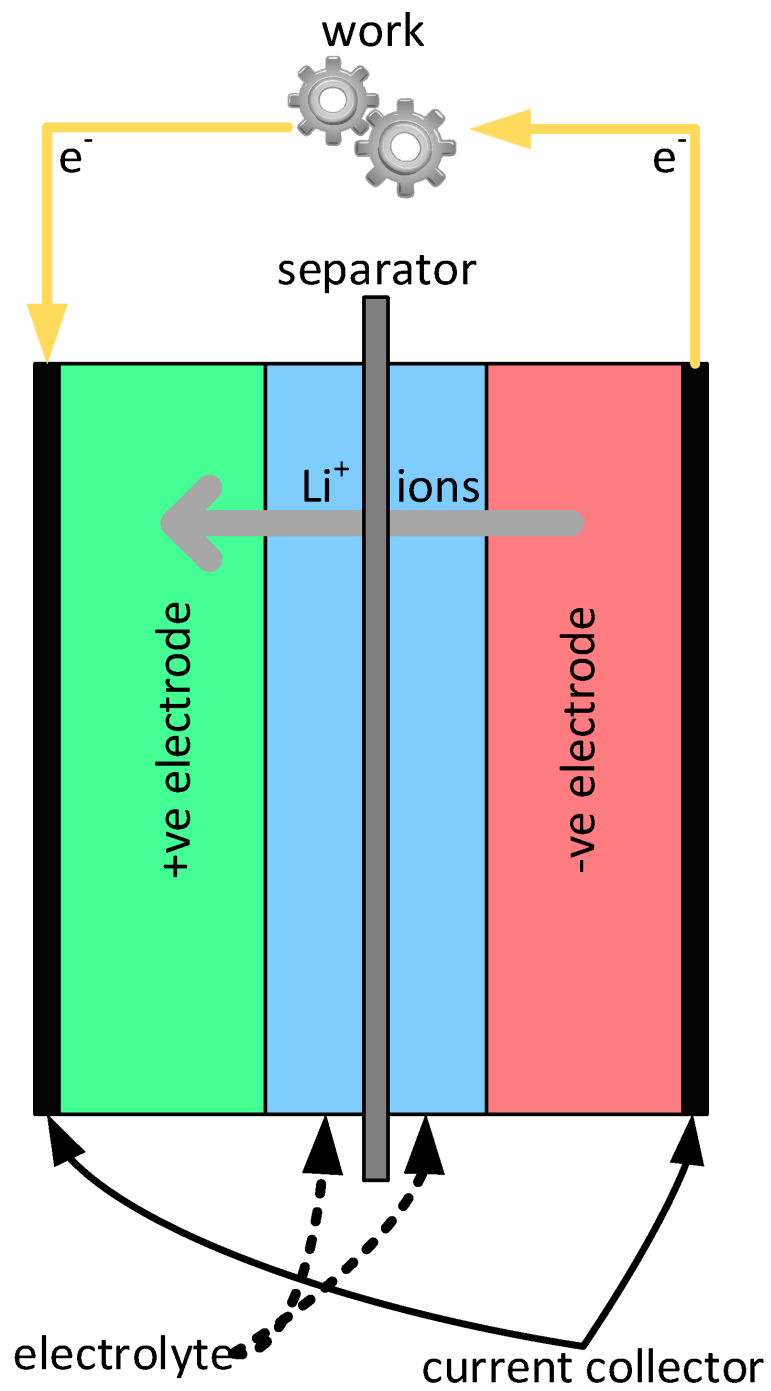


Figure 1.1. The schematic illustration of Li-ion batteries using liquid electrolyte. [86]

1.3 All-Solid-State Lithium-Ion Batteries.

All-solid-state lithium-ion batteries (ASSLiBs) are a type of rechargeable battery that utilize solid-state electrolytes instead of the traditional liquid or gel electrolytes found in conventional lithium-ion batteries (LIBs).[15] In ASSLiBs, both the positive and negative electrodes, as well as the electrolyte, are composed of solid materials. The illustration of ASSLiBS is depicted in Figure 1.2.

The solid-state electrolyte in ASSLiBs acts as a medium for the transport of lithium ions between the electrodes. It offers several advantages over liquid electrolytes, including improved safety, higher thermal stability, and the elimination of leakage and flammability concerns associated with liquid electrolytes. Additionally, solid-state electrolytes can exhibit higher ionic conductivity, enabling faster ion transport within the battery, which can lead to improved power density and charging/discharging rates.

ASSLiBs also have the potential for increased energy density compared to conventional LIBs. This is due to the ability to utilize lithium metal anodes, which have higher energy storage capacity compared to graphite-based anodes commonly used in LIBs. The use of lithium metal anodes, combined with the inherent stability and low reactivity of solid-state electrolytes, can enable the development of batteries with higher energy density and longer-lasting performance.

However, there are some challenges associated with ASSLiBs that need to be addressed for their widespread commercialization. These challenges include optimizing the ionic conductivity of solid-state electrolytes, ensuring good interfacial compatibility between the electrolyte and electrode materials, and minimizing the formation of interfacial resistance, which can hinder battery performance.

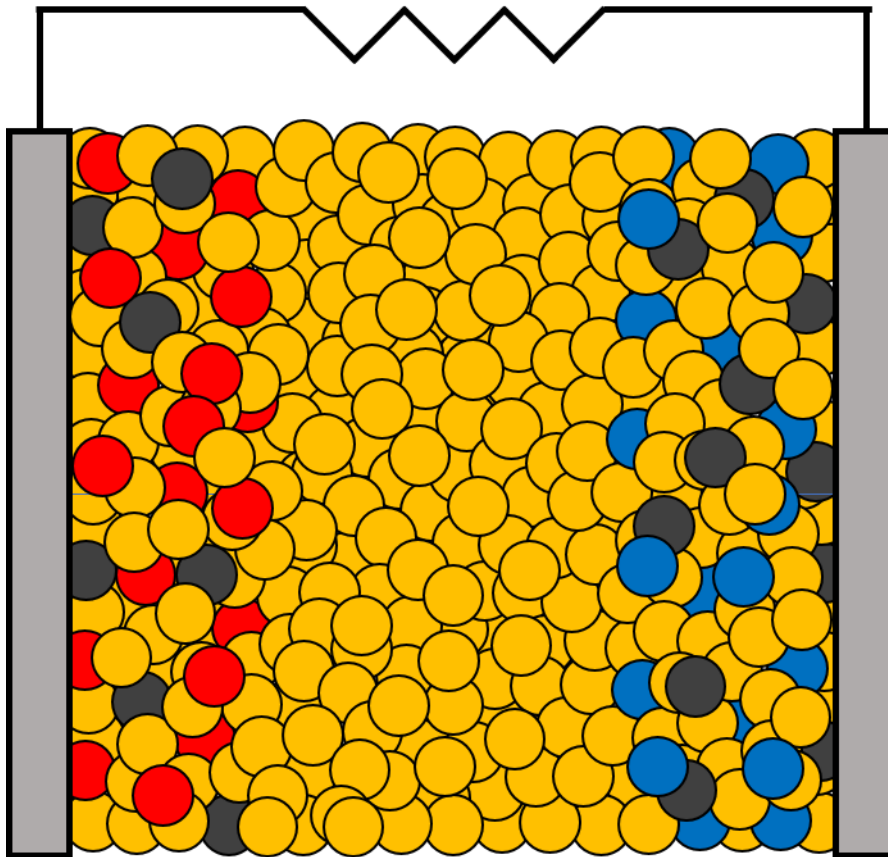
Research and development efforts are actively underway to overcome these challenges and advance the technology of all-solid-state lithium-ion batteries. ASSLiBs hold great promise for next-generation energy storage systems, offering enhanced safety, improved energy density, and the potential for transformative advancements in portable electronics, electric vehicles, and grid-scale energy storage.

While all-solid-state lithium-ion batteries (ASSLiBs) offer numerous advantages, there are still several challenges and limitations that need to be addressed before their

widespread commercialization. Some of the main problems associated with ASSLiBs include:

1. Limited ionic conductivity: Solid-state electrolytes typically have lower ionic conductivity compared to liquid electrolytes used in conventional LIBs. This can result in higher resistance and lower battery performance, particularly at high current rates. Improving the ionic conductivity of solid-state electrolytes is crucial for enhancing the overall performance of ASSLiBs.[16]
2. Interface compatibility and stability: The interfaces between the solid-state electrolyte and electrode materials need to be stable and compatible to ensure efficient ion transport and prevent degradation over cycling. Interfacial reactions and the formation of high resistance layers can hinder battery performance and lifespan.[17]
3. Cost and scalability: The fabrication processes for ASSLiBs often involve complex and expensive manufacturing techniques, such as vacuum deposition or high-temperature sintering. Finding cost-effective and scalable manufacturing methods for solid-state electrolytes and electrode materials is necessary for large-scale production and commercial viability.[17]
4. Mechanical stress and cycling stability: Solid-state electrolytes and electrode materials can experience mechanical stress during cycling due to volume changes and differences in thermal expansion coefficients. This stress can lead to material degradation, cracks, and reduced cycling stability. Developing mechanically robust and durable components is essential for long-term battery performance.[18]
5. Lithium dendrite growth: The use of lithium metal anodes in ASSLiBs can lead to the formation of lithium dendrites, which are needle-like structures that can penetrate the electrolyte and cause short circuits or even safety hazards. Effectively suppressing lithium dendrite formation and preventing electrode degradation is a critical challenge for ASSLiBs.[19]

Researchers and scientists are actively working on addressing these challenges through advancements in solid-state electrolyte materials, interface engineering, cell design, and manufacturing techniques. Overcoming these problems will be instrumental in realizing the full potential of ASSLiBs and enabling their widespread adoption as a safe, high-performance energy storage solution.








-  **Solid Electrolyte**
-  **Positive active material**
-  **Negative active material**
-  **Electron conductive material**
-  **Electrical collector**

Figure 1.2. Schematic illustration of an all-solid-state lithium-ion battery

1.4 Solid Electrolytes

A solid electrolyte (SE) is a type of electrolyte material that is in a solid state, as opposed to liquid or gel electrolytes found in traditional batteries. SEs play a crucial role in various types of solid-state batteries, including all-solid-state lithium-ion batteries (ASSLiBs). The primary function of a solid electrolyte is to facilitate the transport of ions between the cathode and anode in a battery. In the case of lithium-ion batteries, the SE allows for the movement of lithium ions during the charging and discharging processes. The ionic conductivity of the SE is a key factor that determines the overall performance of the battery, as higher conductivity enables faster ion transport and better battery efficiency. SE materials can be classified into different categories, including ceramic, polymer, and composite electrolytes. Ceramic electrolytes, such as lithium garnets (e.g., $\text{Li}_7\text{La}_3\text{Zr}_2\text{O}_{12}$ or LLZO) are known for their stability, while sulfide-based materials (e.g., $\text{Li}_{10}\text{GeP}_2\text{S}_{12}$ or LGPS) for its high ionic conductivity.[20-22] Polymer electrolytes, on the other hand, offer flexibility and easier processing but may have lower ionic conductivity compared to ceramics. Composite electrolytes combine the advantages of both ceramic and polymer materials, aiming to achieve a balance between ionic conductivity, mechanical strength, and stability. Developing SEs with high ionic conductivity, excellent stability, good mechanical properties, and compatibility with electrode materials is crucial for the performance and commercialization of solid-state batteries. Researchers are actively working on improving the conductivity and stability of SEs through material optimization, interface engineering, and advanced manufacturing techniques. The use of solid electrolytes in batteries, particularly in ASSLiBs, offers several advantages over liquid electrolytes, including enhanced safety, improved thermal stability, elimination of leakage, and potential for higher energy density.[23] However, challenges such as optimizing ionic conductivity, ensuring good interfacial compatibility, and controlling interfacial resistance still need to be addressed for the widespread adoption of SE-based solid-state batteries.

1.4.1 Defect Chemistry in Solid Electrolyte

To achieve effective design of fast ion conductors, it is crucial to have a thorough understanding of defect chemistry. At finite temperatures, crystalline solids inherently contain various types of defects, ranging from point defects and extrinsic impurities to grain boundaries. It is important to note that no material can exist in a perfectly crystalline form. Defects in crystalline materials play a significant role in determining the ion transport properties. Point defects, such as vacancies (missing atoms) and interstitials (additional atoms), can create pathways for ion migration. Extrinsic impurities, which are atoms or ions of different species incorporated into the crystal lattice, can also affect the defect chemistry and ion conductivity. Additionally, grain boundaries, which are interfaces between adjacent crystalline regions with different orientations, can influence the overall ion transport behavior. By understanding the nature and behavior of these defects, researchers can manipulate and optimize the structure and composition of materials to enhance their ion conductivity. [24-27] Schottky and Frenkel defects are two types of point defects that occur in crystalline materials (Figure 1.3). [28]

1. Schottky Defect (also known as Scotty Defect): A Schottky defect is a type of point defect in which an equal number of cations and anions are missing from their regular lattice sites within a crystal structure. This defect typically occurs in ionic compounds, such as metal halides or alkali metal compounds, where cations and anions are held together by strong electrostatic forces. The absence of these ions creates vacancies, resulting in a charge-neutral defect. Schottky defects can contribute to the electrical conductivity of ionic materials and are associated with high-temperature stability.
2. Frenkel Defect: A Frenkel defect is a type of point defect in which an ion is displaced from its lattice site and occupies an interstitial position within the crystal lattice. The displaced ion creates a vacancy at its original site. Frenkel defects commonly occur in materials with a large size difference between cations and anions, such as metal oxides or semiconductors. Frenkel defects do not affect the overall charge neutrality of the crystal, but they can influence various material properties, including electrical conductivity, optical behavior, and diffusion of species.

Both Schottky and Frenkel defects are important in understanding the behavior and properties of crystalline materials. These defects can affect the material's electrical and optical properties, as well as its ability to transport ions or participate in chemical reactions. By studying and controlling these defects, researchers can manipulate the properties of materials for specific applications, such as designing solid-state electrolytes for batteries or optimizing the performance of semiconductor devices. In the case of Frenkel defect, the equilibrium constant, K_S , is represented using concentrations rather than activities, as shown in the following expression:

$$K_S = \left(\frac{n_{cv}}{N}\right) \left(\frac{n_{av}}{N}\right) = \exp \left[\frac{-\Delta G_S}{k_B T} \right] \quad (1.4.1.1)$$

In the given expression, n_{cv} represents the number of cation vacancies, n_{av} represents the number of anion vacancies per unit volume, N represents the number of cation or anion sites per unit volume in the crystal, ΔG_S represents the molar Gibbs energy of formation of the Schottky defects, k_B denotes Boltzmann's constant, and T represents the absolute temperature. Since the crystal maintains electroneutrality, the n_{cv} is equal to the number of anion vacancies n_{av} . Therefore, the total number of Schottky defects present in the crystal, denoted as n_s , can be expressed as the sum of cation vacancies and anion vacancies:

$$n_{cv} = n_{av} = n_s = N \exp \left[\frac{-\Delta G_S}{2RT} \right] \quad (1.4.1.2)$$

In many cases, ΔG_S is replaced by the enthalpy of Schottky defect formation, ΔH_S . The Gibbs free energy, which is a measure of the system's total energy available to do work, is defined as follows:

$$G = H - TS \quad (1.4.1.3)$$

The equilibrium constant of the Schottky defect is given by the expression, where H is the standard enthalpy and S is the entropy:

$$K_S = \exp\left[\frac{\Delta S_S}{k_B}\right] \exp\left[\frac{-\Delta H_S}{k_B T}\right] \quad (1.4.1.4)$$

This equation indicates that as the temperature in the system increases, the thermal equilibrium concentration rises rapidly beyond a certain temperature. This phenomenon holds true for the Frenkel defect as well.

1.4.2 Electronic Conductivity

In solid electrolytes, where ions serve as charge carriers, the application of a voltage [V] (V) results in a current [I] (A) flowing through the sample. In this context, solid electrolytes obey Ohm's law, which states that the current is directly proportional to the voltage, and the proportionality constant is the resistance of the electrolyte.

$$I = \frac{V}{R} \quad (1.4.2.1)$$

After that, if the solid electrolyte has a cylindrical shape with a cross-sectional area [A](m²) and a length [L](m), its electrical resistance [R](Ω) can be determined using the following equation. This equation is analogous to the resistance calculation for metal wires and similar conductive materials.

$$R = \rho \frac{L}{A} \quad (1.4.2.2)$$

Here, [ρ] (Ωm) represents the resistivity. By rewriting equation (2.2) for resistivity and taking the reciprocal, the equation can be expressed as follows:

$$\sigma = \frac{1}{\rho} = \frac{L}{RA} \quad (1.4.2.3)$$

Then, $[\sigma]$ (S cm^{-1}) represents a material-specific value known as electrical conductivity. To determine the electrical conductivity of the sample using this equation, it is crucial to accurately measure the cross-sectional area, thickness, and electrical resistance of the sample. These parameters are essential for calculating the conductivity of the solid electrolyte.

1.4.3 Ionic Conductivity

In the case of measuring the resistance of an electron conductor, such as a metal, electrons can flow not only through the sample but also through the external circuit and the measuring instrument. Therefore, the resistance value can be determined by measuring the current against the applied voltage, following Ohm's law. However, when measuring the electrical resistance in an ion conductor, such as an electrolyte, ions can only flow within the sample. In the presence of a DC voltage, as depicted in Figure 1.3a, ions become biased, leading to accumulation and depletion near the electrode interface, causing polarization. This polarization generates a counteracting force against the applied electric field, preventing the movement of ions and resulting in no current flow. To measure the conductivity of ions accurately, as illustrated in Figure 1.3b, an alternating voltage is applied. This helps mitigate the effects of polarization, allowing for the measurement of resistance. The temperature dependence of the tracer diffusion coefficient or diffusivity, D^T , is commonly described by the Arrhenius relation.

$$D^T = D_0 \exp\left(-\frac{E_a}{k_B T}\right) \quad (1.4.3.1)$$

In the given equation, D_0 represents the pre-exponential factor, and E_a is the activation energy for ion migration. From a microscopic perspective, the tracer diffusion coefficient, D_T , can be defined by the Einstein-Smoluchowski relation. [29, 30]

$$D^T = \lim_{t \rightarrow \infty} \frac{\langle r^2(t) \rangle}{2dt} \quad (1.4.3.2)$$

In this context, $\langle r^2 \rangle(t)$ represents the mean square displacement of the particles after time t , and d is the dimensionality of the diffusion. In a solid electrolyte, a mobile

cation moves between stable sites through interconnected diffusion channels within the crystal structure. These channels provide a minimum potential landscape for ion migration. If the mean jump time is shorter than the mean relaxation time τ , the cation will undergo elementary jumps with an average jump length denoted as a_0 . Based on these microscopic quantities, a diffusion coefficient D_{uc} for uncorrelated jumps can be expressed as follows:

$$D^{uc} = \frac{a_0^2}{2d\tau} \quad (1.4.3.3)$$

If the mobile ions hop in three dimensions with a jump vibrational frequency of ν_0 (where ν_0 is the reciprocal of the mean jump time, τ), Equation 1.4.3.1 can be transformed into:

$$D^T = \frac{a_0^2 \nu_0}{6} \exp\left(-\frac{E_a}{k_B T}\right) \quad (1.4.3.4)$$

The ionic conductivity can be determined based on the Nernst-Einstein relationship, utilizing

$$\sigma = \frac{nq^2}{k_B T} D^\sigma \quad (1.4.3.5)$$

n represents the total density of charge carriers, and q is the charge of the mobile ion. The diffusion coefficient D^σ , obtained from conductivity measurements using the Nernst-Einstein relationship (Equation 1.4.3.5), is related to the tracer diffusion coefficient D^T by:

$$D^T = H_R D^\sigma \quad (1.4.3.6)$$

Considering a geometrical factor z that takes into account the potential cross-correlation in diffusion, including the Haven ratio H_R (which represents the ratio between the tracer and charge diffusion coefficients), the ionic conductivity, σ , in solids can be expressed as follows:

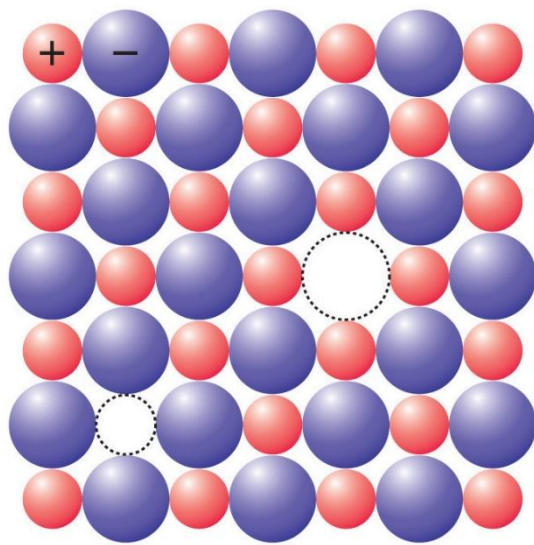
$$\sigma = \frac{nq^2 a_0^2 v_0 z}{6k_B T} \exp\left(-\frac{E_a}{k_B T}\right) = \frac{\sigma_0}{T} \exp\left(-\frac{E_a}{k_B T}\right) \quad (1.4.3.7)$$

In the given equation, σ_0 represents the pre-exponential factor for ion diffusion. The activation energy, E_a , is the sum of the enthalpy required to create defects and overcome the energy barrier for ion migration. However, in heavily defective materials, the enthalpy for defect formation is often neglected. The design of ion conductors has primarily relied on the ion conduction mechanism described in Equation (1.4.3.7). Increasing the pre-exponential factor and decreasing the activation energy for ion transport contribute to the enhancement of ionic conductivity.

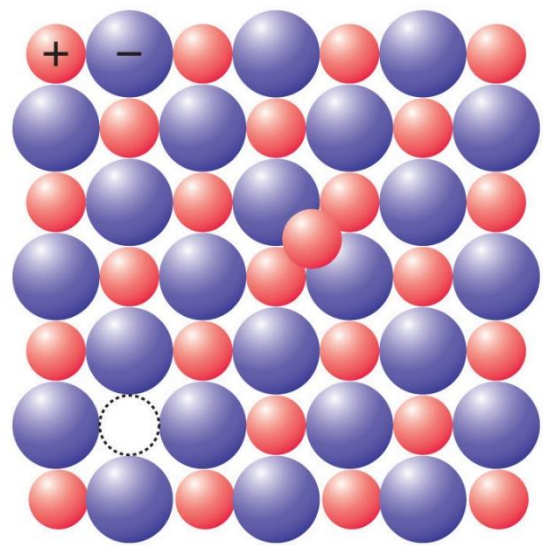
1.4.4 Ions Movement Within the Crystal Lattice.

In crystalline materials, ion conduction typically occurs through specific pathways within the crystal lattice. The ions, often cations, migrate through the crystal structure by hopping between vacant lattice sites. This migration can be facilitated by the presence of defects such as vacancies or interstitial sites, which provide diffusion paths for the ions. The ion conduction mechanism in crystalline materials can be influenced by several factors. One important factor is the coordination environment of the ions within the crystal lattice. The arrangement of neighboring atoms or ions around each lattice site affects the ease with which ions can move through the lattice. The crystal structure of materials containing anionic sublattices with body-centered cubic (BCC)-like frameworks promotes the diffusion of Li-ions by reducing the activation barrier compared to other anionic frameworks.[31] Additionally, the energy barriers associated with ion migration play a crucial role. The activation energy required for ions to overcome these

barriers determines the speed at which ion conduction can occur. Factors such as temperature and crystal structure influence the magnitude of these energy barriers. The presence of mobile charge carriers and their concentration also affects ion conduction. In some cases, the presence of additional mobile ions, such as dopants or impurities, can enhance the overall ionic conductivity of the material. Overall, the ion conduction mechanism in crystalline materials involves the movement of ions through specific diffusion pathways within the crystal lattice, facilitated by defects and influenced by factors such as coordination environment, energy barriers, and mobile charge carriers. Understanding and controlling these mechanisms are essential for the design and optimization of materials with high ionic conductivity. Argyrodite-type solid electrolytes (SEs) are known for their exceptional ionic conductivities, reaching values as high as 24 mS cm^{-1} at room temperature, making them highly promising for various applications.[32] The ion diffusion in these materials follows the concerted migration mechanism, where the movement of mobile ions is influenced by Coulombic interactions with neighboring ions which illustrated in Figure 1.4. This interaction results in a redistribution of mobile ions at high-energy interstitial sites, creating a relatively flat energy landscape with a low activation barrier for ion migration.[33]



(a) Schottky defect



(b) Frenkel defect

Figure 1.3. Idealized representations of intrinsic point defects in an ionic crystal; (a) Schottky defect, (b) Frenkel defect.

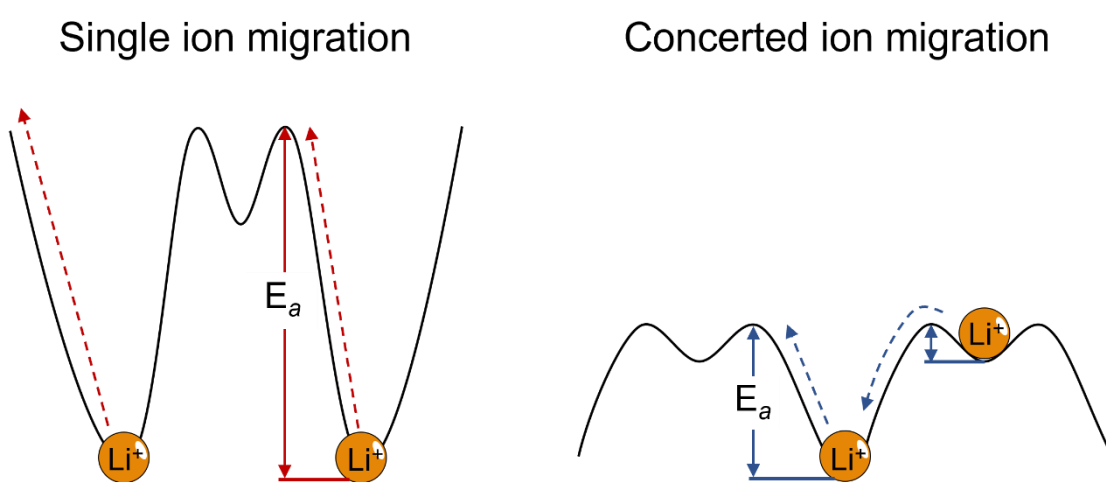


Figure 1.4. Proposed ion migration mechanism of (a) traditional vacancy Li ion diffusion and (b) concerted Li ion migration with a flatter energy landscape induced by the Coulombic interactions between the mobile ions.[87]

1.5 Oxide-based Solid Electrolytes

Oxide-based solid electrolytes are a type of solid-state electrolyte commonly used in solid-state batteries. They are composed of oxide materials that exhibit high ionic conductivity and can serve as an effective medium for the transport of ions.[34, 35] The garnet-type solid electrolytes (SEs), such as $\text{Li}_7\text{La}_3\text{Zr}_2\text{O}_{12}$ (LLZO), are known for their excellent chemical stability against lithium metal. This means that they are less prone to chemical reactions or degradation when in contact with lithium metal compared to oxide-based SEs like LATP ($\text{Li}_{1.7}\text{Al}_{0.3}\text{Ti}_{1.7}(\text{PO}_4)_3$) and LAGP ($\text{Li}_{1.5}\text{Al}_{0.5}\text{Ge}_{1.5}(\text{PO}_4)_3$), which belong to the NASICON-type structure.[36] While oxide-based SEs like LAGP may exhibit comparable ionic conductivity to LLZO, they can experience mechanical and thermal failures due to the chemical reactions that occur between the SE material and the lithium metal electrode. These reactions can lead to the formation of unwanted compounds or interfaces, which can compromise the stability and overall performance of the solid electrolyte.[37] It is worth noting that the chemical stability of a solid electrolyte is an important consideration for its practical application in solid-state batteries. The ability to maintain stable interfaces with lithium metal electrodes is crucial for achieving long-term stability and high-performance battery systems.[36-38] Oxide-based solid electrolytes are generally considered stable against lithium metal due to several factors:

1. **Chemical Inertness:** Oxide materials have a high chemical stability, meaning they are less reactive towards lithium metal. They have a low tendency to undergo chemical reactions with lithium, reducing the likelihood of unwanted side reactions or degradation.[35-39]
2. **Passivation Layer Formation:** When an oxide-based solid electrolyte comes into contact with lithium metal, a thin and stable passivation layer can form on the surface of the electrolyte. This passivation layer acts as a barrier, preventing further reactions between the electrolyte and lithium metal. It effectively isolates the solid electrolyte from direct contact with the lithium, enhancing its stability. [35-39]
3. **Electrochemical Compatibility:** Oxide materials can have a wide electrochemical stability window, meaning they can withstand a range of potential differences

without undergoing chemical breakdown. This is particularly important when in contact with reactive metals like lithium. The stable electrochemical behavior of oxides helps maintain the integrity of the solid electrolyte and prevents excessive chemical reactions. [35-39]

Overall, the combination of chemical inertness, passivation layer formation, and electrochemical compatibility makes oxide-based solid electrolytes more stable against lithium metal. This stability is crucial for the reliable operation and long-term performance of solid-state batteries. [35-39]

While oxide-based solid electrolytes offer several advantages, they also face certain challenges and limitations. Some of the problems associated with oxide-based solid electrolytes include:

1. **Low Ionic Conductivity:** Many oxide-based solid electrolytes exhibit relatively low ionic conductivity compared to other types of electrolytes, such as sulfides or polymer electrolytes. The lower conductivity limits the rate at which ions can move within the electrolyte, affecting the overall performance and power output of solid-state batteries.[40-42]
2. **Brittle Nature:** Oxide materials tend to be inherently brittle, making them susceptible to mechanical failure under stress or strain. This brittleness can lead to issues such as cracking, delamination, or reduced structural integrity, especially in large-scale battery applications or during thermal cycling.[40-42]
3. **Limited Stability at High Temperatures:** Some oxide-based electrolytes may experience stability issues at elevated temperatures. They can undergo chemical reactions or phase transitions that compromise their structural integrity or lead to degradation over time. This limits their suitability for high-temperature applications or imposes constraints on the operating temperature range of solid-state batteries.[40-42]
4. **Interface Compatibility:** Achieving good interface compatibility between oxide-based electrolytes and electrode materials can be challenging. The differences in materials properties, thermal expansion coefficients, and reactivity can result in

interfacial impedance, hindered ion transfer, or even chemical reactions at the interfaces. These issues can negatively impact the overall battery performance and cycling stability.[40-42]

5. **Synthesis Complexity:** Some oxide-based solid electrolytes require complex synthesis methods, such as high-temperature sintering or specialized fabrication techniques. These processes can be time-consuming, energy-intensive, and may require stringent control of the stoichiometry and purity of the materials.[40-42]

Research efforts are focused on addressing these challenges through material optimization, doping strategies, interface engineering, and advanced synthesis techniques. By overcoming these problems, oxide-based solid electrolytes can potentially become more practical and widely adopted in solid-state battery technologies.[42]

1.6 Sulfide-based Solid Electrolytes

Sulfide-based solid electrolytes are a class of materials that have gained significant attention in the development of solid-state batteries. These electrolytes are composed primarily of sulfur and other elements such as lithium, sodium, or phosphorus. Sulfide-based electrolytes offer several advantages for solid-state battery applications. One of the key advantages of sulfide-based electrolytes is their high ionic conductivity. Sulfide materials have inherently high mobility of sulfide ions, allowing for efficient ion transport within the electrolyte. This high ionic conductivity enables faster charging and discharging rates, leading to improved battery performance. [43]

Inorganic glass materials are known for their unique amorphous structure, which is distinct from the regular crystalline arrangement of atoms found in crystalline materials. This amorphous structure provides several advantages for ionic conductivity.[44] One of the primary reasons why inorganic glass materials exhibit higher ionic conductivity compared to their crystalline counterparts is their open structure. In glass materials, the arrangement of atoms is disordered, resulting in a network of interconnected voids and open spaces. This open structure creates pathways for ions to move more freely within the material, facilitating their transport. Additionally, inorganic glass materials possess a

larger free volume compared to crystalline materials. The free volume refers to the empty spaces between atoms or molecules in a material.[45] In glasses, the presence of larger free volume allows for more mobility of ions, as they have greater space to move and diffuse. This enhanced ion mobility contributes to higher ionic conductivity. Furthermore, the absence of long-range order in glass materials eliminates barriers and defects associated with crystal grain boundaries. In crystalline materials, grain boundaries can impede ion diffusion due to the mismatch in crystal structure between adjacent grains. In contrast, the amorphous nature of glass materials ensures a more continuous and unobstructed ion conduction path.[44-45] The $75\text{Li}_2\text{S}\cdot 25\text{P}_2\text{S}_5$ glass was reported in other studies to have similar ionic conductivities, in the range of $10^{-4} \text{ S cm}^{-1}$. [46] In the LPS (lithium phosphorus sulfide) glass system, various sulfide crystals have been discovered, including $\text{Li}_2\text{P}_2\text{S}_6$, $\text{Li}_7\text{P}_3\text{S}_{11}$, Li_3PS_4 , Li_7PS_6 , and $\text{Li}_4\text{P}_2\text{S}_6$. [47-51] The specific crystal phase formed depends on the composition of the glass and the conditions of the heat treatment. Crystallization of glass typically results in a decrease in ionic conduction. This is attributed to the formation of individual crystals within the glass, which generally have lower ionic conductivity compared to the amorphous glass phase. For example, the formation of $\text{Li}_4\text{P}_2\text{S}_6$ crystals, which have a conductivity of around $10^{-7} \text{ S cm}^{-1}$, can significantly reduce the overall ionic conductivity of a glass composition like $67\text{Li}_2\text{S}\cdot 33\text{P}_2\text{S}_5$. [47, 52] However, in the binary $x\text{Li}_2\text{S}\cdot (100 - x)\text{P}_2\text{S}_5$ system, where x is equal to or greater than 70, the glass materials exhibit a unique behavior. At high temperatures, super-ionic metastable crystalline phases precipitate within the glass, resulting in higher ionic conductivity compared to the original glass phase. The ionic conductivity of the glass ceramics formed from this system varies depending on the composition, as different crystalline phases can crystallize from the starting glass. Overall, the presence of crystalline phases in sulfide glass materials can have a significant impact on their ionic conductivity. The type and composition of the crystals formed during the crystallization process determine whether the resulting material exhibits higher or lower ionic conductivity compared to the original glass phase.[52]

Thio-LISICON (Lithium SuperIonic CONductor) structures have been identified in several systems, including $\text{Li}_2\text{S}-\text{GeS}_2$, $\text{Li}_2\text{S}-\text{GeS}_2-\text{ZnS}$, and $\text{Li}_2\text{S}-\text{GeS}_2-\text{Ga}_2\text{S}_3$. These compounds exhibit a specific structural arrangement: sulfur atoms are arranged in a

hexagonal close packing configuration, heavy metal cations occupy tetrahedral sites, and lithium atoms are found in disordered octahedral sites.[53] Six materials have been discovered to possess this thio-LISICON structure: Li_2GeS_3 , Li_4GeS_4 , $\text{Li}_2\text{ZnGeS}_4$, $\text{Li}_{4-2x}\text{Zn}_x\text{GeS}_4$, Li_5GaS_4 , and $\text{Li}_{4+x+y}(\text{Ge}_{1-y-x}\text{Ga}_x)\text{S}_4$. The unique arrangement of atoms in these thio-LISICON materials contributes to their superionic conductivity. This structure allows for the efficient movement of lithium ions within the crystal lattice, enabling high ionic conductivity. These materials hold promise for applications in advanced energy storage devices, such as solid-state batteries. $\text{Li}_{10}\text{GeP}_2\text{S}_{12}$ (LGPS) is a solid electrolyte material that has attracted significant attention due to its exceptional ionic conductivity. It exhibits an impressive ionic conductivity of $1.2 \times 10^{-2} \text{ S cm}^{-1}$ at room temperature, which is comparable to or even higher than that of liquid electrolytes.[54] This property makes LGPS a highly promising candidate for solid-state battery applications. One notable advantage of LGPS is its excellent conductivity at lower temperatures as well. It maintains a high conductivity even in sub-zero conditions, with values of $1.0 \times 10^{-3} \text{ S cm}^{-1}$ at $-30 \text{ }^\circ\text{C}$ and $4.0 \times 10^{-4} \text{ S cm}^{-1}$ at $-45 \text{ }^\circ\text{C}$. [54] This wide temperature range of high ionic conductivity further enhances its suitability for various battery systems, including those requiring operation in extreme temperature environments. The remarkable conductivity of LGPS can be attributed to its unique crystal structure, which provides favorable pathways for lithium-ion migration. The presence of lithium vacancies within the crystal lattice facilitates the movement of lithium ions, contributing to its superior ionic conductivity. The high room temperature conductivity and exceptional low-temperature performance of LGPS make it a highly promising solid electrolyte material for next-generation energy storage devices, offering the potential for enhanced safety, stability, and overall battery performance.[54] The high cost associated with the utilization of Ge metal in LGPS material presents a significant drawback, which has constrained the practical application of LGPS.[55] On the other hand, $\text{Li}_{9.54}\text{Si}_{1.74}\text{P}_{1.44}\text{S}_{11.7}\text{Cl}_{0.3}$ exhibits an outstanding Li ion conductivity, surpassing any previously reported values, with a conductivity of $2.5 \times 10^{-2} \text{ S cm}^{-1}$ at room temperature.

A promising group of solid electrolytes for solid-state batteries is the lithium argyrodite family of sulfide electrolytes, specifically $\text{Li}_6\text{PS}_5\text{X}$ ($\text{X} = \text{Cl}, \text{Br}$). These materials are appealing due to their low cost and high Li^+ conductivity at room

temperature, surpassing $10^{-3} \text{ S cm}^{-1}$. [57] The initial discovery of an argyrodite-type ion conductor was Ag_8GeS_6 , which demonstrated high Ag^+ ionic conductivity and mobility. [58] By substituting Ag^+ with other cations like Cu^+ , and replacing Ge and S with P and halogens, fast ion conductors for Ag^+ or Cu^+ such as $\text{A}_7\text{PS}_5\text{X}$ ($\text{A} = \text{Ag}^+, \text{Cu}^+$; $\text{X} = \text{Cl}, \text{Br}$) can be obtained while maintaining the argyrodite structure. [57, 58] The similarity in ionic radii between Cu^+ and Li^+ enables the potential substitution of Cu^+ by Li^+ ions in the argyrodite structure, resulting in lithium argyrodites. Deiseroth et al. reported the cubic lithium argyrodites with formulas Li_7PS_6 and $\text{Li}_6\text{PS}_5\text{X}$ ($\text{X} = \text{Cl}, \text{Br}, \text{I}$). [57]

Sulfide-based solid electrolytes offer several advantages in the context of solid-state batteries and ion conduction: [55-57, 59]

1. High ionic conductivity: Sulfide-based solid electrolytes often exhibit high ionic conductivity, enabling efficient ion transport within the electrolyte material. This high conductivity facilitates fast charge/discharge rates and promotes overall battery performance.
2. Wide electrochemical stability window: Sulfide-based electrolytes typically have a wide electrochemical stability window, allowing them to operate at higher voltages without undergoing significant degradation or side reactions. This expands the range of potential battery chemistries and improves the overall stability and safety of the battery system.
3. Good compatibility with lithium metal: Sulfide-based solid electrolytes generally exhibit good compatibility with lithium metal, reducing the likelihood of detrimental reactions such as lithium dendrite formation. This compatibility enhances the stability and lifespan of the battery, making it a desirable choice for next-generation lithium batteries.
4. Solid-state nature: Sulfide-based electrolytes are solid-state materials, offering advantages such as improved safety (eliminating the risk of liquid electrolyte leakage or flammability) and enhanced stability at high temperatures. Solid-state electrolytes can also enable the use of higher energy density electrode materials, such as lithium metal or high-voltage cathodes.

5. Potential for cost-effectiveness: Sulfide-based materials can often be synthesized from relatively abundant and low-cost elements, making them potentially more cost-effective compared to other solid electrolyte materials based on rare or expensive elements. This cost advantage can contribute to the commercial viability and widespread adoption of solid-state battery technology.

Overall, the advantages of sulfide-based solid electrolytes make them promising candidates for high-performance, safe, and reliable solid-state battery systems.

Sulfide-based solid electrolytes also have some disadvantages that need to be considered in their application:

1. Chemical reactivity: Sulfide materials can be chemically reactive, particularly with moisture or oxygen. Exposure to these elements can lead to degradation or decomposition of the electrolyte, compromising its performance and stability. Proper encapsulation or protection measures are required to mitigate this issue.
2. Mechanical stability: Some sulfide-based electrolytes may have poor mechanical stability, leading to issues such as cracking, fragmentation, or loss of contact within the solid electrolyte layer. Mechanical instability can result from volume changes during cycling or stress from electrode-material expansion and contraction, affecting the long-term performance and durability of the battery.
3. Interface compatibility: Sulfide-based electrolytes may have challenges in achieving good interface compatibility with electrode materials. For example, the formation of an interfacial layer or side reactions between the electrolyte and electrode can hinder ion transport and degrade battery performance over time. Interface engineering strategies are necessary to address these compatibility issues.
4. Processing complexity: The synthesis and processing of sulfide-based solid electrolytes can be more complex compared to other types of electrolytes. Specialized techniques and conditions are often required to achieve desired material properties, homogeneity, and structural stability. This complexity can impact the scalability and cost-effectiveness of manufacturing processes.

5. Environmental considerations: Sulfide-based materials may contain elements that raise environmental concerns. For example, some sulfide compounds may include heavy metals or other toxic elements. Proper handling, disposal, and recycling methods are necessary to ensure environmental sustainability and minimize potential hazards associated with these materials.
6. Chemical reactivity: While sulfide-based electrolytes can exhibit good electrochemical stability, they may still be susceptible to reactions with certain electrode materials or specific operating conditions. For example, at high potentials, sulfide electrolytes could react with lithium metal or undergo undesired chemical transformations. Proper electrode-electrolyte compatibility and optimization of cell design are necessary to ensure long-term stability.

It's important to note that ongoing research and development efforts are focused on addressing these disadvantages and optimizing the performance of sulfide-based solid electrolytes for practical applications in solid-state batteries.

1.7 Oxysulfide-based Solid Electrolyte

Oxysulfide solid electrolytes are a class of materials that combine both oxygen and sulfur elements in their composition and exhibit ion-conducting properties. These materials have attracted significant attention as potential candidates for solid electrolytes in various electrochemical devices, including solid-state batteries. The oxysulfide solid electrolytes typically consist of a combination of metal cations, oxygen anions, and sulfur anions. The presence of both oxygen and sulfur in the crystal lattice provides unique properties and advantages for ion transport. The oxygen ions (O^{2-}) and sulfur ions (S^{2-}) contribute to the ionic conduction within the material, enabling the transport of charge carriers such as lithium ions (Li^+) or other metal ions. In recent studies, the introduction of oxygen doping has shown to enhance the stability of argyrodite-type solid electrolytes. Various approaches have been explored, including the incorporation of ZnO into Li_6PS_5Br , partial substitution of Li_2O into Li_6PS_5Cl or Li_6PS_5Br , P_2O_5 into $Li_{5.5}PS_{4.5}Cl_{1.5}$, Li_3PO_4 into Li_6PS_5Cl , SnO_2 into Li_6PS_5I , and Li_3PO_4 into mixed halide $Li_6PS_{5-x}O_xCl_{0.5}Br_{0.5}$. [60-

66] These oxygen-doped or substitution strategies have demonstrated significant improvements in stability, particularly when in contact with lithium metal anodes and oxide cathodes. The combination of oxide and sulfide materials offers a promising solution for achieving excellent solid electrolytes for Advanced Solid-State Lithium Batteries (ASSLiBs). By combining the electrochemical stability provided by oxide materials with the high electroconductivity and favorable mechanical properties of sulfide materials, these hybrid electrolytes hold great potential for enabling high-performance battery systems. The synergistic effects of both components create a solid electrolyte that exhibits enhanced stability, efficient ion conduction, and improved overall performance in advanced lithium battery applications. [67-69]

1.8 Synthesize of Sulfide-based Solid Electrolyte

Due to their high reactivity in humid air, sulfides are typically prepared under inert atmospheres. The most commonly used methods for synthesizing sulfide solid-state electrolytes are melt-quenching and ball-milling. These techniques involve high-temperature treatment or prolonged mechanical mixing. However, wet chemical processes have been developed as an alternative and offer significant advantages for scaling up production compared to traditional methods.[55]

1.8.1 Melt Quench

Melt quenching is a commonly employed technique for producing sulfide glass materials. In this method, the initial ingredients, such as Li_2S and P_2S_5 , are placed in a quartz tube and melted at temperatures ranging from 900 to 1100 °C.[69, 70] The molten mixture is then rapidly cooled either by immersion in ice water or by using a twin roller quenching machine. To prevent the loss of P_2S_5 due to its high vapor pressure, the melting reaction is typically conducted in sealed tubes. One strategy to enhance Li ion conductivity is by increasing the concentration of Li ions, which has been found to be effective across various sulfide systems. Another approach involves blending oxide powder with sulfide glass, known as the "mixed anion effect." This mixing technique has

been observed to improve both the conductivity and stability of the resulting mixture in certain systems.[71, 72]

1.8.2 Ball Milling

Ball-milling has emerged as a preferred method for producing finely mixed powders due to its effectiveness and convenience compared to melt-quenching. It operates based on the principles of impact and attrition, allowing for efficient pulverization, amorphization, and mixing of materials. Unlike melt-quenching, ball-milling occurs at room temperature. The process does not involve local melting but instead relies on solid-state inter-diffusion reactions facilitated by point and lattice defects induced by plastic deformation. This solid-state approach enables the amorphization process during ball-milling.[45, 73] In the $\text{Li}_2\text{S}-\text{P}_2\text{S}_5-\text{GeS}_2$ ternary system, ball-milling allows for the formation of amorphous samples over a wider range compared to other methods. The mechanical mixing and grinding action of ball-milling promote the disruption of crystal structures, leading to the formation of amorphous phases. As a result, a larger region of amorphous samples can be achieved through ball-milling in this ternary system.[74] Ball-milling offers a wide range of possibilities for the preparation of new amorphous glassy materials. It is a versatile method that can be used to produce most sulfide glass conductors. By carefully controlling the mixing and subsequent annealing steps, it is also possible to obtain crystalline phases in the material. This flexibility in processing enables the synthesis of a variety of sulfide-based materials with tailored properties for solid-state electrolyte applications.[75]

1.8.3 Liquid Phase Synthesis or Wet Chemical Reactions

Although solid electrolytes prepared through melt-quenching and ball-milling demonstrate high ionic conductivity, these conventional methods are time-consuming, energy-intensive, and challenging to scale up. In contrast, the use of liquid-based methods for solid electrolyte preparation offers several advantages. Wet chemical reactions or liquid phase synthesis enable shorter reaction times and the production of homogeneous materials. Additionally, this method facilitates the formation of intimate electrode-electrolyte interfaces, leading to improved overall performance in solid-state electrolyte

applications.[76-78] Due to the high reactivity of sulfide solid electrolyte (SE) precursors, wet-chemical reactions are typically limited to nonpolar solvents and less polar aprotic solvents. This is because these solvents offer better stability and compatibility with the reactive sulfide materials. The choice of solvent plays a crucial role in ensuring successful synthesis and preventing unwanted side reactions. By using appropriate solvents, the wet-chemical approach can still be effectively utilized for the preparation of sulfide SEs while mitigating reactivity issues.[79, 80]

At room temperature, Li_3PS_4 exists in the γ phase, which is not highly ionically conductive. However, it undergoes a phase transition to the β phase at around 200 °C, which exhibits excellent ionic conductivity. The β - Li_3PS_4 phase is metastable and is conventionally prepared through a solid-state reaction between Li_2S and P_2S_5 at high temperatures. This reaction allows for the formation of the desired β phase with its enhanced ionic conductivity. The high-temperature solid-state synthesis method is commonly employed to produce β - Li_3PS_4 , enabling the material to exhibit its desirable conductivity properties. After the synthesis of $\text{Li}_3\text{PS}_4 \cdot \text{THF}$ powder, the material undergoes a transformation when the THF (tetrahydrofuran) solvent is removed at a temperature of 140 °C. This removal process leads to the development of a nanoporous structure within the material. The resulting Li_3PS_4 material exhibits a high surface area of $15.6 \text{ m}^2 \text{ g}^{-1}$, indicating a large accessible area for electrochemical reactions. The average pore size in this nanoporous structure is measured to be approximately 28 nm, suggesting the presence of interconnected pores within the material. This nanoporous structure enhances the material's properties and provides additional pathways for ionic transport and electrolyte-electrode interactions.[81] The presence of a nanoporous structure in the Li_3PS_4 material induces a high surface energy, leading to a chemical lattice distortion. This distortion has an effect on the phase transition behavior of the material. Specifically, it causes a downward shift in the temperature at which the transition from the γ phase to the β phase occurs. As a result, the metastable β phase is stabilized over a wider temperature range than in non-nanoporous structures. This stabilization of the β phase at lower temperatures expands the operating temperature range for the material, making it more suitable for various applications requiring solid-state electrolytes.[81] Additionally, the dissociation of THF and the formation of the nanoporous structure introduce lattice defects on the surface of the Li_3PS_4 material. These defects create a space-charge region

within the material, which plays a crucial role in enhancing the ionic conductivity. As a result of this enhanced conductivity, the $\text{Li}_3\text{PS}_4\cdot\text{THF}$ material exhibits a high ionic conductivity of $1.6 \times 10^{-4} \text{ S cm}^{-1}$ at $25 \text{ }^\circ\text{C}$. [81] In contrast, when ethyl acetate is employed as the reaction medium, the precursor material undergoes crystallization at a lower temperature of $160 \text{ }^\circ\text{C}$, resulting in the formation of the $\beta\text{-Li}_3\text{PS}_4$ phase. This crystalline phase exhibits a high ionic conductivity of $3.3 \times 10^{-4} \text{ S cm}^{-1}$ at room temperature. [82] In a previous study conducted by our group, Li_3PS_4 was synthesized using a shaking method with ethyl propionate as the reaction medium. Interestingly, the resulting product exhibited a thio-LISICON III structure, deviating from the typical β - or $\gamma\text{-Li}_3\text{PS}_4$ phases. Despite the structural difference, this material demonstrated a considerable conductivity of $2.0 \times 10^{-4} \text{ S cm}^{-1}$ at room temperature. This finding highlights the versatility of synthesis methods and their influence on the resulting crystal structure and conductivity properties of sulfide-based solid electrolytes. [83]

Xu et al. conducted a study on the wet synthesis of metastable glass ceramic $\text{Li}_7\text{P}_3\text{S}_{11}$ and investigated the influence of different solvents on its electrochemical behavior. They examined the effects of using THF (tetrahydrofuran), acetonitrile (ACN), and a mixed solution of THF and ACN. The results showed that ACN facilitated the formation of pure phase $\text{Li}_7\text{P}_3\text{S}_{11}$, indicating a favorable synthesis outcome. In contrast, the use of THF led to the nucleation of a side phase known as $\text{Li}_4\text{P}_2\text{S}_6$. [84] This was evident from the Raman spectra, which showed a distinct peak corresponding to the $\text{P}_2\text{S}_6^{4-}$ vibration in the $\text{Li}_4\text{P}_2\text{S}_6$ phase. Due to the difficulty in removing THF molecules during the evaporation process, they tended to accumulate at the grain boundaries of the $\text{Li}_7\text{P}_3\text{S}_{11}$ sample. This accumulation of THF hindered the migration of lithium ions, which is essential for efficient ion conductivity. As a result, the sample prepared with THF exhibited more cracks and holes, which in turn reduced the energy barrier for the nucleation of the side phase ($\text{Li}_4\text{P}_2\text{S}_6$). [84] In the study conducted by Yao et al., they employed (ACN) as a solvent to synthesize $\text{Li}_7\text{P}_3\text{S}_{11}$. The resulting $\text{Li}_7\text{P}_3\text{S}_{11}$ material exhibited a room temperature conductivity of $1.5 \times 10^{-3} \text{ S cm}^{-1}$. [78] Additionally, $\text{Li}_7\text{P}_3\text{S}_{11}$ can be synthesized using a single solvent, namely 1,2-dimethoxyethane (DME), and the resulting material exhibits an ionic conductivity of $2.5 \times 10^{-4} \text{ S cm}^{-1}$ after undergoing heat treatment. The variation in ionic conductivity observed among materials prepared using different methods could be attributed to differences in crystallinity and the

presence of amorphous impurities. These factors can influence the mobility of ions and affect the overall conductivity of the $\text{Li}_7\text{P}_3\text{S}_{11}$ solid electrolyte.[85]

1.9 Objectives

In this doctoral thesis, the author focuses on addressing several key challenges for the commercialization of all-solid-state Li-ion batteries (ASSLiBs). The specific areas of study include:

- (a) Liquid-phase synthesis of sulfide solid electrolytes: The thesis investigates the development of a liquid-phase synthesis method for sulfide-based solid electrolytes. This approach aims to enable more efficient and scalable production of these electrolyte materials, which is crucial for large-scale manufacturing of ASSLiBs.
- (b) Solvent selection for pure product formation: The thesis explores the selection of appropriate solvents to ensure the formation of pure and high-quality sulfide-based solid electrolytes. Contamination or impurities in the electrolyte materials can significantly affect their electrochemical performance and stability, so careful solvent selection is essential.
- (c) Development of oxygen doping in sulfide-based solid electrolytes: Another significant aspect of the thesis is the investigation of oxygen doping in sulfide-based solid electrolytes. This research seeks to enhance the electrochemical stability and compatibility of the electrolyte materials with lithium metal and oxide cathodes. Oxygen doping has shown promise in improving the overall performance and stability of ASSLiBs.

Overall, this doctoral thesis aims to contribute to the advancement of ASSLiBs by addressing critical issues related to the synthesis, purity, and performance of sulfide-based solid electrolytes, as well as exploring the potential benefits of oxygen doping in these materials.

1.10 Outline

The thesis is organized into five chapters, with Chapter 1 serving as the introduction. Chapters 2 to 5 form the main body of the thesis and follow a consistent structure. Each chapter begins with an introduction, followed by sections on experimental methods, results and discussion, and concludes with a summary of the findings.

In chapter 2, electrochemical properties characterization and examination of $100\text{Li}_3\text{PS}_4\text{-}50\text{LiI-xLi}_3\text{PS}_4$ solid electrolyte by the liquid phase shaking method were conducted. The main experimental technique employed in this study was used to evaluate the electrochemical properties of the solid electrolyte under different conditions. The effects of concentration and heat treatment temperature on the electrolyte were investigated using this technique. The results obtained from this experimental approach were analyzed and discussed in detail in the chapter.

In chapter 3, the focus was on the liquid phase synthesis of $\text{Li}_6\text{PS}_5\text{Cl}$ argyrodite solid electrolyte. The choice of solvent was carefully considered to ensure the production of pure argyrodite solid electrolyte. The mechanism of oxide side reactions was thoroughly analyzed and investigated. The chapter also delved into the exploration of the optimum heat treatment temperature and time in order to achieve the best electrochemical performance of $\text{Li}_6\text{PS}_5\text{Cl}$ argyrodite solid electrolytes. The experimental procedures, results, and discussions regarding these aspects were presented in detail in this chapter.

In chapter 4, the primary focus was on controlling the amount of oxygen doping in pure $\text{Li}_6\text{PS}_5\text{Cl}$ argyrodite solid electrolyte. The purpose of this investigation was to determine the optimal amount of oxygen doping that could further enhance the electrochemical performance of the pure argyrodite material. The chapter detailed the experimental methods employed to introduce controlled amounts of oxygen, as well as the characterization techniques used to assess the resulting electrochemical properties. The findings and discussions presented in this chapter shed light on the impact of oxygen doping on the overall performance of $\text{Li}_6\text{PS}_5\text{Cl}$ argyrodite solid electrolytes.

In chapter 5, the thesis culminated with a comprehensive conclusion that encompassed the collective findings and insights obtained from the various studies conducted throughout the research. This chapter provided a concise summary of the main results and outcomes of the experimental investigations discussed in the preceding

chapters. It also highlighted the key implications and contributions of the research in the field of solid electrolytes. Additionally, the chapter discussed potential avenues for future work, identifying areas that could be explored to further advance the understanding and application of the studied materials. Overall, chapter 5 served as a final reflection on the research conducted in the thesis and offered valuable insights for future research endeavors.

References

- [1] Arunachalam, V. S.; Fleischer, E. L. The Global Energy Landscape and Materials Innovation. *MRS Bulletin* **2008**, *33*, pp. 264–288.
- [2] Yang, Z.; Zhang, J.; Kintner-Meyer, M. C. W.; Lu, X.; Choi, D.; Lemmon, J. P.; Liu, J. Electrochemical Energy Storage for Green Grid. *Chem. Rev.* **2011**, *111*, pp. 3577–3613.
- [3] Tian, Y.; Zeng, G.; Rutt, A.; Shi, T.; Kim, H.; Wang, J.; Koettgen, J.; Sun, Y.; Ouyang, B.; Chen, T.; Lun, Z.; Rong, Z.; Persson, K.; Ceder, G. Promises and Challenges of Next-Generation “beyond Li-Ion” Batteries for Electric Vehicles and Grid Decarbonization. *Chem. Rev.* **2021**, *121*, pp. 1623–1669.
- [4] Gür, T. M. Review of Electrical Energy Storage Technologies, Materials and Systems: Challenges and Prospects for Large-Scale Grid Storage. *Energy Environ. Sci.* **2018**, *11*, pp. 2696–2767.
- [5] Lee, S.; Manthiram, A. Can Cobalt Be Eliminated from Lithium-Ion Batteries? *ACS Energy Lett.* **2022**, *7*, pp. 3058–3063.
- [6] Morimoto, M. Which is the first electric vehicle? *Electr. Eng. Jpn.* **2015**, *192*, pp. 31–38.
- [7] Global Plug-in Vehicle Sales Reached over 3,2 Million in **2020**, <https://www.ev-volumes.com/news/86364/>
- [8] Cheng, Z., Pan, H., Li, F. *et al.* Achieving long cycle life for all-solid-state rechargeable Li-I₂ battery by a confined dissolution strategy. *Nat. Commun.* **2022**, *13*, 125.
- [9] Wang, R., Zhang, X., Cai, Y. *et al.* Safety-reinforced rechargeable Li-CO₂ battery based on a composite solid state electrolyte. *Nano Res.* **2019**, *12*, pp. 2543–2548.
- [10] T. Horiba, "Lithium-Ion Battery Systems," in *Proceedings of the IEEE*, **2014**, *102*, no. 6, pp. 939-950.
- [11] M. A. Hannan, M. M. Hoque, A. Hussain, Y. Yusof and P. J. Ker, "State-of-the-Art and Energy Management System of Lithium-Ion Batteries in Electric Vehicle Applications: Issues and Recommendations," in *IEEE Access*, **2018**, vol. 6, pp. 19362 – 19378.

- [12] Arora, P. and Zhang (John), Z. Battery Separators, *Chemical Reviews*, **2004**, *104* (10), pp. 4419-4462.
- [13] Lagadec, M.F., Zahn, R. & Wood, V. Characterization and performance evaluation of lithium-ion battery separators. *Nat. Energy*. **2019**, *4*, pp. 16–25.
- [14] Bandhauer, T. M., Garimella, S., and Fuller, T. F. A Critical Review of Thermal Issues in Lithium-Ion Batteries, *J. Electrochem. Soc.* **2011**, *158*, R1.
- [15] Takada, K. Progress and Prospective of Solid-State Lithium Batteries. *Acta Mater.* **2013**, *61*, pp. 759–770.
- [16] Lian, P-J., Zhao, B-S., Zhang, L-Q., Xu, N., Wu, M-T., and Gao, X-P. Inorganic sulfide solid electrolytes for all-solid-state lithium secondary batteries, *J. Mater. Chem. A*, **2019**, *7*, pp. 20540-20557.
- [17] Hou, M., Liang, F., Chen, K., Dai, Y., and Xue, D. Challenges and perspectives of NASICON-type solid electrolytes for all-solid-state lithium batteries, *Nanotechnology*, **2020**, *31*, 132003.
- [18] Sakuda, A., Hayashi, A., and Tatsumisago, M. Sulfide Solid Electrolyte with Favorable Mechanical Property for All-Solid-State Lithium Battery. *Sci Rep*, **2013**, *3*, 2261.
- [19] Cao, D., Sun, X., Li, Q., Natan, A., Xiang, P., and Zhu, H. Lithium Dendrite in All-Solid-State Batteries: Growth Mechanisms, Suppression Strategies, and Characterizations, *Matter*, **2020**, *3*, Issue 1, pp. 57-94.
- [20] J.L. Allen, J. Wolfenstine, E. Rangasamy, J. Sakamoto, Effect of substitution (Ta, Al, Ga) on the conductivity of $\text{Li}_7\text{La}_3\text{Zr}_2\text{O}_{12}$, *J. Power Sources*, **2012**, *206*, pp. 315-319.
- [21] Y. Kato, S. Hori, T. Saito, K. Suzuki, M. Hirayama, A. Mitsui, M. Yonemura, H. Iba, R. Kanno, “High-power all-solid-state batteries using sulfide superionic conductors”, *Nature Energy*, **2016**, *1*, 16030.
- [22] J. C. Bachman, S. Muy, A. Grimaud, H. H. Chang, N. Pour, S. F. Lux, O. Paschos, F. Maglia, S. Lupart, P. Lamp, L. Giordano, Y. Shao-Horn, “Inorganic Solid-State Electrolytes for Lithium Batteries: Mechanisms and Properties Governing Ion Conduction”, *Chem. Rev.* **2016**, *116*, pp. 140-162.

- [23] Chang, Z., Yang, H., Zhu, X. *et al.* A stable quasi-solid electrolyte improves the safe operation of highly efficient lithium-metal pouch cells in harsh environments. *Nat. Commun.* **2022**, *13*, 1510.
- [24] Oh, K., Chang, D., Lee, B., Kim, D. H., Yoon, G., Park, I., Kim, B.; Kang, K. Native Defects in $\text{Li}_{10}\text{GeP}_2\text{S}_{12}$ and Their Effect on Lithium Diffusion. *Chem. Mater.* **2018**, *30*, pp. 4995–5004.
- [25] Gorai, P., Long, H., Jones, E., Santhanagopalan, S., Stevanović, V. Defect Chemistry of Disordered Solid-State Electrolyte $\text{Li}_{10}\text{GeP}_2\text{S}_{12}$. *J. Mater. Chem. A.* **2020**, *8*, pp. 3851–3858.
- [26] Lorget, S., Usiskin, R. E., Maier, J. Transport and Charge Carrier Chemistry in Lithium Sulfide. *Adv. Funct. Mater.* **2019**, *29*, pp. 1807688–1807698.
- [27] Maier, J. Defect Chemistry and Ion Transport in Nanostructured Materials Part II. Aspects of Nanoionics. *Solid State Ionics*, **2003**, *157*, pp. 327–334.
- [28] Heleen van Gog and Marijn A. van Huis, Structural and Electronic Properties of Frenkel and Schottky Defects at the $\text{MgO}\{100\}$ Surface: Spin Polarization, Mid-Band Gap States, and Charge Trapping at Vacancy Sites, *The Journal of Physical Chemistry C*, **2019**, *123* (23), pp. 14408-14420
- [29] Einstein, A. Über Die von Der Molekularkinetischen Theorie Der Wärme Geforderte Bewegung von in Ruhenden Flüssigkeiten Suspendierten Teilchen. *Ann. Phys.* **1905**, *322*, pp. 549–560.
- [30] Von Smoluchowski, M. Zur Kinetischen Theorie Der Brownschen Molekularbewegung Und Der Suspensionen. *Ann. Phys.* **1906**, *326*, pp. 756–780.
- [31] Wang, Y., Richards, W. D., Ong, S. P., Miara, L. J., Kim, J. C., Mo, Y., Ceder, G. Design Principles for Solid-State Lithium Superionic Conductors. *Nat. Mater.* **2015**, *14*, pp. 1026–1031.
- [32] Zhou, L., Assoud, A., Zhang, Q., Wu, X., Nazar, L. F. New Family of Argyrodite Thioantimonate Lithium Superionic Conductors. *J. Am. Chem. Soc.* **2019**, *141*, pp. 19002–19013.
- [33] He, X., Zhu, Y., Mo, Y. Origin of Fast Ion Diffusion in Super-Ionic Conductors. *Nat. Commun.* **2017**, *8*, pp. 15893–15898.
- [34] M. Sakakura, K. Mitsuishi, T. Okumura, N. Ishigaki, and Y. Iriyama, Fabrication of Oxide-Based All-Solid-State Batteries by a Sintering Process Based on Function

- Sharing of Solid Electrolytes, *ACS, Applied Materials & Interfaces*, **2022**, *14* (43), pp. 48547-48557.
- [35] Abin, K., Seungjun, w., Minseok, K., Heetaek, P., and Byoungwo, K. Research Progresses of Garnet-Type Solid Electrolytes for Developing All-Solid-State Li Batteries, *Frontiers in Chemistry*, **2020**, *8*.
- [36] Habin C. and Byoungwoo K. Mechanical and Thermal Failure Induced by Contact between a $\text{Li}_{1.5}\text{Al}_{0.5}\text{Ge}_{1.5}(\text{PO}_4)_3$ Solid Electrolyte and Li Metal in an All Solid-State Li Cell, *ACS, Chemistry of Materials*, **2017**, *29* (20), pp. 8611-8619
- [37] Teng, S., Tan, J., and Tiwari, A. Recent developments in garnet based solid state electrolytes for thin film batteries. *Curr. Opin. Solid State Mater. Sci.*, **2014**, *18*, 1, pp. 29-38.
- [38] Han, F., Zhu, Y., He, X., and Mo, Y. Electrochemical Stability of $\text{Li}_{10}\text{GeP}_2\text{S}_{12}$ and $\text{Li}_7\text{La}_3\text{Zr}_2\text{O}_{12}$ Solid Electrolytes. *Advanced Energy Materials*, **2017**, *7*, 1602738.
- [39] G. Ceder, M.K. Aydinol, The electrochemical stability of lithium-metal oxides against metal reduction, *Solid State Ionics*, **1998**, *109*, Issues 1–2, pp. 151-157.
- [40] Janek, J., & Zeier, W. G. A Solid Future for Battery Development. *Nature Energy*, **2016**, *1*(9), 16141.
- [41] Zhang, L., et al. Recent Advances and Challenges of Oxide-Based Solid Electrolytes for All-Solid-State Lithium Batteries. *Advanced Energy Materials*, **2020**, *10*(47), 2002062.
- [42] Wei, R., Chen, S., Gao, T., Liu, W., Challenges, fabrications and horizons of oxide solid electrolytes for solid-state lithium batteries, *Nano Select.* **2021**, *2*, 2256.
- [43] Manthiram, A., Yu, X. & Wang, S. Lithium battery chemistries enabled by solid-state electrolytes. *Nat Rev Mater.* **2017**, *2*, 16103.
- [44] C. Dietrich, D. A. Weber, S. J. Sedlmaier, S. Indris, S. P. Culver, D. Walter, J. Janek, W. G. Zeier, Lithium ion conductivity in Li_2S – P_2S_5 glasses – building units and local structure evolution during the crystallization of superionic conductors Li_3PS_4 , $\text{Li}_7\text{P}_3\text{S}_{11}$ and $\text{Li}_4\text{P}_2\text{S}_7$, *J. Mater. Chem. A.* **2017**, *5*, 18111.
- [45] A. Hayashi, S. Hama, H. Morimoto, M. Tatsumisago, T. Minami, Preparation of Li_2S – P_2S_5 Amorphous Solid Electrolytes by Mechanical Milling, *J. Am. Ceram. Soc.* **2004**, *84*, 477.

- [46] T. Ohtomo, A. Hayashi, M. Tatsumisago, Y. Tsuchida, S. Hama, K. Kawamoto, All-solid-state lithium secondary batteries using the $75\text{Li}_2\text{S}\cdot 25\text{P}_2\text{S}_5$ glass and the $70\text{Li}_2\text{S}\cdot 30\text{P}_2\text{S}_5$ glass–ceramic as solid electrolytes, *J. Power Sources*, **2013**, 233, 231.
- [47] C. Dietrich, D. A. Weber, S. Culver, A. Senyshyn, S. J. Sedlmaier, S. Indris, J. Janek, W. G. Zeier, Synthesis, Structural Characterization, and Lithium Ion Conductivity of the Lithium Thiophosphate $\text{Li}_2\text{P}_2\text{S}_6$, *Inorg. Chem.* **2017**, 56, 6681.
- [48] H. Yamane, M. Shibata, Y. Shimane, T. Junke, Y. Seino, S. Adams, K. Minami, A. Hayashi, M. Tatsumisago, Crystal structure of a superionic conductor, $\text{Li}_7\text{P}_3\text{S}_{11}$, *Solid State Ionics*, **2007**, 178, 1163.
- [49] R. Mercier, J. P. Malugani, B. Fahys, G. Robert, J. Douglade, Structure du tetrathiohypodiphosphate de lithium, *Acta Crystallogr., Sect. B: Struct. Crystallogr. Cryst. Chem.* **1982**, 38, 1887.
- [50] S. T. Kong, Ö. Gün, B. Koch, H. J. Deiseroth, H. Eckert, C. Reiner, Structural Characterisation of the Li Argyrodites Li_7PS_6 and Li_7PSe_6 and their Solid Solutions: Quantification of Site Preferences by MAS-NMR Spectroscopy, *Chem. - Eur. J.* **2010**, 16, 5138.
- [51] R. Mercier, J. P. Malugani, B. Fahys, J. Douglade, G. Robert, Synthèse, structure cristalline et analyse vibrationnelle de l'hexathiohypodiphosphate de lithium $\text{Li}_4\text{P}_2\text{S}_6$, *J. Solid State Chem.* **1982**, 43, 151.
- [52] F. Mizuno, A. Hayashi, K. Tadanaga, M. Tatsumisago, High lithium ion conducting glass-ceramics in the system $\text{Li}_2\text{S}\text{--}\text{P}_2\text{S}_5$, *Solid State Ionics*, **2006**, 177, 2721.
- [53] R. Kanno, T. Hata, Y. Kawamoto, M. Irie, Synthesis of a new lithium ionic conductor, thio-LISICON–lithium germanium sulfide system, *Solid State Ionics*, **2000**, 130, 97.
- [54] N. Kamaya, K. Homma, Y. Yamakawa, M. Hirayama, R. Kanno, M. Yonemura, T. Kamiyama, Y. Kato, S. Hama, K. Kawamoto, A. Mitsui, A lithium superionic conductor, *Nat. Mater.* **2011**, 10, 682.
- [55] Zhang, Q., Cao, D., Ma, Y., Natan, A., Aurora, P., Zhu, H., Sulfide-Based Solid-State Electrolytes: Synthesis, Stability, and Potential for All-Solid-State Batteries. *Adv. Mater.* **2019**, 31, 1901131.

- [56] Y. Kato, S. Hori, T. Saito, K. Suzuki, M. Hirayama, A. Mitsui, M. Yonemura, H. Iba, R. Kanno, High-power all-solid-state batteries using sulfide superionic conductors, *Nat. Energy*, **2016**, *1*, 16030.
- [57] Deiseroth, H.-J., Kong, S.-T., Eckert, H., Vannahme, J., Reiner, C., Zaiß, T. and Schlosser, M., $\text{Li}_6\text{PS}_5\text{X}$: A Class of Crystalline Li-Rich Solids With an Unusually High Li^+ Mobility. *Angewandte Chemie International Edition*, **2008**, *47*: 755-758.
- [58] C. Winkler, *Ber. Dtsch. Chem. Ges.* **1886**, *19*, 210.
- [59] Chuang Yu, Feipeng Zhao, Jing Luo, Long Zhang, Xueliang Sun, Recent development of lithium argyrodite solid-state electrolytes for solid-state batteries: Synthesis, structure, stability and dynamics, *Nano Energy*, **2021**, *83*, 105858.
- [60] Z. Sun, Y. Lai, N. Lv, Y. Hu, B. Li, L. Jiang, J. Wang, S. Yin, K. Li, F. Liu, Insights on the Properties of the O-Doped Argyrodite Sulfide Solid Electrolytes ($\text{Li}_6\text{PS}_{5-x}\text{ClO}_x$, $x=0-1$), *ACS Appl. Mater. Interfaces*. **2021**, *13*, pp. 54924–54935.
- [61] L. Peng, S. Chen, C. Yu, C. Wei, C. Liao, Z. Wu, H.-L. Wang, S. Cheng, J. Xie, Enhancing Moisture and Electrochemical Stability of the $\text{Li}_{5.5}\text{PS}_{4.5}\text{Cl}_{1.5}$ Electrolyte by Oxygen Doping, *ACS Appl. Mater. Interfaces*. **2022**, *14*, pp. 4179–4185.
- [62] Z. Zhang, L. Zhang, X. Yan, H. Wang, Y. Liu, C. Yu, X. Cao, L. van Eijck, B. Wen, All-in-one improvement toward $\text{Li}_6\text{PS}_5\text{Br}$ -Based solid electrolytes triggered by compositional tune, *J. Power Sources*. **2019**, *410-411*, pp. 162–170.
- [63] M. Wu, G. Liu, X. Yao, Oxygen doped argyrodite electrolyte for all-solid-state lithium batteries, *Appl. Phys. Lett.* **2022**, *121*, 203904.
- [64] T. Chen, D. Zeng, L. Zhang, M. Yang, D. Song, X. Yan, C. Yu, Sn-O dual-doped Li-argyrodite electrolytes with enhanced electrochemical performance, *Journal of Energy Chemistry*. **2021**, *59*, pp. 530–537.
- [65] T. Hwang, Y.-J. Lee, S.R. Lee, Y.-C. Ha, M. Cho, S.-M. Lee, K. Cho, The crucial role of oxygen substitution in argyrodite solid electrolytes from the bulk to the surface under atmospheric conditions, *J. Mater. Chem. A Mater.* **2022**, *10*, pp. 16908–16919.
- [66] T. Chen, L. Zhang, Z. Zhang, P. Li, H. Wang, C. Yu, X. Yan, L. Wang, B. Xu, Argyrodite Solid Electrolyte with a Stable Interface and Superior Dendrite Suppression Capability Realized by ZnO Co-Doping, *ACS Appl. Mater. Interfaces*. **2019**, *11*, pp. 40808–40816.

- [67] T. Minami, A. Hayashi, and M. Tatsumisago, Recent progress of glass and glass-ceramics as solid electrolytes for lithium secondary batteries, *Solid State Ionics*, **2006**, *177*, 26–32, pp. 2715-2720.
- [68] M. Tatsumisago, and A. Hayashi, Superionic glasses and glass–ceramics in the $\text{Li}_2\text{S–P}_2\text{S}_5$ system for all-solid-state lithium secondary batteries, *Solid State Ionics*, **2012**, *225*, pp. 342-345.
- [69] Hou, L-P., Li, X-Y., Bi, C-X., Chen, Z-X., Li, Z., Su, L-L., Shi, P., Jin, C-B., Li, B-Q., Huang, J-Q., Zhang, X-Q., and Zhang, Q. Constructing lithium oxysulfide-rich solid electrolyte interphase to shield polysulfides in practical lithium–sulfur batteries, *J. Power Sources*, **2022**, *550*, 232144.
- [70] Z. Zhang and J. H. Kennedy, Synthesis and characterization of the $\text{B}_2\text{S}_3\text{–Li}_2\text{S}$, the $\text{P}_2\text{S}_5\text{–Li}_2\text{S}$ and the $\text{B}_2\text{S}_3\text{–P}_2\text{S}_5\text{–Li}_2\text{S}$ glass systems, *Solid State Ionics*, **1990**, *38*, 217.
- [71] J. H. Kennedy and Z. Zhang, Preparation and Electrochemical Properties of the $\text{SiS}_2\text{–P}_2\text{S}_5\text{–Li}_2\text{S}$ Glass Coformer System, *J. Electrochem. Soc.* **1989**, *136*, 2441.
- [72] M. Tatsumisago, K. Yoneda, N. Machida, and T. Hinami, Ionic conductivity of rapidly quenched glasses with high concentration of lithium ions *J. Non-Cryst. Solids*, **1987**, 95-96, 857.
- [73] R. B. Schwarz, C. C. Koch, Formation of amorphous alloys by the mechanical alloying of crystalline powders of pure metals and powders of intermetallics, *Appl. Phys. Lett.* **1986**, *49*, 146.
- [74] H. Yamamoto, N. Machida, and T. Shigematsu, A mixed-former effect on lithium-ion conductivities of the $\text{Li}_2\text{S–GeS}_2\text{–P}_2\text{S}_5$ amorphous materials prepared by a high-energy ball-milling process, *Solid State Ionics*, **2004**, *175*, 707.
- [75] Z. Zhang, L. Zhang, Y. Liu, C. Yu, X. Yan, B. Xu, and L.-m. Wang, Synthesis and characterization of argyrodite solid electrolytes for all-solid-state Li-ion batteries, *J. Alloys Compd.* **2018**, *747*, 227.
- [76] S. Teragawa, K. Aso, K. Tadanaga, A. Hayashi, and M. Tatsumisago, Preparation of $\text{Li}_2\text{S–P}_2\text{S}_5$ solid electrolyte from *N*-methylformamide solution and application for all-solid-state lithium battery, *J. Power Sources*, **2014**, *248*, 939
- [77] S. Teragawa, K. Aso, K. Tadanaga, A. Hayashi, and M. Tatsumisago, Liquid-phase synthesis of a Li_3PS_4 solid electrolyte using *N*-methylformamide for all-solid-state lithium batteries, *J. Mater. Chem. A*, **2014**, *2*, 5095.

- [78] X. Yao, D. Liu, C. Wang, P. Long, G. Peng, Y.-S. Hu, H. Li, L. Chen, and X. Xu, High-Energy All-Solid-State Lithium Batteries with Ultralong Cycle Life, *Nano Lett.* **2016**, *16*, 7148.
- [79] D. H. Kim, D. Y. Oh, K. H. Park, Y. E. Choi, Y. J. Nam, H. A. Lee, S.-M. Lee, and Y. S. Jung, Infiltration of Solution-Processable Solid Electrolytes into Conventional Li-Ion-Battery Electrodes for All-Solid-State Li-Ion Batteries, *Nano Lett.* **2017**, *17*, 3013.
- [80] T. Inada, K. Takada, A. Kajiyama, M. Kouguchi, H. Sasaki, S. Kondo, M. Watanabe, M. Murayama, and R. Kanno, Fabrications and properties of composite solid-state electrolytes, *Solid State Ionics*, **2003**, *158*, 275.
- [81] Z. Liu, W. Fu, E. A. Payzant, X. Yu, Z. Wu, N. J. Dudney, J. Kiggans, K. Hong, A. J. Rondinone, and C. Liang, Anomalous High Ionic Conductivity of Nanoporous β - Li_3PS_4 , *J. Am. Chem. Soc.* **2013**, *135*, 975.
- [82] N. H. H. Phuc, M. Totani, K. Morikawa, H. Muto, and A. Matsuda, Preparation of Li_3PS_4 solid electrolyte using ethyl acetate as synthetic medium, *Solid State Ionics*, **2016**, *288*, 240.
- [83] N. H. H. Phuc, K. Morikawa, T. Mitsuhiro, H. Muto, and A. Matsuda, Synthesis of plate-like Li_3PS_4 solid electrolyte via liquid-phase shaking for all-solid-state lithium batteries, *Ionics*, **2017**, *23*, 2061.
- [84] R. C. Xu, X. H. Xia, Z. J. Yao, X. L. Wang, C. D. Gu, and J. P. Tu, Preparation of $\text{Li}_7\text{P}_3\text{S}_{11}$ glass-ceramic electrolyte by dissolution-evaporation method for all-solid-state lithium ion batteries, *Electrochim. Acta*, **2016**, *219*, 235.
- [85] S. Ito, M. Nakakita, Y. Aihara, T. Uehara, and N. Machida, A synthesis of crystalline $\text{Li}_7\text{P}_3\text{S}_{11}$ solid electrolyte from 1,2-dimethoxyethane solvent, *J. Power Sources*, **2014**, *271*, 342.
- [86] Miao, Y., Hynan, P., von Jouanne, A., Yokochi, A. Current Li-Ion Battery Technologies in Electric Vehicles and Opportunities for Advancements. *Energies*. **2019**, *12*, 1074.
- [87] H. Gamo, Development of All-Solid-State Batteries with Sulfide Solid Electrolytes, Doctoral Thesis, Toyohashi University of Technology, January **2023**,

Chapter 2

Preparation of $100\text{Li}_3\text{PS}_4\text{-}50\text{LiI-xLi}_3\text{PO}_4$ Solid Electrolytes by Liquid Phase Shaking

2.1 Background

This chapter focuses on enhancing the ionic conductivity of the solid electrolyte by investigating the incorporation of Li_3PO_4 oxide material into the sulfide-based solid electrolyte composed of $\text{Li}_2\text{S-P}_2\text{S}_5\text{-LiI}$. The addition of Li_3PO_4 aims to not only increase the ionic conductivity but also enhance stability against lithium metal. Therefore, the shaking time for this experiment was modified to 3 hours. The primary objective of this study was to determine the optimal concentration of Li_3PO_4 addition and heat treatment temperature to achieve the highest possible ionic conductivity. This was accomplished through XRD measurement, Raman spectra analysis, and impedance analysis. Once the highest ionic conductivity was identified, further examination of the structure and electrochemical properties was conducted using techniques such as voltammogram (CV), DC polarization, and ^{31}P solid MAS-NMR. Additionally, all samples were prepared within a glove box under controlled conditions, including an Ar atmosphere with a dew point of $-90\text{ }^\circ\text{C}$ and room temperature.

2.2 Introduction

The increasing popularity of portable devices like cellular phones, cameras, and personal computers has led to a rise in the demand for power sources and energy storage. Lithium-ion batteries have become a preferred choice due to their lightweight nature, high operating voltage, impressive energy density, and long-lasting performance throughout multiple charge-discharge cycles.[1] Lithium-ion batteries are not only used in portable devices but also in larger energy storage systems such as electric vehicles and stationary

batteries. However, as the size of these systems increases, the demand for higher energy storage capacity also rises. Scaling up the battery size, though, comes with potential safety concerns related to leakage and the risk of ignition, particularly when using organic liquid electrolytes.[2] Lithium-metal and lithium-sulfur batteries are considered promising energy storage systems due to their significantly higher energy densities compared to traditional lithium-ion batteries. In fact, the energy densities of lithium-metal and lithium-sulfur batteries can be two to three times greater than those of conventional lithium-ion batteries.[3, 4] Despite their high energy density, lithium-metal batteries pose safety concerns due to issues such as the formation of lithium dendrites. These dendrites can grow and penetrate the separator, leading to the potential for short circuits and compromising the battery's safety.[5]

In recent decades, all-solid-state lithium-ion batteries (ASSLIBs) have garnered considerable attention from researchers. These batteries are considered the potential next-generation energy storage technology, offering several advantages including enhanced safety, extended cycle life, and increased energy density. These benefits are primarily attributed to the utilization of solid electrolytes (SEs) instead of liquid electrolytes. Therefore, extensive research on high-performance ionic solid electrolytes is crucial to further enhance the electrochemical performance of ASSLIBs.[6] Recently, the $\text{Li}_{10}\text{GeP}_2\text{S}_{12}$ (LGPS) sulfide-based solid electrolyte has been shown to exhibit a high ionic conductivity exceeding $10^{-2} \text{ S cm}^{-1}$ at room temperature. This recent development has garnered significant attention and holds promise for the advancement of solid-state lithium-ion batteries and other energy storage technologies.[7] Despite its impressive ionic conductivity, the use of germanium in the LGPS sulfide-based solid electrolyte poses challenges for commercialization due to its high cost. Additionally, there have been reports suggesting that LGPS may exhibit instability when in contact with lithium metal. These factors present obstacles that need to be addressed before LGPS-based electrolytes can be widely adopted in practical applications.[8] Furthermore, a recent study highlighted the potential of an oxide-based solid electrolyte, $\text{Li}_{6.75}\text{La}_3\text{Zr}_{1.75}\text{Ta}_{0.25}\text{O}_{12}$, which demonstrated relatively high lithium ion conductivity at room temperature, measuring approximately $8.7 \times 10^{-4} \text{ S cm}^{-1}$. [9]

Although previous studies have explored the addition of Li_3PO_4 to sulfide-based solid electrolytes using planetary ball-milling or melt-quenching methods, there is still limited information regarding the reaction between Li_3PO_4 and P_2S_5 in an organic medium. To address this knowledge gap, this study successfully prepared a solid electrolyte (SE) precursor of $100\text{Li}_3\text{PS}_4\text{-}50\text{LiI-xLi}_3\text{PO}_4$ using a liquid-phase shaking method with ethyl propionate. The objective was to incorporate an oxide-based Li_3PO_4 into a sulfide-based $\text{Li}_3\text{PS}_4\text{-LiI}$ system, ensuring the absence of any residual raw materials after heat treatment at temperatures up to $170\text{ }^\circ\text{C}$. The concentration of Li_3PO_4 addition and the heat treatment temperature were thoroughly investigated to determine the optimal conditions for achieving the highest lithium ion (Li^+) conductivity. Remarkably, it was discovered that samples with a 10 mol% addition of Li_3PO_4 and heat treatment at $130\text{ }^\circ\text{C}$ exhibited a notably high Li^+ conductivity of $8.5 \times 10^{-4}\text{ S cm}^{-1}$. These samples also demonstrated remarkable stability against lithium metal, even after undergoing more than 650 cycles of polarization. Additionally, they maintained an energy density of 0.3 mA cm^{-2} without experiencing any short-circuiting issues.

2.3 Experimental Method

Figure 2.1 illustrates the flowchart detailing the preparation of the $100\text{Li}_3\text{PS}_4\text{-}50\text{LiI-xLi}_3\text{PO}_4$ (LPSOI) solid electrolyte using the liquid-phase shaking method. The shaking process was conducted for a duration of 3 hours, with a shaking frequency of 1500 rpm and an amplitude of 1 cm, all performed under an argon (Ar) atmosphere. The reagents, including Li_2S , P_2S_5 , and LiI , were weighed in a molar ratio of 3:1:1 (Li_2S : 0.3827 g, P_2S_5 : 0.6173 g, LiI : 0.3717 g), resulting in the formation of $2\text{Li}_3\text{PS}_4\text{-LiI}$ ($\text{Li}_7\text{P}_2\text{S}_8\text{I}$). The desired amount of Li_3PO_4 was added based on the molar ratio of Li_3PS_4 . For simplicity, $2\text{Li}_3\text{PS}_4\text{-LiI}$ was referred to as $100\text{Li}_3\text{PS}_4\text{-}50\text{LiI}$. All the reagents were mixed together in a 45 ml centrifuge tube made of polypropylene (Labcon) along with 10 mL of ethyl propionate (EP) and 150 zirconia balls (4 mm diameter, approximately 33 g). The mixture was then subjected to shaking at 1500 rpm for 3 hours under an Ar atmosphere. The resulting suspension was dried at room temperature and subsequently at $50\text{ }^\circ\text{C}$ for 1 hour using a rotary vacuum pump. Figure 2.2 depicts the as-retrieved

suspension of the LPSOI solid electrolyte. The obtained powders were further heat-treated in a stepwise manner, starting from 70 °C for 1 hour, followed by 130 °C, 150 °C, and 170 °C for 2 hours each. All the processes were carried out under a dry Ar atmosphere. Figure 2.3 presents the as-retrieved powder of the LPSOI solid electrolyte.

To investigate the crystal structure of the retrieved sample, X-ray diffraction (XRD) analysis was conducted using an Ultima IV X-ray diffractometer from Rigaku. The characterization process was carried out with a special holder that was sealed within an argon (Ar)-filled glove box. This precautionary measure was taken to prevent exposure of the samples to air humidity, ensuring the integrity of the samples during the XRD characterization.

Raman spectroscopy analysis was performed on the sample using an NRS-3100 Raman spectrometer from Jasco. The sample was sealed inside an argon (Ar)-filled glove box during the analysis to prevent any exposure to external air. This precautionary measure ensured the preservation of the sample's properties and minimized any potential interference during the Raman spectroscopy characterization.

Solid-state ^{31}P magic-angle-spinning proton nuclear magnetic resonance (^{31}P -MAS-NMR) was employed using an Avance III 400 NMR spectrometer from Bruker. The measurements were conducted at room temperature using the typical single pulse sequence, while the spinning rate was set to 5 kHz. Prior to the ^{31}P -MAS-NMR analysis, the powdered sample was securely sealed inside a mas-rotor made of zirconia within an argon (Ar)-filled glove box. This precautionary step was taken to prevent any exposure to air humidity, ensuring the integrity of the sample during the ^{31}P -MAS-NMR characterization. Figure 2.4 provides a schematic illustration and outlines the conditions for the MAS-NMR measurements.

The temperature dependence of the ionic conductivity of the retrieved sample was investigated using alternating-current impedance spectroscopy. A Solartron SI 1260 impedance analyzer was utilized for this purpose. The measurements were carried out under a dry argon (Ar) flow, with a frequency range from 1 MHz to 10 Hz. The samples for impedance measurement were prepared by uniaxial pressing, where each sample weighed approximately 80 mg. The pressed samples were shaped into pellets with a

diameter of approximately 1 cm, applying a pressure of 255 MPa at room temperature. To facilitate the impedance measurements, the prepared pellets were placed in a holder made of Polyether ether ketone (PEEK). The holder was equipped with two blocking electrodes made from stainless steel (SUS). The entire setup, including the sample holder and electrodes, was then placed in a glass tube for the temperature-dependence measurements. A continuous flow of Ar gas was maintained during the measurements. The temperature was gradually increased starting from room temperature, with various incremental steps, until reaching 130 °C. The sample was allowed to equilibrate at each temperature for 1 hour before the impedance measurement was performed. Figure 2.5 provides a schematic diagram illustrating the setup of the impedance analyzer used in the study.

Cyclic voltammetry measurements were conducted using a Solartron SI 1287 potentiostat. The cell used for the measurements was prepared by attaching a lithium sheet (Li) with a diameter of 9 mm and a thickness of 0.1 mm to one side of the pelletized solid electrolyte (SE). The SE was sandwiched between stainless steel (SUS) electrodes. The pellets for the SE were prepared by uniaxial pressing, with each sample weighing approximately 80 mg. The pressing process resulted in pellets with a diameter of approximately 1 cm, applying a pressure of 255 MPa at room temperature. The assembled cell configuration was as follows: SUS | Li | SE | SUS. The cell was subjected to cyclic voltammetry measurements at a scan speed of 5 mV/s, with a voltage range of -0.3 to 10 V. This allowed for the observation of the voltage-current characteristics during the cyclic voltammetry test. Figure 2.6 provides a schematic diagram illustrating the setup and conditions for the cyclic voltammetry test.

A DC polarization test was conducted on the solid electrolyte (SE) using lithium metal sheets as nonblocking electrodes. The SE was sandwiched between stainless steel (SUS) electrodes. The SE itself was pelletized with a diameter of 1 cm, utilizing uniaxial cold pressing at a pressure of 255 MPa. To perform the polarization test, lithium metal sheets (Li) with a diameter of approximately 8 mm and a thickness of approximately 0.1 mm were used as the electrode material. The lithium metal sheets were placed on both sides of the pelletized SE, forming a sandwich configuration with the SE in the middle. The prepared cells were then subjected to cycling at a charge-discharge rate of ± 0.3

mA/cm². This process was facilitated using a charge-discharge device (BTS-2004H, Nagano) under a dry argon (Ar) atmosphere at room temperature. Figure 2.7 provides a schematic diagram illustrating the setup and conditions for the DC polarization test.

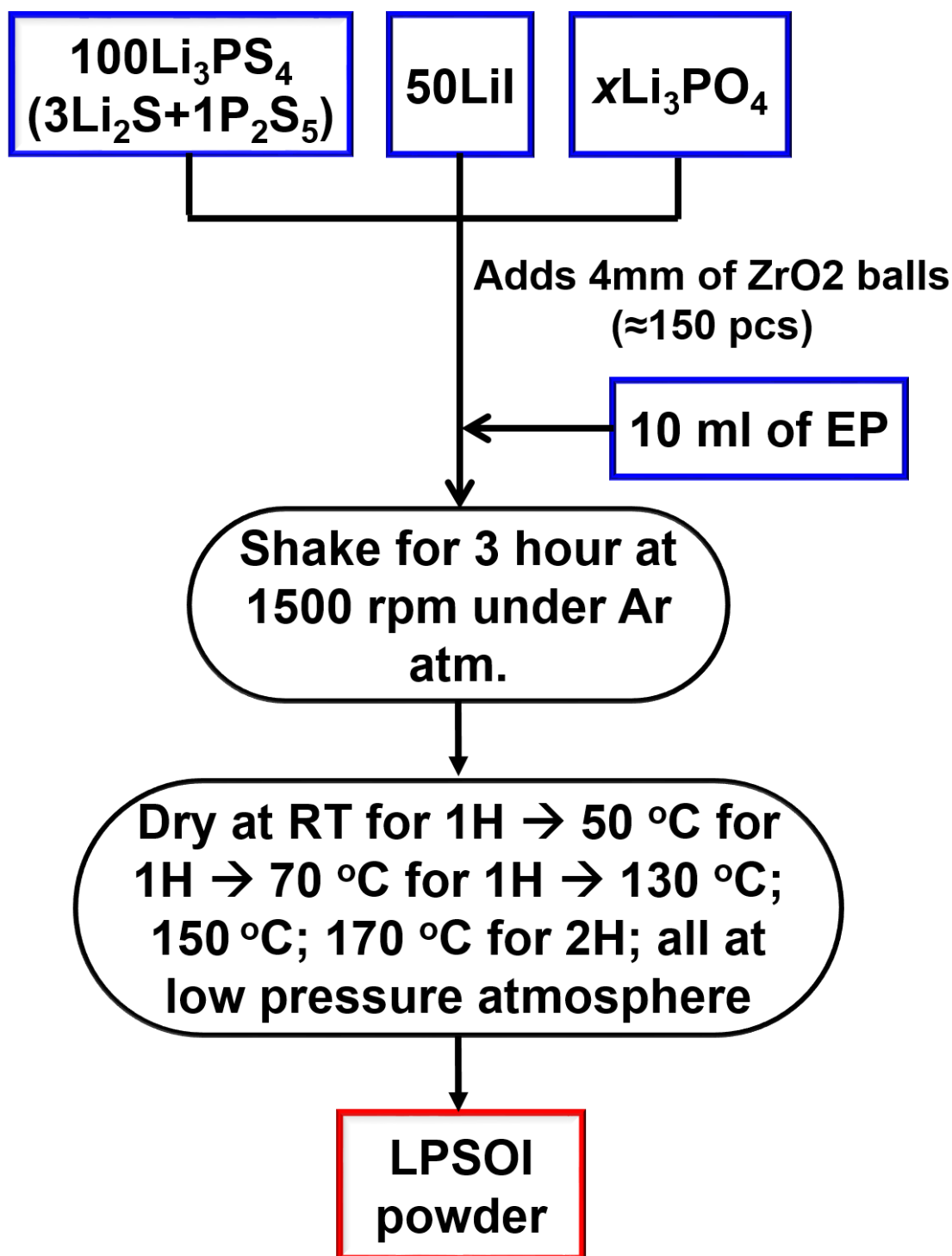


Figure 2.1. Flow chart of the preparation of $100\text{Li}_3\text{PS}_4\text{-}50\text{LiI}\text{-}x\text{Li}_3\text{PO}_4$ ($x=\text{mol}\%$) solid electrolyte with liquid phase shaking method.

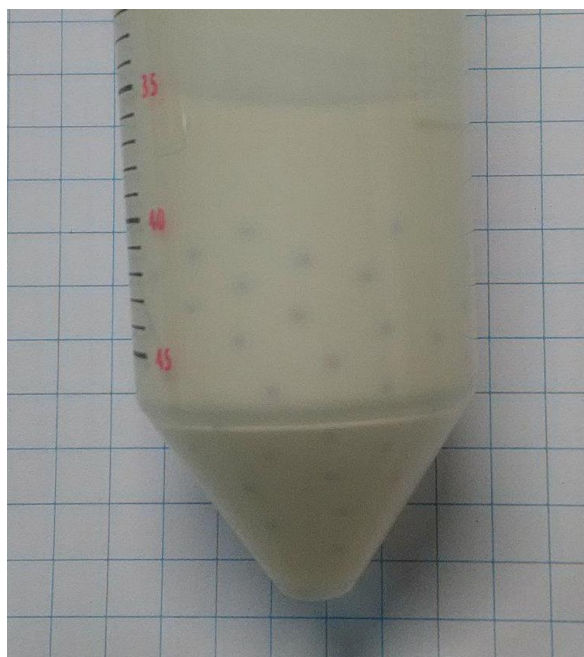


Figure 2.2. Photograph of the as-retrieved $100\text{Li}_3\text{PS}_4\text{-}50\text{LiI-xLi}_3\text{PO}_4$ ($x=\text{mol}\%$) precursor prepared after shaking process for 3 h.

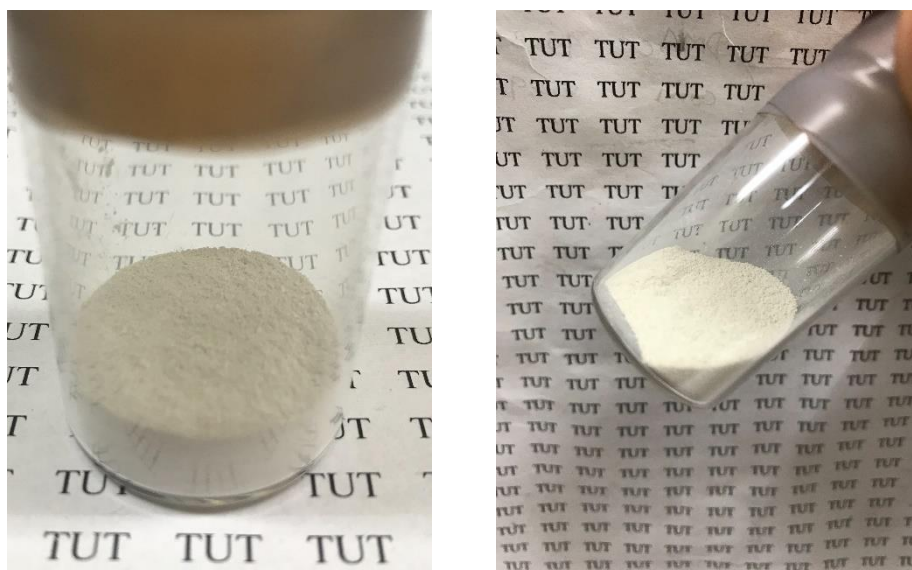


Figure 2.3. Photograph of the as-retrieved powder of $100\text{Li}_3\text{PS}_4\text{-}50\text{LiI-xLi}_3\text{PO}_4$ ($x=\text{mol}\%$) solid electrolyte.

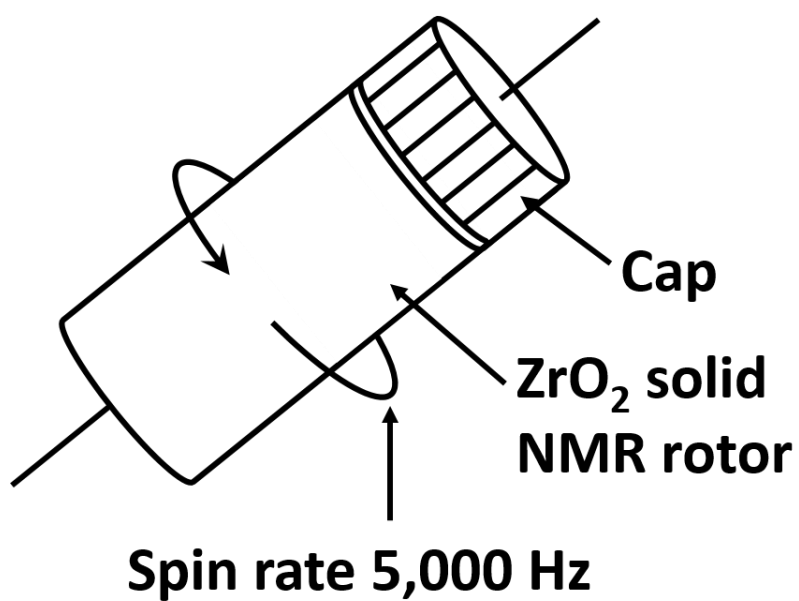


Figure 2.4. Schematic illustration of MAS-NMR measurement

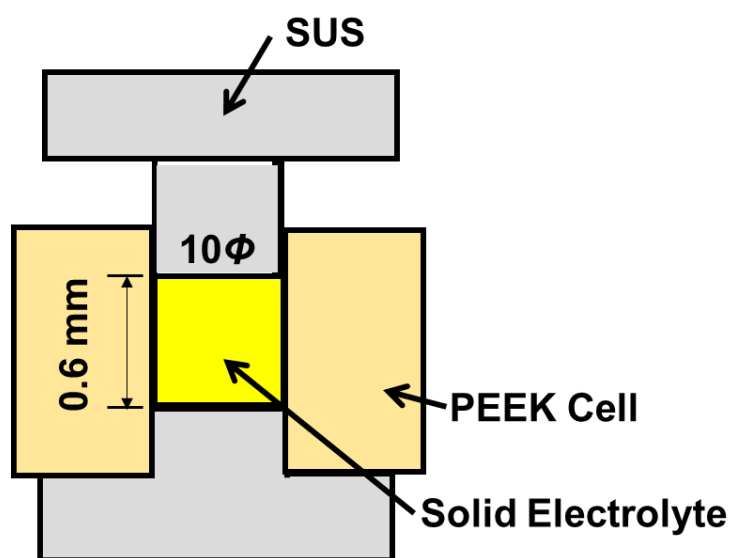
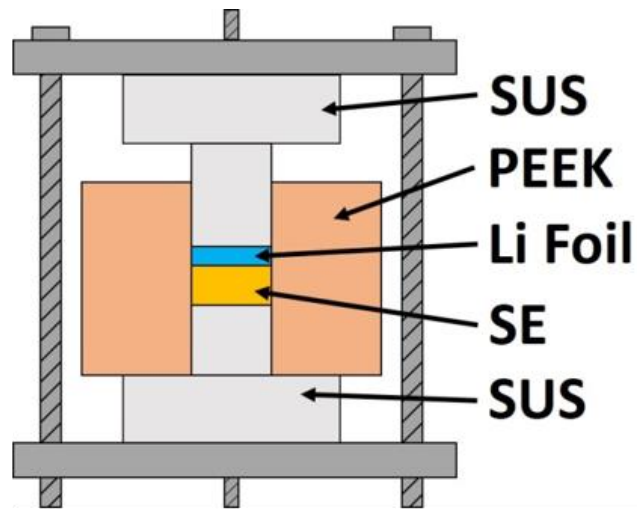
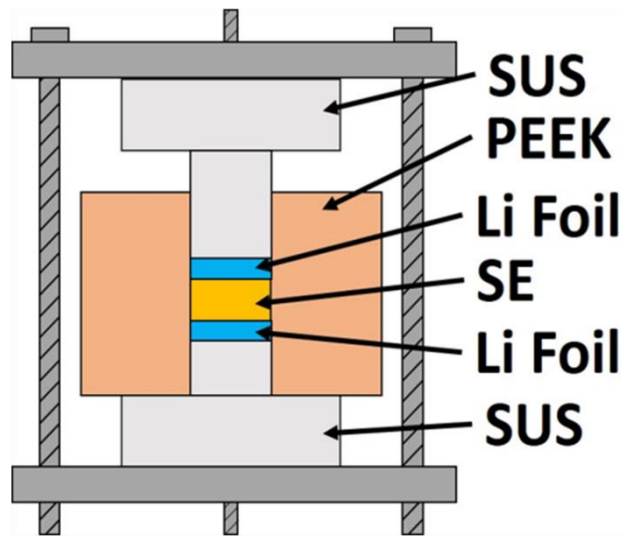


Figure 2.5. Schematic diagram of cell for ionic conductivity measurement.



Scan rate: 5 mV s⁻¹
Scan range: 10 ~ -0.3 V

Figure 2.6. Schematic diagram of cell for cyclic voltammogram test.



J: ± 0.3 mA cm⁻²
Charge time: 1 h
Discharge time: 1 h

Figure 2.7. Schematic diagram of cell for DC polarization test.

2.4 Experimental Results and Discussion

Figure 2.8 displays the XRD patterns of the $100\text{Li}_3\text{PS}_4\text{-}50\text{LiI-xLi}_3\text{PO}_4$ solid electrolyte samples after heat treatment at $130\text{ }^\circ\text{C}$, with different concentrations of Li_3PO_4 added ($0 \leq x \leq 25$). The XRD patterns include the starting materials as the reference. Similarly, Figure 2.9 and Figure 2.10 depict the XRD patterns of the $100\text{Li}_3\text{PS}_4\text{-}50\text{LiI-xLi}_3\text{PO}_4$ samples with the same varying concentrations but heat treated at $150\text{ }^\circ\text{C}$ and $170\text{ }^\circ\text{C}$, respectively. In all three sets of samples with different heat treatment temperatures, the XRD patterns do not show peaks corresponding to the starting materials up to $x = 20$. However, at $x = 25$, peaks attributed to Li_3PO_4 are observed, indicating the successful incorporation of Li_3PO_4 into $\text{Li}_2\text{S-P}_2\text{S}_5\text{-LiI}$ up to a concentration of 20. Regardless of the heat treatment temperature and Li_3PO_4 concentration, a consistent structure is observed in all samples, characterized by peaks from $\text{Li}_7\text{P}_2\text{S}_8\text{I}$, thio-LISICON II, and $\text{Li}_4\text{PS}_4\text{I}$. Previous research by Phuc et al. [10] suggests that a short-duration liquid-phase process (less than 6 hours) can lead to the formation of an thio-LISICON II in $\text{Li}_7\text{P}_2\text{S}_8\text{I}$. The peaks corresponding to these thio-LISICON II become more distinct after the addition of Li_3PO_4 and an increase in heat treatment temperature. These thio-LISICON II and $\text{Li}_4\text{PS}_4\text{I}$ bear resemblance to the glass-ceramic structure of $\text{Li}_7\text{P}_2\text{S}_8\text{I}$ described by Choi et al. [11]. The shaking process using ethyl propionate as a medium successfully facilitated the reaction between the Li_3PS_4 precursor, LiI , and Li_3PO_4 .

Figure 2.11 presents the Raman spectra of the samples obtained with varying concentrations of Li_3PO_4 after heat treatment at $130\text{ }^\circ\text{C}$. In the spectra of the SEs for all Li_3PO_4 concentrations ($0 \leq x \leq 25$), no distinct signals are observed except for the peak of PS_4^{3-} at 417 cm^{-1} . [12-14] The absence of a PO_4^{3-} peak in all prepared samples suggests that either the added PO_4^{3-} reacted with PS_4^{3-} or that the Li_3PO_4 particles were covered by the $\text{Li}_3\text{PS}_4\text{-LiI}$ solid electrolyte. It is important to note that Raman spectroscopy provides information primarily on the surface of particles, which explains why the PO_4^{3-} peak is not observed.

The temperature dependence of the ionic conductivities for the samples subjected to heat treatment at 130 , 150 , and $170\text{ }^\circ\text{C}$ for 2 hours is illustrated in Figure 2.12, 2.13, and 2.14, respectively. The relationship between composition and ionic conductivity at

room temperature is depicted in Figure 2.15. The measured ionic conductivities of the $100\text{Li}_3\text{PS}_4\text{-}50\text{LiI-xLi}_3\text{PO}_4$ solid electrolytes, obtained for various Li_3PO_4 concentrations ($0 \leq x \leq 25$) and heat treatment temperatures (130, 150, 170 °C), are summarized in Table 2.1. When the $\text{Li}_7\text{P}_2\text{S}_8\text{I}$ sample ($x = 0$) was heat treated at different temperatures (130, 150, and 170 °C), the resulting ionic conductivities at room temperature were measured as 6.9×10^{-4} , 7.8×10^{-4} , and $7.3 \times 10^{-4} \text{ S cm}^{-1}$, respectively. Without the addition of Li_3PO_4 , the $x=0$ sample exhibited high conductivity, with the optimum heat treatment at 150 °C. This can be attributed to a well-balanced intensity comparison between the glass and crystal phases, resulting in the formation of a glass-ceramic phase [15]. After incorporating Li_3PO_4 , the $100\text{Li}_3\text{PS}_4\text{-}50\text{LiI-xLi}_3\text{PO}_4$ solid electrolyte, heat treated at 130 °C for 2 hours, showed an increase in ionic conductivity at room temperature. The highest ionic conductivity was observed for $x = 10$, reaching $8.5 \times 10^{-4} \text{ S cm}^{-1}$, which gradually decreased to $5.4 \times 10^{-4} \text{ S cm}^{-1}$ as x increased. The lowest ionic conductivity was observed for $x = 25$, likely due to the presence of residual Li_3PO_4 , which has low ionic conductivity. For the sample heat treated at 150 °C for 2 hours, a decrease in ionic conductivity at room temperature was observed starting from $x = 8$, followed by a gradual increase up to $x = 15$, and then a gradual decrease again. The highest ionic conductivity was measured for $x = 0$, with a value of $7.8 \times 10^{-4} \text{ S cm}^{-1}$, while the lowest conductivity was observed for $x = 25$, measuring $5.5 \times 10^{-4} \text{ S cm}^{-1}$. When the $100\text{Li}_3\text{PS}_4\text{-}50\text{LiI-xLi}_3\text{PO}_4$ solid electrolyte was heat treated at 170 °C, lower conductivity was observed compared to the heat treatment at 150 °C. The highest ionic conductivity was measured for $x = 0$, with a value of $7.3 \times 10^{-4} \text{ S cm}^{-1}$, while $x = 20$ exhibited the lowest conductivity, measuring $5 \times 10^{-4} \text{ S cm}^{-1}$. The addition of Li_3PO_4 and heat treatment at temperatures ≥ 150 °C did not lead to any significant electrochemical improvement in the $\text{Li}_3\text{PS}_4\text{-LiI}$ system. This could be attributed to the poor diffusion of Li_3PO_4 at these higher temperatures with the growth of the $\text{Li}_4\text{PS}_4\text{I}$ crystal phase which reduces the ionic conductivity. Based on the analysis of the ionic conductivity data, it can be concluded that the optimal condition for $100\text{Li}_3\text{PS}_4\text{-}50\text{LiI-xLi}_3\text{PO}_4$ solid electrolytes is a heat treatment at 130 °C for 2 hours with a Li_3PO_4 concentration of $x = 10$ mol%, which exhibited the highest ionic conductivity of $8.5 \times 10^{-4} \text{ S cm}^{-1}$.

Figure 2.16 presents the ^{31}P MAS-NMR spectra of $100\text{Li}_3\text{PS}_4\text{-}50\text{LiI-xLi}_3\text{PO}_4$ samples at $x = 0$ and $x = 10$, obtained after heat treatment at $130\text{ }^\circ\text{C}$. In both spectra, the peak observed at 86.6 ppm can be attributed to the presence of PS_4^{3-} [16]. This observation is consistent with the Raman spectra, which also indicated the existence of this ion in the prepared solid electrolyte. The chemical shift at 65 ppm can be assigned to $\text{PO}_2\text{S}_2^{3-}$ [17, 18], while the peaks at 95 and 75 ppm originate from $\text{P}_2\text{S}_7^{4-}$ and POS_2^- species, respectively [18]. Additionally, a small shoulder around 6 ppm suggests the presence of PO_4^{3-} from $x=10$. The detection of $\text{PO}_2\text{S}_2^{3-}$ indicates that a reaction occurred between the added Li_3PO_4 and the PS_4^{3-} ions in the sample or the P_2S_5 raw material. This finding is intriguing as it suggests that the incorporation of Li_3PO_4 into sulfide-based solid electrolytes took place during either the planetary ball-milling process or the high-temperature solid-state synthesis. However, the addition of Li_3PO_4 also caused a transformation of the PS_4^{3-} tetrahedral structure into POS_2^- in samples with $x = 10$ compared to the intrinsic sample. This observation suggests the formation of $\text{PO}_2\text{S}_2^{3-}$ and POS_3^{3-} species. Furthermore, the intensity of the $\text{P}_2\text{S}_7^{4-}$ peak decreased upon the addition of Li_3PO_4 , indicating that a portion of the phosphorus atoms bonded with both oxygen and sulfur atoms. The reduction in the intensity of the $\text{Li}_7\text{P}_2\text{S}_8\text{I}$ peak in the XRD patterns compared to that of thio-LISICON II further supports the structural changes occurring in the prepared samples, involving the $\text{P}_2\text{S}_7^{4-}$ and PS_4^{3-} tetrahedral. Combining the XRD and ^{31}P -MAS-NMR results, it can be concluded that the addition of Li_3PO_4 promotes the formation of thio-LISICON II structure in the solid electrolyte.

Figure 2.17(a) depicts the cyclic voltammogram of the obtained SE using a $\text{Li}|100\text{Li}_3\text{PS}_4\text{-}50\text{LiI-}0\text{Li}_3\text{PO}_4|\text{SUS}$ cell, where Li and SUS served as the reference and counter electrode, respectively. Similarly, Figure 2.18(a) shows the cyclic voltammogram of the SE using a $\text{Li}|100\text{Li}_3\text{PS}_4\text{-}50\text{LiI-}10\text{Li}_3\text{PO}_4|\text{SUS}$ cell. Both SEs were subjected to heat treatment at $130\text{ }^\circ\text{C}$. In both cases ($x = 0$ and $x = 10$), no peaks were observed in the voltage range of 10 V to -0.3 V , except for the peaks corresponding to the anodic and cathodic reactions of Li. This indicates that the systems at $x = 0$ and $x = 10$ have a wide electrochemical window and remain stable at 0 V versus Li/Li^+ . To further examine the behavior at lower voltages, magnified views of the voltage range were observed for $x = 0$ and $x = 10$, as shown in Figure 2.17(b) and 2.18(b), respectively. From these magnified

views, it can be observed that there is a reduction in current at 1.5 V for both $x = 0$ and $x = 10$. This reduction gradually diminishes after the second and third cycles for $x = 0$, while for $x = 10$, the reduction in current is minimal after the third cycle. According to a study by Yamamoto et al. [19], the reduction in current at 1.5 V during cycling is attributed to the formation of a solid electrolyte interface (SEI) between the SE and Li during the initial scan. Once the SEI is fully formed, the reduction in current diminishes, indicating the stability of the SEI against Li. The absence of this reduction after the third cycle at $x = 10$ suggests that the addition of Li_3PO_4 to $\text{Li}_3\text{PS}_4\text{-LiI}$ results in the formation of a more stable compound against Li, enhancing its stability during cycling. The incorporation of oxysulfide units from the $\text{PO}_2\text{S}_2^{3-}$ and POS_3^{3-} species has been proven to increase the electrochemical stability of the solid electrolyte with $x = 10$. This finding suggests that the presence of these oxysulfide units contributes to the enhanced stability of the solid electrolyte, which is crucial for the performance and longevity of solid-state batteries.

Long-term DC polarization cycling testing was conducted on the obtained SEs with $x = 0$ and $x = 10$. A constant current density of 0.3 mA cm^{-2} was applied at room temperature for 2 hours per cycle. Figure 2.19 illustrates the results of these tests. For the cell using $x = 0$, the initial voltage at 0 hours of operation was 35 mV. As the current was applied, the voltage gradually increased over the course of more than 1200 hours of measurements, reaching 47 mV. This indicates that the SE with $x = 0$ experienced a voltage increase of up to 34% during the testing period. On the other hand, the cell using $x = 10$ started with an initial voltage of 29 mV at 0 hours. After more than 1350 hours of measurement, the voltage decreased slightly to 33 mV. In other words, there was a voltage increase of up to 13% during the testing period. The presence of oxysulfide species, specifically the $\text{PO}_2\text{S}_2^{3-}$ and POS_3^{3-} units, has been found to enhance the stability of the solid electrolyte against lithium metal. This improvement in stability is crucial for the practical application of solid-state batteries, as it helps to mitigate issues such as dendrite formation and electrolyte decomposition, which can lead to short circuits and reduced battery performance. By incorporating oxysulfide units, the solid electrolyte demonstrates enhanced compatibility with lithium metal, thereby improving the overall stability and safety of the battery system. These results demonstrate that the addition of Li_3PO_4 has a significant positive effect on enhancing the stability of the SE against Li metal.

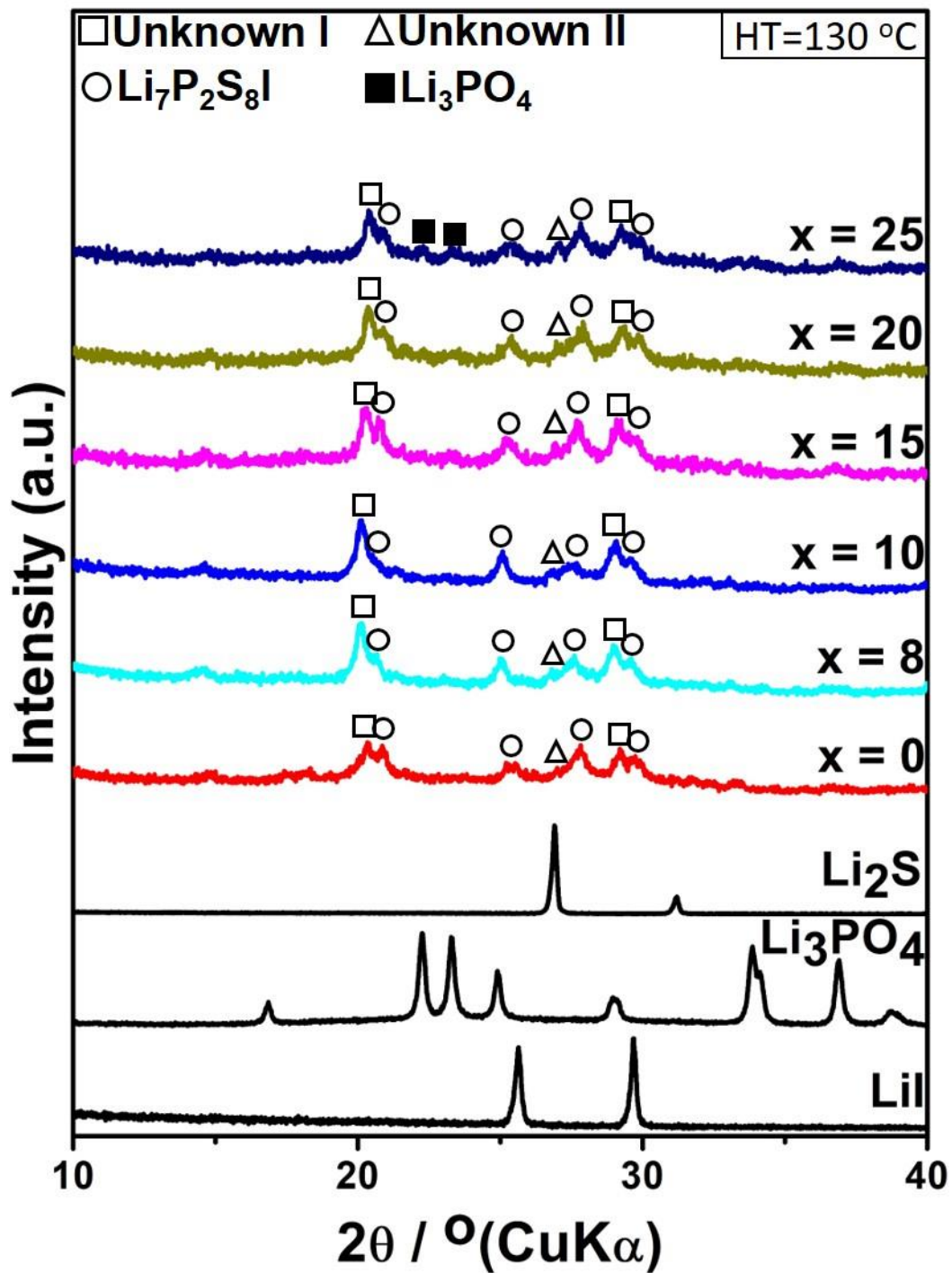


Figure 2.8. XRD patterns of 100Li₃PS₄-50LiI-*x*Li₃PO₄ (*x*=mol%) solid electrolytes heat treated at 130 °C for 2 h.

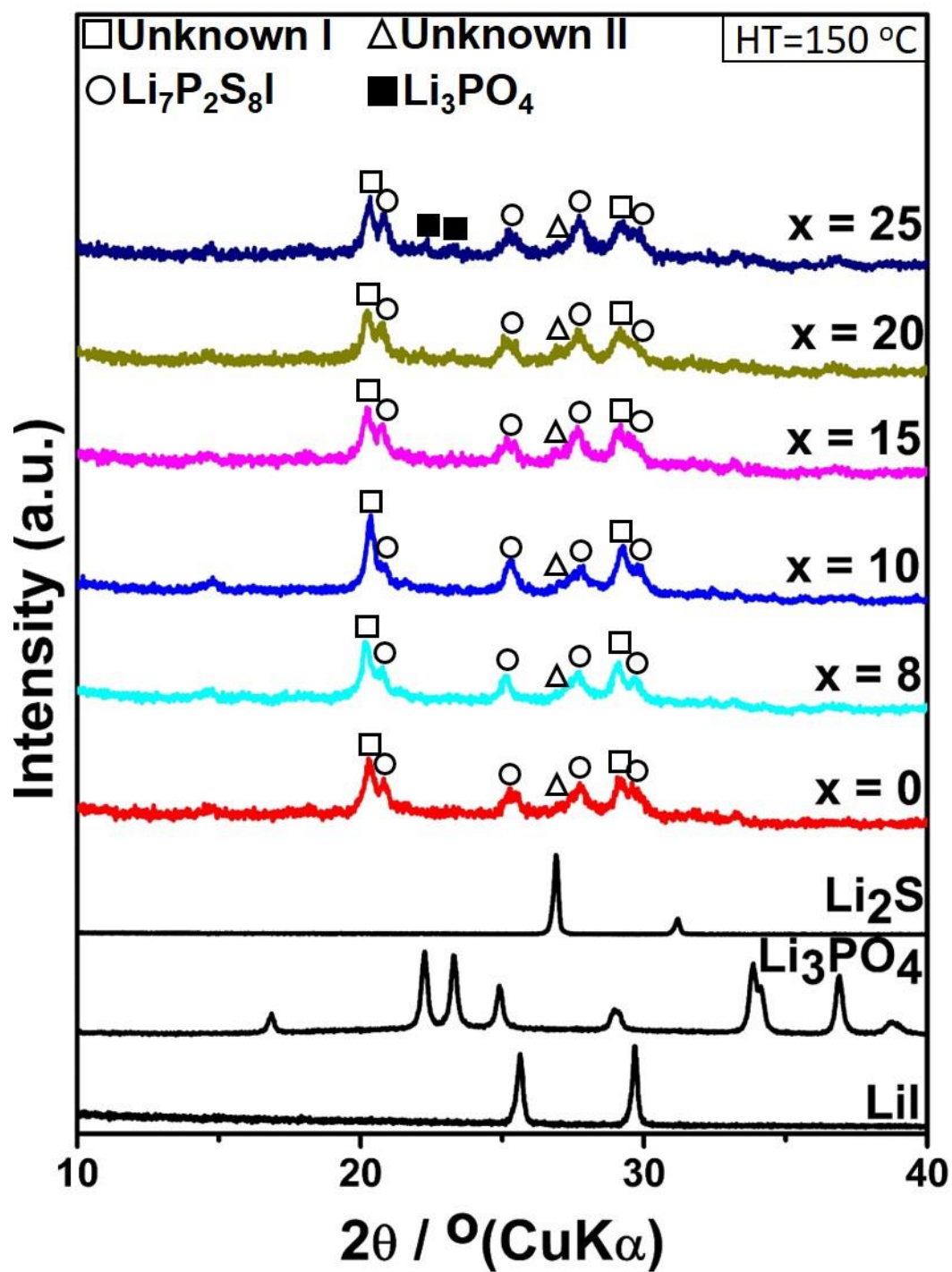


Figure 2.9. XRD patterns of $100\text{Li}_3\text{PS}_4\text{-}50\text{LiI-xLi}_3\text{PO}_4$ ($x=\text{mol}\%$) solid electrolytes heat treated at $150\text{ }^\circ\text{C}$ for 2 h.

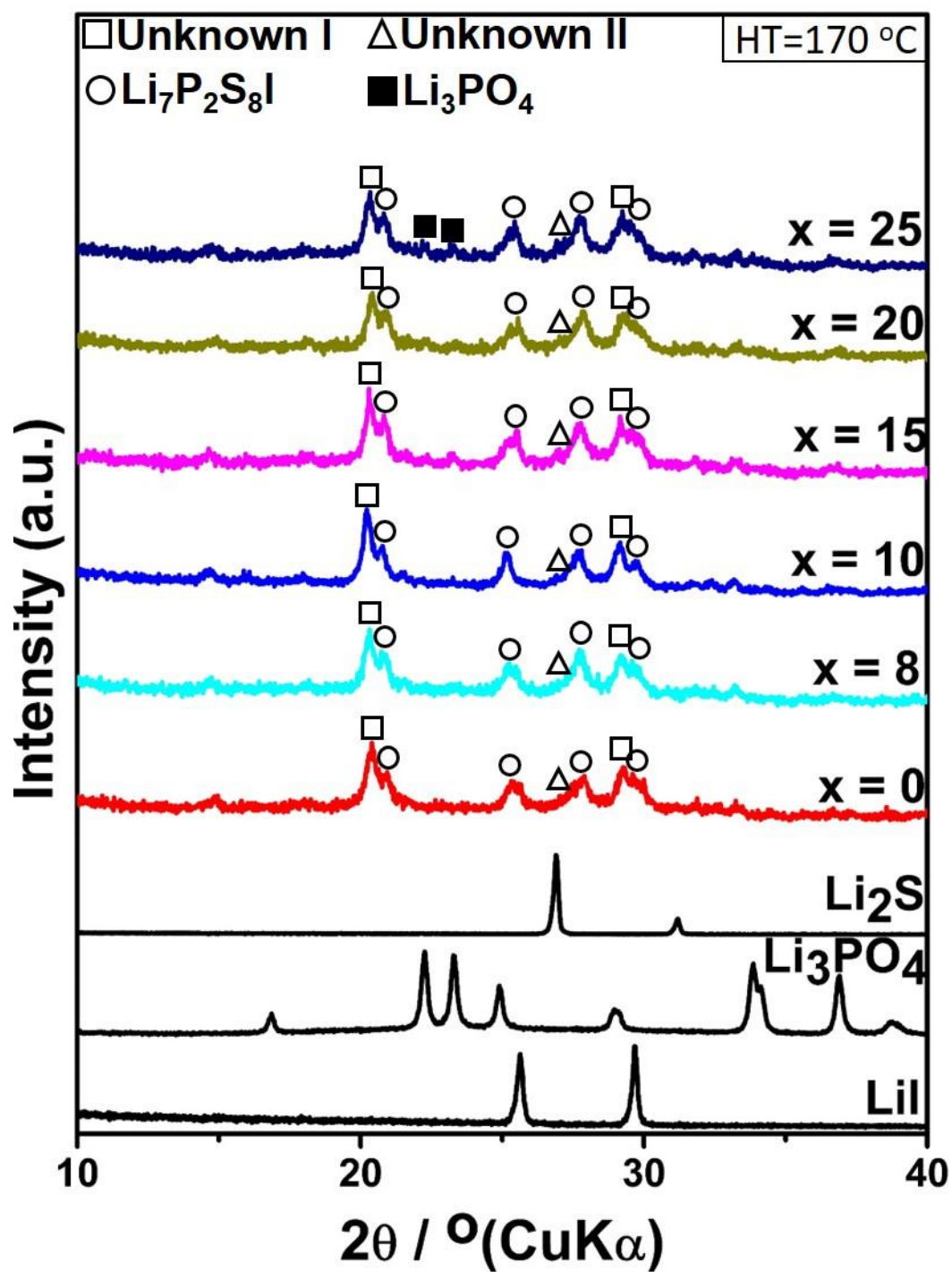


Figure 2.10. XRD patterns of 100Li₃PS₄-50LiI-xLi₃PO₄ (x=mol%) solid electrolytes heat treated at 170 °C for 2 h.

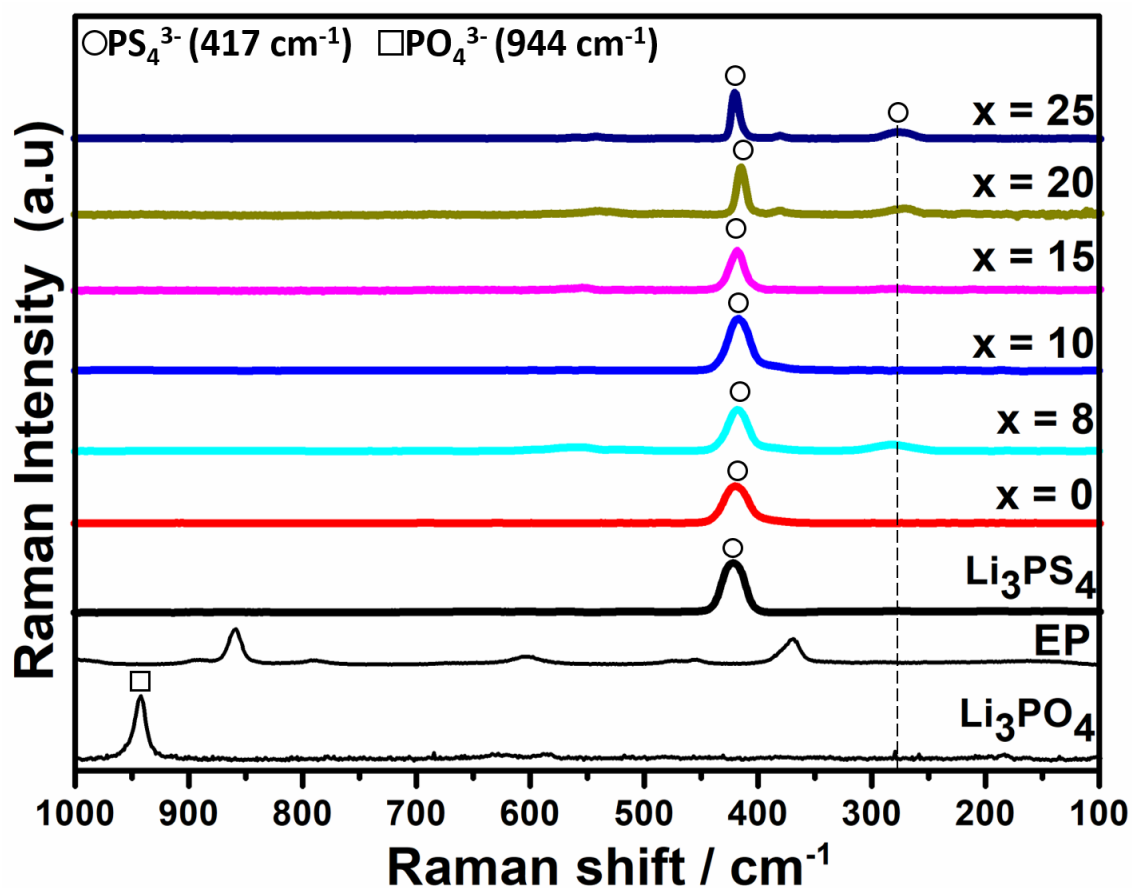


Figure 2.11. Raman spectra of $100\text{Li}_3\text{PS}_4\text{-}50\text{LiI-xLi}_3\text{PO}_4$ ($x=\text{mol}\%$) solid electrolytes after heat treated at 170°C for 2 h.

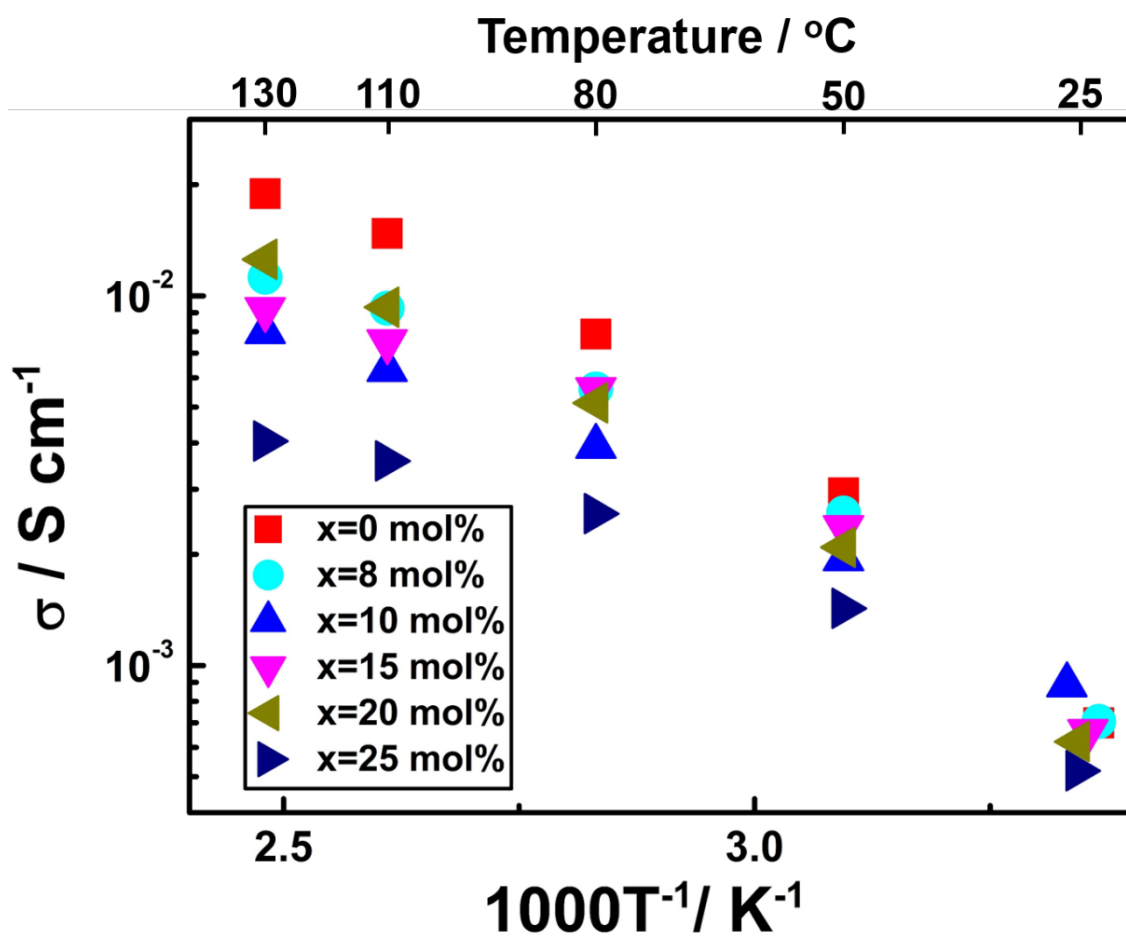


Figure 2.12. Temperature dependence of ionic conductivity of $100\text{Li}_3\text{PS}_4\text{-}50\text{LiI-xLi}_3\text{PO}_4$ ($x=\text{mol}\%$) heat treated at $130\text{ }^\circ\text{C}$

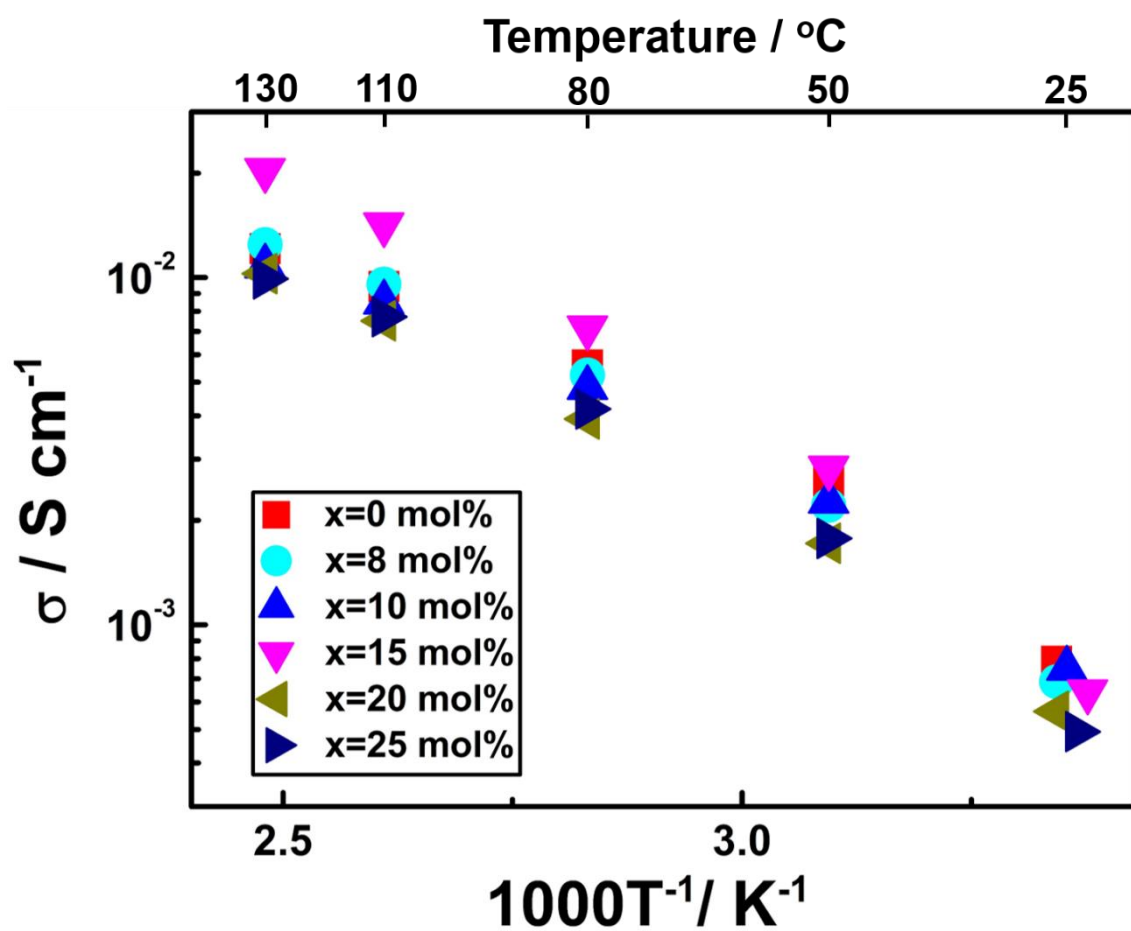


Figure 2.13. Temperature dependence of ionic conductivity of 100Li₃PS₄-50LiI-xLi₃PO₄ (x=mol%) heat treated at 150 °C

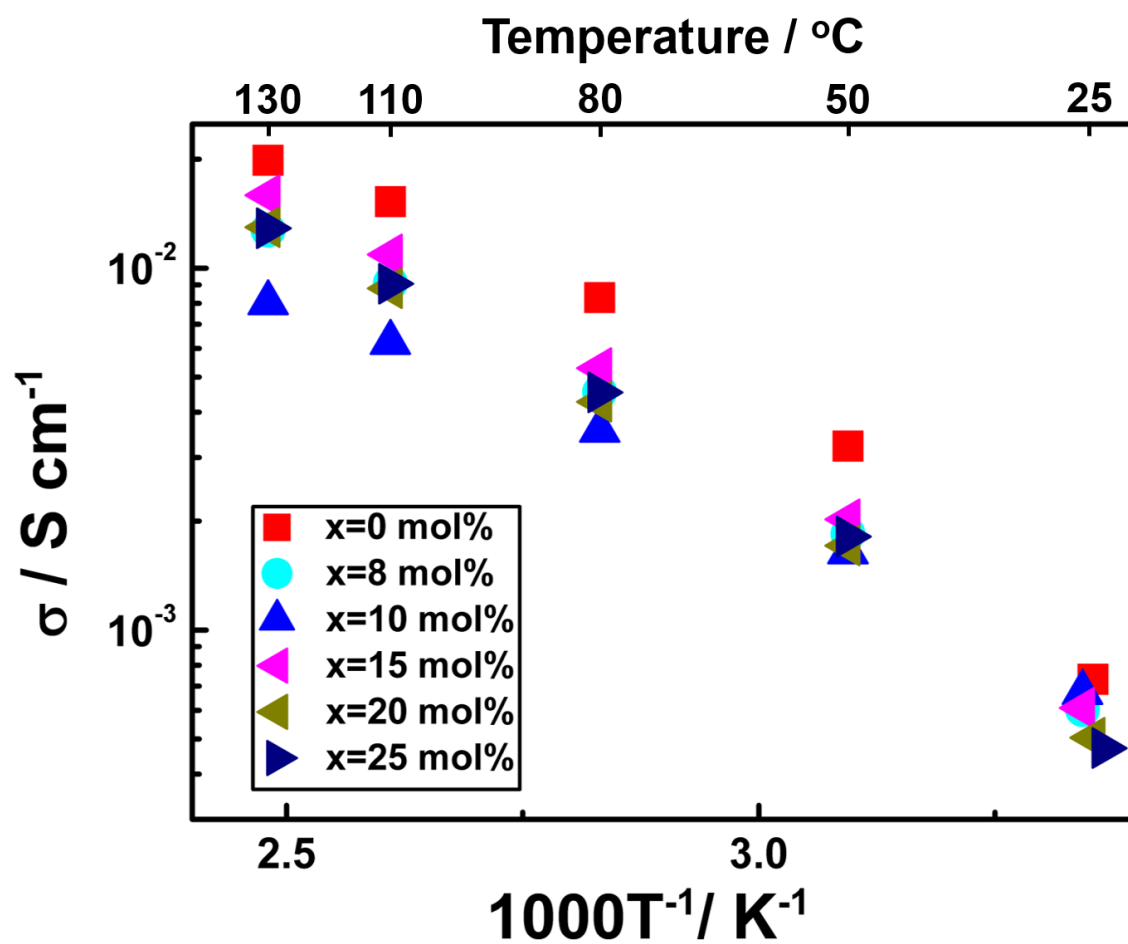


Figure 2.14. Temperature dependence of ionic conductivity of 100Li₃PS₄-50LiI-xLi₃PO₄ (x=mol%) heat treated at 170 °C

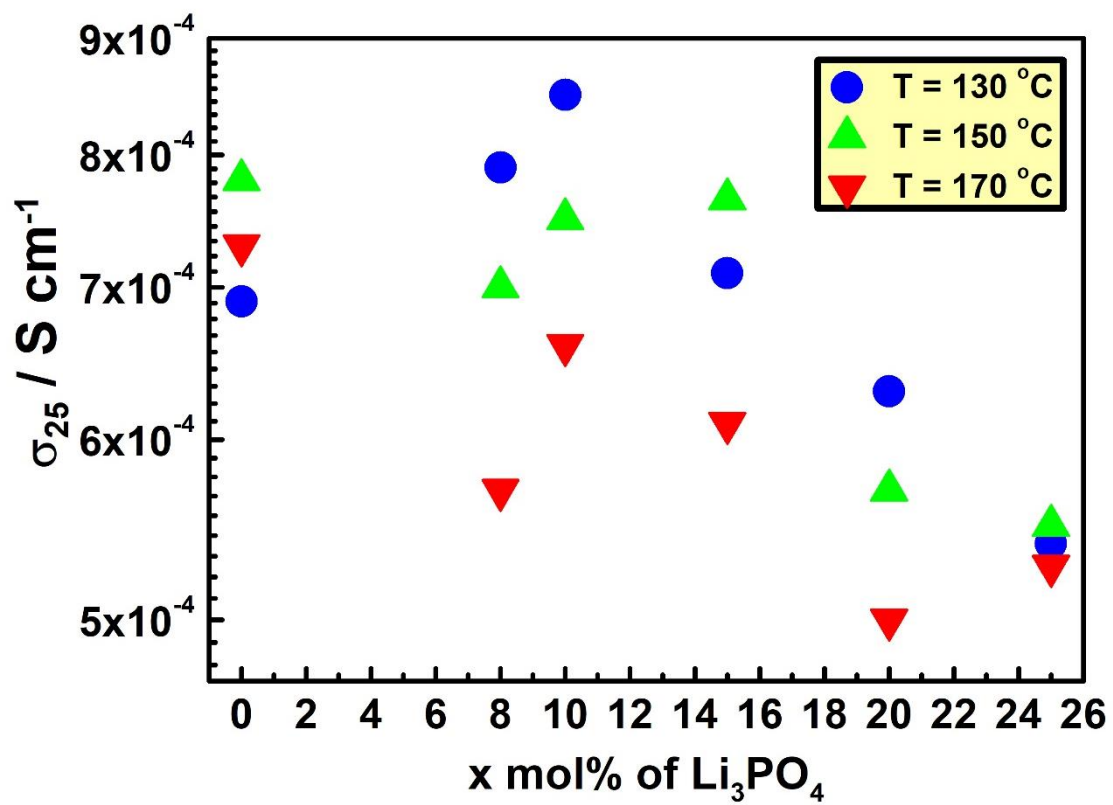


Figure 2.15. Composition dependence of ionic conductivity at room temperature of $100\text{Li}_3\text{PS}_4\text{-}50\text{LiI-xLi}_3\text{PO}_4$ ($x=\text{mol}\%$) with different heat treatment conditions

Table 2.1. Ionic conductivity at room temperature of 100Li₃PS₄-50LiI-xLi₃PO₄ (x=mol%) with different kind of Li₃PO₄ concentration and heat treatment temperature

x (mol weight %)	Heat Treatment (°C)	σ_{25} (S cm⁻¹)
0	130	6.9 x 10 ⁻⁴
	150	7.8 x 10 ⁻⁴
	170	7.3 x 10 ⁻⁴
8	130	7.9 x 10 ⁻⁴
	150	7.0 x 10 ⁻⁴
	170	5.7 x 10 ⁻⁴
10	130	8.5 x 10 ⁻⁴
	150	7.5 x 10 ⁻⁴
	170	6.6 x 10 ⁻⁴
12	130	5.3 x 10 ⁻⁴
	150	6.5 x 10 ⁻⁴
	170	5.5 x 10 ⁻⁴
15	130	7.1 x 10 ⁻⁴
	150	7.65 x 10 ⁻⁴
	170	6.1 x 10 ⁻⁴
20	130	6.3 x 10 ⁻⁴
	150	5.7 x 10 ⁻⁴
	170	5 x 10 ⁻⁴
25	130	5.4 x 10 ⁻⁴
	150	5.5 x 10 ⁻⁴
	170	5.28 x 10 ⁻⁴

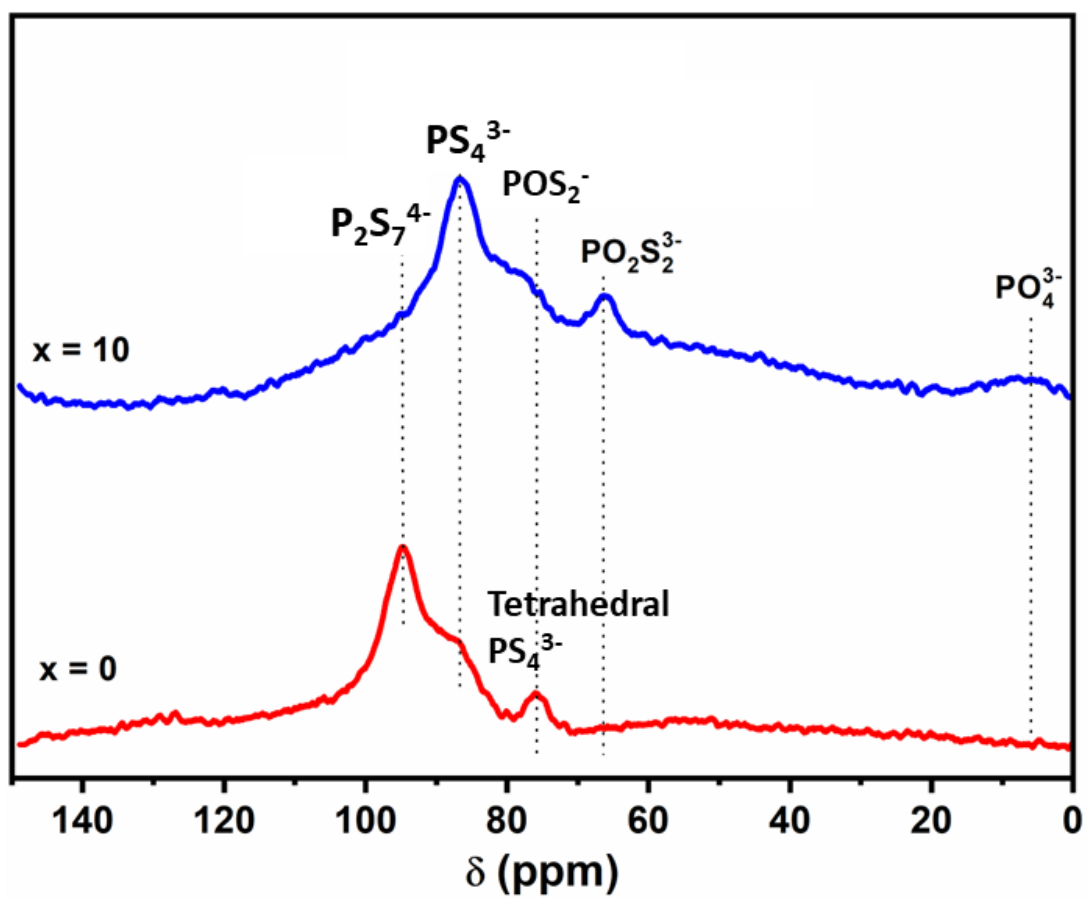


Figure 2.16. ^{31}P MAS-NMR of $100\text{Li}_3\text{PS}_4\text{-}50\text{LiI-xLi}_3\text{PO}_4$ ($x=\text{mol}\%$) solid electrolytes heat treated at 130°C .

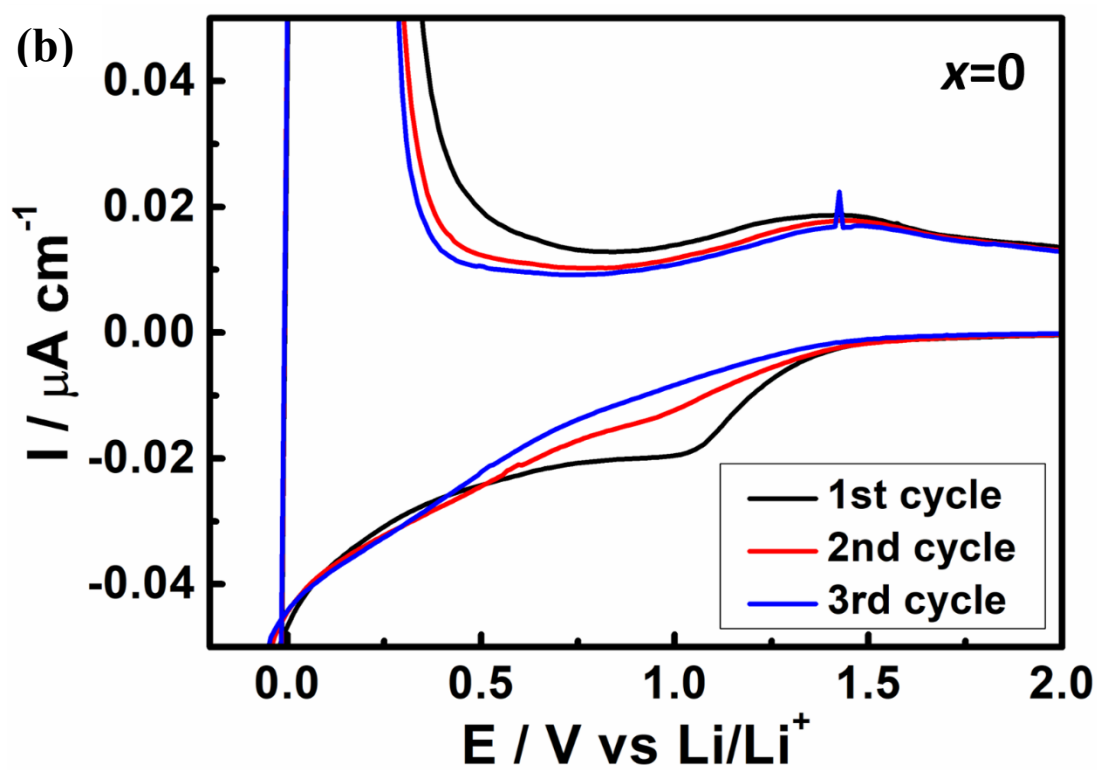
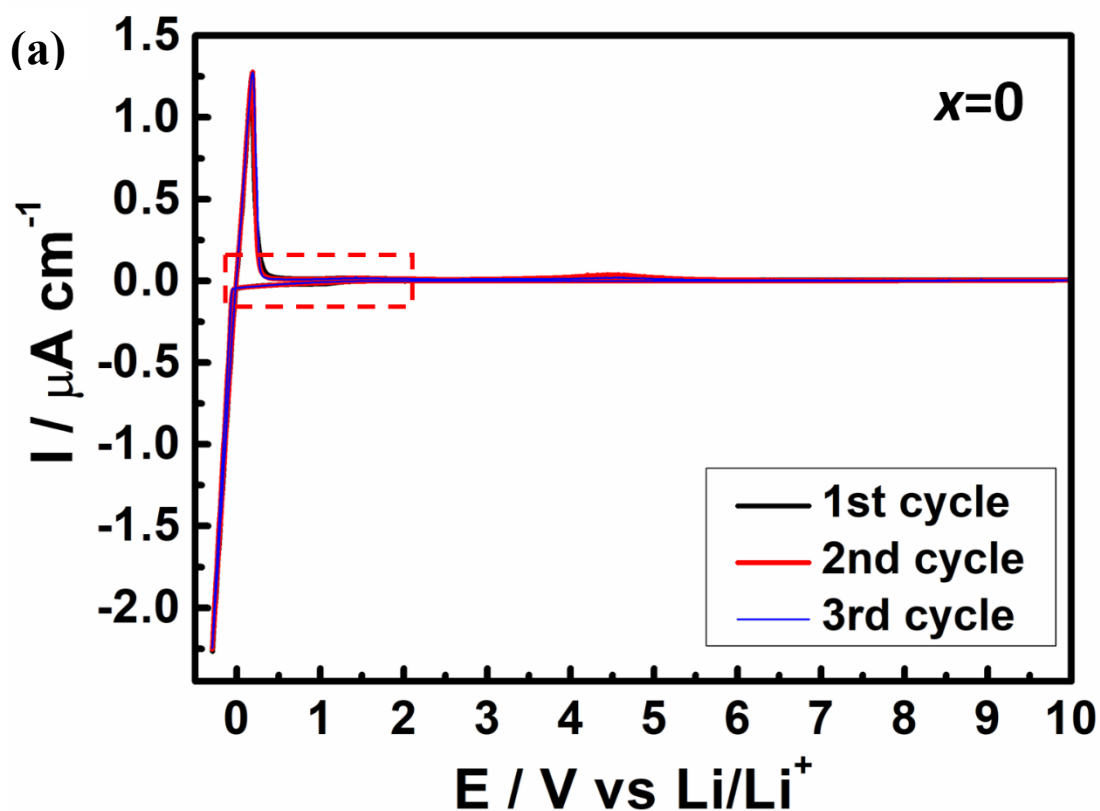


Figure 2.17. (a) Cyclic voltammogram of $\text{Li} | 100\text{Li}_3\text{PS}_4\text{-}50\text{LiI}\text{-}0\text{Li}_3\text{PO}_4$ ($x=\text{mol}\%$) heat treated at $130\text{ }^\circ\text{C} | \text{SUS}$ at a scan rate of 5 mV s^{-1} (b) magnified voltage scale

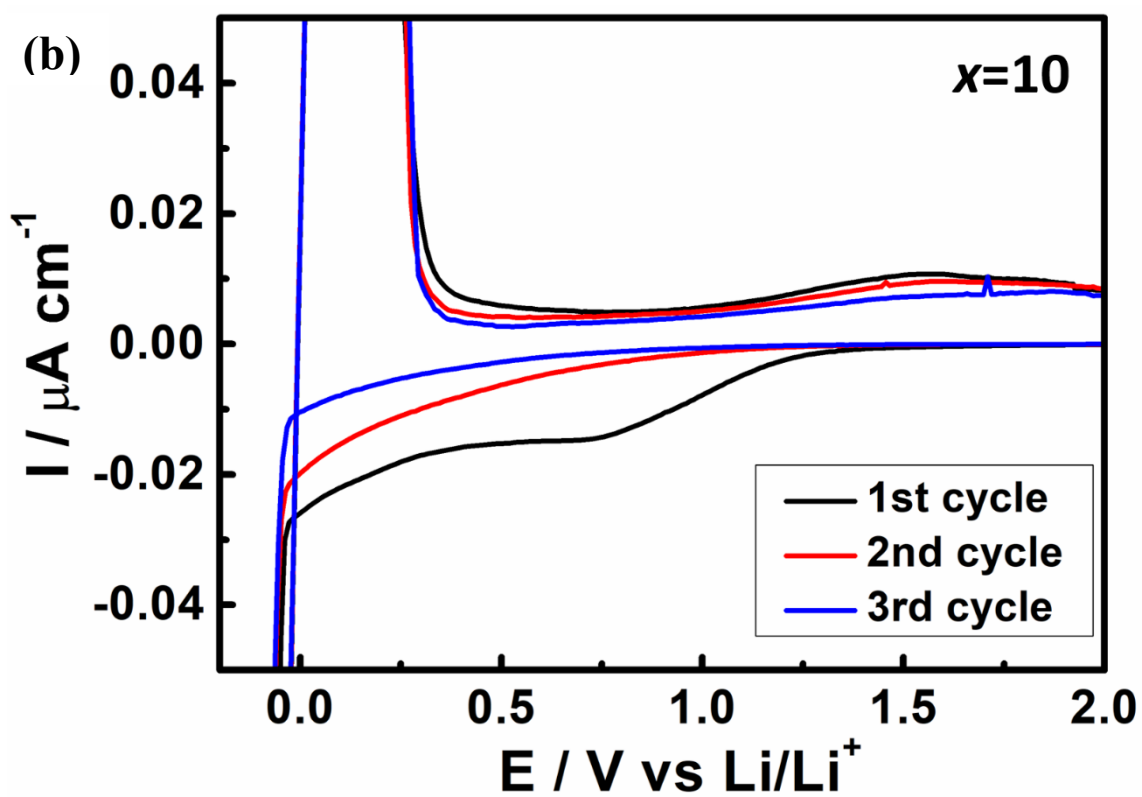
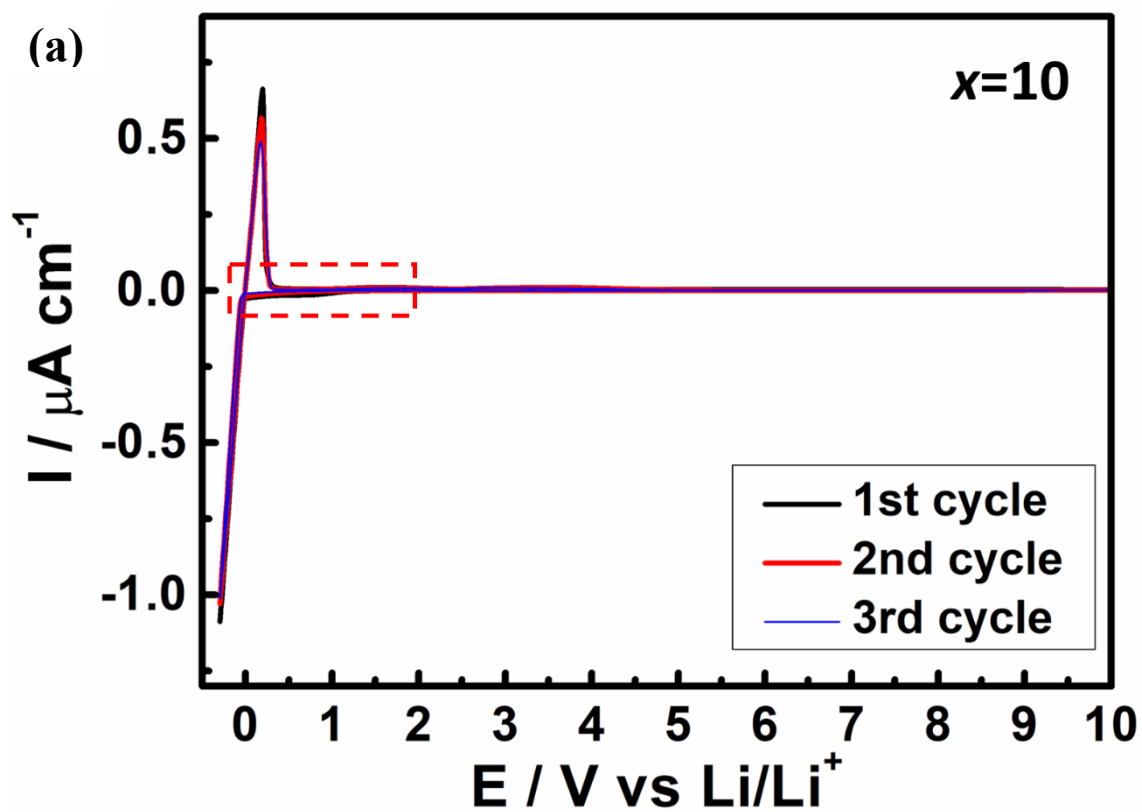


Figure 2.18. (a) Cyclic voltammogram of Li| 100Li₃PS₄-50LiI-10Li₃PO₄ (x =mol%) heat treated at 130 °C |SUS at a scan rate of 5 mV s⁻¹ (b) magnified voltage scale

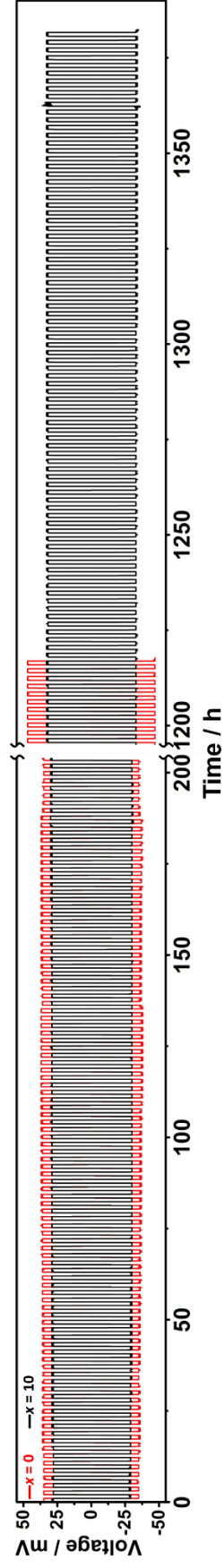


Figure 2.19. DC Polarization curves of Li| 100Li₃PS₄-50Li_{1-x}Li₃PO₄ (x=mol%) |Li with a current density of 0.3 mA cm⁻², 1 h of charge and discharge time.

2.5 Conclusions

The $100\text{Li}_3\text{PS}_4\text{-}50\text{LiI-xLi}_3\text{PO}_4$ SE was successfully synthesized using a low-pressure heat treatment process with ethyl propionate as the solvent. The reaction between Li_3PS_4 and Li_3PO_4 was confirmed by analyzing the ^{31}P MAS-NMR data, which revealed the presence of $\text{PO}_2\text{S}_2^{3-}$ and POS_3^{3-} ions. The addition of Li_3PO_4 resulted in significant improvements in both the ionic conductivity and stability of the SE against Li metal when compared to the SE without Li_3PO_4 . Among the prepared SEs, the sample $100\text{Li}_3\text{PS}_4\text{-}50\text{LiI-}10\text{Li}_3\text{PO}_4$, which was heat treated at $130\text{ }^\circ\text{C}$ for 2 hours, exhibited a high ionic conductivity at room temperature, measuring $8.5 \times 10^{-4}\text{ S cm}^{-1}$. The addition of Li_3PO_4 into the $\text{Li}_3\text{PS}_4\text{-LiI}$ system has been shown to improve the electrochemical stability of the solid electrolyte. This improvement can be attributed to the presence of oxysulfide compounds, specifically the $\text{PO}_2\text{S}_2^{3-}$ and POS_3^{3-} units. These oxysulfide species contribute to enhancing the stability of the solid electrolyte by forming a more favorable electrochemical interface with lithium metal. The incorporation of Li_3PO_4 not only increases the ionic conductivity but also helps to suppress detrimental reactions between the electrolyte and lithium metal, thereby improving the overall electrochemical stability of the solid electrolyte in all-solid-state lithium-ion batteries. This finding demonstrates the effectiveness of incorporating Li_3PO_4 in enhancing the electrochemical performance of the SE.

References

- [1] A. Mauger, C.M. Julien, Critical review on lithium-ion batteries: are they safe? Sustainable? *Ionics*, **2017**, *23*, pp. 1933–1947.
- [2] S. Yubuchi, Y. Ito, T. Matsuyama, A. Hayashi, M. Tatsumisago, 5 V class $\text{LiNi}_{0.5}\text{Mn}_{1.5}\text{O}_4$ positive electrode coated with Li_3PO_4 thin film for all-solid-state batteries using sulfide solid electrolyte, *Solid State Ionics*, **2016**, *285*, pp. 79–82.
- [3] S. Choudhury, R. Mangal, A. Agrawal, L.A. Archer, A highly reversible room-temperature lithium metal battery based on crosslinked hairy nanoparticles, *Nat. Commun.* **2015**, *6*, 10101.
- [4] A. Manthiram, Y. Fu, S.-H. Chung, C. Zu, Y.-S. Su, Rechargeable lithium–sulfur batteries, *Chem. Rev.* **2014**, *114*, pp. 11751–11787.
- [5] C. Cao, Z. B. Li, X.L. Wang, X. B. Zhao, W. Q. Han, Recent advances in inorganic solid electrolytes for lithium batteries, *Front. Energy Res.* **2014**, *2*, 25.
- [6] K. Takada, Progress and prospective of solid-state lithium batteries, *Acta Mater.* **2013**, *61*, pp. 759–770.
- [7] N. Kamaya, K. Homma, Y. Yamakawa, M. Hirayama, R. Kanno, M. Yonemura, T. Kamiyama, Y. Kato, S. Hama, K. Kawamoto, A. Mitsui, A lithium superionic conductor, *Nat. Mater.* **2011**, *10*, pp. 682–686.
- [8] M. Dirican, C. Yan, P. Zhu, X. Zhang, Composite solid electrolytes for all-solid-state lithium batteries, *Mater. Sci. Eng. R. Rep.* **2019**, *136*, pp. 27–46.
- [9] J.L. Allen, J. Wolfenstine, E. Rangasamy, J. Sakamoto, Effect of substitution (Ta, Al, Ga) on the conductivity of $\text{Li}_7\text{La}_3\text{Zr}_2\text{O}_{12}$, *J. Power Sources*, **2012**, *206*, pp. 315–319.
- [10] N. H. H. Phuc, T. Yamamoto, H. Muto, A. Matsuda, Fast synthesis of Li_2S – P_2S_5 – LiI solid electrolyte precursors, *Inorg. Chem. Front.* **2017**, *4*, pp. 1660 – 1664.
- [11] Seon-Joo Choi, Sang-Hun Lee, Yoon-Cheol Ha, Ji-Hyun Yu, Chil-Hoon Doh, Youjin Lee, Jun-Woo Park, Sang-Min Lee, Heon-Cheol Shin, Synthesis and

- electrochemical characterization of a glass-ceramic $\text{Li}_7\text{P}_2\text{S}_8\text{I}$ solid electrolyte for all-solid-state Li-ion batteries, *J. Electrochem. Soc.* **2018**, *165*, pp. A957-A962.
- [12] N. H. H. Phuc, K. Morikawa, M. Totani, H. Muto, A. Matsuda, Synthesis of plate-like Li_3PS_4 solid electrolyte via liquid-phase shaking for all-solid-state lithium batteries, *Ionics*, **2017**, *23*, pp. 2061-2067.
- [13] Z. Liu, W. Fu, E.A. Payzant, X. Yu, Z. Wu, N. J. Dudney, J. Kiggans, K. Hong, A. J. Rondinone, C. Liang, Anomalous high ionic conductivity of nanoporous $\beta\text{-Li}_3\text{PS}_4$, *J. Am. Chem. Soc.*, **2013**, *135*, pp. 875-978.
- [14] K.H. Park, D.Y. Oh, Y.E. Choi, Y.J. Nam, L. Han, J.Y. Kim, H. Xin, F. Lin, S.M. Oh, Y.S. Jung, Solution-processable glass $\text{LiI-Li}_4\text{SnS}_4$ superionic conductors for all solid-state Li-ion batteries, *Adv. Mater.* **2016**, *28*, pp. 1874-1883.
- [15] T. Minami, A. Hayashi, M. Tatsumisago, Recent progress of glass and glass-ceramics as solid electrolytes for lithium secondary batteries, *Solid State Ionics*, **2006**, *177*, pp. 2715-2720.
- [16] M. Gobet, S. Greenbaum, G. Sahu, C. Liang, Structural evolution and Li dynamics in nanophase Li_3PS_4 by solid-state and pulsed-field gradient NMR, *Chem. Mater.* **2014**, *26*, pp. 3558-3564.
- [17] K. Hirai, M. Tatsumisago, M. Takahashi, T. Minami, ^{29}Si and ^{31}P MAS-NMR Spectra of $\text{Li}_2\text{S-SiS}_2\text{-Li}_3\text{PO}_4$ rapidly quenched glasses, *J. Am. Ceram.* **1996**, *79*, pp. 349-352.
- [18] S. Kmiec, A. Joyce, D. Bayko, S. W. Martin, Glass formation and structure of melt quenched mixed oxy-sulfide $\text{Na}_4\text{P}_2\text{S}_{7-x}\text{O}_x$ glasses for $0 \leq x \leq 5$, *Journal of Non-Crystalline Solids*, **2020**, *534*, 119776.
- [19] T. Yamamoto, N. H. H. Phuc, H. Muto, A. Matsuda, Preparation of $\text{Li}_7\text{P}_2\text{S}_8\text{I}$ solid electrolyte and its application in all-solid-state lithium-ion batteries with graphite anode, *Electron. Mater. Lett.* **2019**, *15*, pp. 409 – 414.

Chapter 3

Liquid Phase Synthesis of Pure Argyrodite Solid Electrolyte

3.1 Background

In Chapter 2, the addition of Li_3PO_4 into the $\text{Li}_7\text{P}_2\text{S}_8\text{I}$ solid electrolytes (SEs) system was discussed as a potential method to improve its performance. However, it should be noted that despite the addition of Li_3PO_4 , the achieved ionic conductivity in the $100\text{Li}_3\text{PS}_4\text{-}50\text{LiI-}10\text{Li}_3\text{PO}_4$ SE was still relatively low. Arising from its exceptional ionic conductivity comparable to liquid electrolytes, there is potential in enhancing the appeal of argyrodite by introducing oxygen into the system. However, the high crystallinity phase of argyrodite poses a challenge for the introduction of oxygen. The process of oxygen doping typically requires high-energy mechanical ball milling, which contradicts our goal of achieving mass production of sulfide solid electrolytes. SEs play a crucial role as both electron separators and ion conductors in all-solid-state lithium-ion batteries. Liquid phase synthesis is considered a promising method for synthesizing SEs due to its scalability and lower energy consumption. However, the complexity of SEs prepared by liquid phase synthesis often leads to issues such as impurity formation, which makes liquid electrolytes indispensable. This study aims to investigate and address the production of Li_3PO_4 oxide impurity during the preparation of $\text{Li}_6\text{PS}_5\text{Cl}$ argyrodite through a chemical approach. The approach involves replacing the hydroxide-based solvent with a thiol-based solvent during the liquid phase synthesis process. By implementing this modification, the study aims to overcome the challenges associated with impurity formation and improve the overall quality of the synthesized SEs. Consequently, by successfully eliminating Li_3PO_4 oxide impurities from the $\text{Li}_6\text{PS}_5\text{Cl}$ SEs in this study, a remarkable achievement was made in terms of the SEs' ionic conductivity. The $\text{Li}_6\text{PS}_5\text{Cl}$ SEs synthesized through liquid-phase synthesis exhibited the highest ionic conductivity value ($> 2 \text{ mS cm}^{-1}$) ever reported. This breakthrough highlights the significant impact of removing Li_3PO_4 impurities on enhancing the

conductivity of the SEs. Moreover, the absence of Li_3PO_4 impurities in the argyrodite SEs had a profound effect on the cell's capacity and stability. The removal of Li_3PO_4 led to a substantial increase in the cell's capacity, allowing for greater energy storage. Additionally, the SEs demonstrated remarkable stability, indicating their potential for long-term and reliable battery performance. This finding further emphasizes the importance of addressing impurity issues, such as Li_3PO_4 , in the synthesis of argyrodite SEs to unlock their full potential in battery applications.

3.2 Introduction

Rechargeable all-solid-state Li-ion batteries (ASSLiBs) using non-flammable inorganic solid electrolytes (SEs) show potential for improved safety and increasing power density in comparison with commercialized Li-ion batteries.[1] The development of ASSLiBs has been limited by the poor physical contact between the SE and active material and the lack of SE with ionic conductivities at room temperature. Among the inorganic solid electrolytes, sulfide SEs show excellent mechanical properties and relatively high ionic conductivities.[2,3] One of the most promising materials classes is argyrodite-type $\text{Li}_6\text{PS}_5\text{X}$ ($\text{X} = \text{Cl}, \text{Br}, \text{and I}$).[4–9] Argyrodite-type $\text{Li}_6\text{PS}_5\text{I}$ substituted by Ge^{4+} show a high ionic conductivity of 18 mS cm^{-1} at room temperature, which is comparable to the current liquid organic electrolyte.[10] Argyrodite-type $\text{Li}_{5.3}\text{PS}_{4.3}\text{Cl}_{1.7}$ was recently found to show a very high ionic conductivity of over 10 mS cm^{-1} at room temperature.[11] Given the lower cost of chloride-based argyrodite-type SE than argyrodite-type SEs with other halide ions, industrial and fundamental battery applications mainly concentrate on this compound.[12]

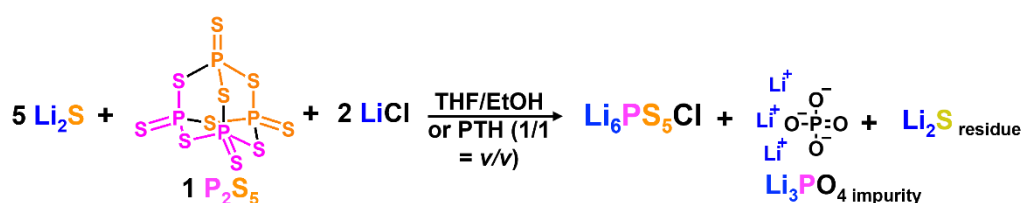
The commercialization of sulfide-based ASSLiBs requires the development of large-scale manufacturing technologies for SEs.[13] SE synthesis methods can be broadly classified into high-energy mechanical ball milling and liquid-phase synthesis. However, the high-energy mechanical ball milling process poses challenges for scaling up due to its high energy consumption. In contrast, liquid-phase synthesis is more suitable for large-scale manufacturing due to its lower cost and higher scalability.[14–16] The choice of organic solvents in liquid-phase synthesis plays a crucial role in the solubility and reactivity of lithium thiophosphates.[17,18]

In the synthesis of argyrodite-type $\text{Li}_6\text{PS}_5\text{Cl}$ SEs, various solvents such as ethyl diamine, anisole, and ethanol (EtOH) have been employed.[19–24] Ethanol, with its high dielectric constant and low boiling point, facilitates the dissolution of argyrodite-type SE precursors. However, the use of ethanol can have detrimental effects, leading to the formation of Li_3PO_4 and enhancing the decomposition kinetics of the anion unit in the precursor solution. [18,24–26] Even when a combination of tetrahydrofuran (THF) and EtOH is used, Li_3PO_4 can still form in the argyrodite-type $\text{Li}_6\text{PS}_5\text{Cl}$ SEs. [24,26] This indicates that Li_3PO_4 is produced through an anionic ring-opening reaction of THF during the wet chemical synthesis process.

Considering these factors, the use of chloride ions, which exhibit stronger nucleophilicity in protic polar solvents compared to bromide and iodide ions, is not preferred for the liquid-phase synthesis of argyrodite-type SEs without impurities such as Li_3PO_4 . However, if $\text{Li}_6\text{PS}_5\text{Cl}$ argyrodite can be synthesized without Li_3PO_4 impurities in the liquid-phase synthesis by using LiCl, it can be adapted to synthesize Li-argyrodite with various compositions. Additionally, in non-protic polar solvents such as acetonitrile, acetone, DMF, and DMSO, lithium cations can be stabilized, while anions are weakly stabilized. The negatively polarized oxygen atoms in these solvents can protrude outside the molecules, allowing them to approach and stabilize lithium cations.

In this study, we present a novel wet chemical reaction mechanism for eliminating the impurity of Li_3PO_4 in chloride-based argyrodite $\text{Li}_6\text{PS}_5\text{Cl}$ using acetonitrile (ACN) and 1-propanethiol (PTH) solvents. The choice of ACN as the organic solvent was motivated by its high dielectric constant, which resulted in significant reactivity in the $\text{Li}_2\text{S-P}_2\text{S}_5$ system. [17] By utilizing PTH as a solvent, the oxygen ion source from ethanol (EtOH) was effectively excluded, as depicted in Figure 3.1a and 3.1b. PTH, with its low boiling point, could be easily removed during the evaporation process. X-ray diffraction (XRD) analysis confirmed the absence of crystalline Li_3PO_4 when using ACN and PTH solvents in the $\text{Li}_6\text{PS}_5\text{Cl}$ crystal structure. This exclusion of Li_3PO_4 impurities had a notable impact on the ionic conductivity and stability against lithium metal, as observed through direct current (DC) polarization measurements. The battery performance exhibited significant improvement, including high capacity retention after multiple cycles, resulting from the elimination of Li_3PO_4 impurities in the $\text{Li}_6\text{PS}_5\text{Cl}$ argyrodite crystal structure.

a. Tetrahydrofuran (THF)/ Ethanol (EtOH) or Propanethiol (PTH) mixed solution



b. Acetonitrile (ACN) / PTH mixed solution

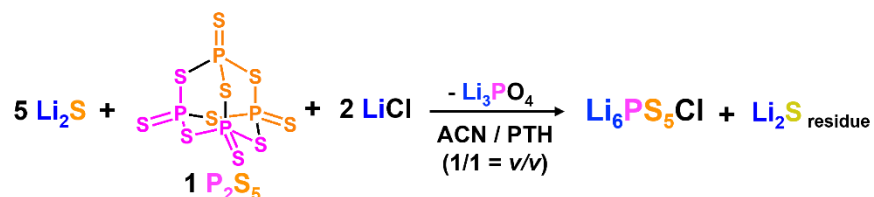


Figure 3.1. Stoichiometry of Li₆PS₅Cl. The illustration comparison reaction between Li₆PS₅Cl by liquid-phase synthesis using **a** Tetrahydrofuran (THF) with Ethanol (EtOH) and **b** Acetonitrile (ACN) with 1-Propanethiol (PTH).

3.3 Experimental Method

3.3.1 Liquid Phase Synthesis

Reagent for synthesis grade of Li_2S (99.9%, Mitsuwa), P_2S_5 (99%, Merck), and LiCl (99.0%, Sigma-Aldrich) was used as raw materials with the total stoichiometry ratio of 5:1:2 to create $\text{Li}_6\text{PS}_5\text{Cl}$. The solution procedure was first separated into two solutions. To begin, we mixed a 3:1 molar ratio of Li_2S and P_2S_5 in 10 ml of THF (anhydrous, 99.9%, Sigma-Aldrich) or ACN (super dehydrated, 99.8%, Fujifilm), and then stirred for 12 h at room temperature or 75 °C, respectively, to form a suspension. Next, the mixture of Li_2S and LiCl with a molar ratio of 2:2 was stirred in 10 ml of EtOH (Super Dehydrated, 99.5%, Fujifilm) at 50 °C or PTH (98%, Tokyo Chemical Industry) at room temperature for 12 h. 3A molecular sieves was added into THF and PTH prior to use in purpose to dehydrate the remaining water content. 100 grams of 3A molecular sieves (around 11.36% of THF's mass) were added into 1 L of THF with a density of 880 $\text{gram}\cdot\text{L}^{-1}$. The same amount was added into the PTH solvent (880 $\text{gram}\cdot\text{L}^{-1}$) or 12.20% of PTH's mass. 3 A molecular sieve was dried at 220 °C for 18 hours to remove the remaining humidity or water vapor inside the molecular sieves before being poured into each solvent. The resultant suspension and solution were mixed then stirred for 12 h at room temperature (for the ACN + PTH case, 50 °C). The resulting solution evaporated at 80 °C for 12 h under low pressure with a diaphragm pump (Buchi V-100 Vacuum Pump). The evaporated precursor was pelletized for 127 MPa at uniaxial press before the heat treatment process. Argyrodite pellet was heat-treated at various temperatures of 550 °C and 600 °C for 2 and 10 h under an Ar flow. Figure 3.2 illustrates the liquid-phase synthesis process for ACN + PTH solvents. All processes were performed under a dry Ar atmosphere.

3.3.2 Mechanical Ball Milling Synthesis

Mechanical BM was used to produce $\text{Li}_6\text{PS}_5\text{Cl}$ and compared with liquid-phase synthesis. Reagents of Li_2S , P_2S_5 , and LiCl were mixed and ground together in an agate mortar for around 15 min. The mixed powder was inserted into a 45 ml zirconia pot and 15 zirconia balls ($\varnothing = 10$ mm). The prepared sample was then milled at the rotation of 600 rpm for 20 h using a planetary BM apparatus (Pulverisette 7, Fritsch Co., Ltd.). Thereon, the pulverized powder was then pressed for 127 MPa at uniaxial press before the heat

treatment process at 550 °C and 600 °C for 2 and 10 h. All processes were performed under a dry Ar atmosphere.

3.3.3 Material Characterization

The crystal structures of the retrieved samples were investigated using XRD (XRD; SmartLab, Rigaku) with an airtight holder to prevent the samples from being exposed to air humidity. The local structure was investigated using Raman spectroscopy (NRS-4500, Jasco) with the samples sealed inside an Ar-filled glove box. Solid-state ^{31}P magic-angle-spinning NMR (^{31}P -MAS-NMR, Avance III 400, Bruker) was performed using the typical single pulse sequence with a spinning rate of 6 kHz. Liquid proton ^1H NMR was measured by solving the samples with dimethyl sulfoxide-d6 (DMSO) using Avance III 400, Bruker. Scanning electron microscope-energy dispersive X-ray spectroscopy (SEM-EDX) images mapping was achieved using Hitachi-S4800 and ULTIM MAX, Oxford Instrument as for the EDX instrument. Thermogravimetry differential thermal analysis TG–DTA (EVO II, Rigaku) was performed under Ar flow with a temperature increase of $5\text{ °C}\cdot\text{min}^{-1}$ inside glovebox with Ar and dry atmosphere.

3.3.4 Electrochemical Performance Measurement

The temperature dependence of the ionic conductivity of the retrieved sample was investigated using alternating-current impedance spectroscopy (SI 1260, Solartron) from 10 MHz to 1 Hz under dry Ar flow. The samples for impedance measurements were prepared by uniaxial pressing around 80 mg of sample powder into pellets (approximately 10 mm in diameter) under a pressure of 255 MPa for 10 minutes at room temperature. The thickness of the argyrodite SE pellets were approximately reach 0.60 mm. The prepared pellets were placed in a holder made from polyether ether ketone (PEEK) with two blocking electrodes made from stainless steel (SUS). The temperature was increased gradually in a controlled fashion, from room temperature to 150 °C at various increments and held at each temperature for 1 h before the impedance measurement. Electrical conductivity was determined by the DC polarization measurements on the pellets with applied voltages of 0.1, 0.15, 0.2, 0.25, and 0.3 V for 30 min each at room temperature. Lithium metal stability measurement using DC polarization tests by using lithium foils as

nonblocking electrodes on both sides of the pelletized SE, then sandwiching them between SUS. The prepared symmetric cells were then cycled at $\pm 0.1 \text{ mA}\cdot\text{cm}^{-2}$ and $\pm 0.2 \text{ mA}\cdot\text{cm}^{-2}$ using a charge-discharge device (BTS-2004H, Nagano) under a dry Ar atmosphere at room temperature. Battery performance for charge and discharge curves were conducted using Li–In alloy as the negative electrode, $\text{Li}_6\text{PS}_5\text{Cl}_{\text{ACN} + \text{PTH}}$ as the electrolyte layer, and $\text{TiS}_2\text{-Li}_6\text{PS}_5\text{Cl}$ composite as the positive electrode. The positive electrodes were fabricated by mixing TiS_2 and SE ($\text{Li}_6\text{PS}_5\text{Cl}$) with the weight ratio of 1:1 on agate mortar with a grind duration of about 15 min. Firstly, SE for about 80 mg was pressed and pelletized at low press into PEEK (inner diameter of 10 mm) with two blocking SUS electrodes. After that, positive electrode powder was kept ($\sim 10 \text{ mg}$) at one side of the pelletized SE, then pressed together at 255 MPa uniaxial pressure at room temperature. After Li–In foil was attached to the other side of the pellet sandwich, it was pressed again at 127 MPa uniaxial pressure at room temperature. The cells were cycled using a charge-discharge device (BST-2004H, Nagano) with voltages cutoff in the range of 1.0 to 2.4 V vs. Li–In at 0.1C. All preparations were conducted inside a dry Ar-filled glovebox.

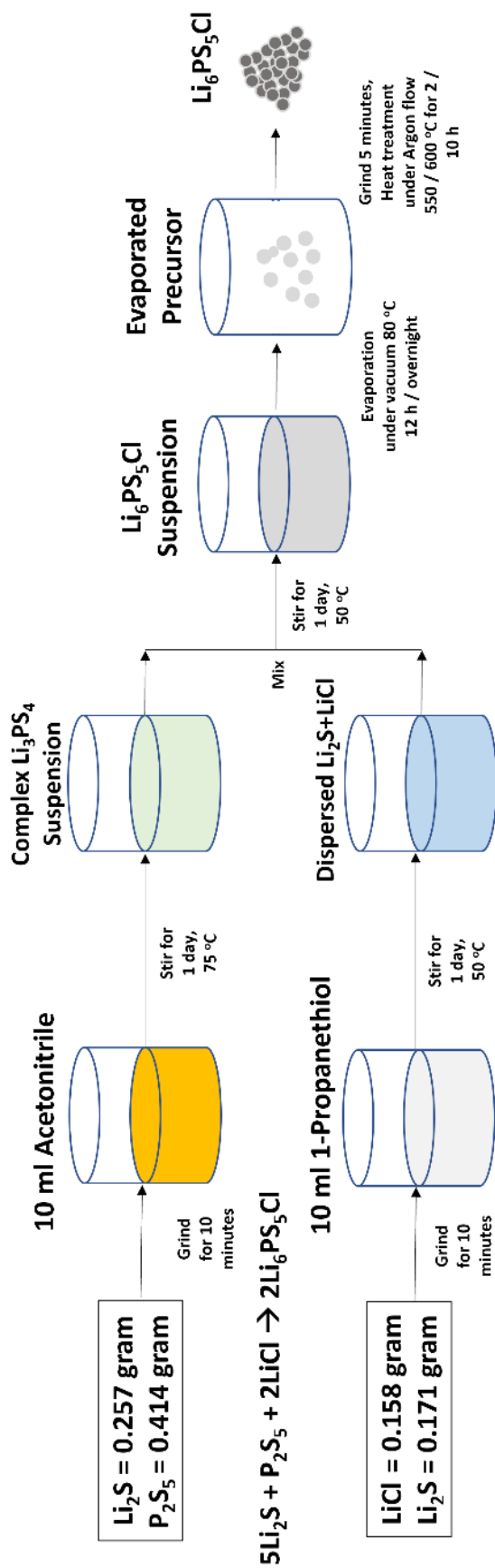


Figure 3.2. Schematic illustration of the liquid-phase synthesis with acetonitrile and 1-propanethiol as the solvents to synthesize Li₆PS₅Cl argyrodite solid electrolyte.

3.4 Result and Discussions

3.4.1 Characterization and ionic conductivity measurement.

Figure 3.3 presents the commonly used mechanism of the Li_3PO_4 formation by omitting the argyrodite structure. The $\text{Li}_6\text{PS}_5\text{Cl}$ using THF and EtOH was argyrodite-type structure (Figure 3.4). The sample formed the impurity of Li_3PO_4 oxide and the remaining of the Li_2S and LiCl as starting materials. The Li_3PO_4 oxide could be produced by the nucleophilic reaction between anion O^- in the hydroxide from ethanol ($\text{OH}^- \text{Li}^+$) and P_2S_5 , which was created by the reaction of EtOH and LiCl , [27] previously matching other's reported results. [24, 26] This finding suggests that the ethanol solvent gave rise to the oxidation whose reaction changes the hydroxyl bond ($-\text{OH}$) into a thiol bond ($-\text{SH}$). The solvent was replaced with the 1-propanethiol (PTH) in this study. The XRD of the $\text{Li}_6\text{PS}_5\text{Cl}$ using the mixed solvent of THF and PTH showed argyrodite-type structure with some residual raw material of Li_2S and LiCl and producing the same Li_3PO_4 crystalline. This structural property is a crystalline structure comparable to that of argyrodite SE which uses THF and EtOH-mixed solvents although the solvent system of THF and PTH (Figure 3.1a) involves no hydroxyl bond. This result indicates that the oxidation formation still occurs via the anionic ring-opening reaction of THF, and the nucleophilic attack from thiorate anion $-\text{S}^-$ of PTH is stronger than that from $-\text{O}^-$ anions of EtOH. The anion of $\text{Li}-\text{X}^-$ may play an important role in THF ring-opening. This was proven from the synthesis of $\beta\text{-Li}_3\text{PS}_4$ using only THF as the solvent and resulted in no Li_3PO_4 oxidation formation. [28, 29] In contrast, the XRD pattern for the sample using the mixed solvent of ACN and PTH showed argyrodite crystalline and a small amount of Li_2S and LiCl without Li_3PO_4 crystalline (Figure 3.4), which results in the excluding of Li_3PO_4 from $\text{Li}_6\text{PS}_5\text{Cl}$ argyrodite SE due to no oxygen source from the system. However, the synthetic mechanism of this oxide was not confirmed in detail. Therefore, we carried out the ^1H NMR spectroscopic studies of Li_3PO_4 oxide formation.

According to this mechanism, as shown in Figure 3.3, the EtOH+THF mixed solutions with LiCl in the presence of Li_2S were evaporated at $80\text{ }^\circ\text{C}$ and examined the ^1H NMR spectra of resulting reaction mixture in DMSO-d_6 , as compared without P_2S_5 and evaporation. TG-DTA curves of $\text{Li}_6\text{PS}_5\text{Cl}$ precursor prepared using EtOH and THF solvents after evaporated at $80\text{ }^\circ\text{C}$ are presented in Figure 3.5, showing an endothermic

peak at 113 °C and a weight loss of around 14%. This behavior indicates the evaporation of EtOH+THF solvents. Thus, the remaining solvent in the reaction mixture should remain even after the evaporation at 80 °C. As the results of Figure 3.6, the NMR spectrum of EtOH+THF mixed solution with LiCl and Li₂S at room temperature resulted in no reaction and interaction. However, after the temperature was promoted from the evaporation process (80 °C), the chemical shift of methylene protons of THF at 3.63 ppm to the low magnetic field was at 3.77 ppm and showed a broad peak at 2.66 ppm, assigned to the hydroxy group (-OH) in the terminal group of ring-opened THF.[30] This data implies the evidence of oxidation from the ring-opening of THF by the negative charge of oxygen (O^-) in ethanol, probably leading to the weak interaction between H^+ of EtOH and Cl^- of LiCl could be occurred with heating as a driving force. This case was similar to the previous report when THF was stirred with halogen CuBr at 60 °C for 24 h, a nucleophilic reaction happened creating a ring opening of THF.[31] The NMR results revealed that the ethanol solvent gave rise to the oxidation.

To investigate the reformation of the O^- anion through the anionic ring-opening reaction of THF and the stronger nucleophilic attack of thiolate anion S^- from PTH compared to O^- anions from EtOH, PTH was utilized under the same EtOH+THF conditions. Figure 3.7 illustrates the NMR results of Li₆PS₅Cl in mixed solvents of PTH and THF after evaporation at 80 °C, along with the PTH+THF mixed solvents in the presence of LiCl and Li₂S. In the PTH solvent with LiCl at room temperature, the chemical shift of the ethylene protons neighboring the thiol (-SH) was observed to shift to a higher magnetic field, from 2.47 to 2.43 ppm. Conversely, in the PTH+THF mixed solution with LiCl and Li₂S, the chemical shift of the SH group in the PTH solvent experienced a larger shift from 1.87 to 2.04 ppm. This can be attributed to a stronger interaction between $\text{S-H}^+ \dots \text{Cl-Li}^+$ and the oxygen in the THF ring. Furthermore, NMR spectra were obtained from Li₆PS₅Cl argyrodite prepared with PTH+THF, and the heat was applied during the evaporation process at 80 °C. The methylene peak of THF slightly shifted to a lower magnetic field, and a broad peak of OH around 2.7 ppm was observed from the terminal group of the ring-opened THF. These observations closely resemble the ring-opened THF in Li₆PS₅Cl argyrodite synthesized using EtOH+THF.

Li₆PS₅Cl/SE_{ACN+PTH} exhibited sharper and smaller particles compared to Li₆PS₅Cl/SE_{THF+EtOH}, as evidenced by SEM images (refer to Figure 3.8). Raman

spectroscopy confirmed the presence of the PS_4^{3-} anions structural unit (see Figure 3.9). $\text{Li}_6\text{PS}_5\text{Cl}/\text{SE}_{\text{ACN}+\text{PTH}}$ and $\text{Li}_6\text{PS}_5\text{Cl}/\text{SE}_{\text{BM}}$ displayed a broad PS_4^{3-} peak at 420 cm^{-1} . In contrast, $\text{Li}_6\text{PS}_5\text{Cl}/\text{SE}_{\text{THF}+\text{EtOH}}$ exhibited the PS_4^{3-} peak at a lower wave number of 416 cm^{-1} . This indicates that the incorporation of oxygen ions in the argyrodite system leads to modifications in the P-S bond. The higher electronegativity of oxygen compared to lithium and sulfur results in lattice distortion/disorder, thereby influencing the strength of the PS bond [32].

The Nyquist plots of electrochemical impedance at room temperature and the temperature dependence of ionic conductivity are depicted in Figure 3.10 and Figure 3.11, respectively, for $\text{Li}_6\text{PS}_5\text{Cl}/\text{SE}_{\text{THF} + \text{EtOH}}$ and $\text{Li}_6\text{PS}_5\text{Cl}/\text{SE}_{\text{ACN} + \text{PTH}}$. These samples displayed ionic conductivities of 1.57 and $1.68\text{ mS}\cdot\text{cm}^{-1}$ at room temperature ($25\text{ }^\circ\text{C}$), respectively. It should be noted that the ionic conductivity of Li_3PO_4 is reported to be in the range of 10^{-7} to $10^{-6}\text{ S}\cdot\text{cm}^{-1}$, which is significantly lower compared to the conductivity of argyrodite (10^{-3} to $10^{-2}\text{ S}\cdot\text{cm}^{-1}$). [33] Figure 3.12 illustrates the activation energy, showing that $\text{Li}_6\text{PS}_5\text{Cl}/\text{SE}_{\text{ACN} + \text{PTH}}$ with the mixed solvents exhibits a lower activation energy of $28.0\text{ kJ}\cdot\text{mol}^{-1}$, whereas $\text{Li}_6\text{PS}_5\text{Cl}/\text{SE}_{\text{THF} + \text{EtOH}}$ has a higher activation energy of $32.0\text{ kJ}\cdot\text{mol}^{-1}$. This finding demonstrates that by increasing the ionic conductivity of $\text{Li}_6\text{PS}_5\text{Cl}/\text{SE}$ argyrodite without the presence of Li_3PO_4 oxidation, the liquid-phase synthesis technique can be effectively employed. The presence of even a small amount of Li_3PO_4 impurity in the solid electrolyte can significantly impede Li-ion transport and lead to an increased activation energy.

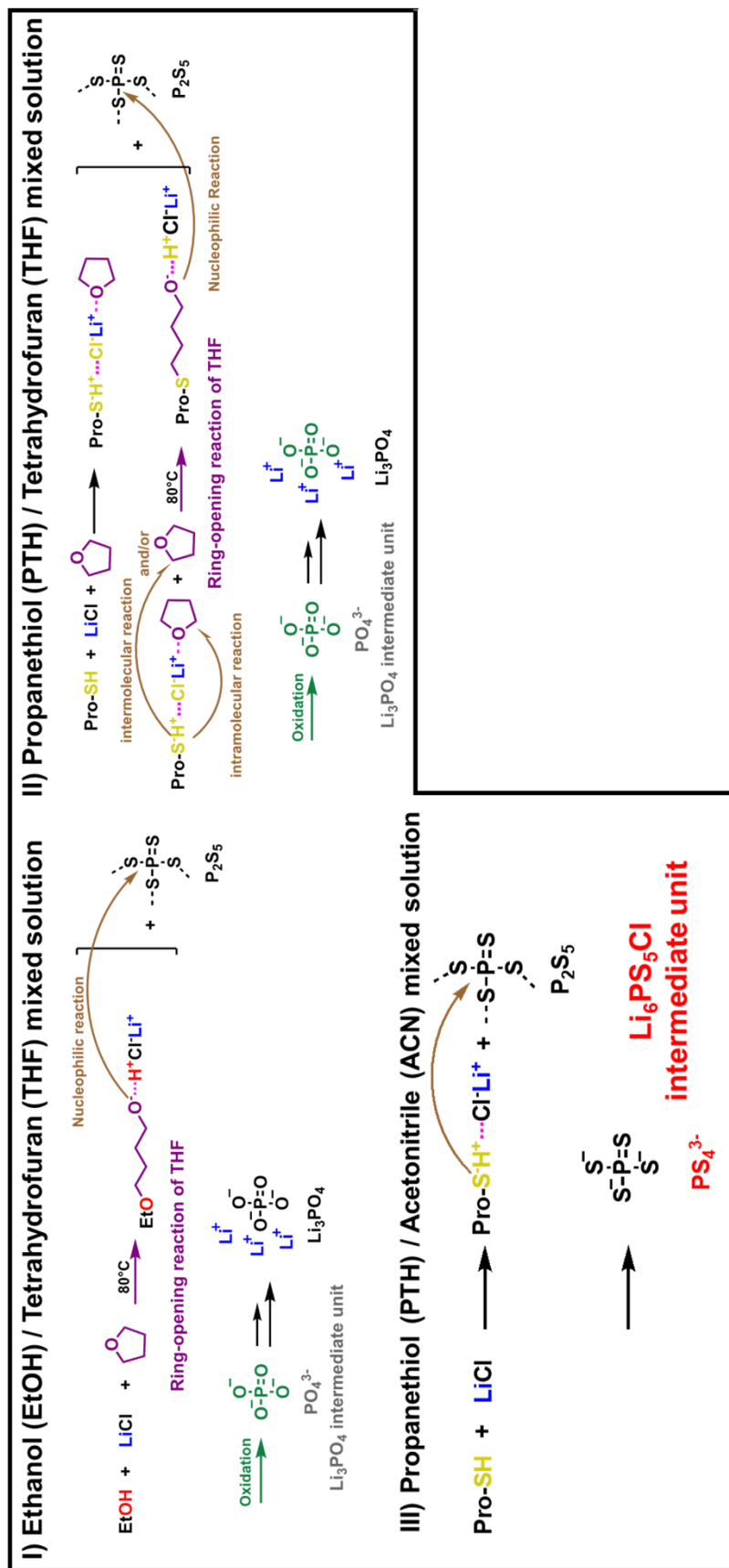


Figure 3.3. The illustration schematic mechanism of the elimination of Li_3PO_4 oxide formation by using acetonitrile (ACN) and 1-propanethiol (PTH) as the solvents.

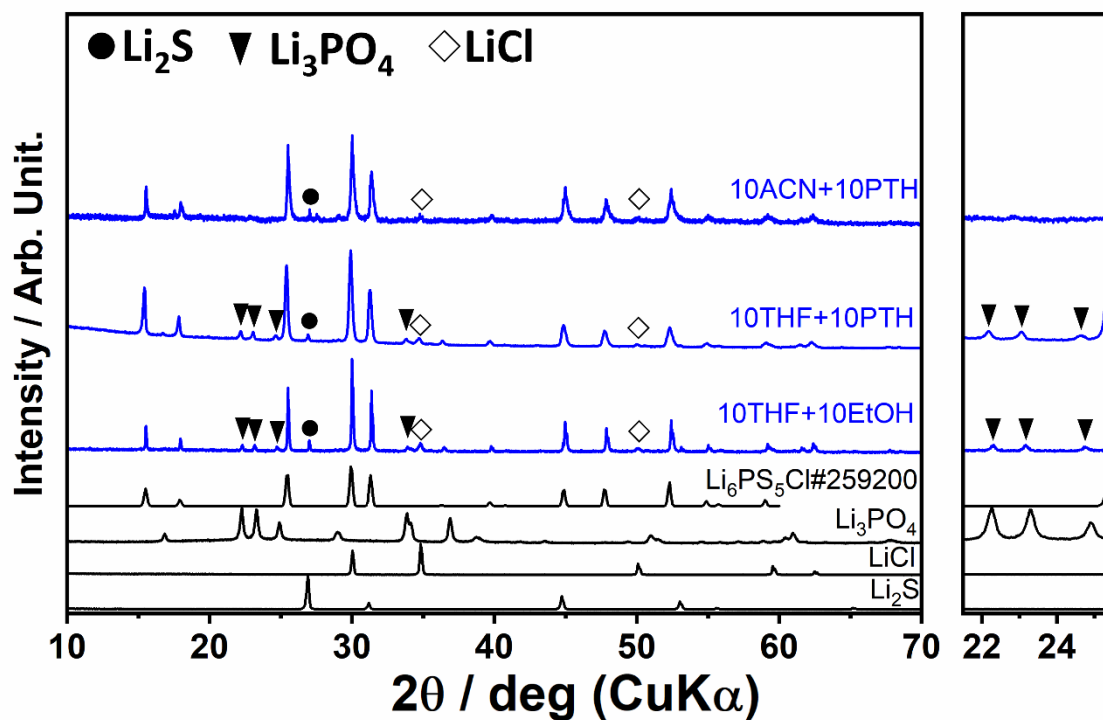


Figure 3.4. XRD patterns of $\text{Li}_6\text{PS}_5\text{Cl}$ prepared by liquid-phase synthesis with THF + EtOH, THF + PTH, and ACN + PTH as the solvent. All the samples were dried at 80 °C for overnight then heat treated at 600 °C for 2 h.

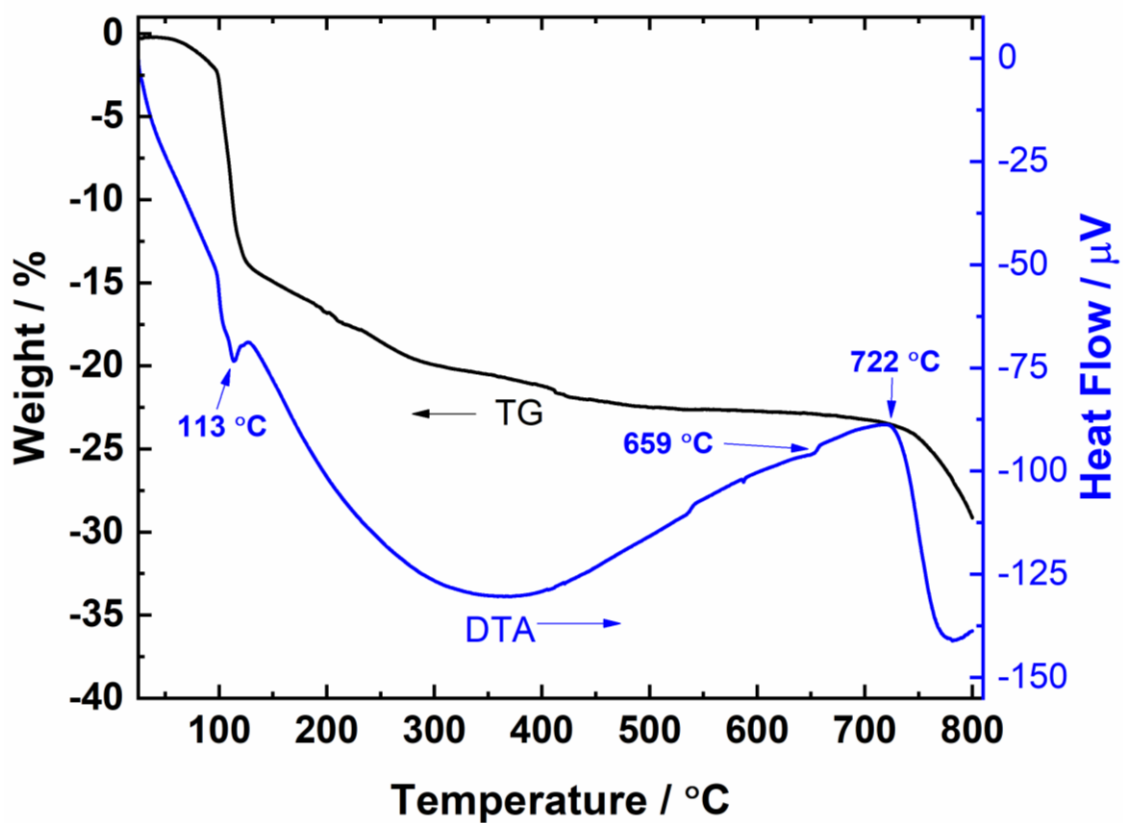


Figure 3.5. TG-DTA curves of $\text{Li}_6\text{PS}_5\text{Cl}$ prepared by liquid phase synthesis using EtOH and THF solvents after evaporated at 80 °C for 12 hours.

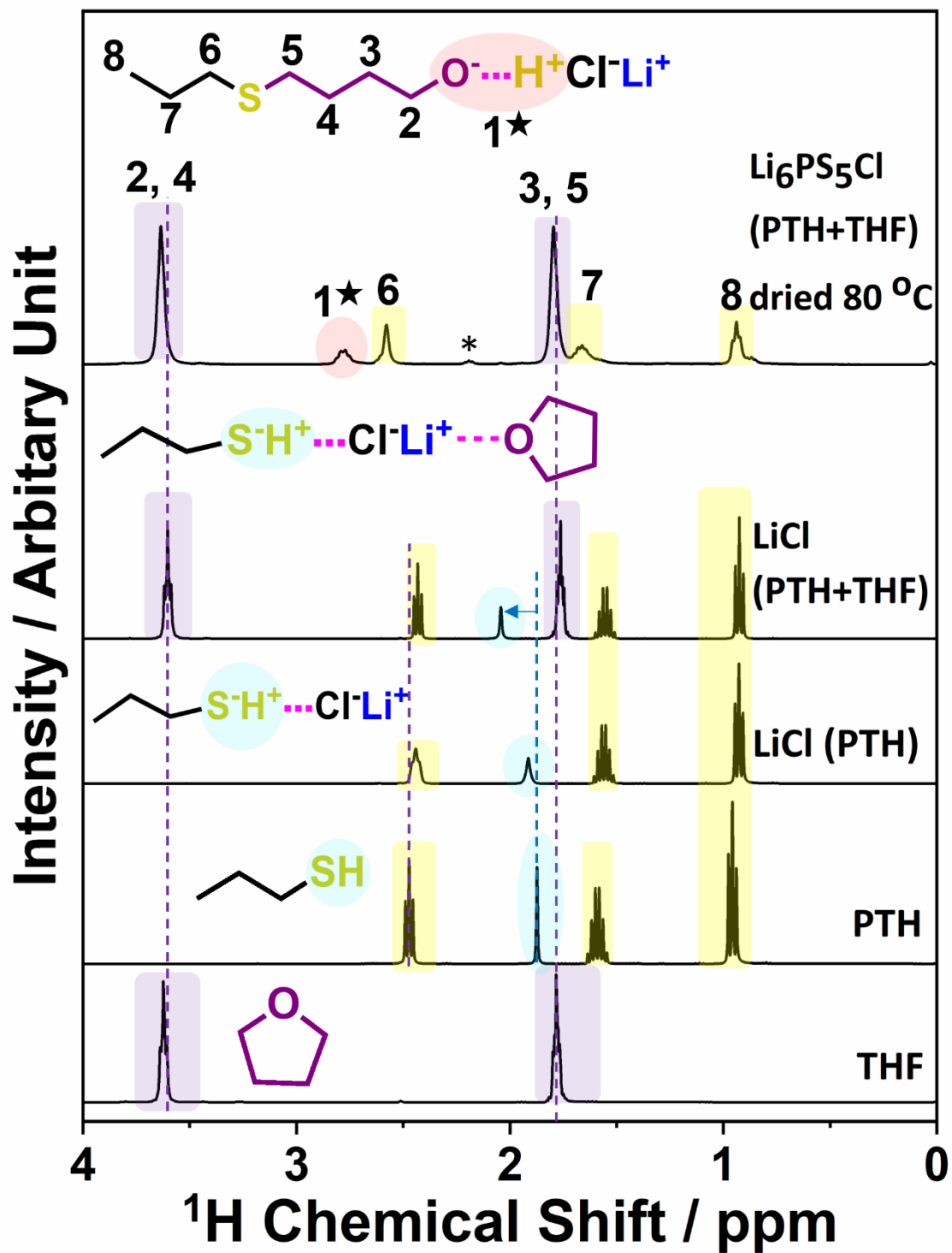


Figure 3.7. ^1H NMR spectra of $\text{Li}_6\text{PS}_5\text{Cl}$ and $\text{Li}_2\text{S-LiCl}$ with ACN + PTH

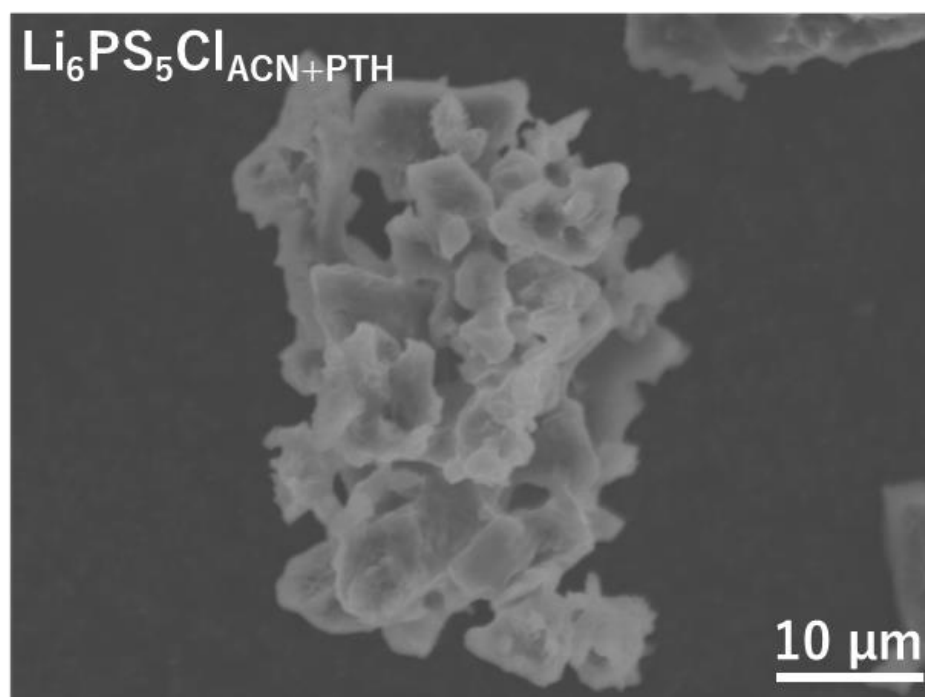
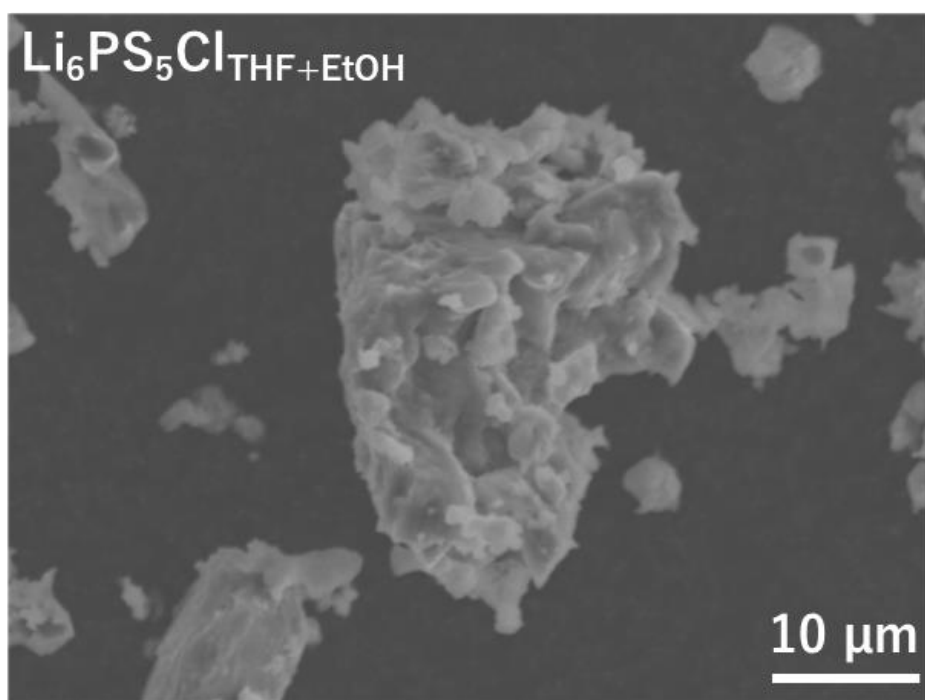


Figure 3.8. Morphology of $\text{Li}_6\text{PS}_5\text{Cl}_{\text{EtOH+THF}}$ and $\text{Li}_6\text{PS}_5\text{Cl}_{\text{ACN+PTH}}$. SEM images of $\text{Li}_6\text{PS}_5\text{Cl}$ with THF + EtOH and ACN + PTH as the solvents after the heat treatment process

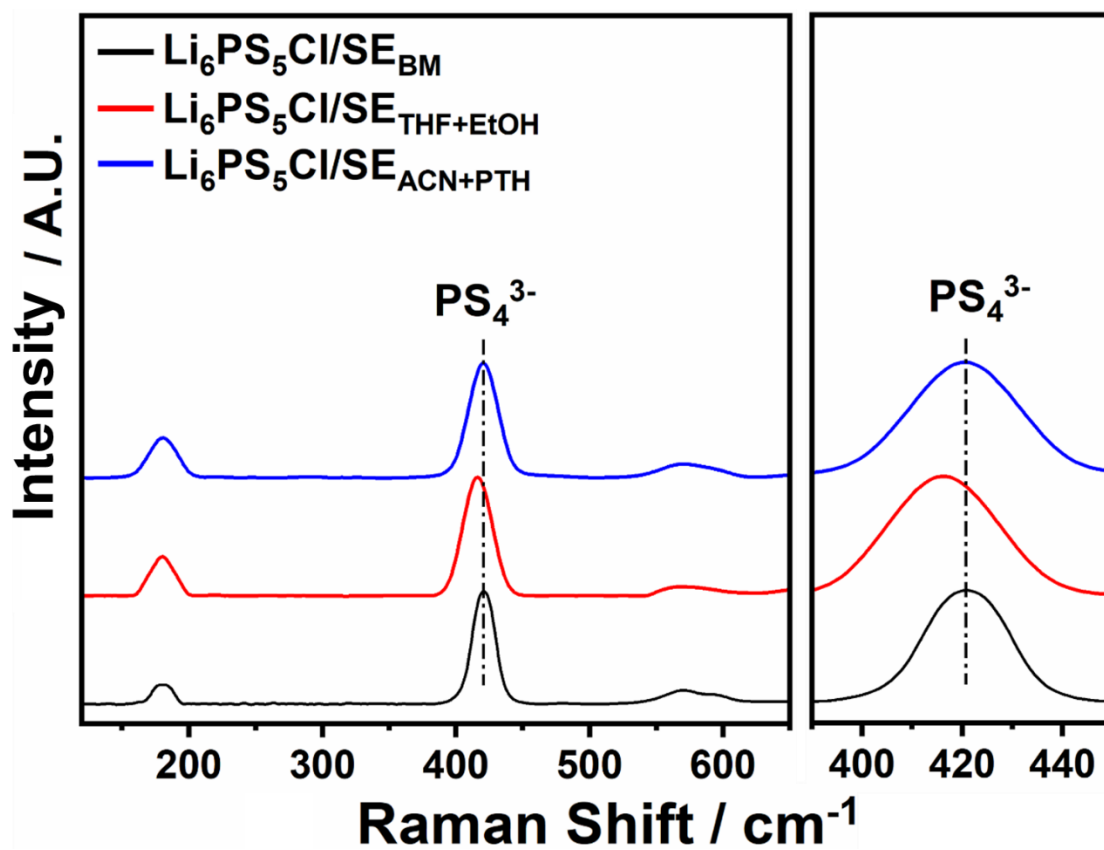


Figure 3.9. Raman spectra patterns of $\text{Li}_6\text{PS}_5\text{Cl}$ with THF + EtOH and ACN + PTH as the solvents and $\text{Li}_6\text{PS}_5\text{Cl}$ prepared by ball milling

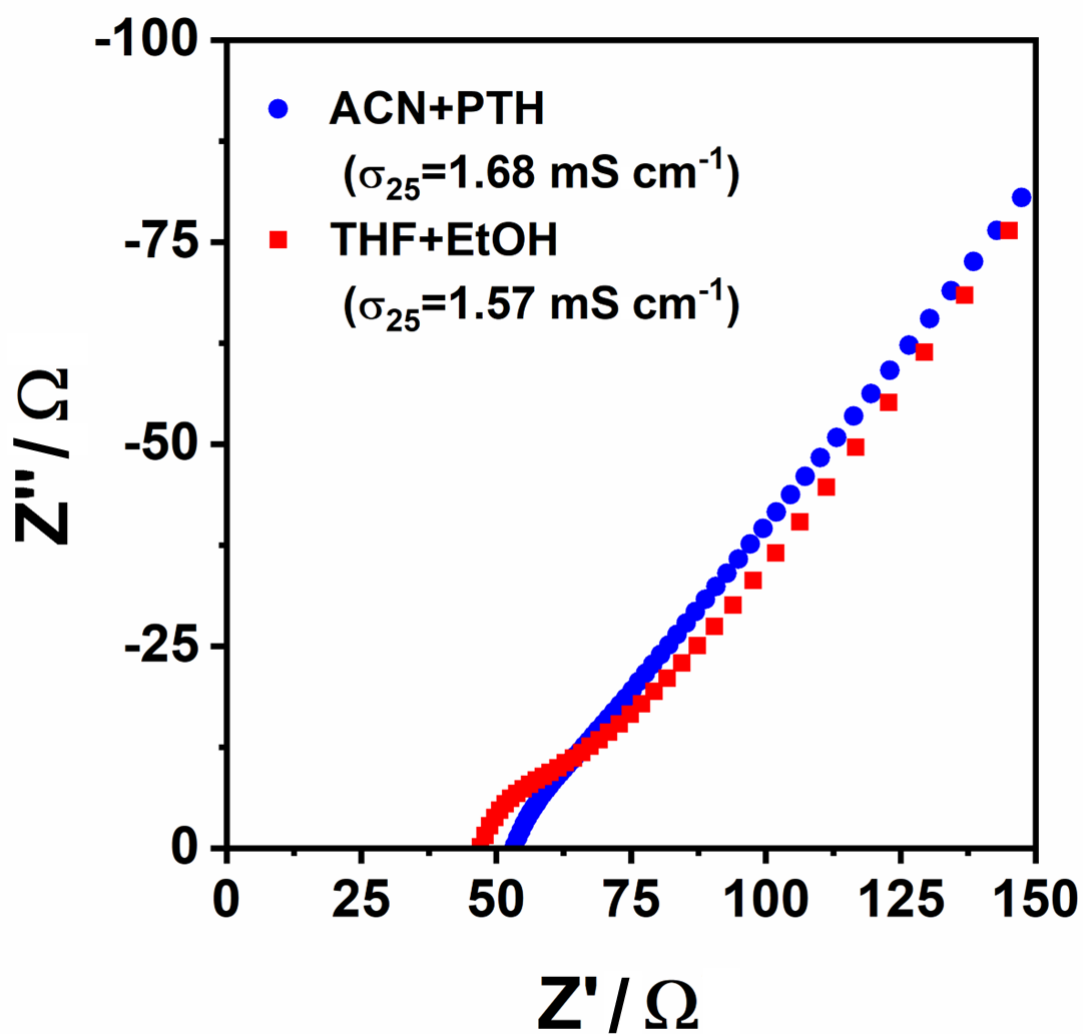


Figure 3.10. Nyquist plots of electrochemical impedance from $\text{Li}_6\text{PS}_5\text{Cl}_{\text{EtOH+THF}}$ and $\text{Li}_6\text{PS}_5\text{Cl}_{\text{ACN+PTH}}$ after heat treated at $600 \text{ }^\circ\text{C}$ for 2 h.

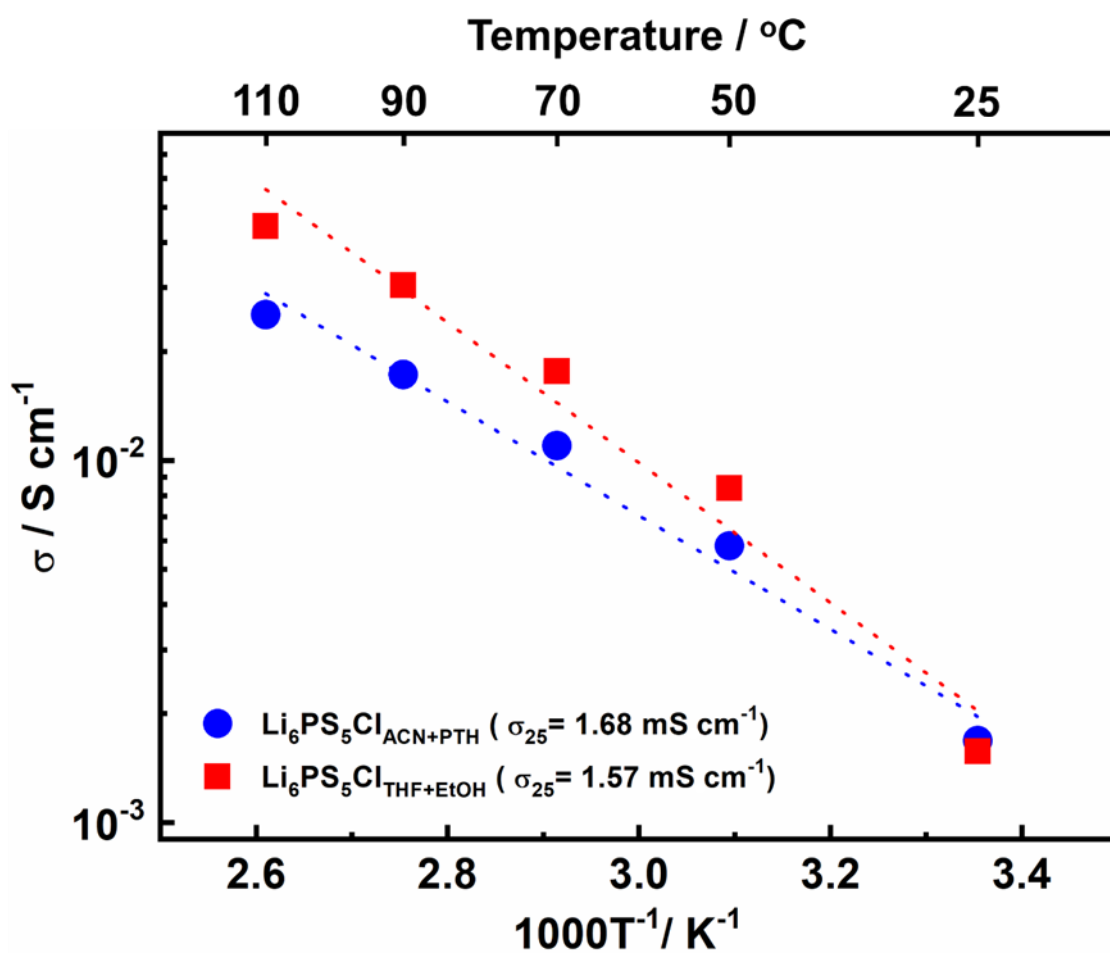


Figure 3.11. Temperature dependence of ionic conductivity from $\text{Li}_6\text{PS}_5\text{Cl}_{\text{EtOH+THF}}$ and $\text{Li}_6\text{PS}_5\text{Cl}_{\text{ACN+PTH}}$ after heat treated at 600 °C for 2 h.

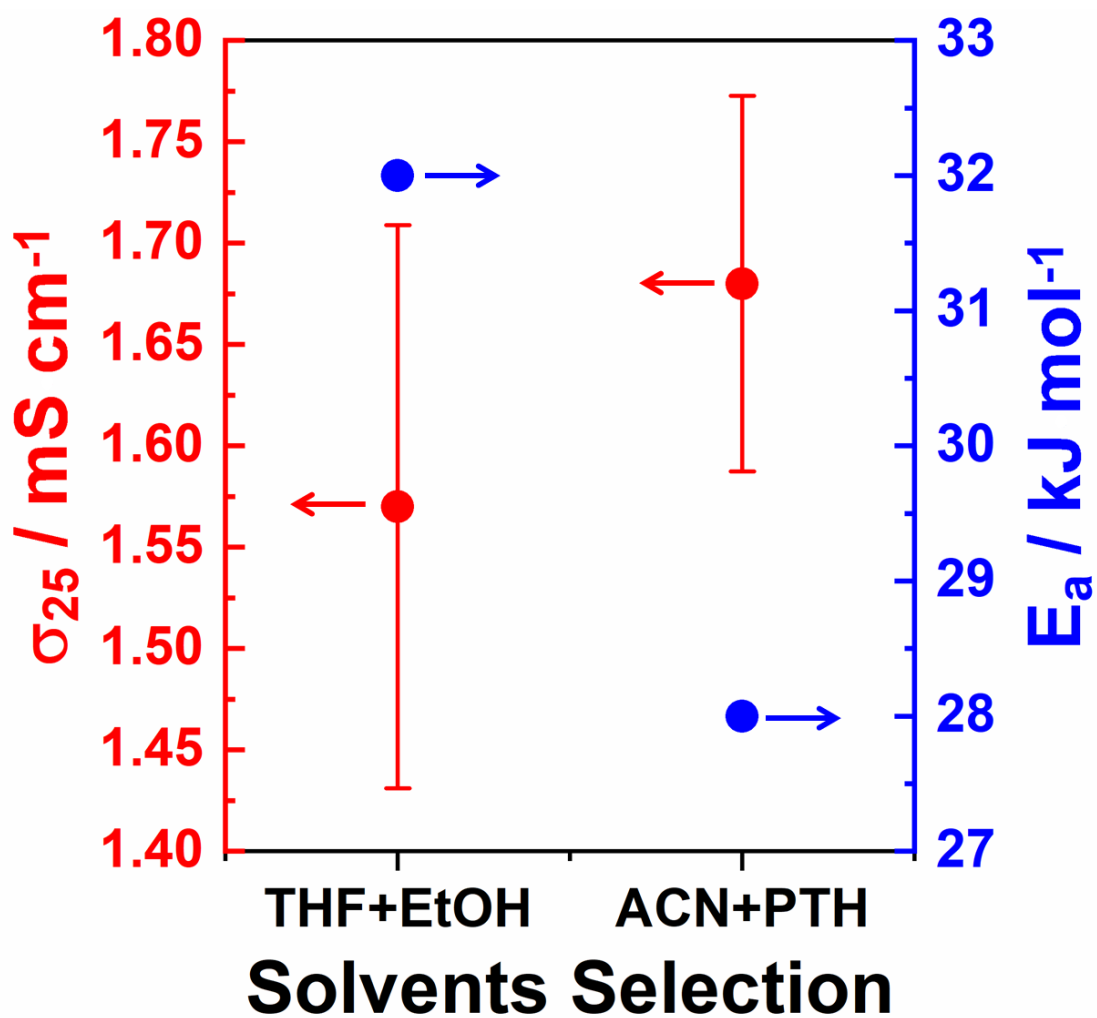


Figure 3.12. Ionic conductivity and activation energy at 25 °C of $\text{Li}_6\text{PS}_5\text{Cl}_{\text{EtOH+THF}}$ and $\text{Li}_6\text{PS}_5\text{Cl}_{\text{ACN+PTH}}$ after heat treated at 600 °C for 2 h.

3.4.2 Heat Treatment Optimization

At room temperature, $\text{Li}_6\text{PS}_5\text{Cl}/\text{SE}_{600}/\text{ACN} + \text{PTH}/2\text{h}$ without Li_3PO_4 phase has ionic conductivity almost the same as $\text{Li}_6\text{PS}_5\text{Cl}/\text{SE}_{600}/\text{THF} + \text{EtOH}/2\text{h}$ with Li_3PO_4 phase. The heat treatment temperature and time were optimized to improve the ionic conductivity further. To determine the optimal heat treatment condition for achieving the high ionic conductivity, we measured the TG-DTA from $\text{Li}_6\text{PS}_5\text{Cl}/\text{SE}_{\text{ACN} + \text{PTH}}$ (Figure 3.13). There are two endothermic peaks at 100 and 185 °C along with the weight decrement of 2% and then 14%, respectively. The endothermic peak at 100 °C indicates the evaporation of the remaining PTH solvent followed by the crystallization of Li_3PS_4 and probably evaporation of the remaining ACN at 185 °C.[34-36] Starting at 630 °C, there is a small endothermic peak which indicates the release of sulfur content. An exothermic peak at 693 °C signed the argyrodite start to partially decompose until began to fully decompose at 761 °C. This is similar to $\text{Li}_6\text{PS}_5\text{Cl}/\text{SE}_{\text{THF} + \text{EtOH}}$ (Figure 3.5) which has a small exothermic peak at 659 °C which is the same indication of sulfur releasement. Moreover, $\text{Li}_6\text{PS}_5\text{Cl}/\text{SE}_{\text{THF} + \text{EtOH}}$ began to full degradation at 722 °C. Furthermore, we will focus on the heat treatment time of 10 hours long, according to literature reported by Yu et al. that 550 °C for 10 hours is the optimum heat treatment condition for the argyrodite system.[37] Temperature higher than 550 °C will increase the amount of LiCl residual and the precipitation of Li_2S which indicate the degradation, while prolonging the heat treatment time above 10 hours might evaporate the lithium content.[37, 38] This analysis is also supported by the TG-DTA result in Figure 3.14 from $\text{Li}_6\text{PS}_5\text{Cl}/\text{SE}_{\text{BM}}$ shows a slight exothermic at 600 °C attributed to the degradation of argyrodite into LiCl with the weight decrement around 2-3%. The releasement of sulfur was signed at 625 °C with a small endothermic peak which is similar to other argyrodite that was prepared with liquid phase synthesis. The second exothermic peak at 675 °C indicates the argyrodite starts to partially decompose and is followed to start fully decompose at 781 °C along with the 45% weight reduction. Figure 3.15 shows the XRD patterns of $\text{Li}_6\text{PS}_5\text{Cl}/\text{SE}_{\text{ACN} + \text{PTH}/10\text{h}}$ and $\text{Li}_6\text{PS}_5\text{Cl}/\text{SE}_{\text{THF} + \text{EtOH}/10\text{h}}$ heat treatment at 550 °C and 600 °C. $\text{Li}_6\text{PS}_5\text{Cl}/\text{SE}_{550}/\text{THF} + \text{EtOH}/10\text{h}$ showed the peaks corresponding to Li_2S and LiCl of the starting materials, oxidation of Li_3PO_4 , and the main peak of argyrodite. The peak intensities of residual and oxide increased after the heat treatment temperature at 600 °C for the same amount of

time, which indicates that the argyrodite phase starts to degrade at this temperature. The intensity of the Li_3PO_4 oxide increased at 600 °C. This observation indicates that a higher heat temperature encourages Li_3PO_4 development. $\text{Li}_6\text{PS}_5\text{Cl}/\text{SE}_{600/\text{ACN} + \text{PTH}/10\text{h}}$ involved the degradation of the $\text{Li}_6\text{PS}_5\text{Cl}$ phase with Li_2S and LiCl as the starting material. On the other hand, $\text{Li}_6\text{PS}_5\text{Cl}/\text{SE}_{550/\text{ACN} + \text{PTH}/10\text{h}}$ formed a crystalline of argyrodite with almost an unnoticeable peak of Li_2S .

The $\text{Li}_6\text{PS}_5\text{Cl}$ with BM technique was used as a reference structure. As shown in Figure 3.16, the XRD patterns of $\text{Li}_6\text{PS}_5\text{Cl}/\text{SE}_{550/\text{BM}/10\text{h}}$ and $\text{Li}_6\text{PS}_5\text{Cl}/\text{SE}_{600/\text{BM}/10\text{h}}$ showed a crystalline phase of argyrodite-type structure without residual material and, of course, oxidation. There is an obvious peak of Li_2S remaining in the $\text{Li}_6\text{PS}_5\text{Cl}/\text{SE}_{\text{BM}}$ as-synthesized by BM's method. This suggests that the heat treatment process is necessary to obtain an argyrodite crystalline phase with high purity. To study further the local structure of the argyrodite SE, we examined a solid ^{31}P MAS-NMR measurement for $\text{Li}_6\text{PS}_5\text{Cl}/\text{SE}_{\text{ACN} + \text{PTH}}$, $\text{Li}_6\text{PS}_5\text{Cl}/\text{SE}_{\text{THF} + \text{EtOH}}$, and $\text{Li}_6\text{PS}_5\text{Cl}/\text{SE}_{\text{BM}}$. In Figure 3.17, the ^{31}P MAS-NMR spectroscopy of the $\text{Li}_6\text{PS}_5\text{Cl}/\text{SE}_{\text{BM}}$ displays the peak at 88 ppm belonging to PS_4^{3-} anion and the inevitable spinning sidebands. $\text{Li}_6\text{PS}_5\text{Cl}$ with the mixed solvent of THF and EtOH contains not only the anion of PS_4^{3-} at 88 ppm, but also the chemical shift of PO_4^{3-} anion at 10 ppm.[39] This finding proved that EtOH and the oxygen release from the THF ring-opening effect promote the formation of Li_3PO_4 oxide. The argyrodite with the ACN and PTH mixed solvent involved no oxides, such as Li_3PO_4 , as shown in ^{31}P MAS-NMR spectroscopy. Our study demonstrated that $\text{Li}_6\text{PS}_5\text{Cl}$ prepared by the liquid-phase method using ACN + PTH have a crystalline and local structure similar to $\text{Li}_6\text{PS}_5\text{Cl}$ using the BM method, that is highly pure crystal phase without oxides. This led to the study of the industrial-scale production of $\text{Li}_6\text{PS}_5\text{Cl}$ using the liquid-phase synthesis method.

Investigation of heat treatment condition impact on ionic conductivity for each $\text{Li}_6\text{PS}_5\text{Cl}/\text{SE}_{\text{THF} + \text{EtOH}}$ and $\text{Li}_6\text{PS}_5\text{Cl}/\text{SE}_{\text{ACN} + \text{PTH}}$ sample was conducted by using electrochemical impedance spectroscopy. Figure 3.18 shows the Nyquist plots of electrochemical impedance for $\text{Li}_6\text{PS}_5\text{Cl}/\text{SE}_{\text{THF} + \text{EtOH}}$ and $\text{Li}_6\text{PS}_5\text{Cl}/\text{SE}_{\text{ACN} + \text{PTH}}$ heat-treated at 550 °C and 600 °C for 10 h, respectively, along with a graph for the temperature dependence of ionic conductivity and the relation with the activation energy from it at Figure 3.19. The ionic conductivity for $\text{Li}_6\text{PS}_5\text{Cl}/\text{SE}_{550/\text{THF} + \text{EtOH}/10\text{h}}$ was $1.80 \text{ mS}\cdot\text{cm}^{-1}$ at

room temperature with an activation energy of $28.3 \text{ kJ}\cdot\text{mol}^{-1}$, whereas the ionic conductivity of $\text{Li}_6\text{PS}_5\text{Cl}/\text{SE}_{600}/\text{THF} + \text{EtOH}/10\text{h}$ decreased to $1.47 \text{ mS}\cdot\text{cm}^{-1}$ with an activation energy of $30.1 \text{ kJ}\cdot\text{mol}^{-1}$. The decrement of the ionic conductivity and the increment of the activation energy was relevant for the XRD patterns result shown in Figure 3.15, in which $\text{Li}_6\text{PS}_5\text{Cl}/\text{SE}_{600}/\text{THF} + \text{EtOH}$ partially decomposed into Li_2S and LiCl . The higher temperature at $600 \text{ }^\circ\text{C}$ induces a higher crystallinity of Li_3PO_4 in $\text{Li}_6\text{PS}_5\text{Cl}$, which becomes a factor for decreasing the ionic conductivity at room temperature from the $\text{Li}_6\text{PS}_5\text{Cl}/\text{SE}_{550}/\text{THF} + \text{EtOH}$ sample. In comparison, $\text{Li}_6\text{PS}_5\text{Cl}/\text{SE}_{600}/\text{ACN} + \text{PTH}/10\text{h}$ exhibited ionic conductivity of $2.13 \text{ mS}\cdot\text{cm}^{-1}$ at room temperature and activation energy of $25.2 \text{ kJ}\cdot\text{mol}^{-1}$. Alternatively, the ionic conductivity of $\text{Li}_6\text{PS}_5\text{Cl}/\text{SE}_{550}/\text{ACN} + \text{PTH}/10\text{h}$ increased to $2.75 \text{ mS}\cdot\text{cm}^{-1}$ and the activation energy reduce to $24.8 \text{ kJ}\cdot\text{mol}^{-1}$. When the heat treatment temperature was increased to $600 \text{ }^\circ\text{C}$, the Li_2S crystalline phase was still present, with a minor amount of LiCl crystalline phase appearing as an impurity, whereas the LiCl crystalline phase was not sighted at $550 \text{ }^\circ\text{C}$. $\text{Li}_6\text{PS}_5\text{Cl}/\text{SE}_{\text{ACN}} + \text{PTH}$ without Li_3PO_4 impurity may cause the degradation of Li_2S and LiCl formation for higher temperature heat treatment. The degrading crystalline phase from the $\text{Li}_6\text{PS}_5\text{Cl}/\text{SE}_{\text{ACN}} + \text{PTH}$ sample caused a decrease in ionic conductivity. Longer periods of heat treatment is beneficial for achieving the highly crystallized argyrodite-type phase. Taking this into consideration, the heat treatment temperature at $550 \text{ }^\circ\text{C}$ for 10 h was the optimum for argyrodite in this study as we stated in the previous section.[37]

For the basic comparison, the ionic conductivity of argyrodites ($\text{Li}_6\text{PS}_5\text{Cl}/\text{SE}_{550}/\text{BM}$ and $\text{Li}_6\text{PS}_5\text{Cl}/\text{SE}_{600}/\text{BM}$) was prepared with the ball milling method and heat treatment at $550 \text{ }^\circ\text{C}$ and $600 \text{ }^\circ\text{C}$ were examined. From Figure 20, 21, and 22, the Nyquist plot of electrochemical impedance, the temperature dependence of ionic conductivity, and heat treatment temperature dependence of activation energy from both samples was confirmed. The ionic conductivity at room temperature of $\text{Li}_6\text{PS}_5\text{Cl}/\text{SE}_{550}/\text{BM}/10\text{h}$ were $2.90 \text{ mS}\cdot\text{cm}^{-1}$ with an activation energy of $29.0 \text{ kJ}\cdot\text{mol}^{-1}$, while the ionic conductivity of $\text{Li}_6\text{PS}_5\text{Cl}/\text{SE}_{600}/\text{BM}/10\text{h}$ at room temperature decreased to $2.20 \text{ mS}\cdot\text{cm}^{-1}$ and the activation energy was increased to $30.6 \text{ kJ}\cdot\text{mol}^{-1}$. The decrease in ionic conductivity resulted from the degradation of the argyrodite crystalline phase. This is also the same as the explanation from argyrodite that prepared with liquid phase synthesis, the increment of heat treatment temperature $> 550 \text{ }^\circ\text{C}$ will resulting the degradation of LiCl and

precipitation of Li_2S . [37] After measuring the ionic conductivity of $\text{Li}_6\text{PS}_5\text{Cl}/\text{SE}_{\text{BM}}$, the ionic conductivity at room temperature and the activation energy from both $\text{Li}_6\text{PS}_5\text{Cl}/\text{SE}_{\text{BM}}$ and $\text{Li}_6\text{PS}_5\text{Cl}/\text{SE}_{\text{ACN} + \text{PTH}}$ liquid-phase synthesis method were compared. Both methods achieved the highest ionic conductivity from this study with heat treatment temperature at 550 °C for 10 h. The Nyquist plots of electrochemical impedance, the temperature dependence of ionic conductivity, and the comparison of activation energy and ionic conductivity were shown in Figure 23, 24, and 25. As previously stated, the ionic conductivity of the $\text{Li}_6\text{PS}_5\text{Cl}/\text{SE}_{\text{BM}/550/10\text{h}}$ was $2.90 \text{ mS}\cdot\text{cm}^{-1}$ at room temperature. At the same time, $\text{Li}_6\text{PS}_5\text{Cl}/\text{SE}_{\text{ACN} + \text{PTH}/550/10\text{h}}$ was $2.75 \text{ mS}\cdot\text{cm}^{-1}$ for the ionic conductivity at room temperature. The BM method and the subsequent heat treatment allow to create a highly pure crystalline phase of argyrodite without any residual trace. $\text{Li}_6\text{PS}_5\text{Cl}/\text{SE}_{\text{BM}}$ has a higher ionic conductivity at room temperature than $\text{Li}_6\text{PS}_5\text{Cl}/\text{SE}_{\text{ACN} + \text{PTH}}$, which corresponds to the small amount of Li_2S residual materials in $\text{Li}_6\text{PS}_5\text{Cl}/\text{SE}_{\text{BM}}$. The SEM image of $\text{Li}_6\text{PS}_5\text{Cl}/\text{SE}_{\text{BM}}$ itself in Figure 3.26 shows that the morphology of the SE is bulkier than $\text{Li}_6\text{PS}_5\text{Cl}/\text{SE}_{\text{ACN} + \text{PTH}}$ (Figure 3.8). However, the activation energy of $\text{Li}_6\text{PS}_5\text{Cl}/\text{SE}_{\text{ACN} + \text{PTH}}$ ($24.8 \text{ kJ}\cdot\text{mol}^{-1}$) has the upper hand due to the lower value of the activation energy compared to the $\text{Li}_6\text{PS}_5\text{Cl}/\text{SE}_{\text{BM}}$ ($29.0 \text{ kJ}\cdot\text{mol}^{-1}$). Furthermore, the crystallite size comparison from each $\text{Li}_6\text{PS}_5\text{Cl}/\text{SE}_{\text{BM}}$, $\text{Li}_6\text{PS}_5\text{Cl}/\text{SE}_{\text{ACN} + \text{PTH}}$, and $\text{Li}_6\text{PS}_5\text{Cl}/\text{SE}_{\text{THF} + \text{EtOH}}$ could be found in supplementary Table 3.1 by using the Debye-Scherrer equation. [40] The smallest average crystallite size could be get from $\text{Li}_6\text{PS}_5\text{Cl}/\text{SE}_{\text{THF} + \text{EtOH}}$ at 102 nm, then followed by $\text{Li}_6\text{PS}_5\text{Cl}/\text{SE}_{\text{ACN} + \text{PTH}}$ with 136 nm. The largest average crystallite size could be attributed to $\text{Li}_6\text{PS}_5\text{Cl}/\text{SE}_{\text{BM}}$ which is 139 nm. The larger the crystallite size response to higher the ionic conductivity results, however, the correlation between crystallite size and conductivity from the argyrodite system requires further analysis. [37] Eventually, the ionic conductivity difference at room temperature was insignificant and comparable for both $\text{Li}_6\text{PS}_5\text{Cl}/\text{SE}_{\text{BM}}$ and $\text{Li}_6\text{PS}_5\text{Cl}/\text{SE}_{\text{ACN} + \text{PTH}}$.

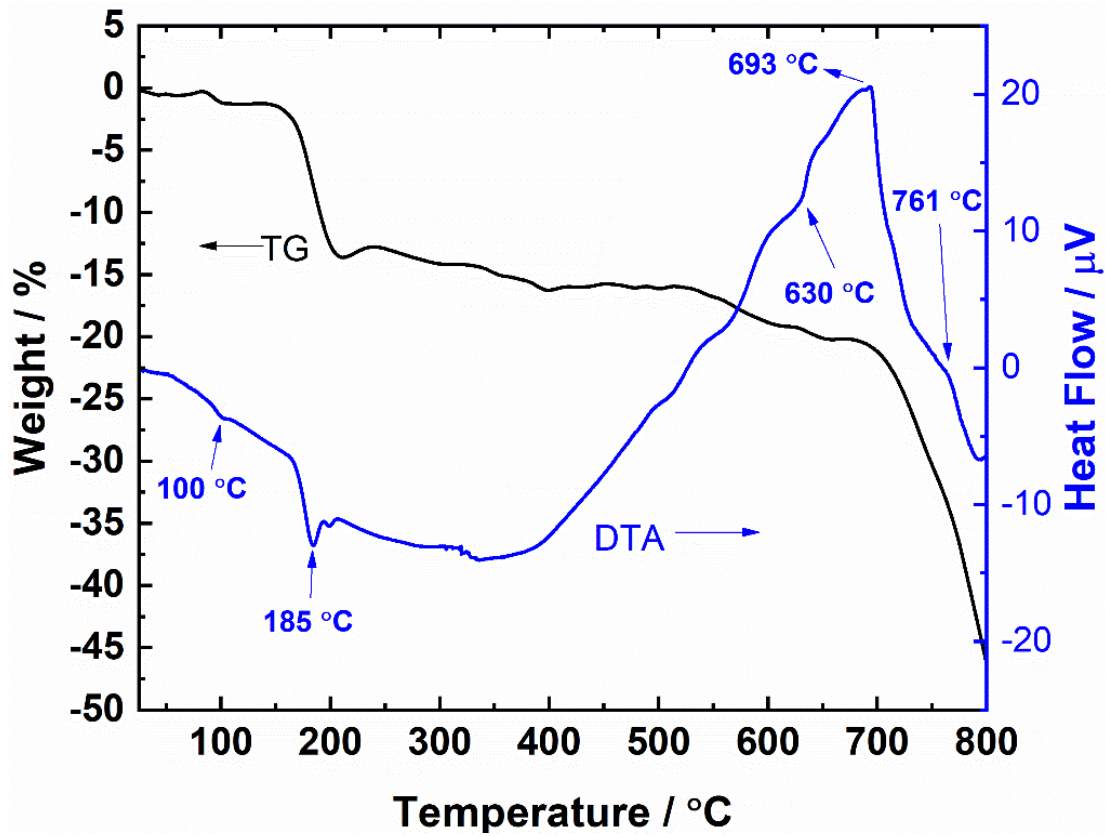


Figure 3.13. TG-DTA curves of $\text{Li}_6\text{PS}_5\text{Cl}$ prepared by liquid phase synthesis using ACN and PTH solvents after evaporated at 80 $^\circ\text{C}$ for 12 hours.

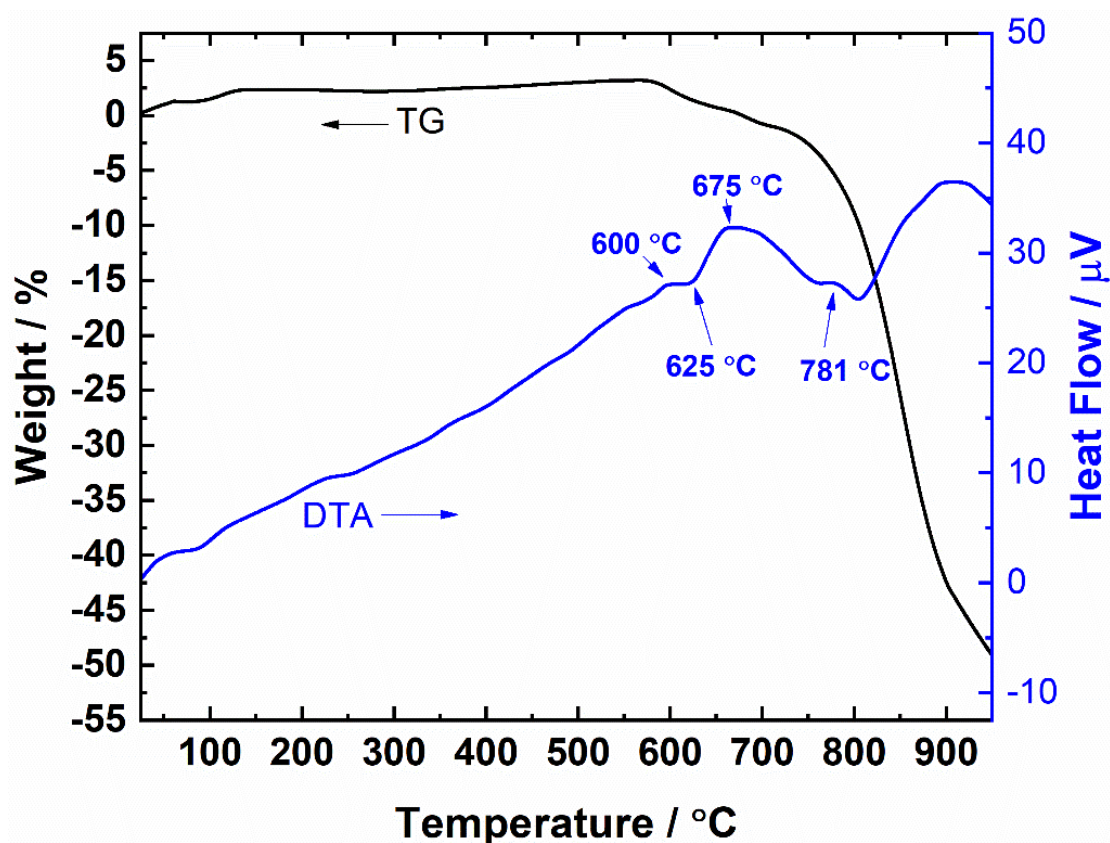


Figure 3.14. TG-DTA curves of $\text{Li}_6\text{PS}_5\text{Cl}$ prepared by mechanical ball milling at 600 rpm for 20 h without the heat treatment process.

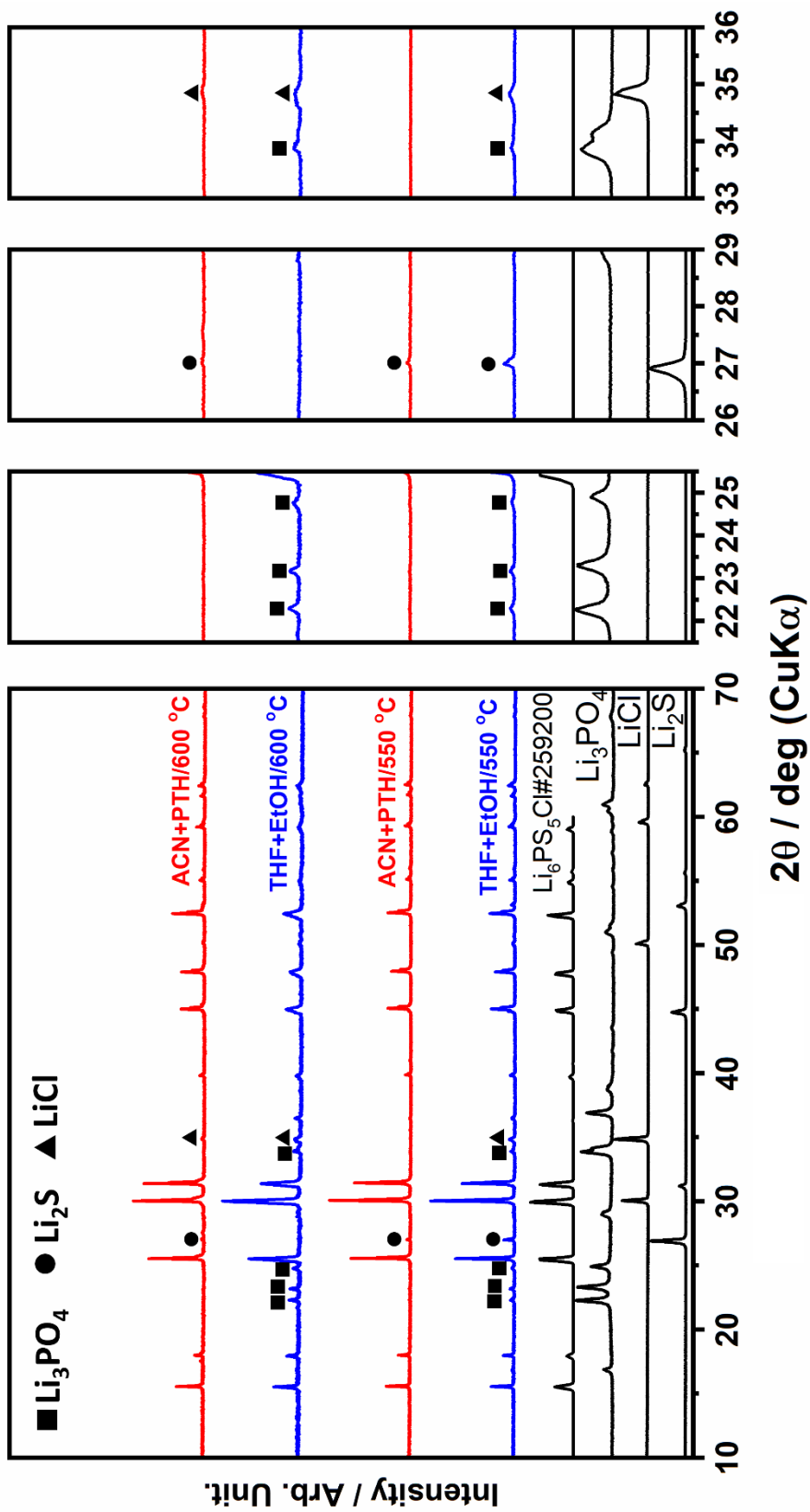


Figure 3.15. XRD patterns of $\text{Li}_6\text{PS}_5\text{Cl}$ prepared by liquid-phase synthesis with THF + EtOH and ACN + PTH solvents. All the samples were dried at 80 °C overnight then heat-treated at 550 °C and 600 °C for 10 h

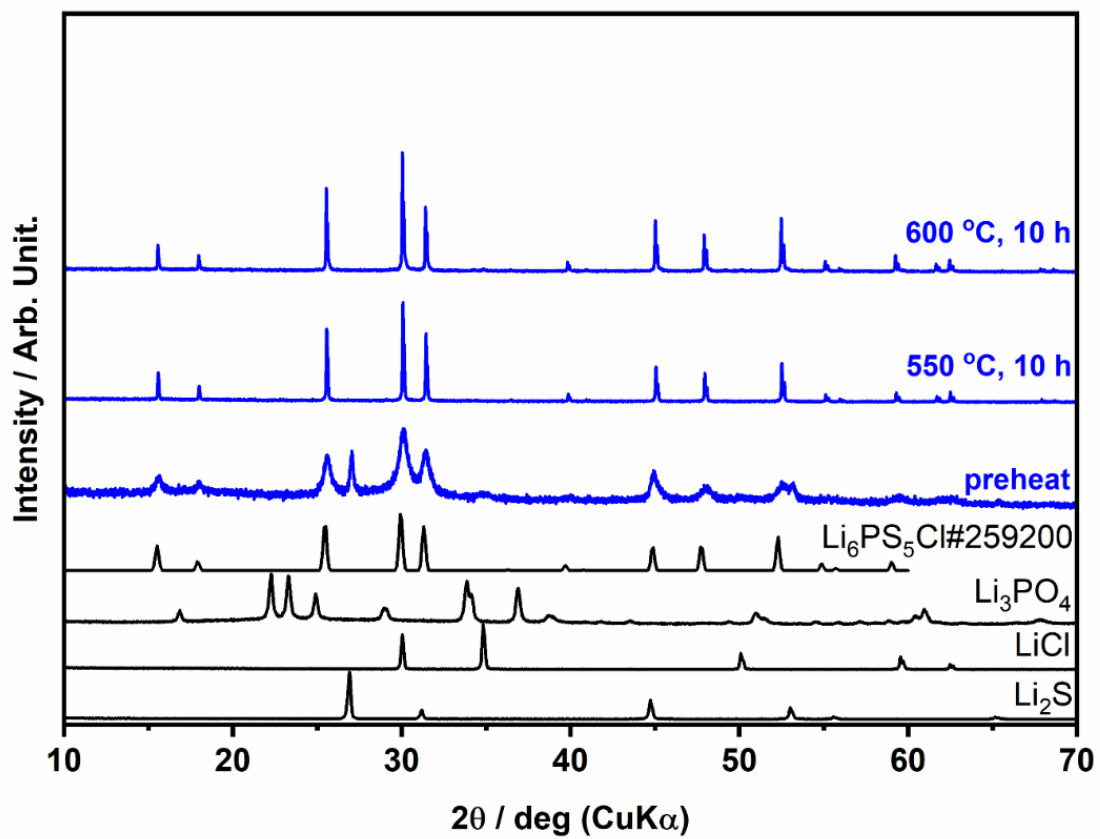


Figure 3.16. XRD patterns of $\text{Li}_6\text{PS}_5\text{Cl}$ prepared using mechanical ball milling at 600 rpm for 20 h.

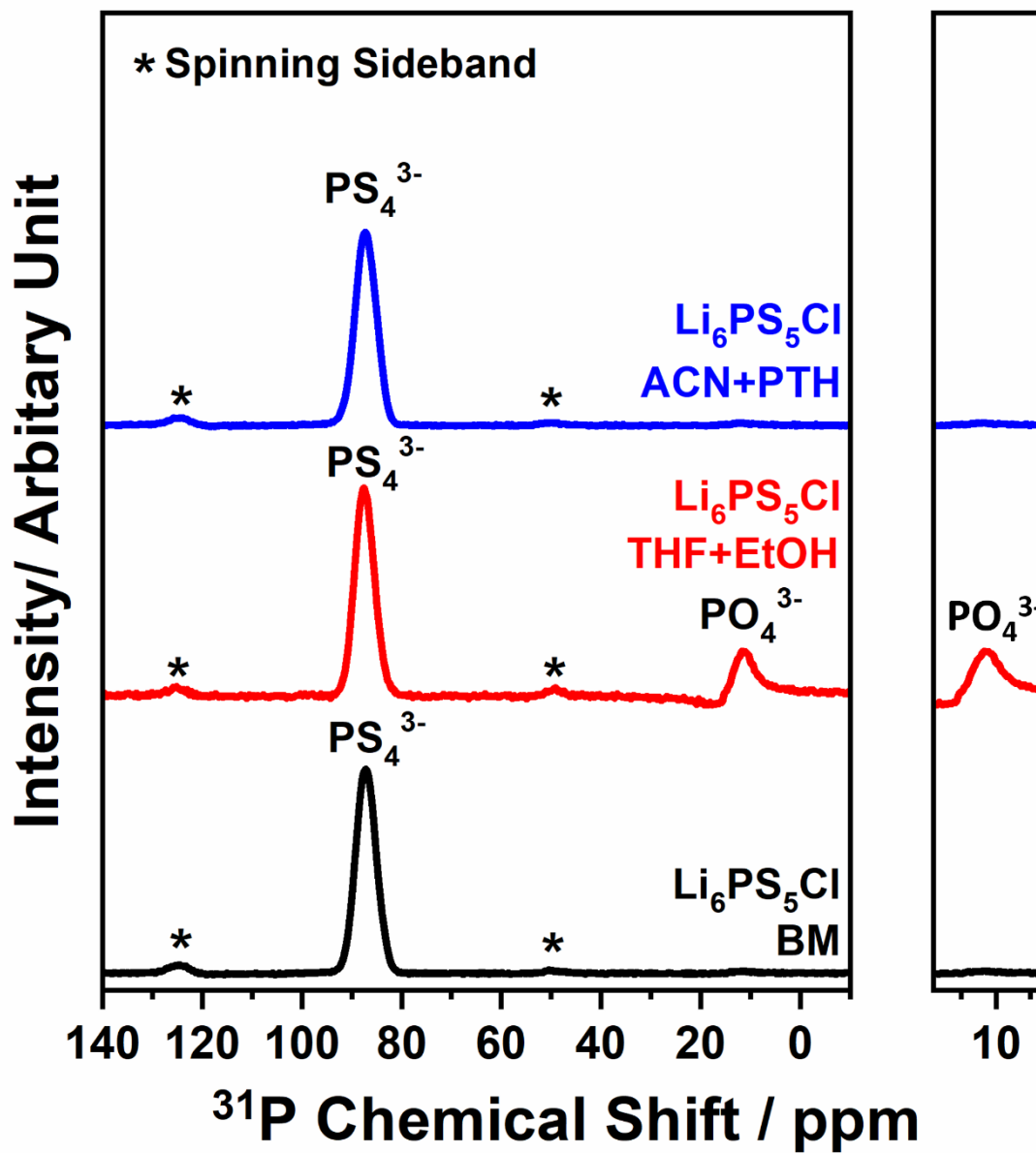


Figure 3.17. ^{31}P MAS-NMR results from $\text{Li}_6\text{PS}_5\text{Cl}$ prepared by ball milling and liquid-phase methods with different types of solvent from THF + EtOH and ACN + PTH after the heat treatment processes.

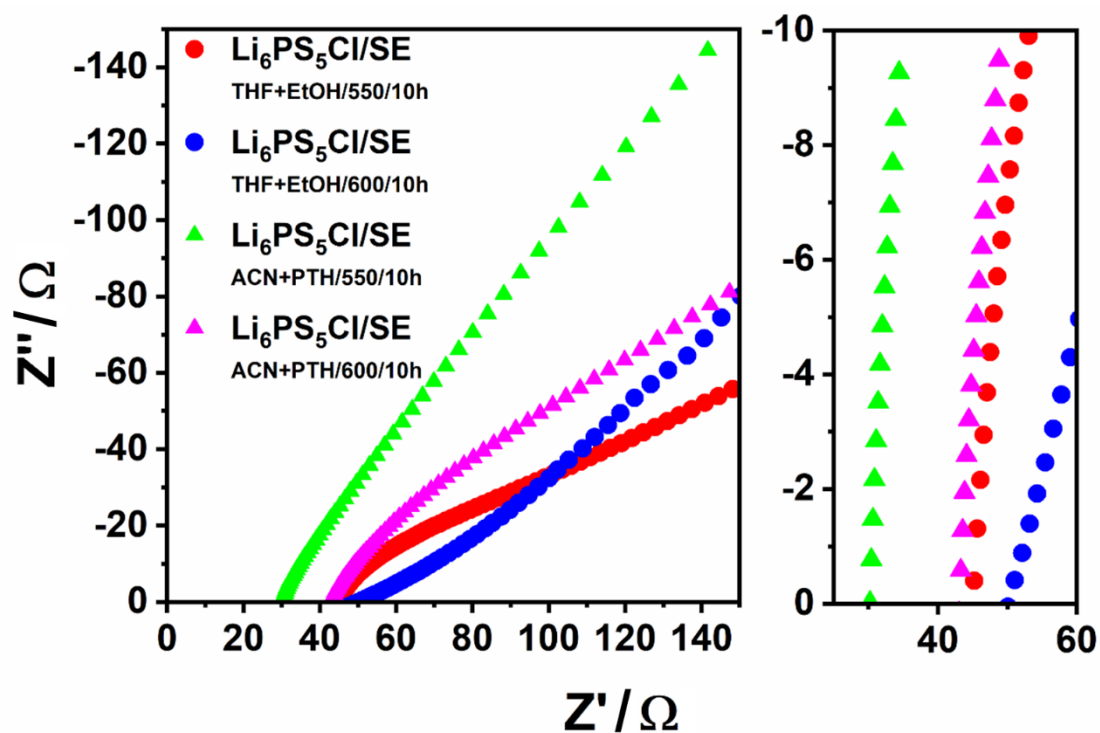


Figure 3.18. Nyquist plots of electrochemical impedance at room temperature from $\text{Li}_6\text{PS}_5\text{Cl}$ with THF + EtOH and ACN + PTH as the solvents after dried and heat-treated at 550 °C and 600 °C for 10 h.

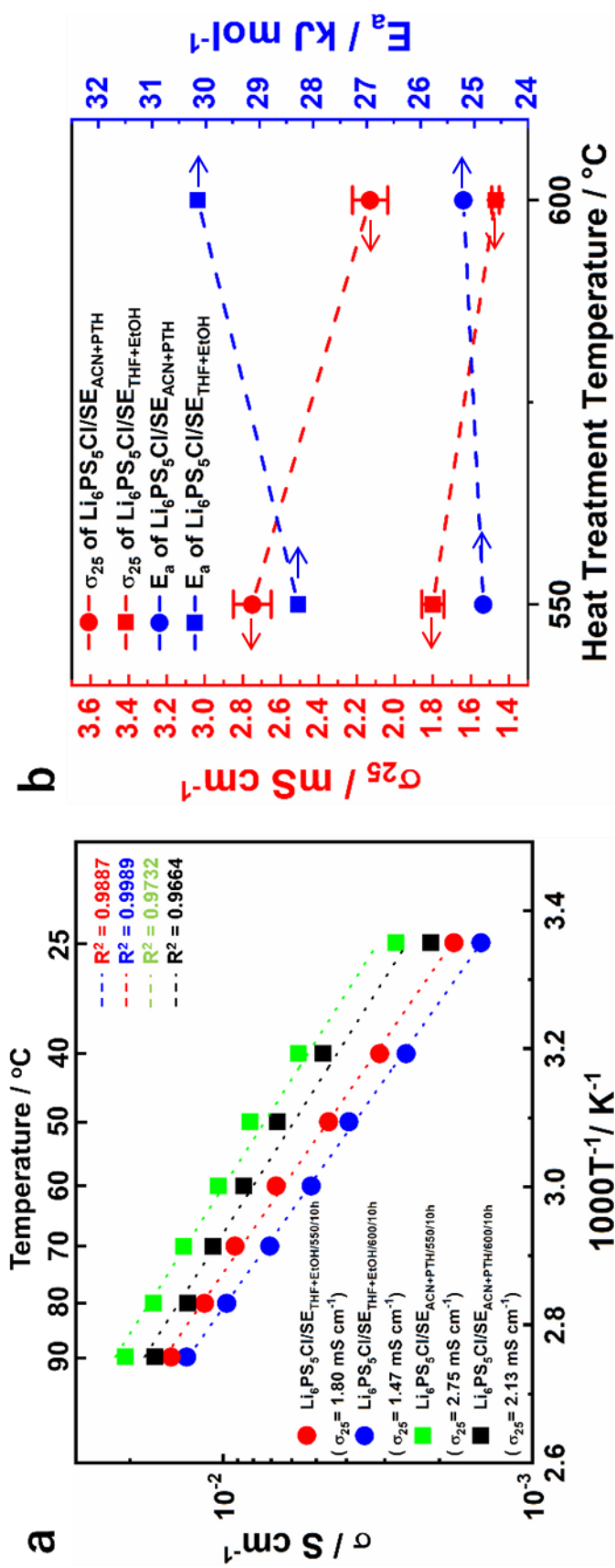


Figure 3.19. Ionic conductivity for Li_6PS_5Cl by liquid phase synthesis. **a** Temperature dependence of ionic conductivity and **b** heat treatment dependence of ionic conductivity with activation energy from Li_6PS_5Cl prepared using liquid phase synthesis using ACN+PTH and THF+EtOH after heat-treated at 550 °C and 600 °C for 10 h.

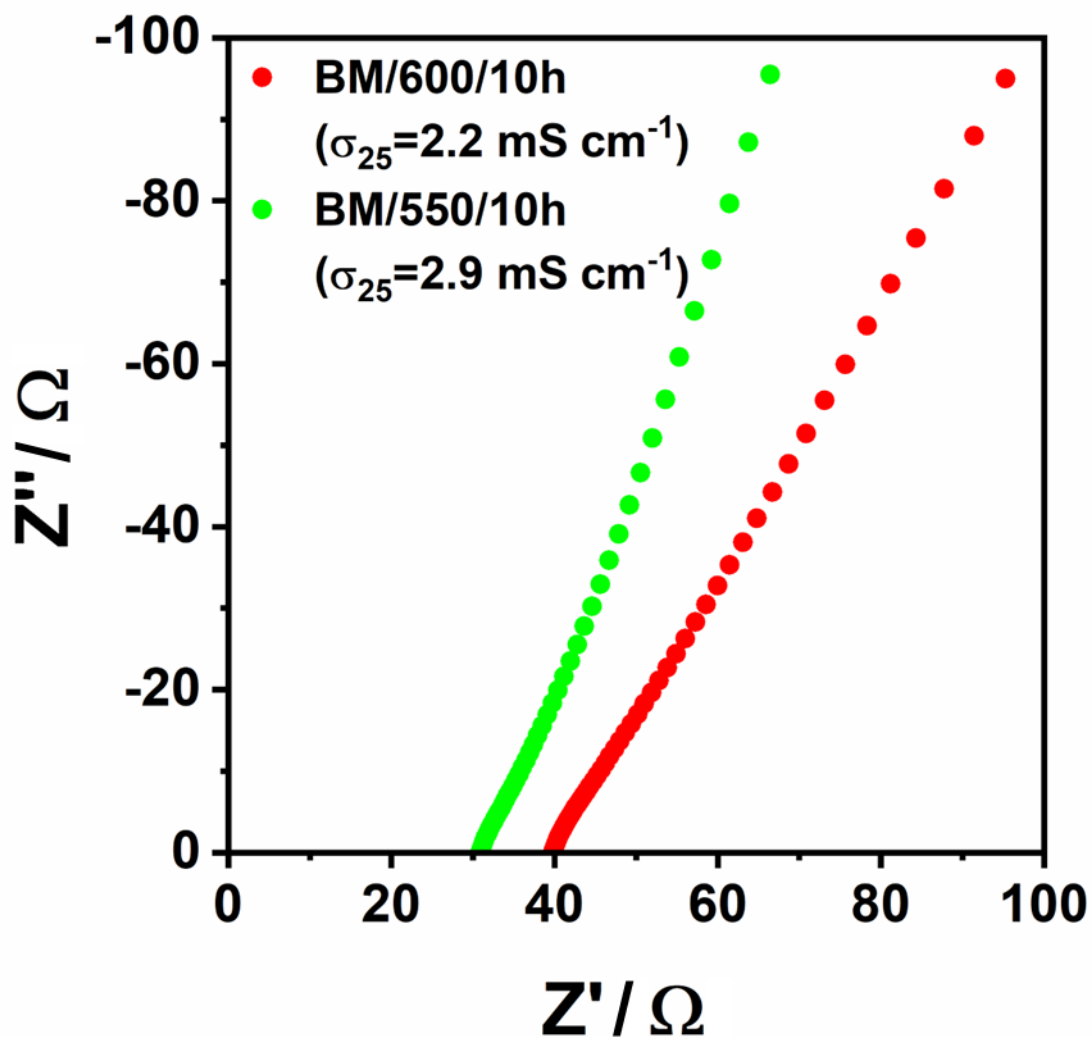


Figure 3.20. Nyquist plots of electrochemical impedance at room temperature from $\text{Li}_6\text{PS}_5\text{Cl}/\text{SE}_{\text{BM}}$ after heat treated for 10 h.

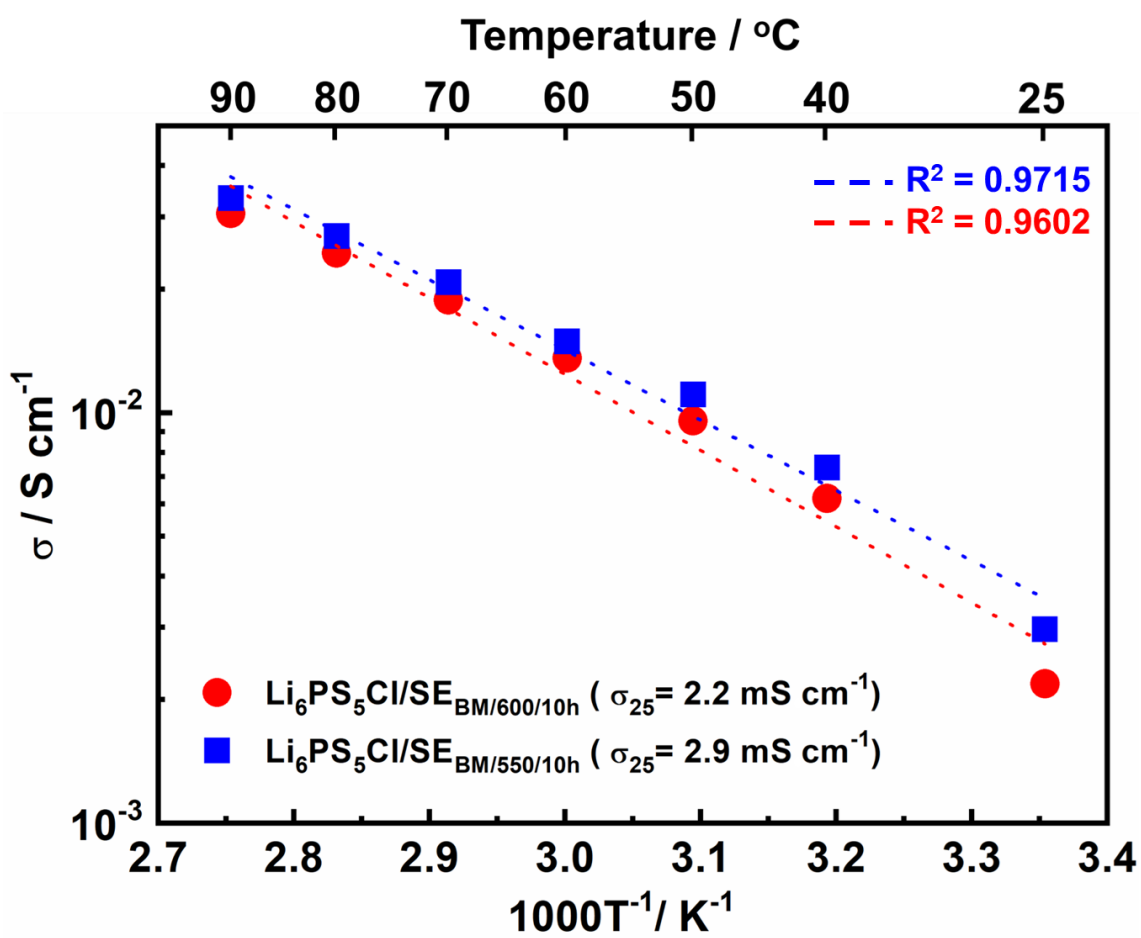


Figure 3.21. Temperature dependence of ionic conductivity from Li_6PS_5Cl/SE_{BM} after heat treated for 10 h.

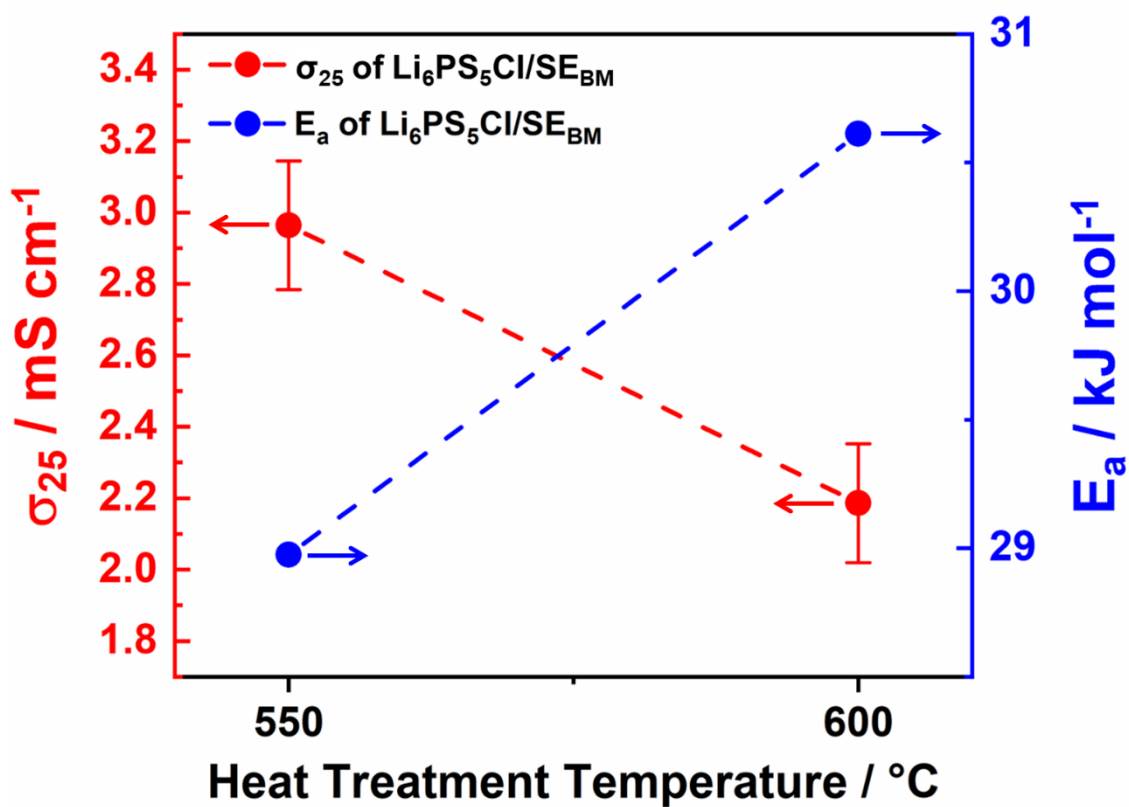


Figure 3.22. Heat treatment temperature dependence of ionic conductivity with activation energy from $\text{Li}_6\text{PS}_5\text{Cl}/\text{SE}_{\text{BM}}$ after heat treated for 10 h.

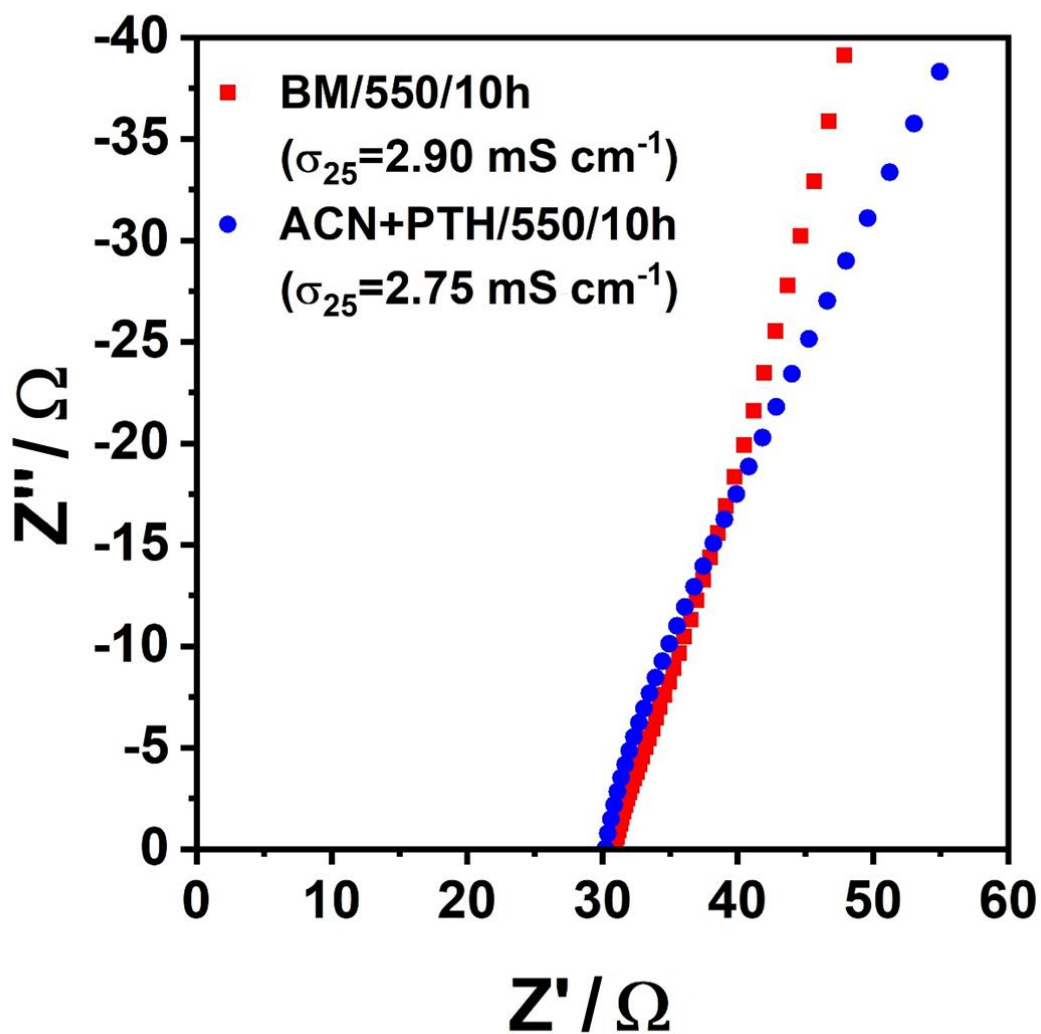


Figure 3.23. Nyquist plots of electrochemical impedance at room temperature from $\text{Li}_6\text{PS}_5\text{Cl}_{\text{BM}}$ and $\text{Li}_6\text{PS}_5\text{Cl}_{\text{ACN+PTH}}$ after heat treated at $550 \text{ }^\circ\text{C}$ for 10 h.

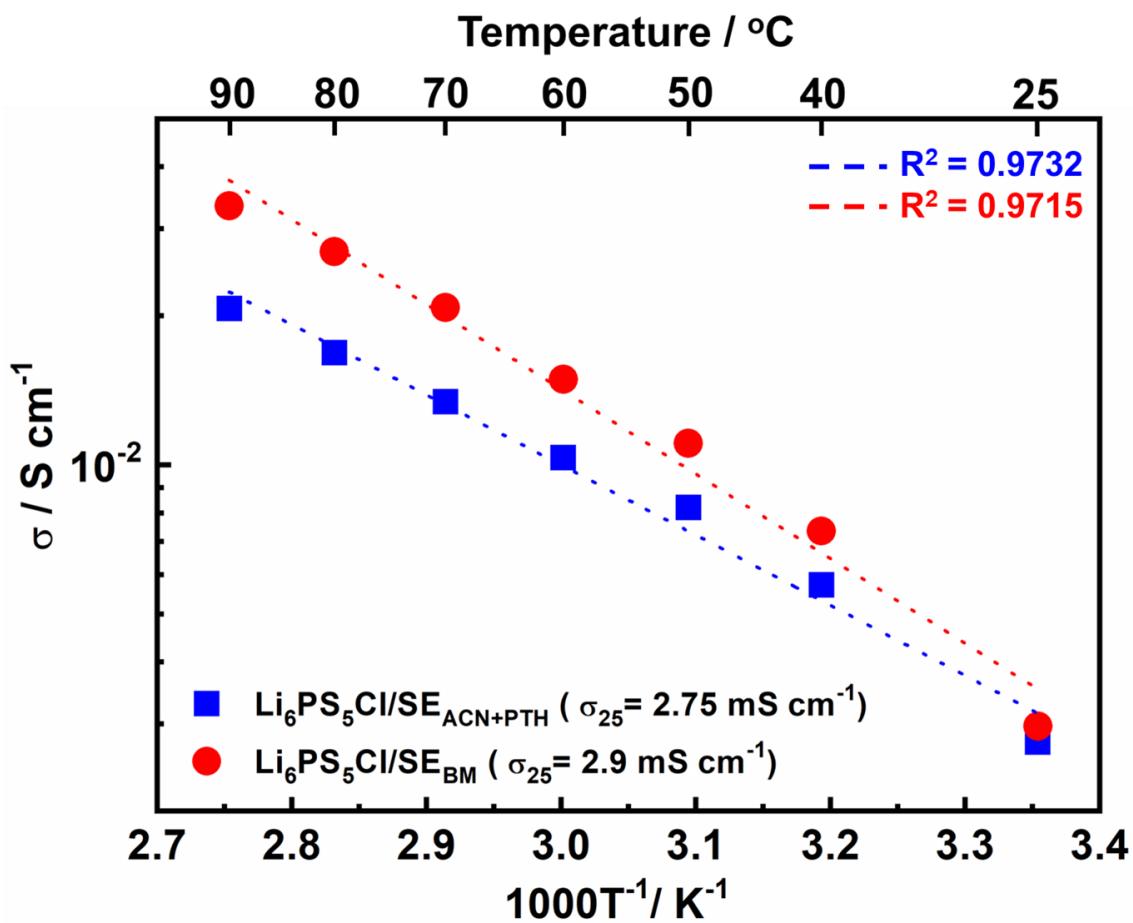


Figure 3.24. Temperature dependence of ionic conductivity from $\text{Li}_6\text{PS}_5\text{Cl}_{\text{BM}}$ and $\text{Li}_6\text{PS}_5\text{Cl}_{\text{ACN+PTH}}$ after heat treated at 550 °C for 10 h.

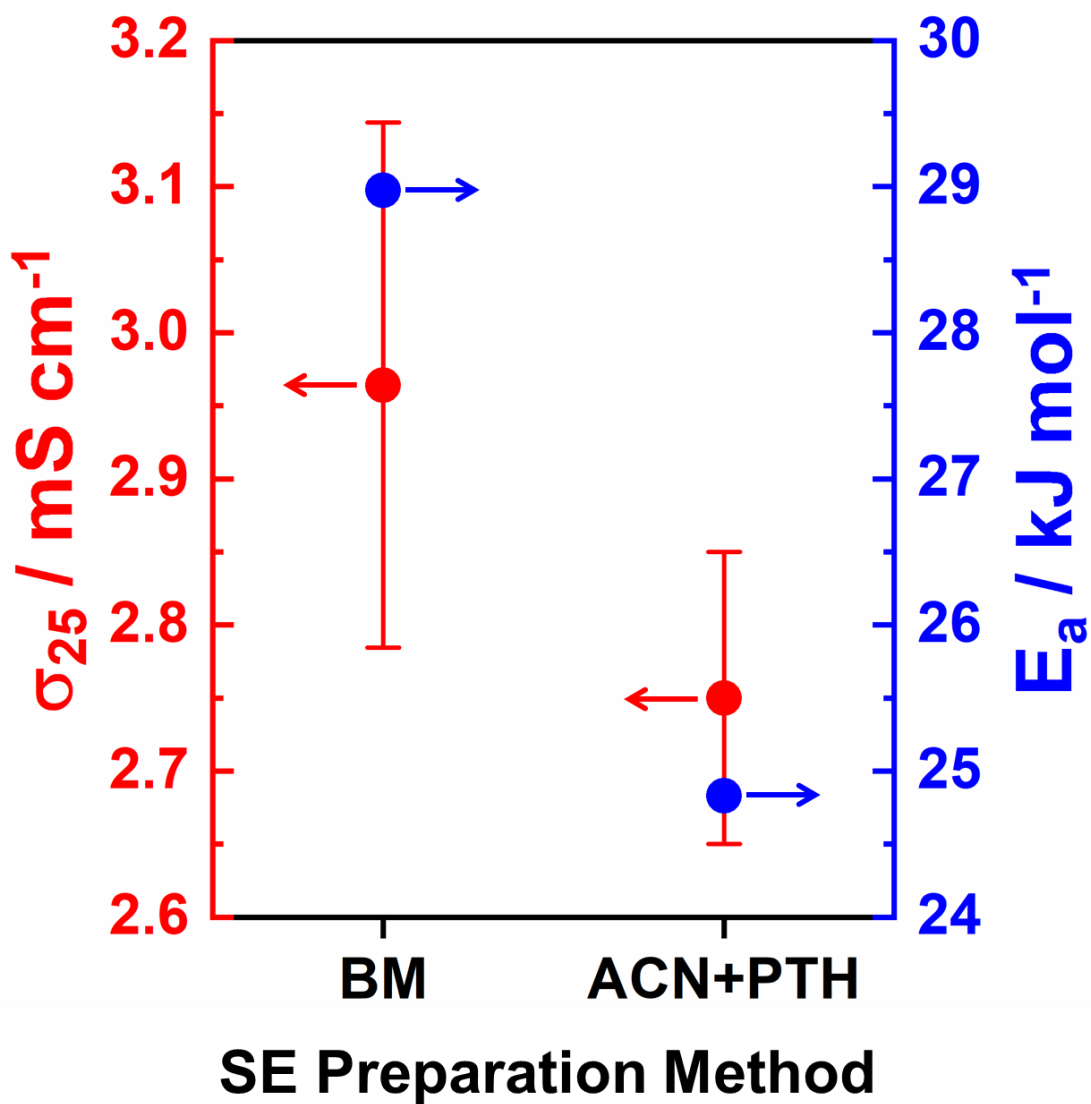


Figure 3.25. Heat treatment temperature dependence of ionic conductivity with activation energy from $\text{Li}_6\text{PS}_5\text{Cl}_{\text{BM}}$ and $\text{Li}_6\text{PS}_5\text{Cl}_{\text{ACN+PTH}}$ after heat treated at 550 °C for 10 h.

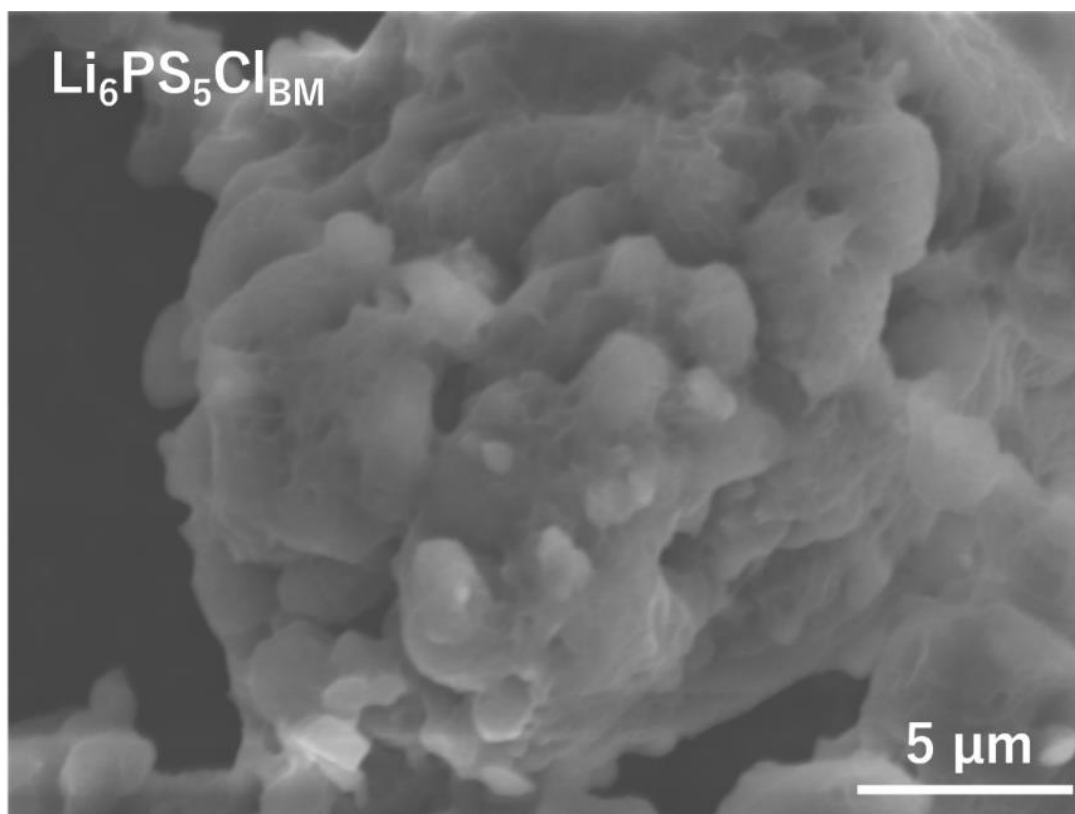


Figure 3.26. SEM image of $\text{Li}_6\text{PS}_5\text{Cl}$ prepared using ball milling method at 600 rpm for 20 h then heat treated at 550 °C for 10 h.

Table 3.1. Crystallite size obtained from XRD data analysis and calculated using Debye-Scherrer equation, ionic conductivity, and electronic conductivity at room temperature from Li₆PS₅Cl/SEs

Sample	<i>K</i>	λ (nm)	2θ (°)	FWHM (°)	<i>D</i> (nm)	Average <i>D</i> (nm)	Ionic σ_{25} (S cm ⁻¹)	Electronic σ_{25} (S cm ⁻¹)
Li₆PS₅Cl/SE BM/550/10h	0.9	0.154 18	15.57293	0.0646	124.21609	139.249	2.90×10^{-3}	2.25×10^{-9}
			17.9996	0.0581	138.54512			
			25.55993	0.0596	136.78411			
			30.06754	0.0596	138.12305			
			31.43902	0.0599	137.88438			
			45.0582	0.0591	145.63848			
			47.96085	0.0603	144.30256			
52.52083	0.0597	148.49824						
Li₆PS₅Cl/SE THF+EtOH/550/10h	0.9	0.154 18	15.53828	0.0692	115.95416	102.774	1.80×10^{-3}	7×10^{-7}
			17.96439	0.0694	115.98098			
			25.51733	0.0732	111.36129			
			30.02502	0.0794	103.66894			
			31.39374	0.0753	109.67273			
			45.00593	0.1041	82.666734			
			47.90108	0.0903	96.339173			
52.45381	0.1024	86.550679						
Li₆PS₅Cl/SE ACN+PTH/550/10h	0.9	0.154 18	15.56069	0.0508	157.95752	136.428	2.75×10^{-3}	4.35×10^{-9}
			17.98897	0.053	151.87459			
			25.55236	0.0576	141.53144			
			30.05994	0.0589	139.76209			
			31.43036	0.0583	141.66550			
			45.05297	0.0716	120.21049			
			47.95182	0.0699	124.47982			
52.51225	0.0778	113.94624						

3.4.3 Lithium Metal Stability and Battery Performance Measurement

Electrochemical performance measurements from DC polarization galvanostatic and battery performance tests were performed to further understand the role of the Li_3PO_4 exclusion for the argyrodite $\text{Li}_6\text{PS}_5\text{Cl}/\text{SE}$. Here we demonstrated the symmetrical lithium cell from $\text{Li} \mid \text{Li}_6\text{PS}_5\text{Cl}/\text{SE}_m \mid \text{Li}$ ($m = \text{BM}, \text{THF} + \text{EtOH}, \text{ACN} + \text{PTH}$) with the current density of $0.1 \text{ mA}\cdot\text{cm}^{-2}$ for the first 100 cycles (200 h) and increase to $0.2 \text{ mA}\cdot\text{cm}^{-2}$ starting from the 101st cycle at room temperature. Figure 3.27 shows the voltage profiles from the lithium metal stability measurement. $\text{Li}_6\text{PS}_5\text{Cl}/\text{SE}_{\text{BM}}$ had an initial overpotential of 6 mV without detectable overpotential alterations until 10 h. The overpotential was suddenly dropped to 0 mV (inset 2 mV from Figure 3.27), which indicates a short circuit caused by the lithium dendrite already reaching the opposite side of the electrode. The stability was extremely poor despite $\text{Li}_6\text{PS}_5\text{Cl}/\text{SE}_{\text{BM}}$ having the highest ionic conductivity without any Li_3PO_4 oxide formation. This result is similar to the sulfide SEs that was prepared by mechanical ball milling that was reported by Li Y et.al and Gamo H. et.al.[15, 41] There are many reasons for the lithium dendrite to grow: low ion transport, high electronic conductivity, and poor mechanical property of SEs.[42-44] Electronic conductivity for each type SEs are shown in Figure 3.28. $\text{Li}_6\text{PS}_5\text{Cl}/\text{SE}_{\text{BM}}$, $\text{Li}_6\text{PS}_5\text{Cl}/\text{SE}_{\text{THF} + \text{EtOH}}$, and $\text{Li}_6\text{PS}_5\text{Cl}/\text{SE}_{\text{ACN} + \text{PTH}}$ exhibited electron conductivities of $2.25 \times 10^{-9} \text{ S}\cdot\text{cm}^{-1}$, $7 \times 10^{-7} \text{ S}\cdot\text{cm}^{-1}$, and $4.35 \times 10^{-9} \text{ S}\cdot\text{cm}^{-1}$, respectively. $\text{Li}_6\text{PS}_5\text{Cl}/\text{SE}_{\text{THF} + \text{EtOH}}$ owned the highest electronic conductivity among the others, which supports the reason $\text{Li}_6\text{PS}_5\text{Cl}/\text{SE}_{\text{THF} + \text{EtOH}}$ was unstable against lithium metal and the potential was gradually increased during lithium metal stability measurement. On contrary, $\text{Li}_6\text{PS}_5\text{Cl}/\text{SE}_{\text{ACN} + \text{PTH}}$ has an electron conductivity around 100 times lower than $\text{Li}_6\text{PS}_5\text{Cl}/\text{SE}_{\text{THF} + \text{EtOH}}$ and therefore the increment of the potential is also lower, which makes $\text{Li}_6\text{PS}_5\text{Cl}/\text{SE}_{\text{ACN} + \text{PTH}/550/10\text{h}}$ has better lithium metal stability compared to $\text{Li}_6\text{PS}_5\text{Cl}/\text{SE}_{\text{THF} + \text{EtOH}}$. $\text{Li}_6\text{PS}_5\text{Cl}/\text{SE}_{\text{BM}}$ has the lowest electron conductivity compared to the other two that were prepared with liquid phase synthesis, but the higher crystallinity phase might cause a lower contact area between SE and lithium metal electrodes, leading to lower interfacial compatibility.[43] In the case of $\text{Li}_6\text{PS}_5\text{Cl}/\text{SE}_{\text{THF} + \text{EtOH}}$, the voltage profile at the initial period showed unstable overpotential between 5 and 21 mV in stripping and plating. This indicates that the thickness of the Solid Electrolyte Interface (SEI) was different, which

may result from the existence of the Li_3PO_4 crystalline phase that blocks the path for Li^+ ion movement. Inset 3 in Figure 3.27 shows that after 200 h, the cycling of $\text{Li}_6\text{PS}_5\text{Cl}/\text{SE}_{\text{THF} + \text{EtOH}}$ revealed a violent increment of the overpotential from 21 to 154 mV (~630% of overpotential increment). Although the SE was not short-circuited, the overpotential dramatically increased because of the production of a layer of resistive passivation. The overpotential increment got worse when the current density increased to $0.2 \text{ mA}\cdot\text{cm}^{-2}$, where the SE was already broken in this state. My previous report on Chapter 2 regarding the addition of oxide compound of Li_3PO_4 into $\text{Li}_7\text{P}_2\text{S}_8\text{I}$ (LPSI) using liquid-phase shaking method resulted in magnificent lithium metal stability compared to pristine LPSI.[45] This result was not consistent with $\text{Li}_6\text{PS}_5\text{Cl}/\text{SE}_{\text{THF} + \text{EtOH}}$, which contains Li_3PO_4 .[45] The LPSI doped with Li_3PO_4 involves an oxysulfide bond compound from PO_xS_y , which causes the SE to have high lithium metal stability. In the instance of $\text{Li}_6\text{PS}_5\text{Cl}/\text{SE}_{\text{THF} + \text{EtOH}}$, Li_3PO_4 was produced through a nucleophilic reaction that did not create chemical bonds with the argyrodite itself, as seen in the ^{31}P MAS-NMR result. There is no oxysulfide bond formed, simply the bond between PS_4^{3-} and PO_4^{3-} .[45] $\text{Li} | \text{Li}_6\text{PS}_5\text{Cl}/\text{SE}_{\text{ACN} + \text{PTH}} | \text{Li}$ symmetric cell showed identical overpotential profiles at 6 mV at the initial stage. The alterations of the overpotential were insignificantly increased to 13 mV (~117% of overpotential increment) at the end of the $0.1 \text{ mA}\cdot\text{cm}^{-2}$ current density (after 200 h). When the measurement continues to a higher current density of $0.2 \text{ mA}\cdot\text{cm}^{-2}$, the overpotential of the symmetric cell using $\text{Li}_6\text{PS}_5\text{Cl}/\text{SE}_{\text{ACN} + \text{PTH}}$ increased up to 26 mV. As the measurement continues at $0.2 \text{ mA}\cdot\text{cm}^{-2}$ of the current density, the SE could maintain its overpotential without any alteration for the next 47 h. The overpotential was dropped to 15 mV, which indicates the lithium dendrites have already grown and penetrated the interface of $\text{Li}_6\text{PS}_5\text{Cl}/\text{SE}_{\text{ACN} + \text{PTH}}$. In sum, $\text{Li}_6\text{PS}_5\text{Cl}/\text{SE}_{\text{ACN} + \text{PTH}}$ exhibits magnificent lithium metal stability compared to $\text{Li}_6\text{PS}_5\text{Cl}/\text{SE}_{\text{THF} + \text{EtOH}}$ because of no impurity of the Li_3PO_4 in $\text{Li}_6\text{PS}_5\text{Cl}/\text{SE}_{\text{ACN} + \text{PTH}}$.

To understand the efficacy of the argyrodite prepared for this study and the effect of the Li_3PO_4 impurity on it, a $\text{Li-In} | \text{Li}_6\text{PS}_5\text{Cl}/\text{SE}_{\text{ACN} + \text{PTH}} | \text{TiS}_2\text{-Li}_6\text{PS}_5\text{Cl}$ ($m = \text{THF} + \text{EtOH}$, $\text{ACN} + \text{PTH}$) half-cell was assembled then measured, using $\text{Li}_6\text{PS}_5\text{Cl}/\text{SE}_{\text{ACN} + \text{PTH}}$ as the electrolyte layer. The use of Li-In alloy as the negative electrode material benefits the interface stability and mechanical properties compared to intrinsic Li metal. This measurement focuses on $\text{Li}_6\text{PS}_5\text{Cl}$ performance and the difference between the

presence and absence of the Li_3PO_4 impurity in $\text{Li}_6\text{PS}_5\text{Cl}$. Figure 3.29 shows the charge and discharge capacity curve cycled under a cycle rate of 0.1 C at room temperature. $\text{TiS}_2\text{-Li}_6\text{PS}_5\text{Cl/SE}_{\text{THF} + \text{EtOH}}$ composite exhibited the initial discharge capacity at $197.68 \text{ mAh}\cdot\text{g}^{-1}$ and initial charge capacity of $182.8 \text{ mAh}\cdot\text{g}^{-1}$, while $\text{TiS}_2\text{-Li}_6\text{PS}_5\text{Cl/SE}_{\text{ACN} + \text{PTH}}$ composite exhibited the initial discharge and charge capacity at 222.4 and $221.7 \text{ mAh}\cdot\text{g}^{-1}$, respectively. The discharge and charge capacity from the $\text{TiS}_2\text{-Li}_6\text{PS}_5\text{Cl/SE}_{\text{ACN} + \text{PTH}}$ composite was superior to the $\text{TiS}_2\text{-Li}_6\text{PS}_5\text{Cl/SE}_{\text{THF} + \text{EtOH}}$ composite, which can be explained by the existence of insulating Li_3PO_4 in the SEs. Figure 3.13 and 14 show the cycling performance and Coulombic efficiency from both samples up to 30 cycles. $\text{TiS}_2\text{-Li}_6\text{PS}_5\text{Cl/SE}_{\text{THF} + \text{EtOH}}$ composite showed the discharge capacity of only $87 \text{ mAh}\cdot\text{g}^{-1}$ with the Coulombic efficiency at 98.4% at the 30th cycle. This implies a discharge capacity retention rate of around 44% from the beginning to the 30th cycle. In contrast, the $\text{TiS}_2\text{-Li}_6\text{PS}_5\text{Cl/SE}_{\text{ACN} + \text{PTH}}$ composite discharge capacity at the 30th cycle reached $148.7 \text{ mAh}\cdot\text{g}^{-1}$ with the Coulombic efficiency of 95%. It had a higher capacity retention rate of approximately 67% compared to the $\text{TiS}_2\text{-Li}_6\text{PS}_5\text{Cl/SE}_{\text{THF} + \text{EtOH}}$ composite. The presence of the Li_3PO_4 results in lower contact between the electrode and SE and hinders the path of the Li^+ ions. As a result, the $\text{TiS}_2\text{-Li}_6\text{PS}_5\text{Cl/SE}_{\text{THF} + \text{EtOH}}$ composite containing Li_3PO_4 showed a lower initial discharge capacity and lower capacity retention rate than $\text{TiS}_2\text{-Li}_6\text{PS}_5\text{Cl/SE}_{\text{ACN} + \text{PTH}}$ composite. In contrast, the Coulombic efficiency of $\text{TiS}_2\text{-Li}_6\text{PS}_5\text{Cl/SE}_{\text{ACN} + \text{PTH}}$ composite (95%) is lower than that of $\text{TiS}_2\text{-Li}_6\text{PS}_5\text{Cl/SE}_{\text{THF} + \text{EtOH}}$ composite (98.4%). This phenomenon may be described by the decomposition reaction at the interface between TiS_2 and SEs. TiS_2 has the electrochemical window range at 0.9-2.8 V while $\text{Li}_6\text{PS}_5\text{Cl}$ argyrodite stable electrochemical operating window at 1.70-2.01 V.^[46, 47] The great difference between electrochemical window between TiS_2 and $\text{Li}_6\text{PS}_5\text{Cl}$ may cause decomposition reaction in the interface between them. We believe that $\text{TiS}_2\text{-Li}_6\text{PS}_5\text{Cl/SE}_{\text{ACN} + \text{PTH}}$ composite involves intimate contact at the interface due to the absence of Li_3PO_4 , which causes a severe decomposition reaction.[48] SEM-EDX mapping from the positive active material composites with the corresponding Ti, Cl, S, and P elements from both $\text{TiS}_2\text{-Li}_6\text{PS}_5\text{Cl/SE}_{\text{THF} + \text{EtOH}}$ composite (Figure 3.32a, b, c, d, and e) and $\text{TiS}_2\text{-Li}_6\text{PS}_5\text{Cl/SE}_{\text{ACN} + \text{PTH}}$ composite (Figure 3.33a, b, c, d, and E) were determined. The absence of the sulfur and titanium elements was observed in part of the $\text{TiS}_2\text{-Li}_6\text{PS}_5\text{Cl/SE}_{\text{THF} + \text{EtOH}}$ composite particles, whereas the phosphorus element was slightly

concentrated in that region shown in Figure 3.32b and d. This experimental result indicates that this region was the existence of the Li_3PO_4 , which was consistent with the XRD and NMR results. The agglomeration of the Li_3PO_4 from the SEM-EDX mapping also corresponds to the unidentical overpotential profile from $\text{TiS}_2\text{-Li}_6\text{PS}_5\text{Cl/SE}_{\text{THF} + \text{EtOH}}$ using the galvanostatic DC polarization measurement. The distribution of the chlorine element originating from the argyrodite phase was homogeneous. SEM-EDX mapping of $\text{TiS}_2\text{-Li}_6\text{PS}_5\text{Cl/SE}_{\text{ACN} + \text{PTH}}$ composite showed particle morphology with no concentrated phosphorus element and sulfur atom, indicating the absence of a Li_3PO_4 phase from the composite structure and the SE. Our discovery on the mechanism and exclusion of Li_3PO_4 from $\text{Li}_6\text{PS}_5\text{Cl/SE}$ argyrodite systems prepared using liquid-phase synthesis will significantly contribute to fundamental scientific research from the chemical aspect of the ASSLiBs development. Therefore, we believe this finding will pave the way for the future engineering of energy storage devices.

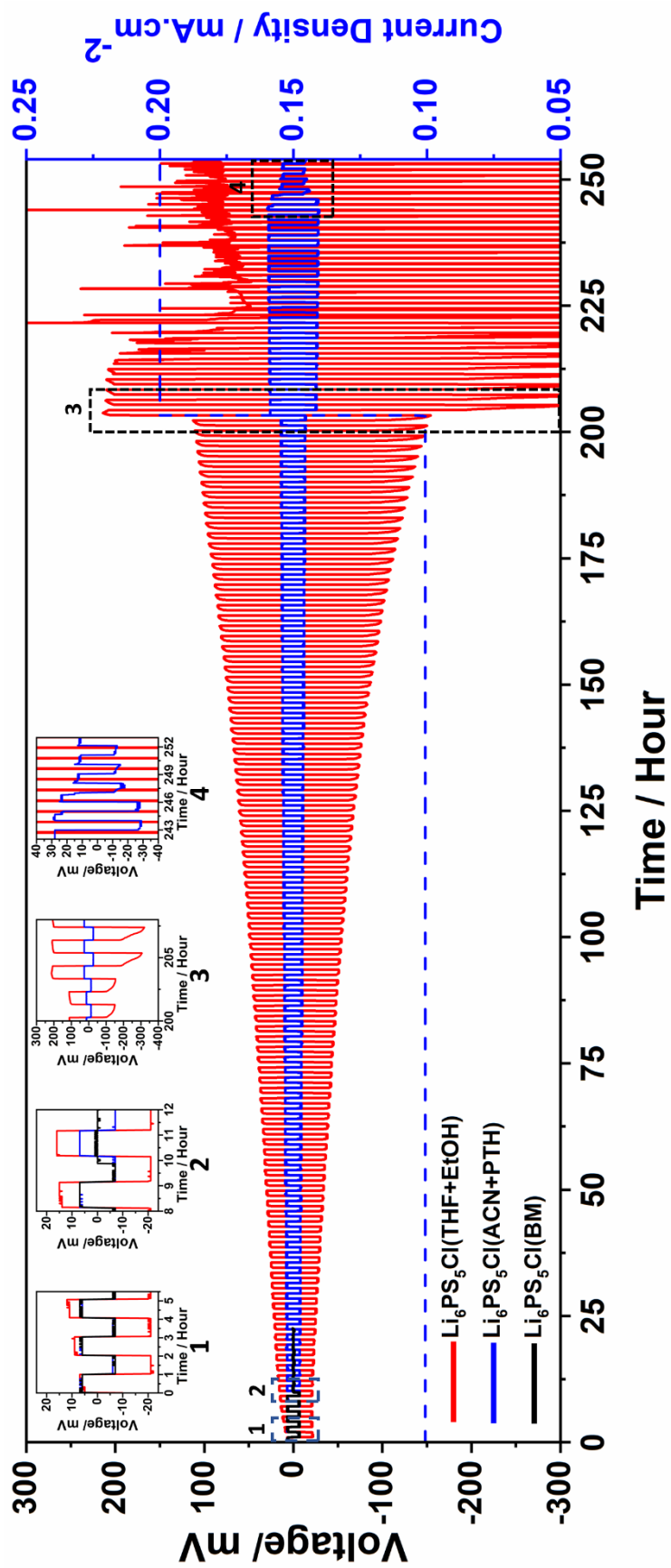


Figure 3.27. Galvanostatic DC polarization of symmetrical cell from Li | Li₆PS₅Cl *m* | Li (*m* = BM, THF + EtOH, ACN + PTH) at room temperature with 1 h for each charge and discharge.

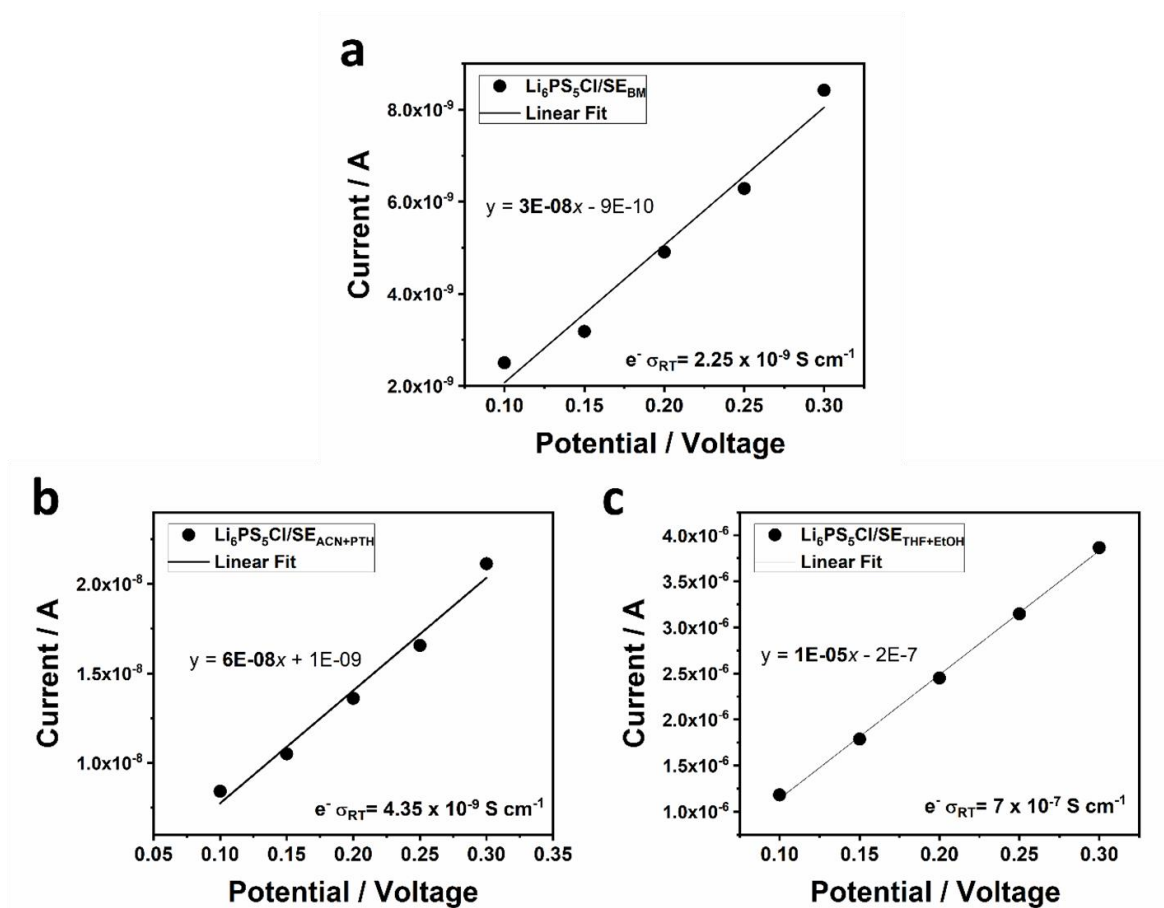


Figure 3.28. Electronic conductivity of $\text{Li}_6\text{PS}_5\text{Cl}$ SEs. Current versus applied voltage of **a** $\text{Li}_6\text{PS}_5\text{Cl}/\text{SE}_{\text{BM}}$, **b** $\text{Li}_6\text{PS}_5\text{Cl}/\text{SE}_{\text{ACN+PTH}}$, and **c** $\text{Li}_6\text{PS}_5\text{Cl}/\text{SE}_{\text{THF+EtOH}}$ after heat treated at 550°C for 10h

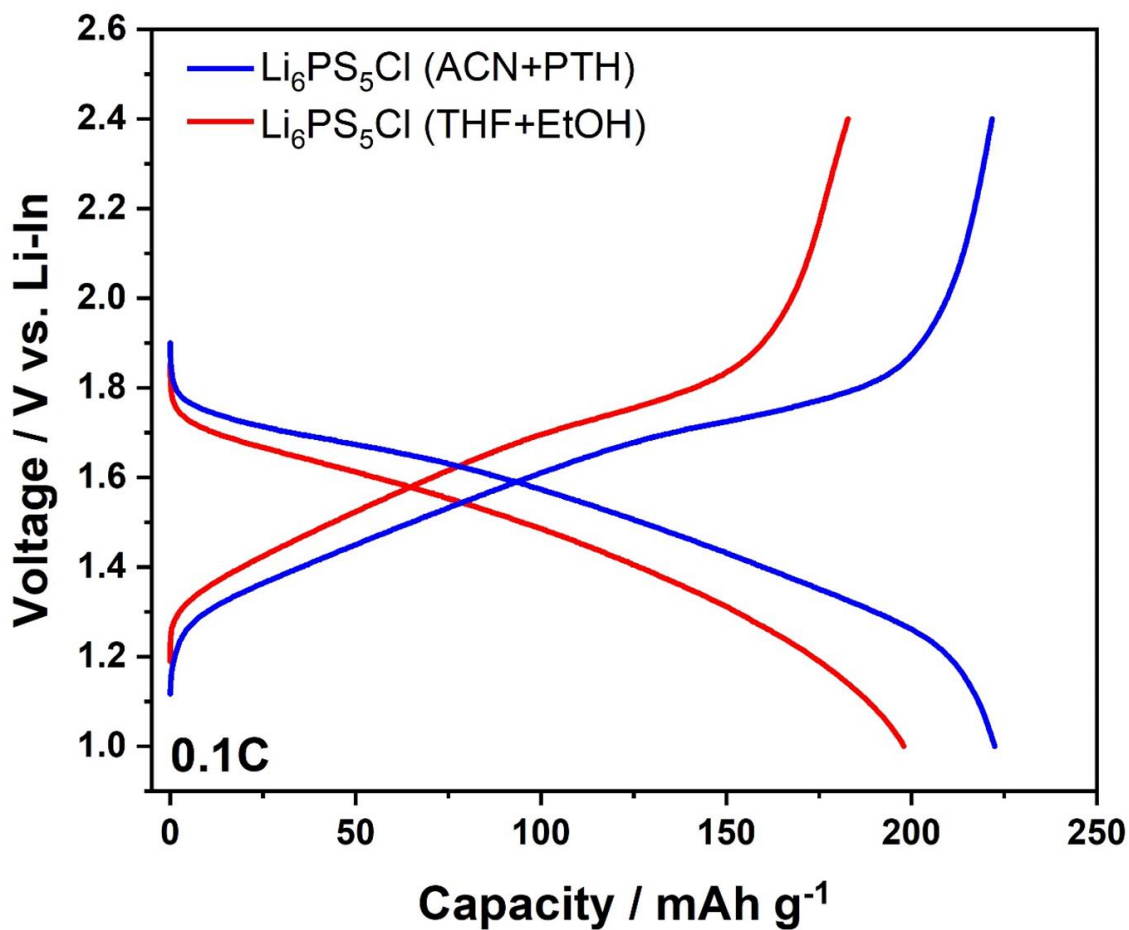


Figure 3.29. Charge and discharge capacity curve for Li-In | $\text{Li}_6\text{PS}_5\text{Cl}$ ACN + PTH | $\text{TiS}_2\text{-Li}_6\text{PS}_5\text{Cl}$ m ($m = \text{THF} + \text{EtOH}, \text{ACN} + \text{PTH}$) at room temperature with 0.1C rate

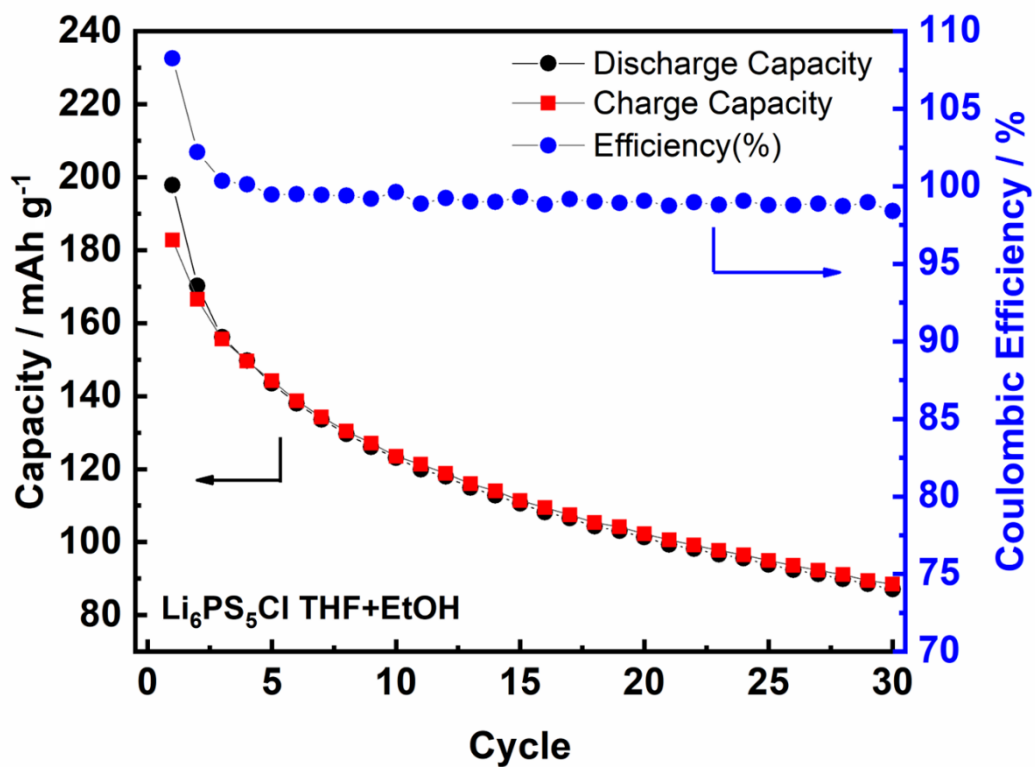


Figure 3.30. Cycling performance of half cells of Li–In | Li₆PS₅Cl_{ACN} + PTH | TiS₂-Li₆PS₅Cl THF + EtOH cycled at 30 °C under 0.1C cycle rate in the voltage range of 3.0–2.4 V vs. Li–In.

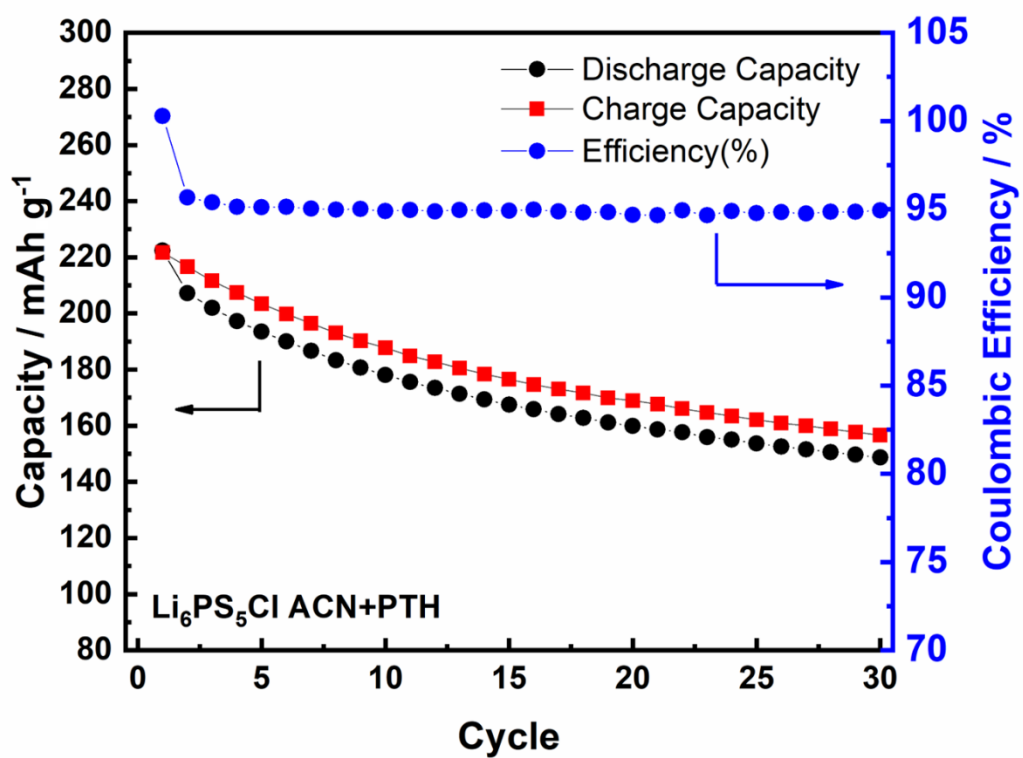


Figure 3.31. Cycling performance of half cells of Li-In | Li₆PS₅Cl ACN + PTH | TiS₂-Li₆PS₅Cl ACN + PTH cycled at 30 °C under 0.1C cycle rate in the voltage range of 3.0–2.4 V vs. Li-In.

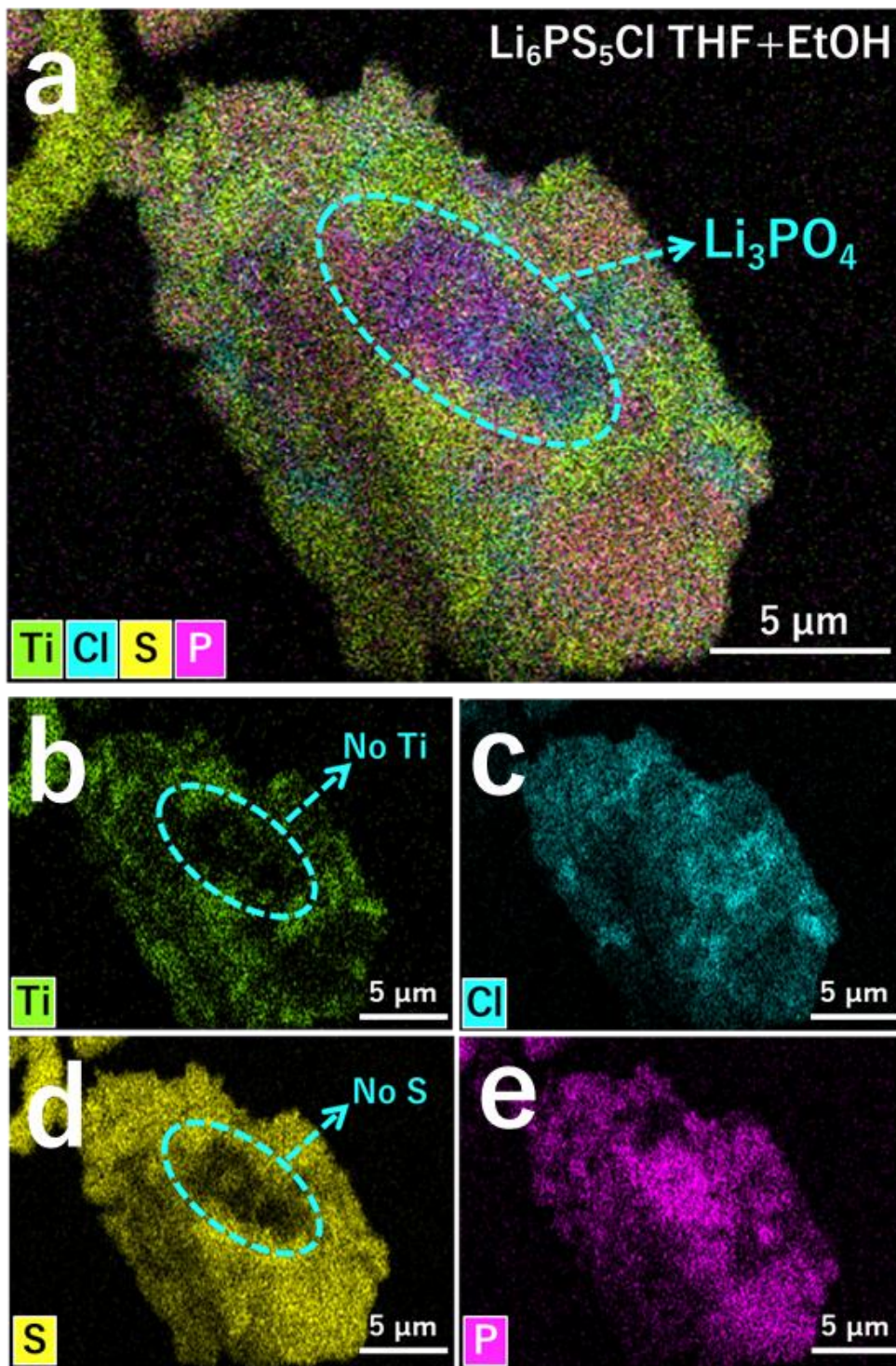


Figure 3.32. SEM-EDX mappings from (a) $\text{TiS}_2\text{-Li}_6\text{PS}_5\text{Cl THF + EtOH}$ composite of (b)Ti, (c)Cl, (d)S, and (e)P elements for the selected regions

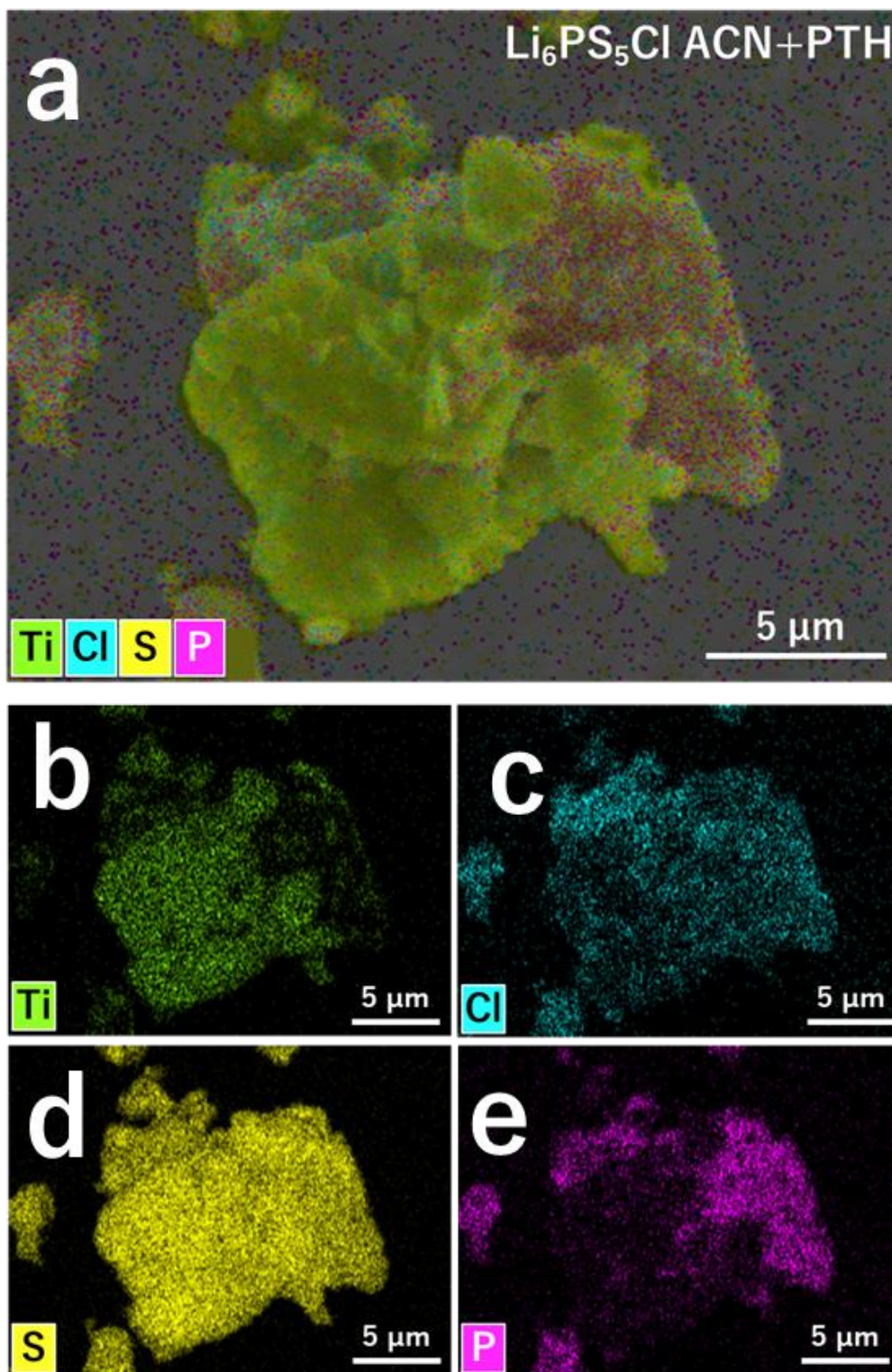


Figure 3.33. SEM-EDX mappings from (a) $\text{TiS}_2\text{-Li}_6\text{PS}_5\text{Cl ACN + PTH}$ composite of (b)Ti, (c)Cl, (d)S, and (e)P elements for the selected region

3.5 Conclusions

In summary, I demonstrated promising solvents and methods for the scalable liquid phase synthesis of $\text{Li}_6\text{PS}_5\text{Cl}$ argyrodite solid electrolyte with no impurity of Li_3PO_4 impurity was formed on the structure, showing the enhanced ionic conductivity, Li metal anode stability, and battery cycle performance. The hydroxyl bond from the EtOH and anionic reaction from THF's ring-opening effect from Li-X^- nucleophilic attack were successfully excluded by using ACN and PTH as the solvents. The use of ACN and PTH allows to synthesize $\text{Li}_6\text{PS}_5\text{Cl}$ argyrodite without any Li_3PO_4 impurity, which is observed from the XRD and the ^{31}P MAS-NMR results. The ionic conductivity of $\text{Li}_6\text{PS}_5\text{Cl}$ without Li_3PO_4 increased from that of the sample with Li_3PO_4 because of the absence of the huge resistance from Li_3PO_4 . Moreover, $\text{Li}_6\text{PS}_5\text{Cl}$ without Li_3PO_4 showed a better Li dendrite growth suppression compared with $\text{Li}_6\text{PS}_5\text{Cl}$ containing Li_3PO_4 impurity. Our synthetic method of Li- argyrodite designed by understanding chemistry declared a best condition in the liquid phase synthesis. Therefore, it would be adaptable to the liquid-phase synthesis of sulfur-containing Li-argyrodite of various compositions due to higher nucleophilicity of LiCl than that of lithium bromide (LiBr) and lithium iodide (LiI). Regarding the battery performance, we found the increment of the charge and discharge capacity and more stable cycle performance owned to $\text{Li}_6\text{PS}_5\text{Cl}$ without any Li_3PO_4 impurity on it. The high Li-anode stability and the improved battery cycle performance from the $\text{Li}_6\text{PS}_5\text{Cl}$ could happen due to no other than the exclusion of the impurity Li_3PO_4 which resulting higher ionic conductivity. The design of the chemical factor's solvent selection for the preferable liquid phase synthesis without any impurity could discover a feasible path for applicable high electrochemical performance battery with high stability against either Li-anode or cathode with the possibility of mass production.

References

- [1] Takada, K. Progress and Prospective of Solid-State Lithium Batteries. *Acta Mater.* **2013**, *61* (3), pp. 759–770.
- [2] Kamaya, N., Homma, K., Yamakawa, Y., Hirayama, M., Kanno, R., Yonemura, M., Kamiyama, T., Kato, Y., Hama, S., Kawamoto, K., Mitsui, A. A Lithium Superionic Conductor. *Nat. Mater.* **2011**, *10* (9), pp. 682–686.
- [3] Seino, Y., Ota, T., Takada, K., Hayashi, A., Tatsumisago, M. A Sulphide Lithium Super Ion Conductor Is Superior to Liquid Ion Conductors for Use in Rechargeable Batteries. *Energy Environ. Sci.* **2014**, *7* (2), pp. 627–631.
- [4] Brinek, M., Hiebl, C., Wilkening, H. M. R. Understanding the Origin of Enhanced Li-Ion Transport in Nanocrystalline Argyrodite-Type $\text{Li}_6\text{PS}_5\text{I}$. *Chem. Mater.* **2020**, *32* (11), pp. 4754–4766.
- [5] Hanghofer, I., Gadermaier, B., Wilkening, H. M. R. Fast Rotational Dynamics in Argyrodite-Type $\text{Li}_6\text{PS}_5\text{X}$ (X: Cl, Br, I) as Seen by ^{31}P Nuclear Magnetic Relaxation—On Cation–Anion Coupled Transport in Thiophosphates. *Chem. Mater.* **2019**, *31* (12), pp. 4591–4597.
- [6] Hanghofer, I., Brinek, M., Eisbacher, S. L., Bitschnau, B., Volck, M., Hennige, V., Hanzu, I., Rettenwander, D., Wilkening, H. M. R. Substitutional Disorder: Structure and Ion Dynamics of the Argyrodites $\text{Li}_6\text{PS}_5\text{Cl}$, $\text{Li}_6\text{PS}_5\text{Br}$ and $\text{Li}_6\text{PS}_5\text{I}$. *Phys. Chem. Chem. Phys.* **2019**, *21* (16), pp. 8489–8507.
- [7] Stamminger, A. R., Ziebarth, B., Mrovec, M., Hammerschmidt, T., Drautz, R. Ionic Conductivity and Its Dependence on Structural Disorder in Halogenated Argyrodites $\text{Li}_6\text{PS}_5\text{X}$ (X = Br, Cl, I). *Chem. Mater.* **2019**, *31* (21), pp. 8673–8678.
- [8] Adeli, P., Bazak, J. D., Huq, A., Goward, G. R., Nazar, L. F. Influence of Aliovalent Cation Substitution and Mechanical Compression on Li-Ion Conductivity and Diffusivity in Argyrodite Solid Electrolytes. *Chem. Mater.* **2021**, *33* (1), pp. 146–157.
- [9] Deiseroth, H.-J., Kong, S.-T., Eckert, H., Vannahme, J., Reiner, C., Zaiß, T., Schlosser, M. $\text{Li}_6\text{PS}_5\text{X}$: A Class of Crystalline Li-Rich Solids With an Unusually High Li^+ Mobility. *Angew. Chem. Int. Ed.* **2008**, *47* (4), pp. 755–758.

- [10] Hogrefe, K., Minafra, N., Hanghofer, I., Banik, A., Zeier, W. G., Wilkening, H. M. R. Opening Diffusion Pathways through Site Disorder: The Interplay of Local Structure and Ion Dynamics in the Solid Electrolyte $\text{Li}_{6+x}\text{P}_{1-x}\text{Ge}_x\text{S}_5\text{I}$ as Probed by Neutron Diffraction and NMR. *J. Am. Chem. Soc.* **2022**, *144* (4), pp. 1795–1812.
- [11] Feng, X., Chien, P.-H., Wang, Y., Patel, S., Wang, P., Liu, H., Immediato-Scuotto, M., Hu, Y.-Y. Enhanced Ion Conduction by Enforcing Structural Disorder in Li-Deficient Argyrodites $\text{Li}_{6-x}\text{PS}_{5-x}\text{Cl}_{1+x}$. *Energy Stor. Mater.* **2020**, *30*, pp. 67–73.
- [12] Zhou, L., Minafra, N., Zeier, W. G., Nazar, L. F. Innovative Approaches to Li-Argyrodite Solid Electrolytes for All-Solid-State Lithium Batteries. *Acc. Chem. Res.* **2021**, *54* (12), pp. 2717–2728.
- [13] Miura, A., Rosero-Navarro, N. C., Sakuda, A., Tadanaga, K., Phuc, N. H. H., Matsuda, A., Machida, N., Hayashi, A., Tatsumisago, M. Liquid-Phase Syntheses of Sulfide Electrolytes for All-Solid-State Lithium Battery. *Nat. Rev. Chem.* **2019**, *3* (3), pp. 189–198.
- [14] Teragawa, S., Aso, K., Tadanaga, K., Hayashi, A., Tatsumisago, M. Liquid-Phase Synthesis of a Li_3PS_4 Solid Electrolyte Using N-Methylformamide for All-Solid-State Lithium Batteries. *J. Mater. Chem. A* **2014**, *2* (14), 5095.
- [15] Gamo, H., Nishida, J., Nagai, A., Hikima, K., Matsuda, A. Solution Processing via Dynamic Sulfide Radical Anions for Sulfide Solid Electrolytes. *Adv. Energy Sustainability Res.* **2022**, *3* (7), 2200019.
- [16] Matsuda, A., Muto, H., N.H.H. Phuc, Preparation of Li_3PS_4 Solid Electrolyte by Liquid-Phase Shaking Using Organic Solvents with Carbonyl Group as Complex Forming Medium. *The Journal of the JSPM.* **2016**, *63* (11), pp. 976–980.
- [17] Gamo, H., Nagai, A., Matsuda, A. The Effect of Solvent on Reactivity of the Li_2S – P_2S_5 System in Liquid-Phase Synthesis of $\text{Li}_7\text{P}_3\text{S}_{11}$ Solid Electrolyte. *Sci. Rep.* **2021**, *11* (1), 21097.
- [18] Ruhl, J., Riegger, L. M., Ghidui, M., Zeier, W. G. Impact of Solvent Treatment of the Superionic Argyrodite $\text{Li}_6\text{PS}_5\text{Cl}$ on Solid-State Battery Performance. *Adv. Energy Sustainability Res.* **2021**, *2* (2), 2000077.
- [19] Maniwa, R., Calpa, M., Rosero-Navarro, N. C., Miura, A., Tadanaga, K. Synthesis of Sulfide Solid Electrolytes from Li_2S and P_2S_5 in Anisole. *J. Mater. Chem. A* **2021**, *9* (1), pp. 400–405.

- [20] Han, A., Tian, R., Fang, L., Wan, F., Hu, X., Zhao, Z., Tu, F., Song, D., Zhang, X., Yang, Y. A Low-Cost Liquid-Phase Method of Synthesizing High-Performance $\text{Li}_6\text{PS}_5\text{Cl}$ Solid-Electrolyte. *ACS Appl. Mater. Interfaces* **2022**, *14* (27), pp. 30824–30838.
- [21] Subramanian, Y., Rajagopal, R., Ryu, K.-S. High Ionic-Conducting Li-Argyrodites Synthesized Using a Simple and Economic Liquid-Phase Approach and Their Application in All Solid-State-Lithium Batteries. *Scr. Mater.* **2021**, *204*, 114129.
- [22] Heo, Y. J., Seo, S., Hwang, S., Choi, S. H., Kim, D. One-pot Aprotic Solvent-enabled Synthesis of Superionic Li-argyrodite Solid Electrolyte. *Int J Energy Res.* **2022**, *46* (12), pp. 17644–17653.
- [23] Rajagopal, R., Subramanian, Y., Jung, Y. J., Kang, S., Ryu, K.-S. Rapid Synthesis of Highly Conductive $\text{Li}_6\text{PS}_5\text{Cl}$ Argyrodite-Type Solid Electrolytes Using Pyridine Solvent. *ACS Appl. Energy Mater.* **2022**, *5* (8), pp. 9266–9272.
- [24] Zhou, L., Park, K.-H., Sun, X., Lalère, F., Adermann, T., Hartmann, P., Nazar, L. F. Solvent-Engineered Design of Argyrodite $\text{Li}_6\text{PS}_5\text{X}$ ($\text{X} = \text{Cl}, \text{Br}, \text{I}$) Solid Electrolytes with High Ionic Conductivity. *ACS Energy Lett.* **2019**, *4* (1), pp. 265–270.
- [25] Ito, A., Kimura, T., Sakuda, A., Tatsumisago, M., Hayashi, A. Liquid-Phase Synthesis of Li_3PS_4 Solid Electrolyte Using Ethylenediamine. *J Solgel Sci Technol.* **2022**, *101* (1), pp. 2–7.
- [26] Yubuchi, S., Uematsu, M., Hotehama, C., Sakuda, A., Hayashi, A., Tatsumisago, M. An Argyrodite Sulfide-Based Superionic Conductor Synthesized by a Liquid-Phase Technique with Tetrahydrofuran and Ethanol. *J. Mater. Chem. A* **2019**, *7* (2), pp. 558–566.
- [27] Hsueh, M.-L., Huang, B.-H., Wu, J., Lin, C.-C. Synthesis, Characterization, and Catalytic Studies of Lithium Complexes: Efficient Initiators for Ring-Opening Polymerization of l-Lactide. *Macromolecules* **2005**, *38* (23), pp. 9482–9487.
- [28] Liu, Z., Fu, W., Payzant, E. A., Yu, X., Wu, Z., Dudney, N. J., Kiggans, J., Hong, K., Rondinone, A. J., Liang, C. Anomalous High Ionic Conductivity of Nanoporous $\beta\text{-Li}_3\text{PS}_4$. *J. Am. Chem. Soc.* **2013**, *135* (3), pp. 975–978.
- [29] Takahashi, M., Yang, S., Yamamoto, K., Ohara, K., Phuc, N. H. H., Watanabe, T., Uchiyama, T., Sakuda, A., Hayashi, A., Tatsumisago, M., Muto, H., Matsuda, A., Uchimoto, Y. Improvement of Lithium Ionic Conductivity of Li_3PS_4 through

Suppression of Crystallization Using Low-Boiling-Point Solvent in Liquid-Phase Synthesis. *Solid State Ion* **2021**, *361*, 115568.

- [30] Kolahdouzan, K., Ogba, O. M., O'Leary, D. J. ¹H NMR Studies of Intramolecular OH/OH Hydrogen Bonds via Titratable Isotope Shifts. *J. Org. Chem.* **2022**, *87* (3), pp. 1732–1744.
- [31] Pan, C., Xia, K., Parker, S., Tillman, E. Identity of Low-Molecular-Weight Species Formed in End-To-End Cyclization Reactions Performed in THF. *Polymers (Basel)* **2018**, *10* (8), 844.
- [32] Chen, T., Zhang, L., Zhang, Z., Li, P., Wang, H., Yu, C., Yan, X., Wang, L., Xu, B. Argyrodite Solid Electrolyte with a Stable Interface and Superior Dendrite Suppression Capability Realized by ZnO Co-Doping. *ACS Appl. Mater. Interfaces* **2019**, *11* (43), pp. 40808–40816.
- [33] Takada, K., Osada, M., Ohta, N., Inada, T., Kajiyama, A., Sasaki, H., Kondo, S., Watanabe, M., Sasaki, T. Lithium Ion Conductive Oxysulfide, Li₃PO₄–Li₃PS₄. *Solid State Ion* **2005**, *176* (31–34), pp. 2355–2359.
- [34] Wang, Y., Lu, D., Bowden, M., el Khoury, P. Z., Han, K. S., Deng, Z. D., Xiao, J., Zhang, J.-G., Liu, J. Mechanism of Formation of Li₇P₃S₁₁ Solid Electrolytes through Liquid Phase Synthesis. *Chem. Mater.* **2018**, *30* (3), pp. 990–997.
- [35] Rangasamy, E., Liu, Z., Gobet, M., Pilar, K., Sahu, G., Zhou, W., Wu, H., Greenbaum, S., Liang, C. An Iodide-Based Li₇P₂S₈I Superionic Conductor. *J. Am. Chem. Soc.* **2015**, *137* (4), pp. 1384–1387.
- [36] Wang, H., Hood, Z. D., Xia, Y., Liang, C. Fabrication of Ultrathin Solid Electrolyte Membranes of β-Li₃PS₄ Nanoflakes by Evaporation-Induced Self-Assembly for All-Solid-State Batteries. *J. Mater. Chem. A* **2016**, *4* (21), pp. 8091–8096.
- [37] Yu, C., Ganapathy, S., Hageman, J., van Eijck, L., van Eck, E. R. H., Zhang, L., Schwietert, T., Basak, S., Kelder, E. M., Wagemaker, M. Facile Synthesis toward the Optimal Structure-Conductivity Characteristics of the Argyrodite Li₆PS₅Cl Solid-State Electrolyte. *ACS Appl. Mater. Interfaces* **2018**, *10* (39), pp. 33296–33306.
- [38] Huang, M., Shoji, M., Shen, Y., Nan, C.-W., Munakata, H., Kanamura, K. Preparation and Electrochemical Properties of Zr-Site Substituted

- $\text{Li}_7\text{La}_3(\text{Zr}_{2-x}\text{M}_x)\text{O}_{12}$ ($\text{M} = \text{Ta}, \text{Nb}$) Solid Electrolytes. *J. Power Sources* **2014**, *261*, pp. 206–211.
- [39] Kmiec, S., Joyce, A., Martin, S. W. Glass Formation and Structural Analysis of $\text{Na}_4\text{P}_2\text{S}_{7-x}\text{O}_x$, $0 \leq x \leq 7$ Sodium Oxy-Thiophosphate Glasses. *J. Non-Cryst. Solids* **2018**, *498*, pp. 177–189.
- [40] Holzwarth, U., Gibson, N. The Scherrer Equation versus the “Debye-Scherrer Equation.” *Nat. Nanotechnol.* **2011**, *6* (9), pp. 534–534.
- [41] Li, Y., Arnold, W., Jasinski, J. B., Thapa, A., Sumanasekera, G., Sunkara, M., Narayanan, B., Druffel, T., Wang, H. Interface Stability of LiCl-Rich Argyrodite $\text{Li}_6\text{PS}_5\text{Cl}$ with Propylene Carbonate Boosts High-Performance Lithium Batteries. *Electrochim. Acta* **2020**, *363*, 137128.
- [42] Han, F., Westover, A. S., Yue, J., Fan, X., Wang, F., Chi, M., Leonard, D. N., Dudney, N. J., Wang, H., Wang, C. High Electronic Conductivity as the Origin of Lithium Dendrite Formation within Solid Electrolytes. *Nat. Energy* **2019**, *4* (3), pp. 187–196.
- [43] Wang, S., Zhang, W., Chen, X., Das, D., Ruess, R., Gautam, A., Walther, F., Ohno, S., Koerver, R., Zhang, Q., Zeier, W. G., Richter, F. H., Nan, C., Janek, J. Influence of Crystallinity of Lithium Thiophosphate Solid Electrolytes on the Performance of Solid-State Batteries. *Adv. Energy Mater.* **2021**, *11* (24), 2100654.
- [44] Peng, L., Chen, S., Yu, C., Liao, C., Sun, M., Wang, H.-L., Zhang, L., Cheng, S., Xie, J. Unraveling the Crystallinity on Battery Performances of Chlorine-Rich Argyrodite Electrolytes. *J. Power Sources* **2022**, *520*, 230890.
- [45] Indrawan, R. F., Yamamoto, T., Nguyen, H. H. P., Muto, H., Matsuda, A. Liquid-Phase Synthesis of $100\text{Li}_3\text{PS}_4\text{-}50\text{LiI-xLi}_3\text{PO}_4$ Solid Electrolytes. *Solid State Ion* **2020**, *345*, 115184.
- [46] Han, X., Wang, M., Yu, J., Wang, S. Optimization of Structural Expansion and Contraction for TiS_2 by Controlling the Electrochemical Window of Intercalation/Delithiation. *Mater. Adv.* **2022**, *3* (3), pp. 1652–1659.
- [47] Zhu, Y., He, X., Mo, Y. Origin of Outstanding Stability in the Lithium Solid Electrolyte Materials: Insights from Thermodynamic Analyses Based on First-Principles Calculations. *ACS Appl. Mater. Interfaces* **2015**, *7* (42), pp. 23685–23693.

- [48] Banerjee, A., Wang, X., Fang, C., Wu, E. A., Meng, Y. S. Interfaces and Interphases in All-Solid-State Batteries with Inorganic Solid Electrolytes. *Chem. Rev.* **2020**, *120* (14), pp. 6878–6933.

Chapter 4

Oxygen-doped Argyrodite Solid Electrolyte by Liquid Phase Synthesis

4.1 Background

After successfully synthesizing pure argyrodite through a liquid phase synthesis method in Chapter 3, the focus of the research will now shift towards controllable oxygen doping of $\text{Li}_6\text{PS}_5\text{Cl}$ argyrodite SEs. The objective is to introduce controlled amounts of oxygen into the argyrodite structure to investigate its effects on the electrochemical performance and stability of the solid electrolyte. By exploring the possibilities of oxygen doping, we aim to further improve the properties of the argyrodite SEs and pave the way for their application in advanced energy storage devices.

The background for exploring oxygen doping in solid electrolytes stems from the aim to enhance the electrochemical performance and stability of sulfide-based solid electrolytes. Oxygen doping involves intentionally introducing oxygen atoms into the crystal structure of sulfide-based solid electrolytes, such as argyrodite. This addition can improve the stability of the solid electrolyte interface (SEI), enhance chemical and electrochemical stability, and potentially enhance ion conductivity. By incorporating oxygen, researchers aim to overcome the challenges of sulfide-based solid electrolytes, such as poor stability and limited ion conductivity, and develop solid electrolytes with improved performance, stability, and compatibility with electrode materials. The ultimate goal is to advance the practical applications of all-solid-state Li-ion batteries in various industries.

The argyrodite solid electrolyte $\text{Li}_6\text{PS}_5\text{Cl}$ is one of the promising candidates due to its high Li-ion conductivity for the application of all-solid-state lithium-ion batteries (ASSLIBs). Unfortunately, $\text{Li}_6\text{PS}_5\text{Cl}$ argyrodite exhibits low stability against lithium metal anodes and oxide cathodes. One way to improve stability is by oxygen doping into

$\text{Li}_6\text{PS}_5\text{Cl}$ argyrodite. In this work, $\text{Li}_6\text{PS}_{5-2.5x}\text{O}_{2.5x}\text{Cl}$ ($x = 0, 0.05, \text{ and } 0.10$) solid electrolytes with oxygen doping were successfully synthesized using liquid-phase synthesis for the first time. Therefore, the solid electrolyte with $x = 0.05$ exhibits high ionic conductivity with enhanced electrochemical stability against lithium metal and oxide cathodes. Argyrodites with $x = 0.05$ and $x = 0.10$ show superior capacity retention and higher Coulomb efficiency compared to $x = 0$. Moreover, the solid electrolytes also demonstrate better stability during Li symmetrical cell measurements. This experiment provides a controllable amount of oxygen doping into the $\text{Li}_6\text{PS}_5\text{Cl}$ argyrodite solid electrolyte system in order to achieve high performance of ASSLIBs through liquid-phase synthesis.

4.2 Introduction

The modernization of technology results in an increased demand for power sources and energy storage [1]. All-solid-state lithium-ion batteries (ASSLIBs) are considered one of the most promising energy storage options due to their low weight density, high energy density, and high operating potential, as well as their enhanced safety compared to conventional batteries with flammable liquid electrolytes [2–4]. Initially, significant research efforts were focused on developing oxide-based materials that can conduct lithium ions. However, oxide-based SEs such as $\text{Li}_7\text{La}_3\text{Zr}_2\text{O}_{12}$ (LLZO), $\text{Li}_{3x}\text{La}_{2/3-x}\text{TiO}_3$ (LLTO), $\text{Li}_{1.3}\text{Al}_{0.3}\text{Ti}_{1.7}(\text{PO}_4)_3$ (LATP), and $\text{Li}_{6.25}\text{Ga}_{0.25}\text{La}_3\text{Zr}_2\text{O}_{12}$ (LGLZO) exhibit lithium-ion conductivity ranging from 10^{-3} to 1 mS cm^{-1} , which is significantly lower than the lithium-ion conductivity of over 10 mS cm^{-1} observed in organic liquid electrolytes at room temperature, despite their excellent electrochemical stability [5–8]. Sulfide-based solid electrolytes have gained attention due to their superior ionic conductivity and formability at room temperature [9,10]. One prominent sulfide-based solid electrolyte is $\text{Li}_{9.54}\text{Si}_{1.74}\text{P}_{1.44}\text{S}_{11.7}\text{Cl}_{0.3}$, which demonstrates an ionic conductivity of 25 mS cm^{-1} , surpassing that of conventional liquid electrolytes [11,12]. Furthermore, $\text{Li}_{10}\text{GeP}_2\text{S}_{12}$ and argyrodite-type solid electrolytes ($\text{Li}_6\text{PS}_5\text{X}$, $\text{X} = \text{Cl, Br, and I}$) have an ionic conductivity in the range of 10^{-3} to $10^{-2} \text{ S cm}^{-1}$, comparable to conventional liquid electrolytes [13–15]. However, the widespread application of

$\text{Li}_{10}\text{GeP}_2\text{S}_{12}$ is still limited due to the high cost of germanium [16]. On the other hand, $\text{Li}_6\text{PS}_5\text{Cl}$ argyrodite solid electrolytes, with similar conductivity to $\text{Li}_{10}\text{GeP}_2\text{S}_{12}$ but significantly lower cost, show great potential for commercialization. Argyrodite-type sulfides have recently emerged as promising SEs with three favorable pathways for lithium-ion migration, allowing contact with inorganic electrodes while maintaining rigidity and moderate electrochemical windows [17–19].

The term "argyrodite" is derived from the mineral Ag_8GeS_6 , which served as inspiration for the discovery of high ionic conductivity in $\text{Li}_6\text{PS}_5\text{X}$ ($\text{X} = \text{Cl}, \text{Br}, \text{and I}$) by Deiseroth et al. This compound exhibited a disordered Li^+ content similar to the mobility observed in the argyrodite mineral structure [20]. The reported conductivities for $\text{Li}_6\text{PS}_5\text{Cl}$, $\text{Li}_6\text{PS}_5\text{Br}$, and $\text{Li}_6\text{PS}_5\text{I}$ were initially measured at 1.9 mS cm^{-1} , 0.7 mS cm^{-1} , and $1.3 \times 10^{-6} \text{ S cm}^{-1}$, respectively [21–23]. Therefore, the low-cost production, high ionic conductivity, and favorable mechanical properties of the chloride-based argyrodite solid electrolyte make it suitable for use in ASSLiBs. However, it should be noted that argyrodite solid electrolytes face challenges related to poor electrochemical interface stability with lithium metal anodes and oxide cathodes, especially during high voltage charging [24,25]. Additionally, like other sulfide-based solid electrolytes, argyrodite SEs are metastable and tend to decompose upon exposure to air, limiting their further application. Therefore, the development of promising solid electrolytes requires not only high ionic conductivity but also considerations of structural and electrochemical stabilities.

Extensive studies have been conducted to address instability issues through techniques such as external surface coating and structural modifications [26–28]. In the past decades, structural modifications of solid electrolytes, such as doping or composition substitution, have shown promising results due to their simplified methods and wide applicability. One of the most promising doping agents is the introduction of oxygen into sulfide-based solid electrolytes, as it has the ability to enhance the electrochemical stability of solid electrolyte interfaces (SEI) [29–32]. Our research group has successfully introduced oxygen doping into sulfide-based solid electrolytes, such as incorporating Li_3PO_4 into Li_3PS_4 , Li_3PO_4 into $\text{Li}_7\text{P}_2\text{S}_8\text{I}$, and Li_4SiO_4 into $\text{Li}_7\text{P}_2\text{S}_8\text{I}$, resulting in improved stability against lithium metal anode [33–35]. Furthermore, the introduction of oxygen

doping into argyrodite has recently been reported to improve stability. Examples include the incorporation of ZnO into $\text{Li}_6\text{PS}_5\text{Br}$, partial substitution of Li_2O into $\text{Li}_6\text{PS}_5\text{Cl}$ or $\text{Li}_6\text{PS}_5\text{Br}$, P_2O_5 into $\text{Li}_{5.5}\text{PS}_{4.5}\text{Cl}_{1.5}$, Li_3PO_4 into $\text{Li}_6\text{PS}_5\text{Cl}$, SnO_2 into $\text{Li}_6\text{PS}_5\text{I}$, and Li_3PO_4 into mixed halide $\text{Li}_6\text{PS}_{5-x}\text{O}_x\text{Cl}_{0.5}\text{Br}_{0.5}$. All of these oxygen-doped or substitution argyrodite systems demonstrate significant improvement in stability against lithium metal anode and oxide cathode [36–42]. Despite their good performance, all of the reported oxygen-doped argyrodites still utilize the mechanical ball milling process as the synthesis method. However, scaling up this process for mass production presents challenges due to its high energy consumption and the difficulty in controlling the atmosphere due to the air sensitivity of sulfides [43]. Conversely, liquid-phase synthesis is more suitable for large-scale manufacturing due to its high scalability and low-cost production [44,45].

Organic solvents play a crucial role in dissolving and facilitating reactions involving lithium thiophosphate. The choice of appropriate organic solvents is important, with high polarity and high dielectric constant being favorable for the dissolution of argyrodite SEs precursors [46]. Ethanol (EtOH) is widely recognized as an effective solvent for dissolving argyrodite due to its high dielectric constant and low boiling point. However, the use of EtOH can result in the formation of unwanted Li_3PO_4 , which has low ionic conductivity and can hinder the overall ionic conductivity of the argyrodite system [47]. Alternatively, high molecular weight solvents like Ethylenediamine (EDA), Ethanedithiol (EDT), and their combination have shown promise as dissolution mediums for argyrodite systems [48,49]. These solvents offer increased dissolubility of the solute, but it is important to consider their higher boiling points, which can make solvent removal more challenging and energy-intensive [50,51].

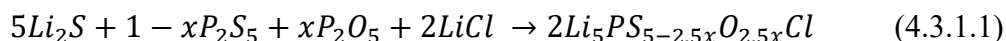
In our research, we have successfully used Acetonitrile (ACN) and 1-propanethiol (PTH) as solvents for synthesizing $\text{Li}_6\text{PS}_5\text{Cl}$ argyrodite SEs through liquid-phase synthesis. This method has effectively prevented the formation of Li_3PO_4 and resulted in the highest reported ionic conductivity for SEs with the same composition [52]. Controlling the amount of oxygen incorporated into the argyrodite structure is crucial for oxygen-doping through liquid-phase synthesis. Therefore, selecting a solvent that minimizes the formation of oxide impurities is of utmost importance, as it enables precise control of the oxygen doping level in argyrodite.

In this study, we propose the oxygen doping of P₂O₅ into the Li₆PS₅Cl argyrodite SEs system using liquid-phase synthesis with a solvent combination of ACN and PTH. While previous studies have reported the addition of P₂O₅ into argyrodite SEs through mechanical ball milling, the utilization of an organic solvent medium for synthesis has not been explored. Therefore, we have successfully synthesized Li₆PS_{5-2.5x}O_{2.5x}Cl argyrodite SEs using the liquid-phase synthesis method for the first time. X-ray diffraction (XRD) measurements confirmed the incorporation of the oxide compound P₂O₅ (x=5) into the argyrodite structure without any residual Li₃PO₄ impurities. Additionally, the composition with x=5 demonstrated the highest stability in terms of cycle performance against both the Li metal anode and oxide cathode materials.

4.3 Experimental Method

4.3.1 Sample Preparation

The stoichiometry used in this study is expressed as equation 4.3.1.1:



Samples of Li₆PS_{5-2.5x}O_{2.5x}Cl (x = 0, 0.05, 0.10) were prepared by liquid phase synthesis based on the process reported by our group previously.[52] Reagents of synthesis-grade Li₂S (99.9%, Mitsuwa), P₂S₅ (99%, Merck), P₂O₅ (98.5%, Tokyo Chemical Industry), and LiCl (99.0%, Sigma-Aldrich) were used as raw materials in the synthesis. P₂O₅ reagent was dried under low pressure using diaphragm pump (Buchi, V-100) at 200 °C for 24 h prior to use. To initiate the synthesis, we mixed a 3:1-x:x (x = 0, 0.05, 0.10) molar ratio of Li₂S, P₂S₅, and P₂O₅ in 10 mL of ACN (super-dehydrated, 99.8%, Fujifilm) and then stirred the mixture for 12 h at 75 °C to form a suspension. Subsequently, Li₂S and LiCl were mixed in a molar ratio of 2:2 and stirred in 10 mL of PTH (98%, Tokyo Chemical Industry) at 50 °C for 12 h. 3A molecular sieves were added into PTH prior to use with the purpose of dehydrating the remaining water content. 100 grams of 3A molecular sieves, which accounts for 12.20% of the mass of PTH, was added to 500 ml of the PTH solvent. The 3A molecular sieves were dried at 220 °C for 18 hours to eliminate any remaining humidity or water vapor within the molecular sieves prior to

being added to the PTH solvent. The resulting suspension and solution were combined and stirred for 12 hours at 50 °C. Subsequently, the stirred mixture was evaporated at 80 °C for 12 hours under low pressure using a diaphragm pump (Buchi, V-100). The obtained precursor was then ground and pelletized at a uniaxial pressure of 127 MPa before undergoing the heat treatment process. $\text{Li}_6\text{PS}_{5-2.5x}\text{O}_{2.5x}\text{Cl}$ pellets was heat-treated at 550 °C for 10 h under an Ar flow using a glass tube furnace. All processes were conducted inside glovebox under a dry Ar atmosphere.

4.3.2 Material Characterization

The crystal structures of the retrieved samples were analyzed using XRD (XRD; SmartLab, Rigaku) with an airtight holder to protect the samples from exposure to air humidity. Raman spectra (Laser Raman Spectrometer, Jasco, NRS-4500) was performed to investigate the local structure inside a sealed container, which was carried out inside an Ar-filled glovebox. Solid-state ^{31}P magic-angle-spinning NMR (^{31}P MAS-NMR, Avance III 400, Bruker) analysis was conducted using the typical single-pulse sequence with a spinning rate of 6 kHz. Scanning electron microscope-energy dispersive x-ray spectroscopy (SEM-EDX) images mapping was achieved using Hitachi-S4800 and ULTIM MAX, Oxford Instrument as for the EDX instrument.

4.3.3 Electrochemical Performance Measurement

The temperature dependence of the ionic conductivity of the retrieved sample was investigated using alternating current (AC) impedance spectroscopy (SI 1260, Solartron) in the frequency range of 10 MHz to 1 Hz under a dry Ar flow. The samples for impedance measurements were prepared by uniaxial pressing approximately 80 mg of the sample powder into pellets with a diameter of approximately 10 mm. The pressing was performed under a pressure of 255 MPa (uniaxial press) for 10 minutes at room temperature. The thickness of the argyrodite SE pellets was approximately 0.60 mm. The prepared pellets were placed in a holder made from polyether ether ketone (PEEK), with two blocking electrodes made from stainless steel (SUS). The temperature was increased gradually in

a controlled manner, starting from room temperature and reaching up to 130 °C, with various temperature increments. At each temperature, the samples were held for 1 hour (except for 40 and 50 °C, where they were held for 2 hours) before conducting the impedance measurement. Cyclic voltammogram (CV) measurements were performed using a potentiostat (SI 1287, Solartron). The sample pellets, weighing approximately 80 mg each, were prepared by applying a pressure of 255 MPa at room temperature to uniaxially pressed pellets with a diameter of approximately 1 cm. The cell assembly consisted of sandwiching a lithium sheet (Li) with a diameter of 9 mm and a thickness of 0.1 mm between SUS electrodes and the pelletized solid electrolyte (SE). The resulting cell, denoted as Li | SE | SUS, was subjected to measurements with a scan speed of 5 mV s⁻¹, covering a voltage range from -0.3 to 10 V vs. Li/Li⁺. The electrical conductivity was determined by performing Direct Current (DC) polarization measurements (SI 1287, Solartron) on the pellets. Applied voltages of 0.1, 0.15, 0.2, 0.25, and 0.3 V were used, and each voltage was applied for a duration of 30 minutes at room temperature. The measurement of lithium metal stability was conducted using DC polarization tests. Lithium sheets were used as non-blocking electrodes on both sides of the pelletized solid electrolyte, which were then sandwiched between stainless steel (SUS) plates. The prepared symmetric cells were cycled at ±0.1 V using a charge-discharge device (BTS 2004H, Nagano) under a dry Ar atmosphere at room temperature. The battery performance analysis for charge and discharge curves was carried out using a Li-In alloy as the negative electrode, Li₆PS_{5-2.5x}O_{2.5x}Cl (where x = 0, 0.05, and 0.10) as the electrolyte layer, and a composite consisting of LiNi_{0.33}Mn_{0.33}Co_{0.33}O₂ (NMC₁₁₁), Li₆PS_{5-2.5x}O_{2.5x}Cl (where x = 0, 0.05, and 0.10), and Acetylene black (AB) in a weight ratio of 70:30:3 as the positive electrode. The positive electrodes were fabricated by thoroughly homogenizing NMC₁₁₁-Li₆PS_{5-2.5x}O_{2.5x}Cl-AB using an agate mortar for approximately 15 minutes. Prior to utilization, the NMC₁₁₁ was coated with 1 wt% of NB and subsequently subjected to a heat treatment at 300 °C for 30 min. 10 mg of the cathode composite was deposited onto one side of the pelletized Li₆PS_{5-2.5x}O_{2.5x}Cl (low pressure) inside a PEEK container with an inner diameter of 10 mm, then pressed it together at 255 MPa uniaxial pressure at room temperature for 10 min. Once the Li-In foil was affixed to the opposite side of the pellet sandwich, the assembly underwent another pressing step at a uniaxial pressure of 127 MPa at room temperature for 5 min. The cells underwent

cycling using a charge-discharge device (BST-2004H, Nagano) with a voltage cutoff ranging from 2.0 to 3.8 V vs Li-In at a rate of 0.1C. All preparations were conducted within a dry Ar-filled glovebox.

4.4 Result and Discussion

4.4.1 Structure Analysis of $\text{Li}_6\text{PS}_{5-2.5x}\text{O}_{2.5x}\text{Cl}$

Figure 4.1 illustrates the XRD patterns obtained from the liquid phase synthesis of $\text{Li}_6\text{PS}_{5-2.5x}\text{O}_{2.5x}\text{Cl}$ ($x=0, 0.05, \text{ and } 0.10$) using ACN+PTH as the solvents. A standard sample of pure argyrodite ($\text{Li}_6\text{PS}_5\text{Cl}$) or undoped argyrodite solid electrolytes ($x=0$) was successfully synthesized, and its structure was confirmed to match the argyrodite structure found in ICSD#259200. Only a negligible amount of Li_2S was detected. The absence of Li_3PO_4 side reaction formation at $x=0$ indicates the successful utilization of ACN+PTH in synthesizing pure argyrodite.[52] In the case of P_2O_5 -doped argyrodite, $\text{Li}_6\text{PS}_{4.875}\text{O}_{0.125}\text{Cl}$ ($x=0.05$) exhibits a structure similar to $x=0$, primarily characterized by the argyrodite structure with a small trace of Li_2S . However, a small peak corresponding to LiCl was observed in the P_2O_5 -doped argyrodite at $x=0.05$. Figure 4.1 also demonstrates that a higher level of P_2O_5 doping in the argyrodite at $x=0.10$ maintains a similar structure to that observed at $x=0.05$. However, $x=0.10$ exhibits a peak corresponding to Li_3PO_4 , indicating the occurrence of an oxidation side reaction. The smaller size of the oxygen atom and its higher electronegativity compared to sulfur contribute to oxygen's tendency to form chemical bonds.[53] Excess amounts of P_2O_5 can induce the oxidation of Li_3PS_4 , which is chemically more stable than Li_3PS_4 . The absence of Li_3PO_4 at $x=0.05$ indicates the successful partial substitution of sulfur atoms with oxygen atoms within the lithium thiophosphate system of argyrodite solid electrolytes.

Further structural investigations of oxygen substitution into sulfide were conducted using Raman spectroscopy, as depicted in Figure 4.2. The spectra of all samples ($x=0, 0.05, \text{ and } 0.10$) exhibit a weak peak at 570 cm^{-1} , which can be attributed to the PS_4^{3-} unit.[54] Pure argyrodite or $x=0$ indicates the main structural unit of PS_4^{3-} with a broad peak observed at 420 cm^{-1} . The PS_4^{3-} peak for $x=0.05$ then shifts to a lower wavenumber at 417 cm^{-1} . Furthermore, for $x=0.10$, it shifts even lower than $x=0.05$,

reaching 416 cm^{-1} . The higher electronegativity of oxygen relative to lithium and sulfur leads to lattice distortion/disorder, resulting in varied P-S bond strengths.[42,53] This indicates that the addition of oxygen doping into lithium thiophosphate from argyrodite modifies the P-S bond and overlaps the PS_4^{3-} unit with the POS_3^{3-} unit, which aligns precisely with a study by Sun et al.[36]

^{31}P MAS-NMR analysis was conducted to further examine the local structure of $\text{Li}_6\text{PS}_{5-2.5x}\text{O}_{2.5x}\text{Cl}$ ($x=0, 0.05, \text{ and } 0.10$), as shown in Figure 4.3. For $x=0$, the spectrum exhibits a peak at 88 ppm corresponding to the PS_4^{3-} anion, along with the accompanying spinning side-bands. Upon the addition of 5 mol% of P_2O_5 at $x=0.05$, the PS_4^{3-} anion experiences a chemical shift to a lower value at 87.5 ppm, indicating an interaction between the oxygen and the PS_4^{3-} anion. A stronger interaction between oxygen and the PS_4^{3-} anion was observed in $x=0.10$. The PS_4^{3-} anion in $x=0.10$ shifted to 87.1 ppm, which can be attributed to the higher concentration of oxygen derived from P_2O_5 . However, the increased amount of oxygen in $x=0.10$ led to the appearance of the PO_4^{3-} anion at 12 ppm. This observation is consistent with the XRD result shown in Figure 4.1, indicating the occurrence of oxidation side reactions of Li_3PO_4 . The shift in the ^{31}P MAS-NMR chemical shift confirms the substitution of sulfur with oxygen and the alteration of the P-S bond from the PS_4^{3-} anion to form the POS_3^{3-} anion, which is considered to overlap with PS_4^{3-} . This phenomenon is consistent with our previous study.

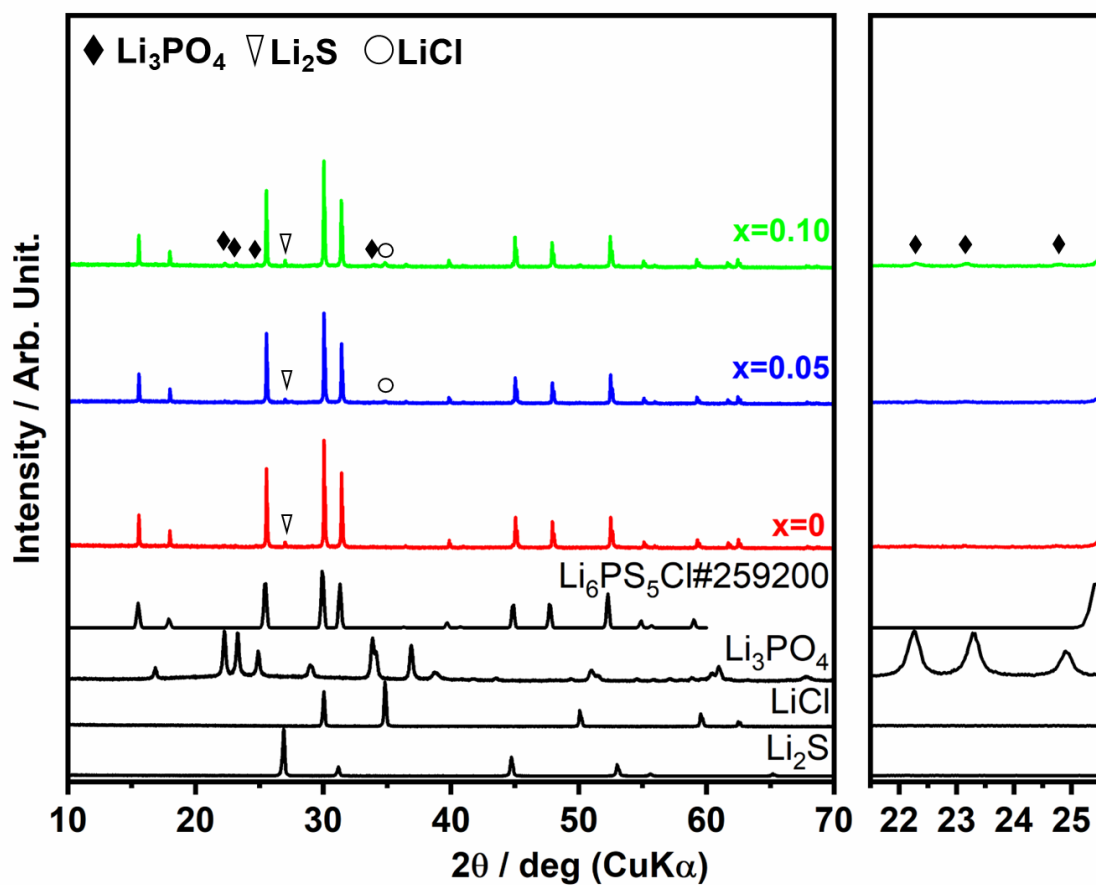


Figure 4.1. XRD patterns of $\text{Li}_6\text{PS}_{5-2.5x}\text{O}_{2.5x}\text{Cl}$ SEs prepared by liquid phase synthesis using ACN+PTH as the solvents heat treated at 550°C for 10 h.

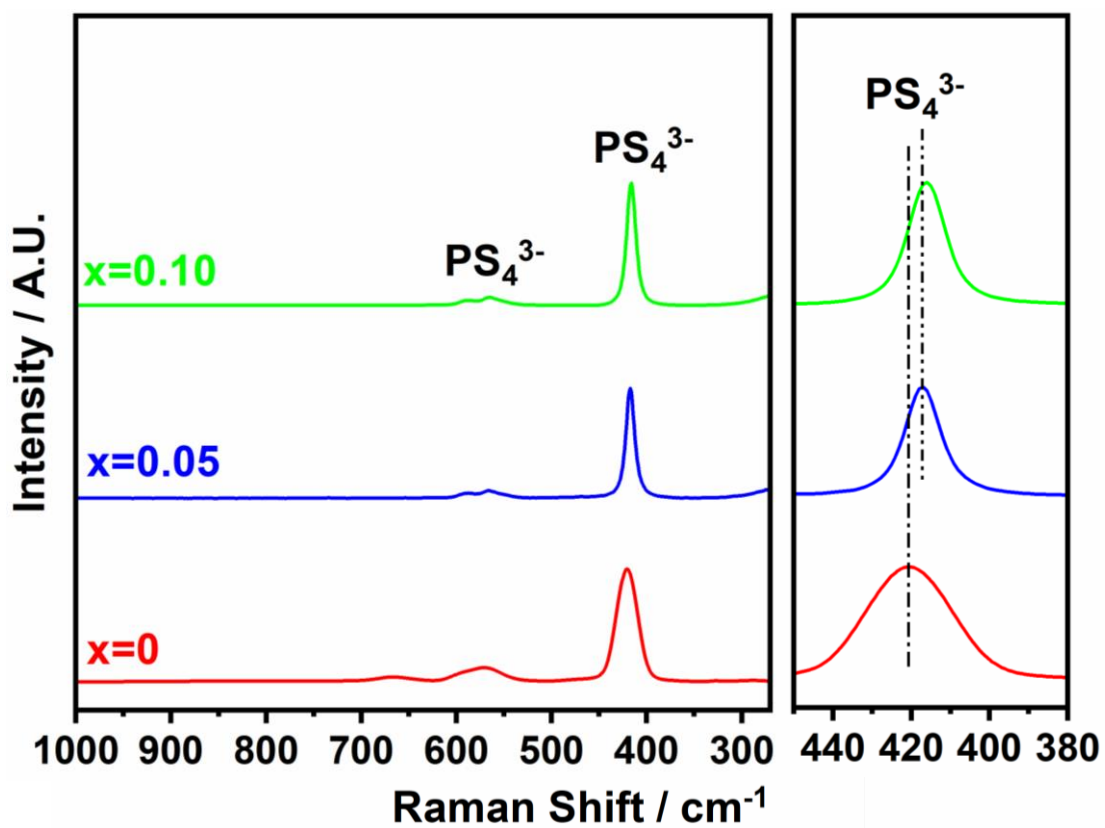


Figure 4.2. Raman Spectroscopy of $\text{Li}_6\text{PS}_{5-2.5x}\text{O}_{2.5x}\text{Cl}$ SEs prepared by liquid phase synthesis using ACN+PTH as the solvents heat treated at 550 °C for 10 h.

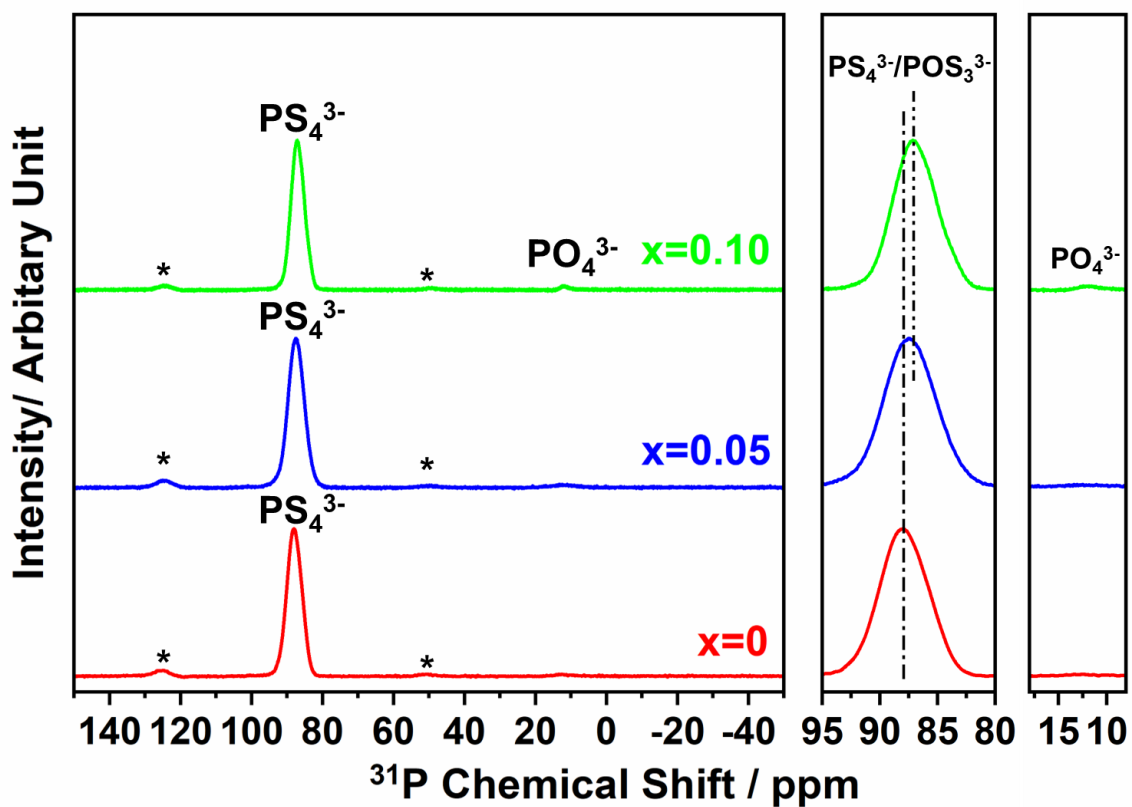


Figure 4.3. ^{31}P MAS-NMR patterns of $\text{Li}_6\text{PS}_{5-2.5x}\text{O}_{2.5x}\text{Cl}$ SEs prepared by liquid phase synthesis using ACN+PTH as the solvents heat treated at 550 °C for 10 h.

4.4.2 Electrochemical Performance of $\text{Li}_6\text{PS}_{5-2.5x}\text{O}_{2.5x}\text{Cl}$

Ionic conductivity measurements were performed to investigate the difference in the effect of P_2O_5 dopant on $\text{Li}_6\text{PS}_{5-2.5x}\text{O}_{2.5x}\text{Cl}$ using temperature-dependent AC impedance. As shown in Figure 4.4, an increase in P_2O_5 content resulted in a decrease in the ionic conductivity of $\text{Li}_6\text{PS}_{5-2.5x}\text{O}_{2.5x}\text{Cl}$. For the undoped sample ($x=0$), the ionic conductivity at room temperature was measured at 2.75 mS cm^{-1} . In comparison, for $x=0.05$ and $x=0.10$, the corresponding ionic conductivities at room temperature were found to be 2.63 and 2.57 mS cm^{-1} , respectively. The activation energies for each sample were calculated from the corresponding Arrhenius plot of the temperature dependence of ionic conductivity, as shown in Figure 4.5. For $x=0$, $x=0.05$, and $x=0.10$, the activation energies were determined to be 24.8 , 26.5 , and 26.3 kJ mol^{-1} , respectively. Pure argyrodite exhibits the lowest activation energy, resulting in its highest ionic conductivity. Upon the addition of P_2O_5 , the activation energy increases due to the contribution of defect interaction from oxygen.[55] However, it is interesting to note that the activation energy for $x=0.10$ (26.3 kJ mol^{-1}) was slightly lower than that for $x=0.05$ (26.5 kJ mol^{-1}), indicating a non-linear relationship with the decrease in ionic conductivity. This could be attributed to the partial formation of Li_3PO_4 from the oxygen present in $x=0.10$, which reduces the defects introduced by single oxygen substitution in the argyrodite single crystal phase. Although there is a difference in activation energy between $x=0.05$ and $x=0.10$, the difference is so small that it can be neglected. Furthermore, the addition of P_2O_5 into the argyrodite structure leads to a reduction in ionic conductivity.

Cyclic voltammogram (CV) was performed to assess the surface stability of the $\text{Li}_6\text{PS}_{5-2.5x}\text{O}_{2.5x}\text{Cl}$ solid electrolytes (SEs) using a $\text{Li} \mid \text{Li}_6\text{PS}_{5-2.5x}\text{O}_{2.5x}\text{Cl}$ ($x=0, 0.05, 0.10$) \mid SUS cell configuration. In this setup, Li served as the reference electrode, and SUS was used as the counter electrode with the range of scan between 10 V to -0.3V , starting from initial potential of 2V . Figure 4.6 displays the cyclic voltammetry (CV) results for the $x=0$ sample, revealing the reduction (Lithium plating) and oxidation (Lithium dissolution) reactions occurring within the potential range of -0.3 V to 0.3 V .[56] In the first cycle, a small oxidation peak is observed at 1.7 V , which gradually increases in subsequent cycles, covering the potential range of 1.4 V to 3.2 V . This observation indicates the oxidation of free S^{2-} ions, leading to the degradation of the interface in the $x=0$ SEs over

cycling.[40,56,57] Furthermore, the CV results for $x=0.05$ and $x=0.10$ are shown in Figure 4.7 and 4.8, respectively, demonstrating similar oxidation and reduction peaks corresponding to lithium dissolution and plating as observed in $x=0$. However, no additional peaks are observed, indicating that both $x=0.05$ and $x=0.10$ provide a wide electrochemical window and exhibit stability at 0 V versus Li/Li^+ . This result further confirms that oxygen doping improves the electrochemical stability of $\text{Li}_6\text{PS}_{5-2.5x}\text{O}_{2.5x}\text{Cl}$ SEs, which is consistent with previous findings reported for other sulfides.[36–38,40,56,58]

DC polarization was performed to further investigate the electrochemical stability of $\text{Li} \mid \text{Li}_6\text{PS}_{5-2.5x}\text{O}_{2.5x} \mid \text{Li}$ symmetric cells against lithium metal. The symmetric cells were cycled under constant current density at 0.1 mA cm^{-2} under room temperature, with each charge and discharge cycle lasting 1 h. Figure 4.9 shows the lithium metal stability measurement from a lithium symmetrical cell of $\text{Li}_6\text{PS}_{5-2.5x}\text{O}_{2.5x}$ ($x=0, 0.05, 0.10$). At $x=0$, there is a stable potential of 14 mV until the potential profile suddenly drops to 9 mV after 33 cycles or 66 hours of measurement time, which appears to indicate a short circuit. On the other hand, $x=0.05$ can run for significantly longer, up to 395 hours or approximately 197 cycles. The initial voltage for $x=0.05$ is 15 mV, gradually increasing until it reaches 30 mV at the 197th cycle, and then a short circuit occurs. The increment of potential could be degradation of the SEI from $x=0.05$ which increases the resistance from it. Although the potential increment reaches 200% after 197 cycles, the addition of oxygen into argyrodite has proven to improve the stability of lithium metal at $x=0.05$ for approximately 5.5 times longer than pure argyrodite ($x=0$). Furthermore, at $x=0.10$, there is a stable potential profile at 15 mV from the initial stage for 104 hours or 52 cycles until a short circuit occurs, indicated by a sudden drop in potential to 7 mV. Compared to $x=0$, $x=0.10$ has a higher stability because it can keep a longer stability measurement time. However, $x=0.10$ is not as stable as $x=0.05$. This is due to the excess amount of P_2O_5 , resulting in the formation of Li_3PO_4 as an oxidation side product. Li_3PO_4 separates from the argyrodite system and acts as an impurity, compromising the stability of the argyrodite system. Li_3PO_4 itself has an ionic conductivity reported at $10^{-7} - 10^{-6} \text{ S cm}^{-1}$, which is significantly lower than argyrodite SEs.[59] The low ionic conductivity of Li_3PO_4 could hinder or block the transport of lithium ions.[52] Moreover, the introduction of P_2O_5 has successfully increased the stability of Li metal in $\text{Li}_6\text{PS}_{5-2.5x}\text{O}_{2.5x}\text{Cl}$ by enhancing the

redox stability of sulfide electrolytes, mitigating the side reactions at the interface, and suppressing Li dendrite growth.[38,60,61]

To verify the effect of oxygen doping in improving the air stability of $\text{Li}_6\text{PS}_5\text{-}_{2.5x}\text{O}_{2.5x}\text{Cl}$ SEs, an analysis of structural changes was performed on the SEs after exposure to an air atmosphere with a humidity level of approximately 35% for 10 and 30 minutes. The structural change analysis was performed using XRD measurement to analyze the crystal structure of the SEs. The XRD results of $x=0$, $x=0.05$, and $x=0.10$ after exposure to an air atmosphere for 10 min and 30 min are shown in Figure 4.10 and 4.11, respectively. After exposure for 10 min, $x=0$ exhibits two additional crystal phases of Li_3PS_4 and LiOH . On the other hand, the crystal structures of $x=0.05$ and $x=0.10$ remain the same as before the exposure, as shown in Figure 4.1. The XRD patterns indicate that the undoped argyrodite ($x=0$) undergoes degradation and becomes unstable after 10 minutes of exposure to air. On the other hand, the doped argyrodite compositions ($x=0.05$, 0.10) remain stable and unaffected by air exposure. Upon extending the exposure time to 30 minutes, all samples, including $x=0$, $x=0.05$, and $x=0.10$, eventually exhibit the degradation phase, characterized by the presence of Li_3PS_4 and LiOH from the XRD result. The hydrolysis mechanism of argyrodite mainly consists of two steps. In the first step, $\text{Li}_6\text{PS}_5\text{Cl}$ degrades into Li_3PS_4 , Li_2S , and LiCl . In the second step, these components react with H_2O , resulting in the formation of Li_3PO_4 , H_2S , LiCl , and LiOH as the final products.[62,63] The XRD pattern result shows the addition of oxygen was successfully increase the stability against air from argyrodite for up to 10 min. The mechanism by which H_2O is converted into H_2S through the penetration of oxygen into the surface of sulfur from the argyrodite can be inhibited by the pre-doped oxygen in $\text{Li}_6\text{PS}_5\text{-}_{2.5x}\text{O}_{2.5x}\text{Cl}$. Hwang et al. reported that the substitution of an oxygen atom at the 4d sites will retain crystal cubic symmetry due to the strong electronegativity from the oxygen atom.[64] Furthermore, PO_3^{3-} was reported to be the most stable structure on the surface.[64] Additionally, Raman spectroscopy and ^{31}P MAS-NMR results confirmed the presence of the PO_3^{3-} structure for $x=0.05$ and $x=0.10$, as explained in the corresponding study. The study further indicated that $x=0.05$ and $x=0.10$ compositions are more stable compared to $x=0$. This conclusion was supported by CV measurements, lithium metal stability tests, and air exposure stability tests.

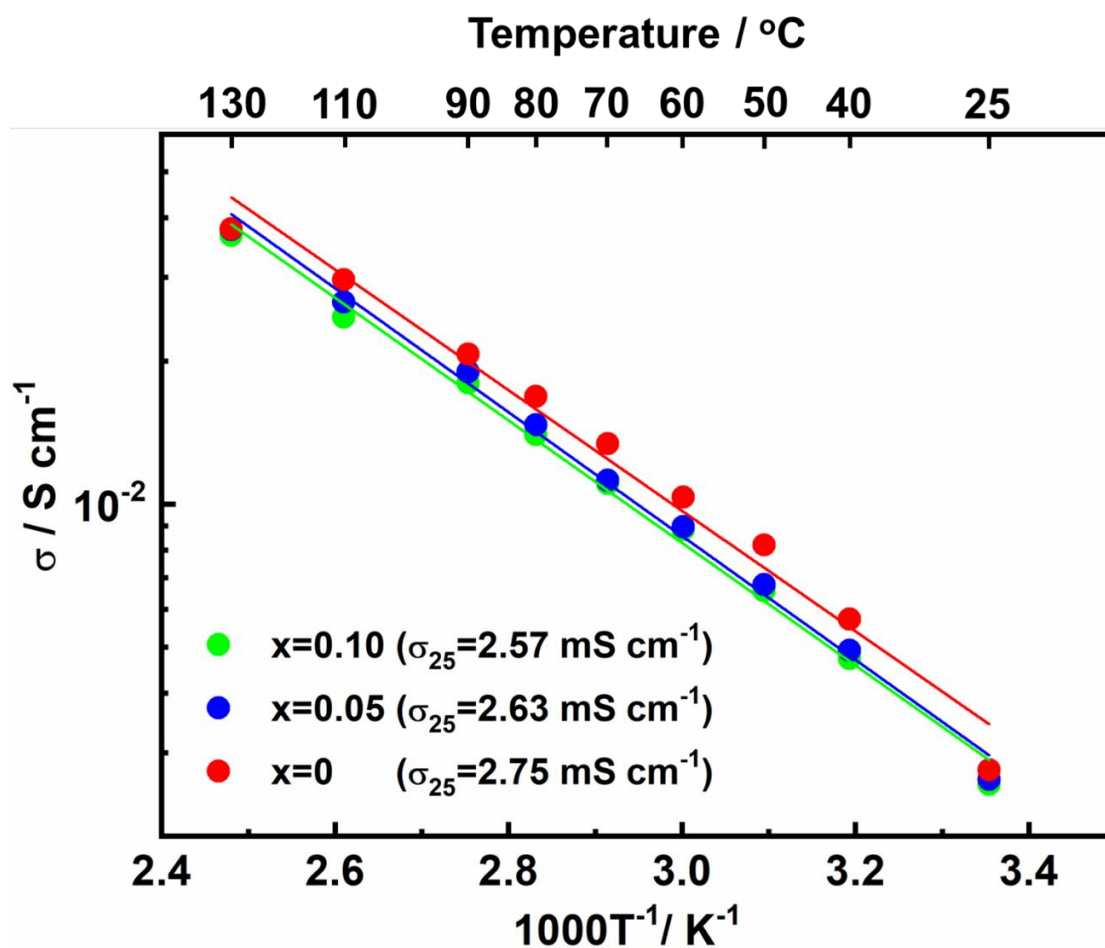


Figure 4.4. Temperature dependence of ionic conductivity from $Li_6PS_{5-2.5x}O_{2.5x}Cl$ SEs prepared by liquid phase synthesis using ACN+PTH as the solvent then heat treated at 550 °C for 10 h.

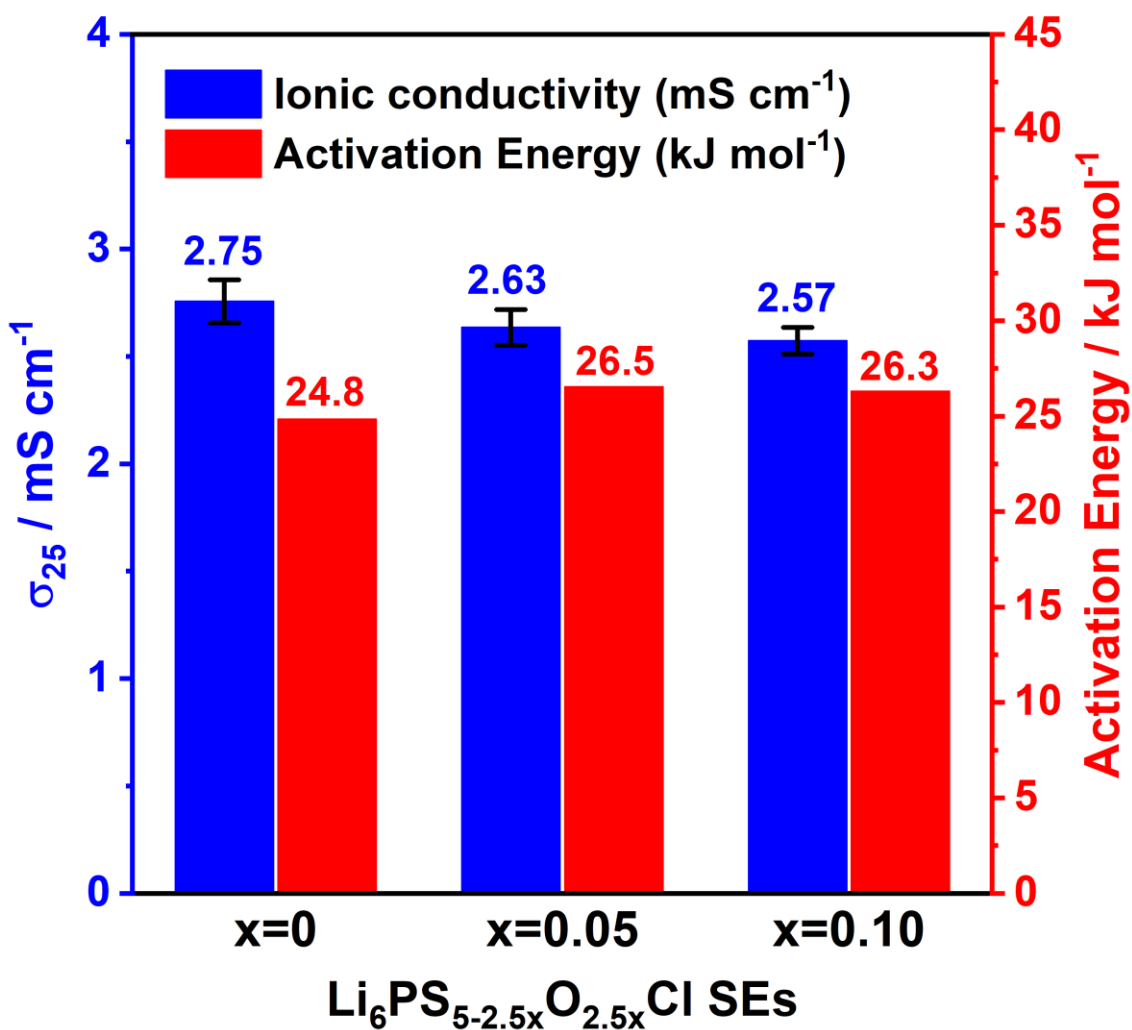


Figure 4.5. Graph of ionic conductivity and activation energy at room temperature of Li₆PS_{5-2.5x}O_{2.5x}Cl SEs prepared by liquid phase synthesis using ACN+PTH as the solvent then heat treated at 550 °C for 10 h correspond to Figure 4.4.

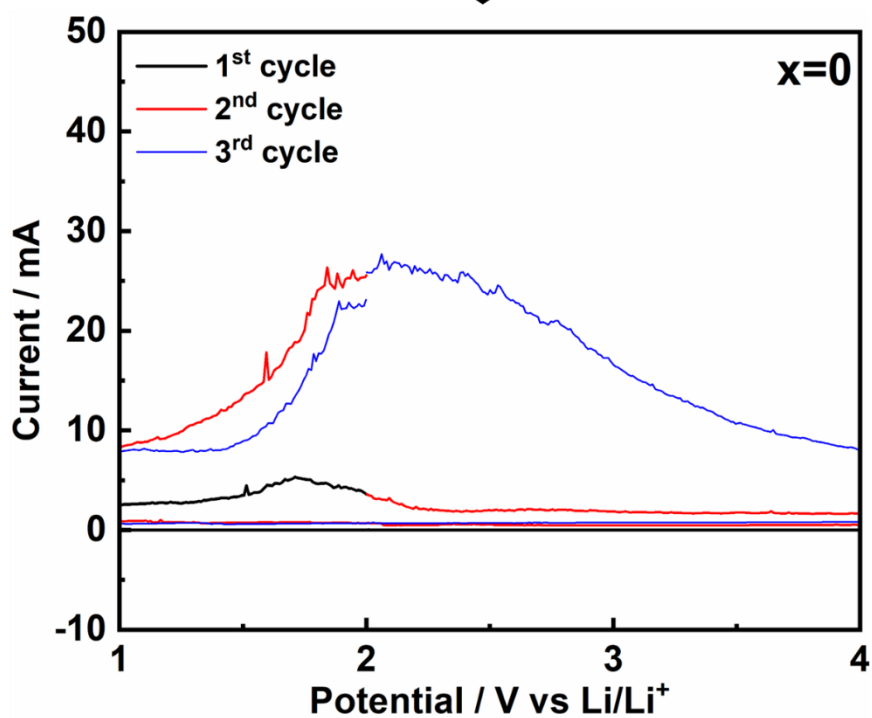
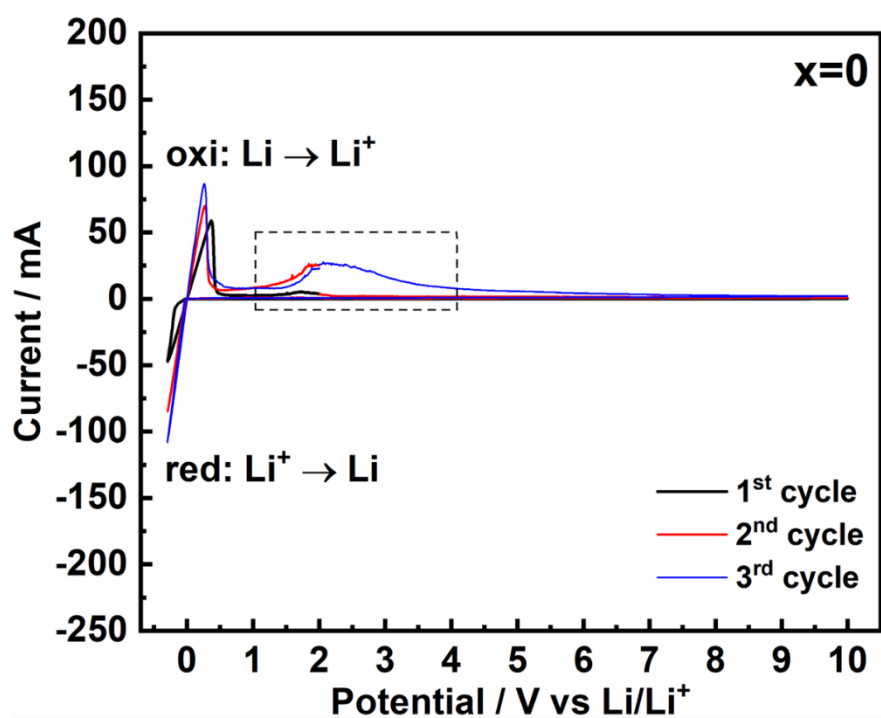


Figure 4.6. Cyclic voltammogram of Li | Li₆PS_{5-2.5x}O_{2.5x}Cl x=0 | SUS at room temperature with a scan rate of 5 mV s⁻¹.

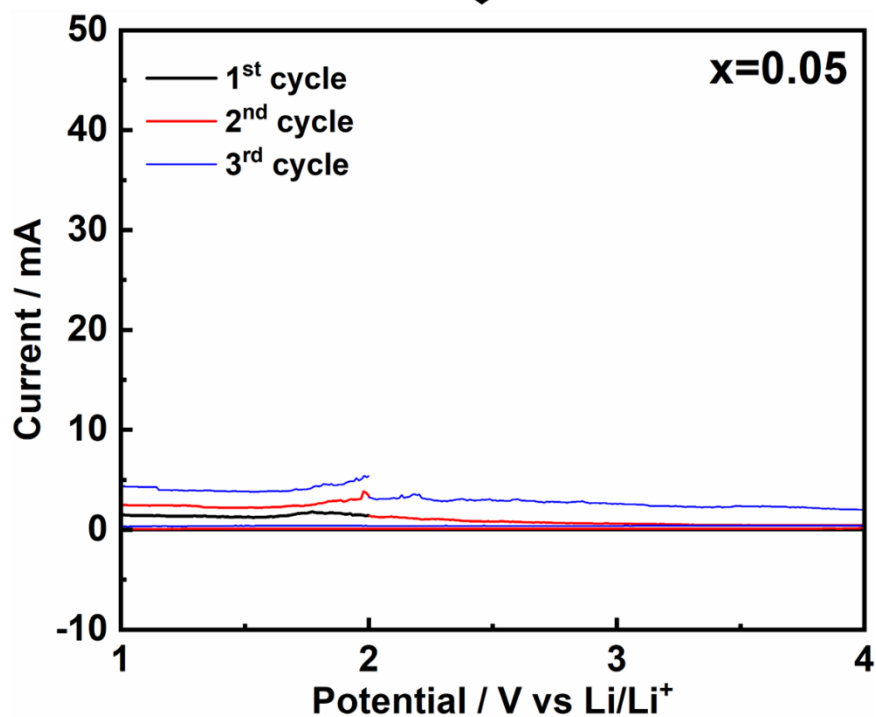
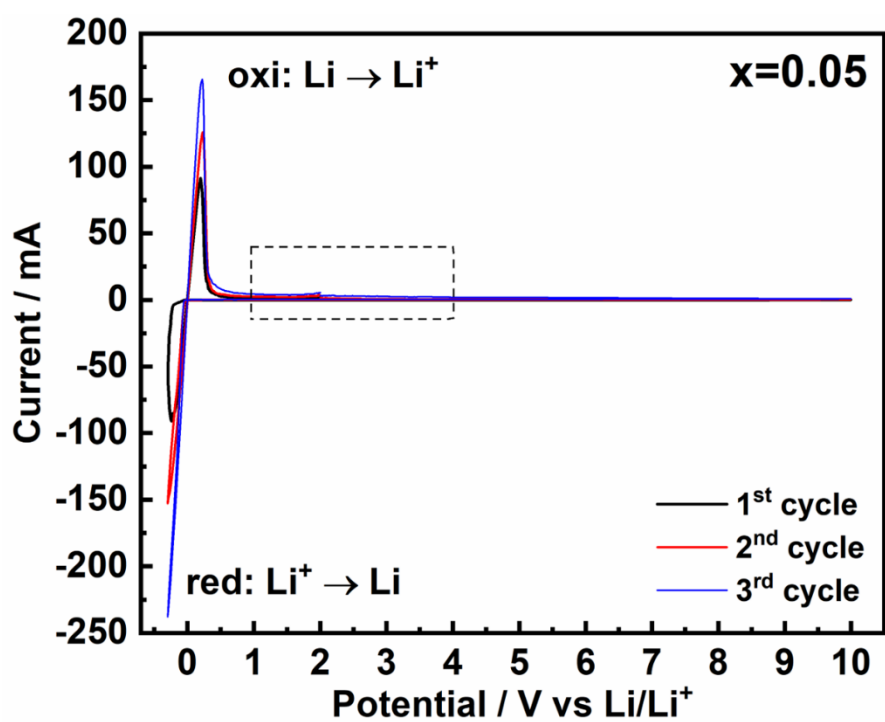


Figure 4.7. Cyclic voltammogram of Li | $\text{Li}_6\text{PS}_{5-2.5x}\text{O}_{2.5x}\text{Cl}$ $x=0.05$ | SUS at room temperature with a scan rate of 5 mV s^{-1} .

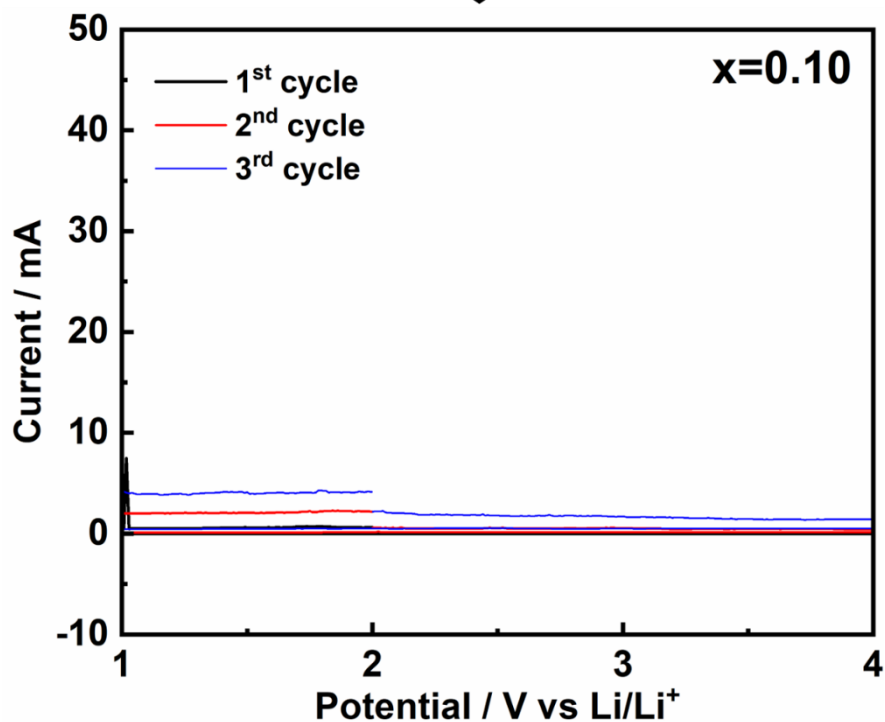
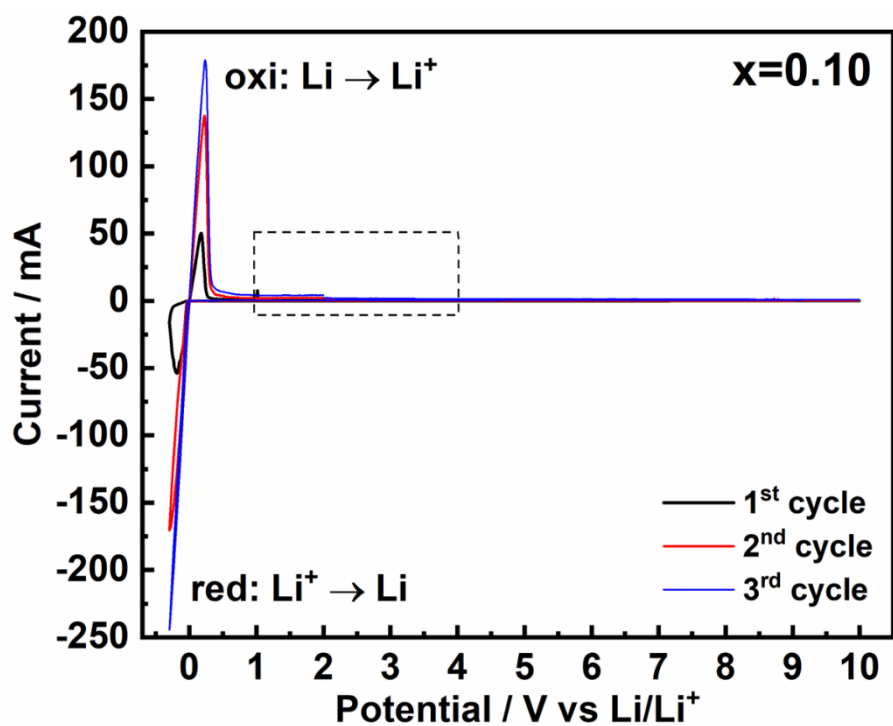


Figure 4.8. Cyclic voltammogram of Li | Li₆PS_{5-2.5x}O_{2.5x}Cl $x=0.10$ | SUS at room temperature with a scan rate of 5 mV s⁻¹.

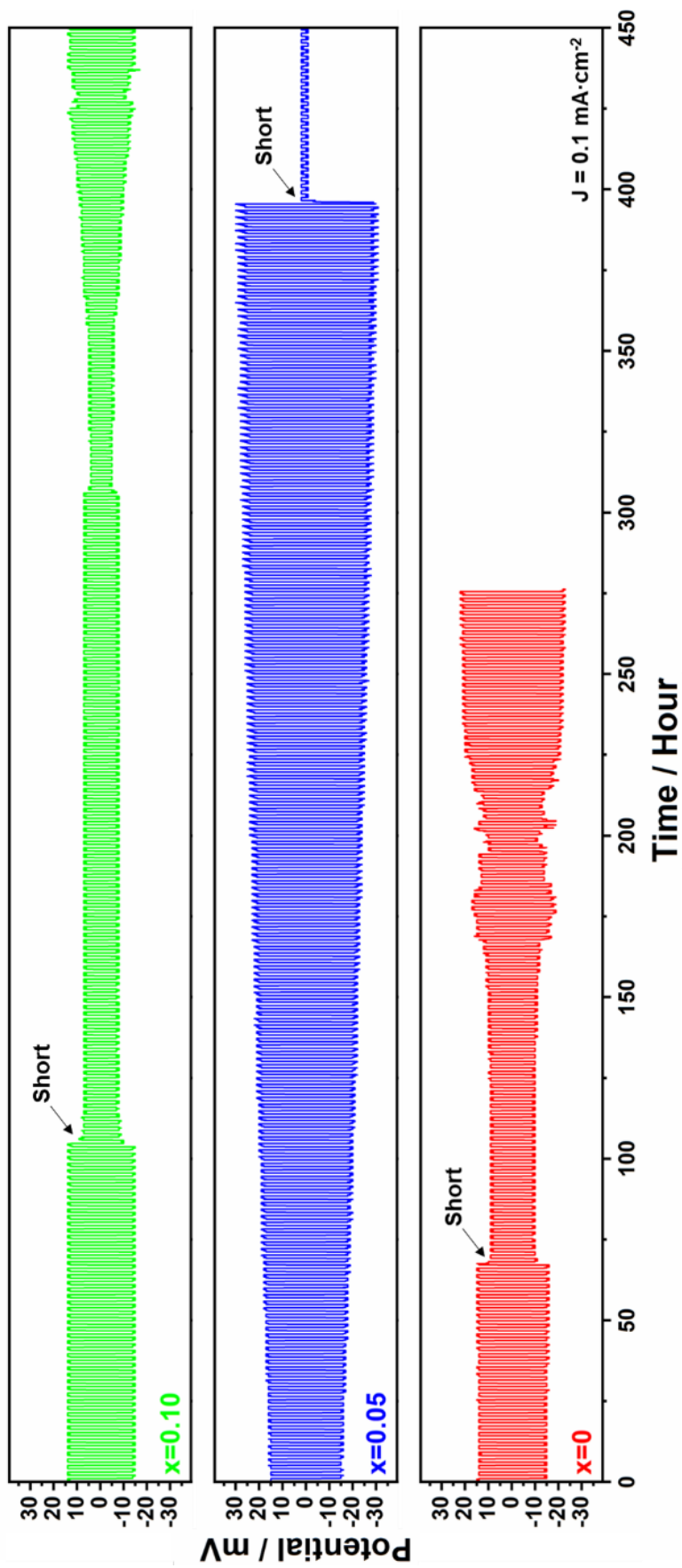


Figure 4.9. Galvanostatic DC polarization of a symmetrical cell from Li | $\text{Li}_6\text{PS}_{5-2.5x}\text{O}_{2.5x}\text{Cl}$ ($x=0, 0.05, 0.10$) | Li at room temperature, with 1 h for each charge and discharge.

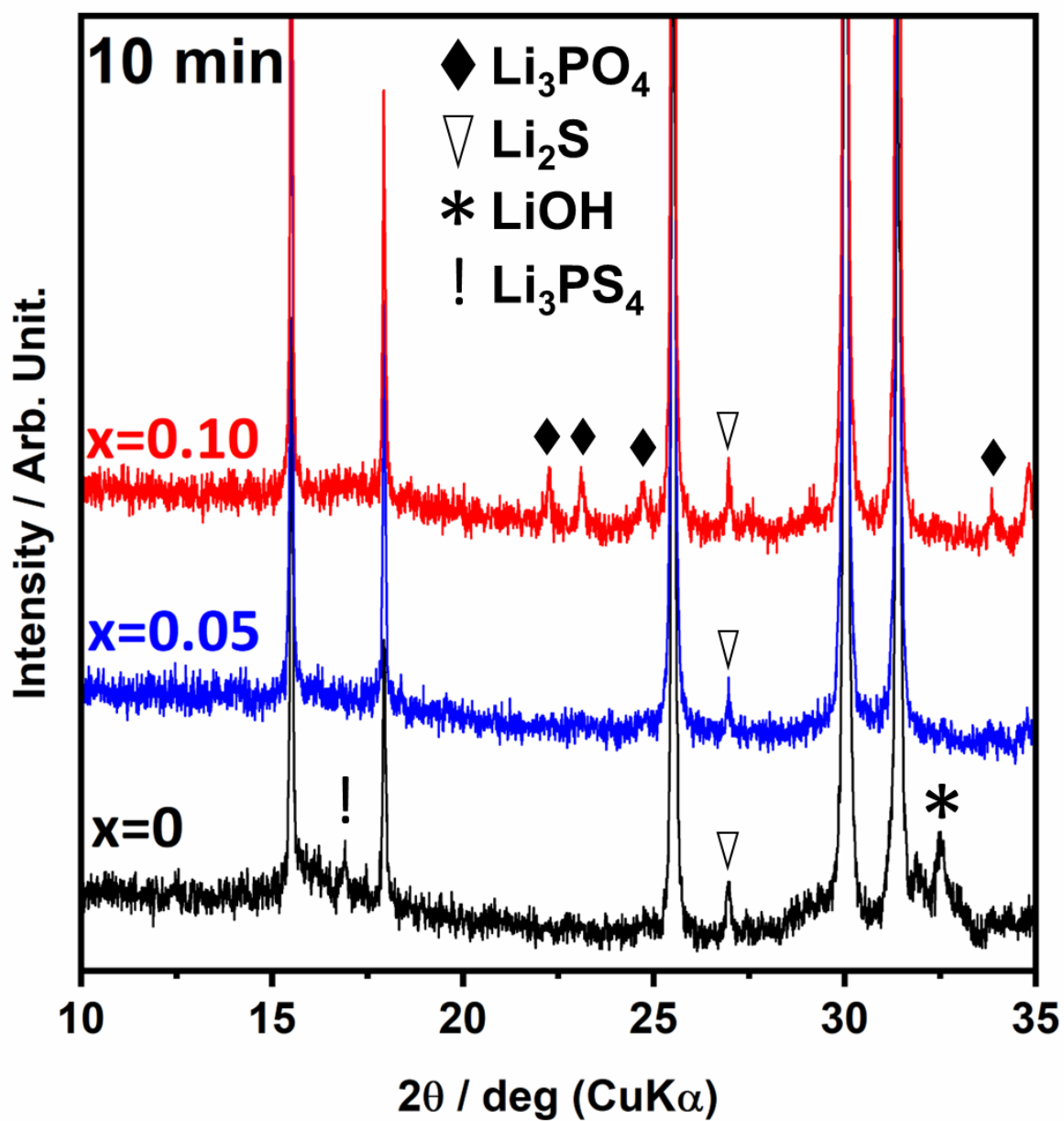


Figure 4.10. XRD patterns of $\text{Li}_6\text{PS}_{5-2.5x}\text{O}_{2.5x}\text{Cl}$ ($x=0, 0.05, 0.10$) after being exposed to air atmosphere for 10 min with the humidity level approximately at 35%.

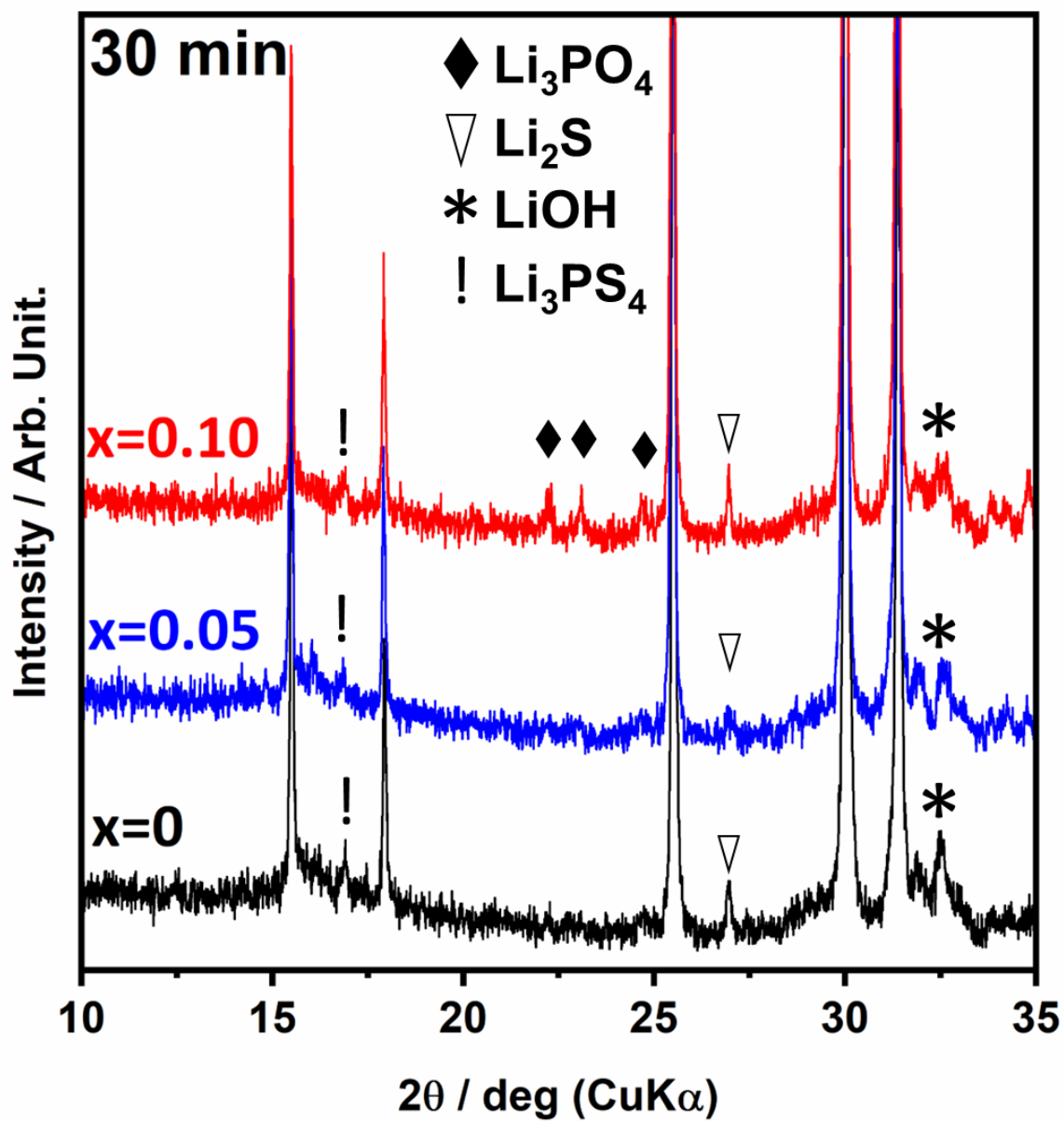


Figure 4.11. XRD patterns of $\text{Li}_6\text{PS}_{5-2.5x}\text{O}_{2.5x}\text{Cl}$ ($x=0, 0.05, 0.10$) after being exposed to air atmosphere for 30 min with the humidity level approximately at 35%.

4.4.3 Battery Cycle Performance of $\text{Li}_6\text{PS}_{5-2.5x}\text{O}_{2.5x}\text{Cl}$

In order to comprehensively assess the compatibility of the SEs, $\text{Li}_6\text{PS}_{5-2.5x}\text{O}_{2.5x}\text{Cl}$ ($x=0, 0.05, 0.10$), with an oxide cathode, all-solid-state batteries were constructed. These batteries were assembled using NCM_{111} as the cathode material and Li-In as the anode material. Figure 4.12 illustrates the performance of $x=0$, where an initial charge and discharge are observed at 220 and 145 mAh g^{-1} , respectively, with a coulombic efficiency of 66%. The charge and discharge capacity then gradually decrease until 100th cycle with the charge capacity at 55 mAh g^{-1} and discharge capacity at 53 mAh g^{-1} with coulombic efficiency at 97%. In comparison to the undoped argyrodite ($x=0$), $x=0.05$ exhibits a slightly lower initial charge capacity of 208 mAh g^{-1} but a higher discharge capacity of 151 mAh g^{-1} that was shown in Figure 4.13. It also demonstrates a higher coulombic efficiency of 73%. Notably, the charge and discharge capacities of $x=0.05$ remain remarkably stable at the 100th cycle, with values of 132 and 129 mAh g^{-1} , respectively, and a coulombic efficiency of 98%. Lastly, the battery cycle performance of $x=0.10$ is depicted in Figure 4.14, showing an initial charge capacity of 208 mAh g^{-1} and discharge capacity of 148 mAh g^{-1} , with a coulombic efficiency of 71%. At the 100th cycle, $x=0.10$ exhibits a lower capacity stability compared to $x=0.05$ but still higher than $x=0$. The charge and discharge capacities are 69 mAh g^{-1} and 67 mAh g^{-1} , respectively, with a coulombic efficiency of 97%. The discrepancy in the initial charge capacity between $x=0$ and $x=0.05$ and $x=0.10$ can be attributed to the superior ionic conductivity of $x=0$. The higher ionic conductivity of $x=0$ enables more efficient transport of lithium ions within the material, leading to a higher initial charge capacity. However, the surface of $x=0$ exhibited instability and degradation directly during cycling, leading to a lower initial discharge capacity compared to $x=0.05$ and $x=0.10$. This observation aligns with the CV result shown in Figure 4.6. The presence of oxygen in the SEs of $\text{Li}_6\text{PS}_{5-2.5x}\text{O}_{2.5x}\text{Cl}$ contributes to the higher stability and compatibility of $x=0.05$ and $x=0.10$ with the oxide cathode material. As a result, $x=0.05$ and $x=0.10$ demonstrate higher initial discharge capacity and capacity stability compared to $x=0$. The comparison of discharge cycle performance and coulombic efficiency was shown in Figure 4.15. The average coulombic efficiencies for $x=0$, $x=0.05$, and $x=0.10$ are 96.3%, 97.4%, and 96.6%, respectively. In terms of average capacity retention, $x=0$ exhibits 99%, $x=0.05$ shows 99.8%, and $x=0.10$

demonstrates 99.2%. Due to the poor surface stability of $x=0$, it exhibits the lowest average coulombic efficiency and lowest capacity retention compared to the other compositions. On the other hand, $x=0.05$ demonstrates the highest average coulombic efficiency and highest capacity retention compared to $x=0$ and $x=0.10$. This improvement can be attributed to the oxygen substitution in the sulfur atom, which enhances the surface stability of the material against the oxide cathode.[39,64] In comparison, $x=0.10$ exhibits an average coulombic efficiency and capacity retention that fall between $x=0.05$ and $x=0$. On one hand, the oxygen substitution in $x=0.10$ increases the surface stability of $\text{Li}_6\text{PS}_{5-2.5x}\text{O}_{2.5x}\text{Cl}$ SEs against the oxide cathode, similar to $x=0.05$. However, the excess oxygen in $x=0.10$ still allows for the formation of Li_3PO_4 oxide side reactions, which can act as a barrier for Li-ion transport. Therefore, $x=0.10$ shows a lower average coulombic efficiency and capacity retention compared to $x=0.05$ but higher than $x=0$.

SEM-EDX measurements were conducted to analyze the elemental composition of $\text{NMC}_{111} + \text{Li}_6\text{PS}_{5-2.5x}\text{O}_{2.5x}\text{Cl}$ ($x=0, 0.05, 0.10$) + AB composites. Figure 4.16 displays the SEM-EDX images of $x=0$, revealing a homogeneous distribution of P, S, and Cl elements, which can be attributed to $\text{Li}_6\text{PS}_5\text{Cl}$. However, O was only observed in conjunction with Ni, Mn, and Co, which are elements present in NMC_{111} . This indicates that no oxygen was detected in the argyrodite phase. Figure 4.17 displays the SEM-EDX images of $x=0.05$. In this observed sample, a similar homogeneous distribution of P, S, and Cl elements is observed, characteristic of argyrodite SEs. However, in addition to the presence of oxygen in conjunction with Ni, Mn, and Cl elements belonging to NMC_{111} , a small amount of oxygen is also observed on the surface of the argyrodite phase, indicating the presence of oxygen-doped argyrodite. Figure 4.18 displays the SEM-EDX images of $x=0.10$. In this sample, a similar homogeneous distribution of P, S, and Cl elements characteristic of argyrodite is observed. A high concentration of oxygen is also found in conjunction with Ni, Mn, and Co elements from NMC_{111} . Although a small amount of oxygen is observed on the surface of the argyrodite phase, it is challenging to observe oxygen more extensively on the argyrodite surface. This could be attributed to the possibility that oxygen from $x=0.10$ has partially separated from the argyrodite, resulting in the formation of Li_3PO_4 impurity. Table 4.1 presents the calculation of the molecular weights for each element in the $\text{Li}_6\text{PS}_{5-2.5x}\text{O}_{2.5x}\text{Cl}$ ($x=0, 0.05, 0.10$) composites. Theoretical molecular weight ratios of Ni, Mn, and Co (NMC) with oxygen from NMC_{111}

are expected to be 1:2. In the case of $x=0$, the NMC:O ratio is found to be 1:1.77, which is similar to the theoretical ratio of NMC:O from NMC₁₁₁. This further confirms that $x=0$ does not contain oxygen. Furthermore, the NMC:O ratio from $x=0.05$ is calculated to be 1:3.05, indicating the presence of oxygen in the Li₆PS_{5-2.5x}O_{2.5x}Cl SEs with $x=0.05$. This ratio suggests that oxygen is indeed incorporated into the SEs through P₂O₅ doping, confirming the presence of oxygen in $x=0.05$ SEs. On the other hand, for $x=0.10$, the NMC:O ratio is calculated to be 1:3.27. Although the oxygen content is slightly higher than in $x=0.05$, it is still lower than expected. This discrepancy could be attributed to the fact that oxygen from $x=0.10$ partially separates and forms Li₃PO₄ oxidation, resulting in a lower observed oxygen content in the SEs.

Figure 4.19 presents a comparison of the rate performance, ranging from 0.1C to 2C, of Li-In | Li₆PS_{5-2.5x}O_{2.5x}Cl ($x=0, 0.05, x=0.10$) | NMC₁₁₁ at room temperature. For $x=0$, the discharge capacity at 0.1C, 0.2C, 0.4C, 0.5C, 1C, and 2C are measured at 145, 109, 73, 61, 21, and 2.6 mAh g⁻¹, respectively. After that, the capacity reverses back at 0.5C to 58 mAh g⁻¹ with a capacity retention of 99.5% at the 35th cycle. The low discharge capacity observed for $x=0$ at the 2C rate performance can be attributed to the degradation of the SEI on the surface of $x=0$ from the first cycle onwards. This degradation negatively affects the ion transport and electrochemical performance of the system, resulting in a significantly reduced capacity at higher discharge rates. Moving on to the doped argyrodite at $x=0.05$, the discharge capacities at different rates were measured as follows: 151 mAh g⁻¹ at 0.1C, 140 mAh g⁻¹ at 0.2C, 130 mAh g⁻¹ at 0.4C, 126 mAh g⁻¹ at 0.5C, 108 mAh g⁻¹ at 1C, and 80 mAh g⁻¹ at 2C. Remarkably, the discharge capacity remained high and reversible when cycled back to 0.5C, reaching 125 mAh g⁻¹ with a capacity retention of 99.9% at the 35th cycle. This demonstrates the excellent rate performance and cycling stability of the doped argyrodite at $x=0.05$. In comparison, for the doped argyrodite at $x=0.10$, the discharge capacities at various rates were observed as follows: 148 mAh g⁻¹ at 0.1C, 124 mAh g⁻¹ at 0.2C, 110 mAh g⁻¹ at 0.4C, 103 mAh g⁻¹ at 0.5C, 76 mAh g⁻¹ at 1C, and 38 mAh g⁻¹ at 2C. After cycling back to 0.5C, the discharge capacity recovered to 102.8 mAh g⁻¹, demonstrating a capacity retention of 99.8% at the 35th cycle. The presence of Li₃PO₄ oxide in $x=0.10$ results in a lower discharge capacity compared to $x=0.05$. However, despite this decrease, the performance of $x=0.10$ is still better than that of the undoped argyrodite ($x=0$). Overall, the oxygen-doped argyrodite exhibits

excellent cycle and rate performance with high reversibility. This can be attributed to the electrochemically stable surface provided by the oxysulfide compound present in the $\text{Li}_6\text{PS}_{5-2.5x}\text{O}_{2.5x}\text{Cl}$ SEs. The incorporation of oxygen into sulfides helps to suppress the chemical diffusion of the cathode/electrolyte, thereby reducing side reactions between the oxide cathode and SEI. This improved stability at the interface contributes to the enhanced performance and durability of the oxygen-doped argyrodite SEs in all-solid-state batteries. We believe that this study will significantly expand the application of oxysulfide SEs, allowing them to be used more freely with both lithium metal and oxide electrodes. These findings have the potential to pave the way for their practical implementation on an industrial scale.

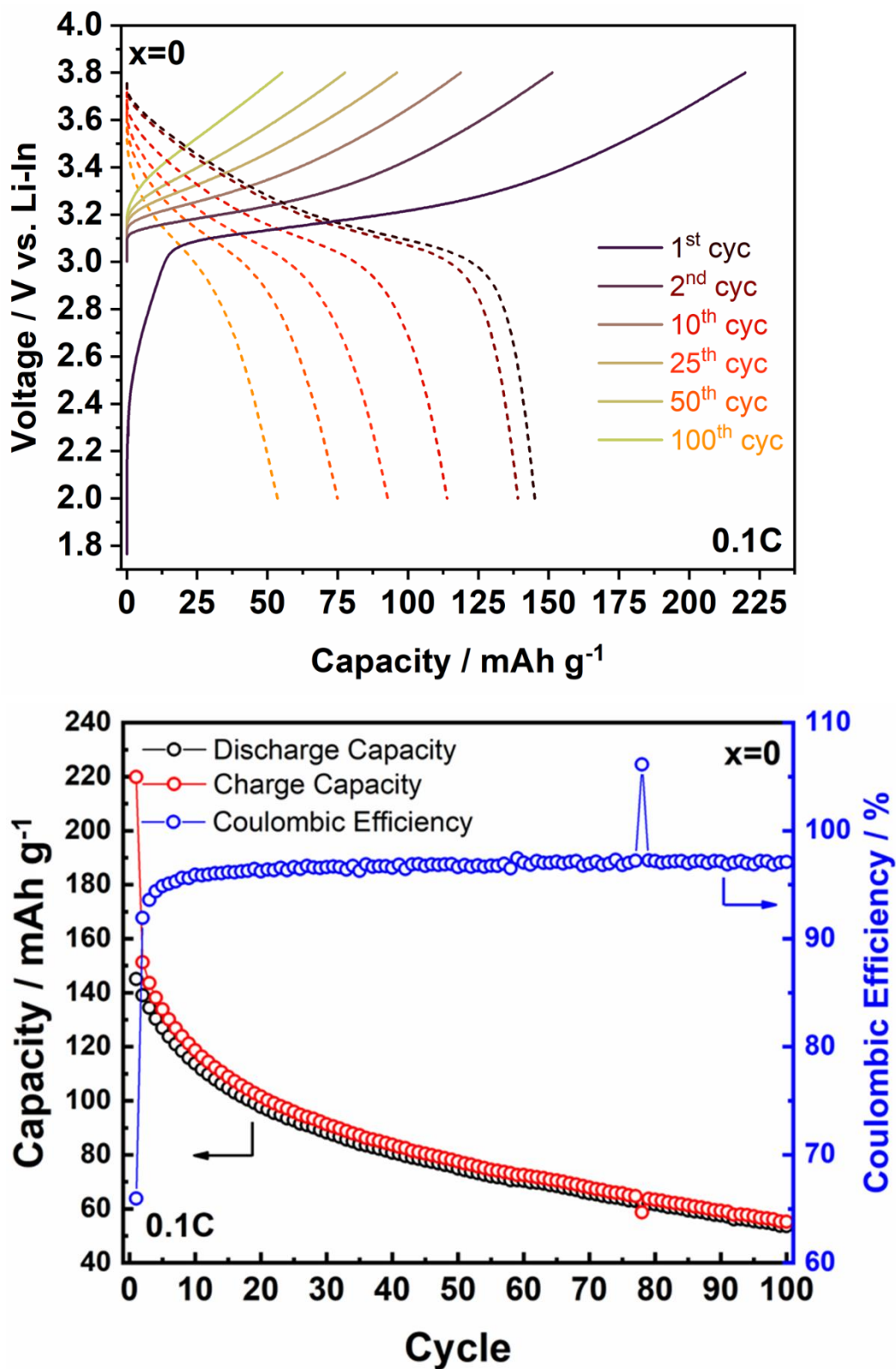


Figure 4.12. Charge and discharge capacity curves for Li-In | Li₆PS_{5-2.5x}O_{2.5x}Cl (x=0) | NMC₁₁₁ with at room temperature with 0.1C rate.

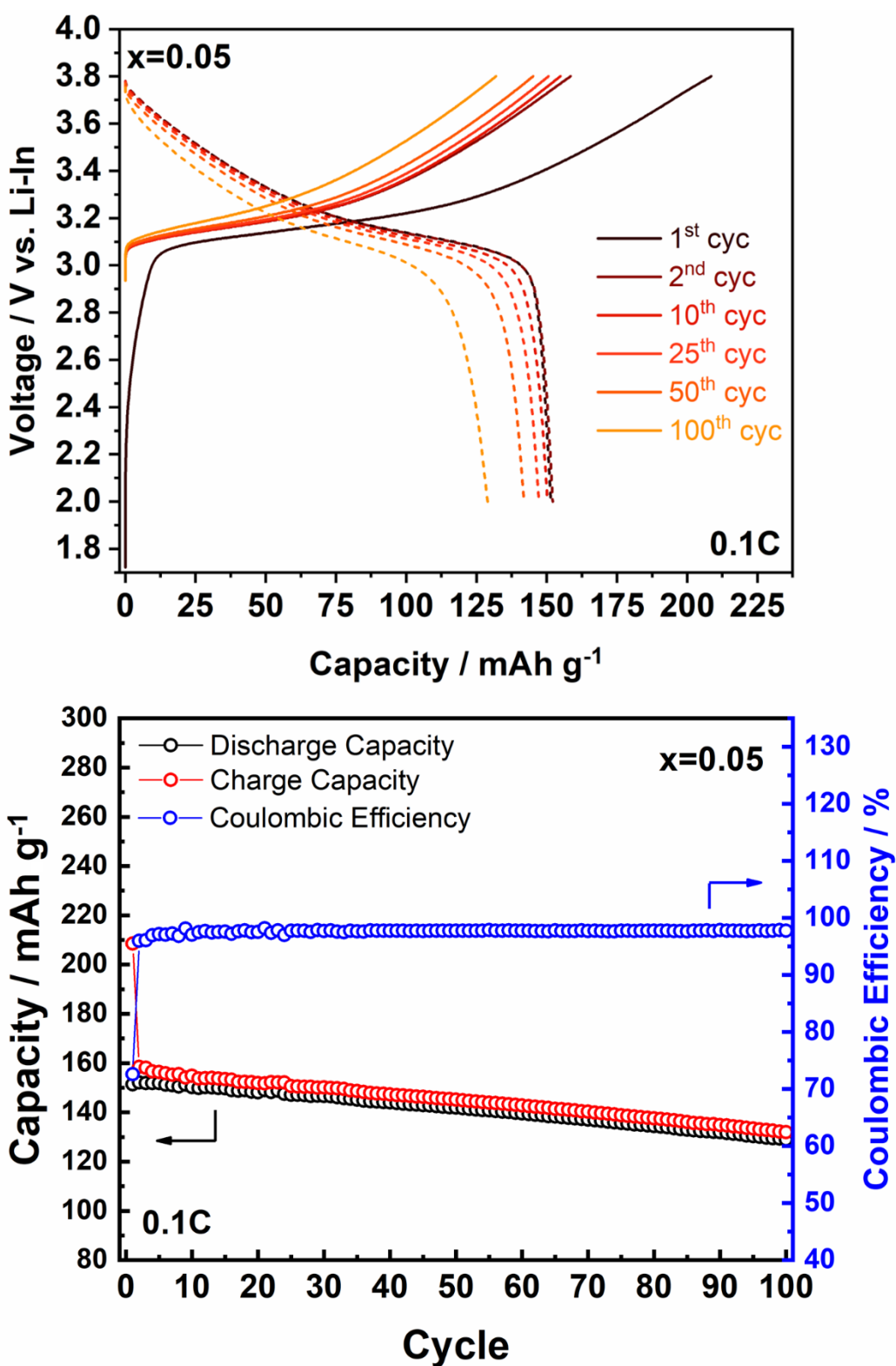


Figure 4.13. Charge and discharge capacity curves for Li-In | Li₆PS_{5-2.5x}O_{2.5x}Cl (x=0.05) | NMC₁₁₁ with at room temperature with 0.1C rate.

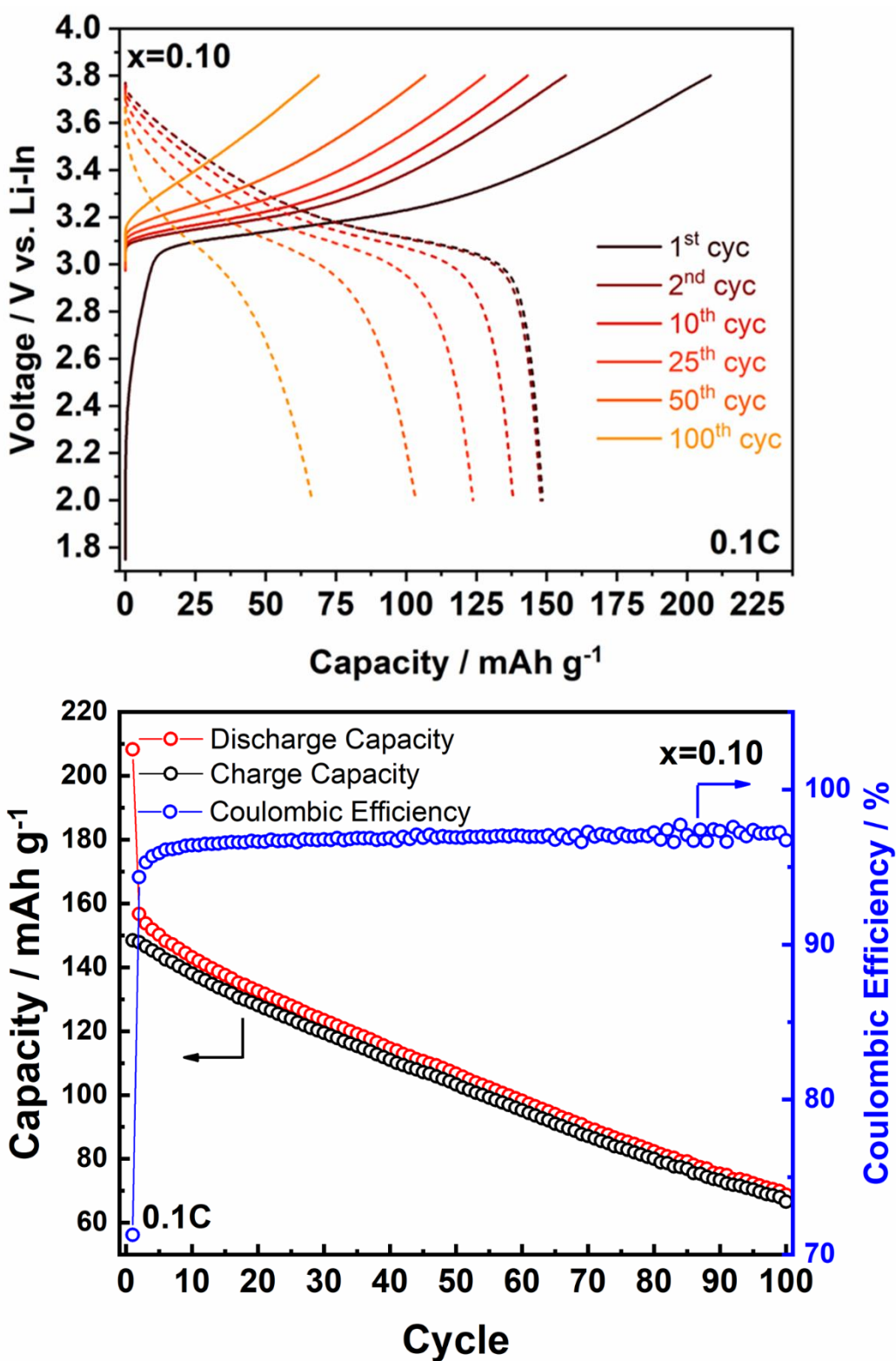


Figure 4.14. Charge and discharge capacity curves for Li-In | Li₆PS_{5-2.5x}O_{2.5x}Cl (x=0.10) | NMC₁₁₁ with at room temperature with 0.1C rate.

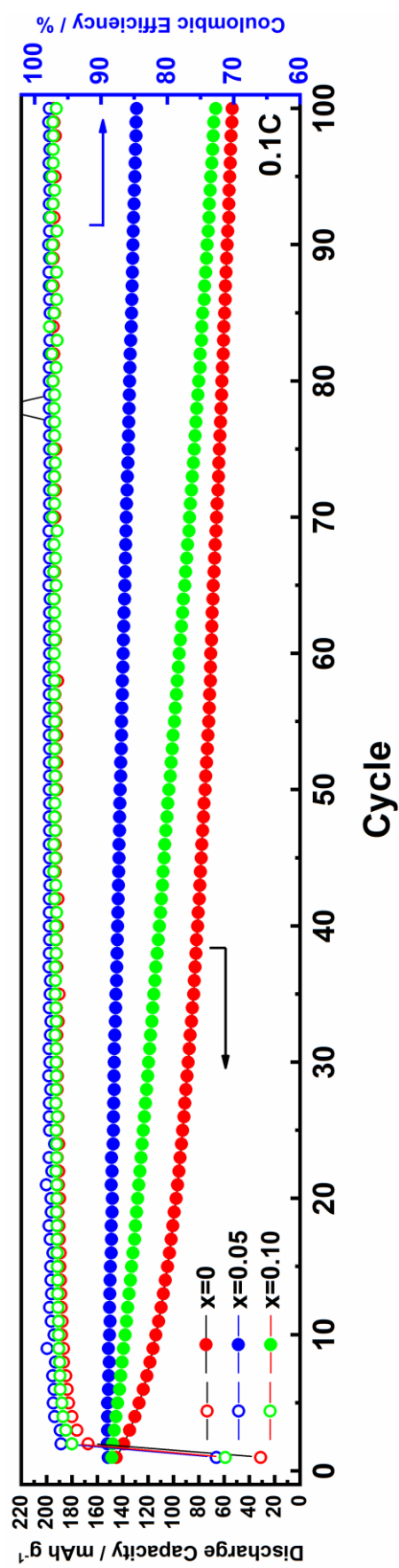


Figure 4.15. Discharge capacity and coulombic efficiency curves for Li-In | Li₆PS_{5-2.5x}O_{2.5x}Cl (x=0, 0.05, 0.10) | NMC₁₁₁ with at room temperature with 0.1C rate.

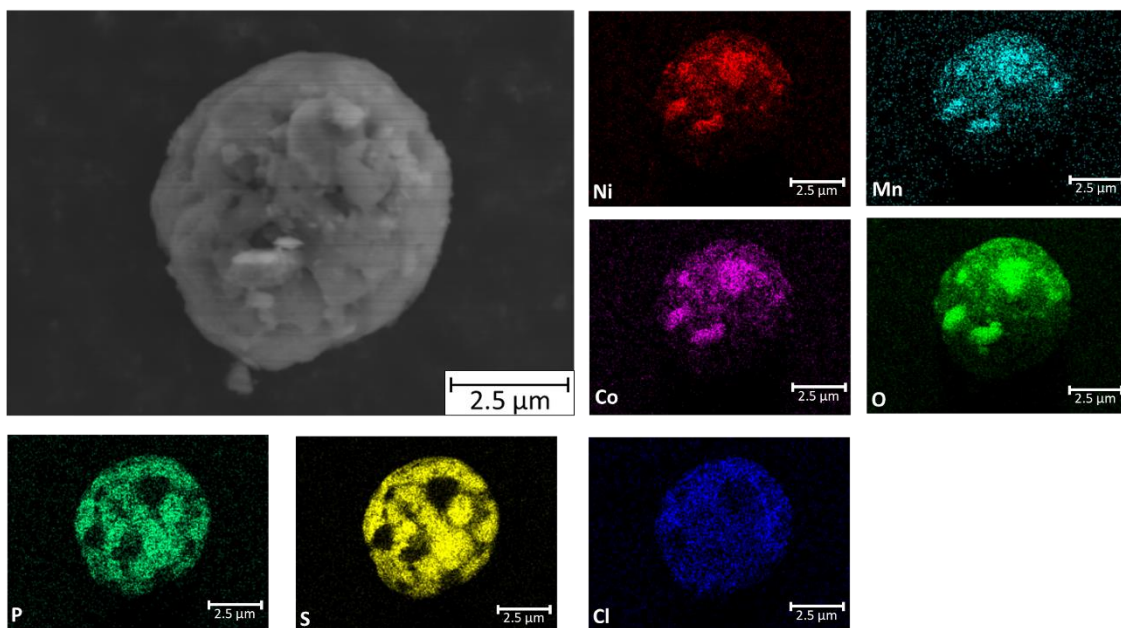


Figure 4.16. SEM–EDX mappings from the $\text{Li}_6\text{PS}_5\text{Cl}$ ($x=0$) + NMC_{111} + AB composite of Ni, Mn, Co, O, P, S, and Cl elements for the selected regions.

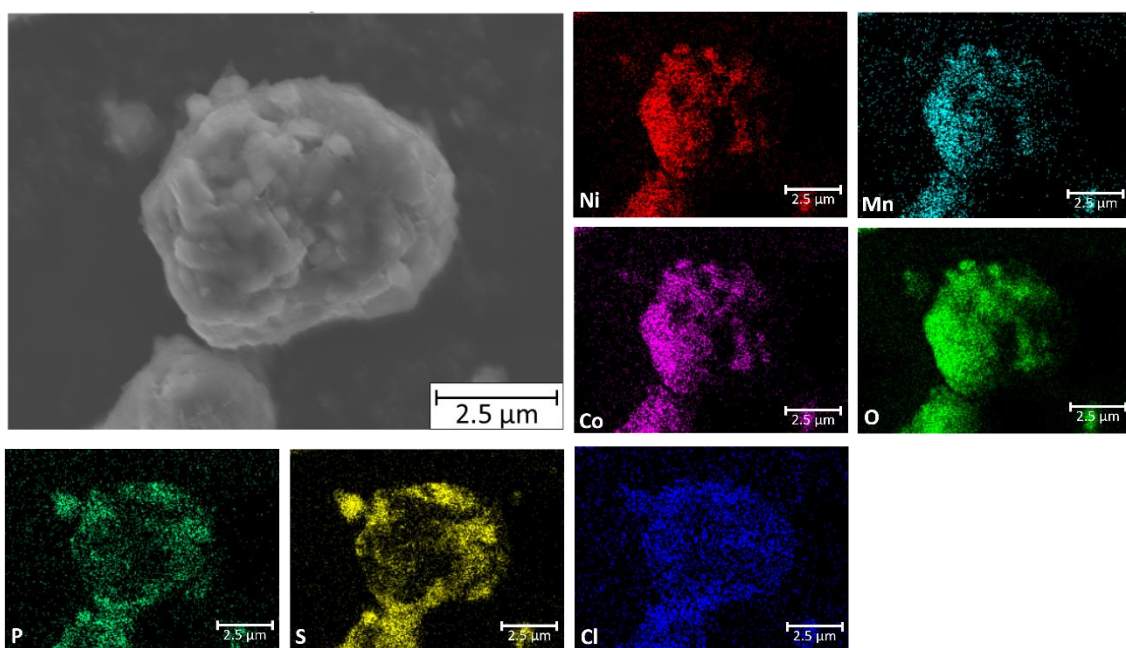


Figure 4.17. SEM – EDX mappings from the $\text{Li}_6\text{PS}_5\text{Cl}$ ($x=0.05$) + NMC_{111} + AB composite of Ni, Mn, Co, O, P, S, and Cl elements for the selected regions.

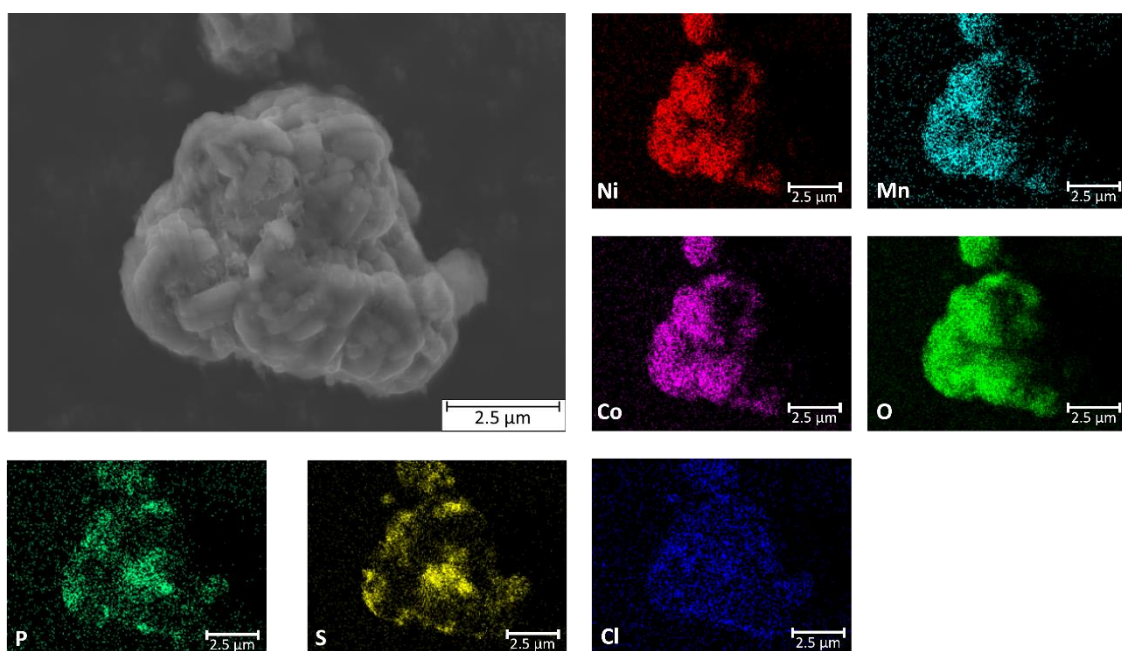


Figure 4.18. SEM–EDX mappings from the $\text{Li}_6\text{PS}_5\text{Cl}$ ($x=0.10$) + NMC_{111} + AB composite of Ni, Mn, Co, O, P, S, and Cl elements for the selected regions.

Table 4.1. Atomic weight ratio corresponding of $\text{Li}_6\text{PS}_{5-2.5x}\text{O}_{2.5x}\text{Cl}$ ($x=0, 0.05, 0.10$) + NMC111 + AB composites corresponding to SEM-EDX measurements from Figure 4.16, 4.17, and 4.18.

Element	Atomic Weight (%)		
	x=0	x=0.05	x=0.10
S	32.1	23.94	6.31
O	27.39	48.69	56.09
Cl	13.48	3.47	1.46
P	10.19	6.34	1.69
Co	5.45	5.29	5.865
Mn	5.1	5.01	5.34
Ni	4.89	5.68	5.92
Total NMC	15.44	15.98	17.125
NMC:O Ratio	1 : 1.77	1 : 3.05	1 : 3.27

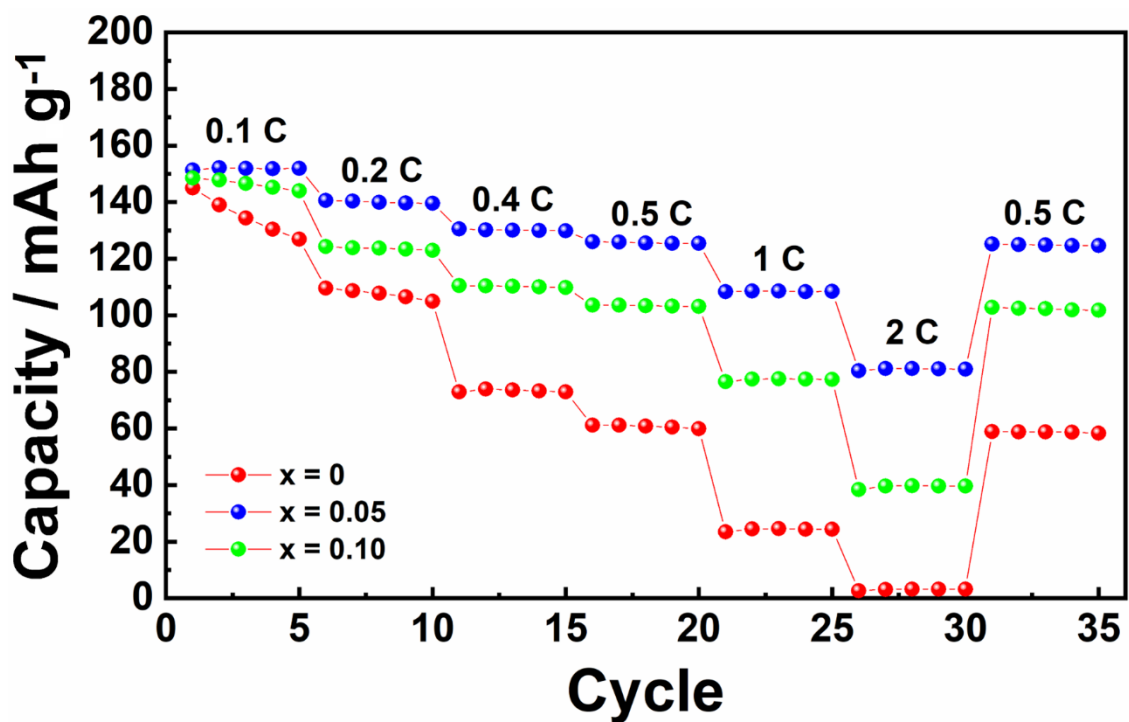


Figure 4.19. Cycle and rate performance of Li-In | Li₆PS_{5-2.5x}O_{2.5x}Cl (x=0, 0.05, x=0.10) | NMC₁₁₁ at room temperature.

4.5 Conclusions

In summary, this study demonstrates the promising potential of oxygen-doped argyrodite solid electrolytes (SEs) with delicate electrochemical performance. The successful incorporation of oxygen into the argyrodite SEs was achieved through the implementation of a liquid phase synthesis method, which holds promise for efficient mass production. $\text{Li}_6\text{PS}_{4.875}\text{O}_{0.125}\text{Cl}$, or $x=0.05$, exhibits excellent and remarkable electrochemical stability when paired with a lithium metal anode, NMC_{111} oxide cathode, and exposure to air. On the other hand, $\text{Li}_6\text{PS}_{4.75}\text{O}_{0.25}\text{Cl}$, or $x=0.10$, shows improved stability compared to $x=0$, but its performance is compromised by the occurrence of a Li_3PO_4 side reaction. The substitution of oxygen in argyrodite SEs contributes to the enhanced stability of the system by incorporating the POS_3^{3-} anion, which helps inhibit chemical reactions at the surface of the SEs. This improvement in stability was further confirmed through measurements using 31P MAS-NMR and Raman spectroscopy, which provided evidence of the presence of POS_3^{3-} in the SEs. Overall, the SEs with $x=0.05$ ($\text{Li}_6\text{PS}_{4.875}\text{O}_{0.125}\text{Cl}$) demonstrate remarkable stability, high capacity retention, and excellent reversibility. The system achieved an impressive capacity retention of 99.8%, indicating minimal capacity loss over cycling. In general, the addition of P_2O_5 to $\text{Li}_6\text{PS}_5\text{Cl}$ can enhance the overall electrochemical stability of the solid electrolyte, particularly on its surface. This improvement can be attributed to the formation of oxysulfide compounds, specifically the POS_3^{3-} unit. The presence of POS_3^{3-} contributes to the enhancement of the electrochemical interface and helps to mitigate undesirable reactions between the solid electrolyte and the electrode material, thereby improving the overall stability of the solid electrolyte. By incorporating P_2O_5 into $\text{Li}_6\text{PS}_5\text{Cl}$, the solid electrolyte exhibits improved performance and increased resistance to degradation, making it a promising candidate for various energy storage applications. This highlights the exceptional performance and long-term stability of the SEs with this oxygen doping level.

References

- [1] C. Bussar, P. Stöcker, Z. Cai, L. Moraes Jr., D. Magnor, P. Wiernes, N. van Bracht, A. Moser, D.U. Sauer, Large-scale integration of renewable energies and impact on storage demand in a European renewable power system of 2050—Sensitivity study, *J Energy Storage*. **2016**, *6*, pp. 1–10.
- [2] J.B. Goodenough, K.-S. Park, The Li-Ion Rechargeable Battery: A Perspective, *J Am Chem Soc*. **2013**, *135*, pp. 1167–1176.
- [3] R. Schmich, R. Wagner, G. Hörpel, T. Placke, M. Winter, Performance and cost of materials for lithium-based rechargeable automotive batteries, *Nat Energy*. **2018**, *3*, pp. 267–278.
- [4] P. Oh, H. Lee, S. Park, H. Cha, J. Kim, J. Cho, Improvements to the Overpotential of All-Solid-State Lithium-Ion Batteries during the Past Ten Years, *Adv Energy Mater*. **2020**, *10*, 2000904.
- [5] T. Ohnishi, K. Mitsuishi, K. Nishio, K. Takada, Epitaxy of $\text{Li}_{3x}\text{La}_{2/3-x}\text{TiO}_3$ Films and the Influence of La Ordering on Li-Ion Conduction, *Chemistry of Materials*. **2015**, *27*, pp. 1233–1241.
- [6] P. Canepa, J.A. Dawson, G. Sai Gautam, J.M. Statham, S.C. Parker, M.S. Islam, Particle Morphology and Lithium Segregation to Surfaces of the $\text{Li}_7\text{La}_3\text{Zr}_2\text{O}_{12}$ Solid Electrolyte, *Chemistry of Materials*. **2018**, *30*, pp. 3019–3027.
- [7] S. Li, Z. Huang, Y. Xiao, C. Sun, Chlorine-doped $\text{Li}_{1.3}\text{Al}_{0.3}\text{Ti}_{1.7}(\text{PO}_4)_3$ as an electrolyte for solid lithium metal batteries, *Mater Chem Front*. **2021**, *5*, pp. 5336–5343.
- [8] Y. Lu, X. Meng, J.A. Alonso, M.T. Fernández-Díaz, C. Sun, Effects of Fluorine Doping on Structural and Electrochemical Properties of $\text{Li}_{6.25}\text{Ga}_{0.25}\text{La}_3\text{Zr}_2\text{O}_{12}$ as Electrolytes for Solid-State Lithium Batteries, *ACS Appl Mater Interfaces*. **2019**, *11*, pp. 2042–2049.
- [9] H. Liu, Y. Liang, C. Wang, D. Li, X. Yan, C. Nan, L. Fan, Priority and Prospect of Sulfide-Based Solid-Electrolyte Membrane, *Advanced Materials*. **2022**, *2206013*.
- [10] K. Hikima, M. Totani, S. Obokata, H. Muto, A. Matsuda, Mechanical Properties of Sulfide-Type Solid Electrolytes Analyzed by Indentation Methods, *ACS Appl Energy Mater*. **2022**, *5*, pp. 2349–2355.

- [11] Y. Kato, S. Hori, T. Saito, K. Suzuki, M. Hirayama, A. Mitsui, M. Yonemura, H. Iba, R. Kanno, High-power all-solid-state batteries using sulfide superionic conductors, *Nat Energy*. **2016**, *1*, 16030.
- [12] M. V. Reddy, C.M. Julien, A. Mauger, K. Zaghbi, Sulfide and Oxide Inorganic Solid Electrolytes for All-Solid-State Li Batteries: A Review, *Nanomaterials*. **2020**, *10*, 1606.
- [13] N. Kamaya, K. Homma, Y. Yamakawa, M. Hirayama, R. Kanno, M. Yonemura, T. Kamiyama, Y. Kato, S. Hama, K. Kawamoto, A. Mitsui, A lithium superionic conductor, *Nat Mater*. **2011**, *10*, pp. 682–686.
- [14] D.H.S. Tan, E.A. Wu, H. Nguyen, Z. Chen, M.A.T. Marple, J.-M. Doux, X. Wang, H. Yang, A. Banerjee, Y.S. Meng, Elucidating Reversible Electrochemical Redox of $\text{Li}_6\text{PS}_5\text{Cl}$ Solid Electrolyte, *ACS Energy Lett*. **2019**, *4*, pp. 2418–2427.
- [15] J. Zhang, C. Zheng, L. Li, Y. Xia, H. Huang, Y. Gan, C. Liang, X. He, X. Tao, W. Zhang, Unraveling the Intra and Intercycle Interfacial Evolution of $\text{Li}_6\text{PS}_5\text{Cl}$ -Based All-Solid-State Lithium Batteries, *Adv Energy Mater*. **2020**, *10*, 1903311.
- [16] J.C. Bachman, S. Muy, A. Grimaud, H.-H. Chang, N. Pour, S.F. Lux, O. Paschos, F. Maglia, S. Lupart, P. Lamp, L. Giordano, Y. Shao-Horn, Inorganic Solid-State Electrolytes for Lithium Batteries: Mechanisms and Properties Governing Ion Conduction, *Chem Rev*. **2016**, *116*, pp. 140–162.
- [17] C. Yu, S. Ganapathy, E.R.H. van Eck, H. Wang, S. Basak, Z. Li, M. Wagemaker, Accessing the bottleneck in all-solid state batteries, lithium-ion transport over the solid-electrolyte-electrode interface, *Nat Commun*. **2017**, *8*, 1086.
- [18] A. Sakuda, A. Yamauchi, S. Yubuchi, N. Kitamura, Y. Idemoto, A. Hayashi, M. Tatsumisago, Mechanochemically Prepared $\text{Li}_2\text{S}-\text{P}_2\text{S}_5-\text{LiBH}_4$ Solid Electrolytes with an Argyrodite Structure, *ACS Omega*. **2018**, *3*, pp. 5453–5458.
- [19] A.R. Stamminger, B. Ziebarth, M. Mrovec, T. Hammerschmidt, R. Drautz, Ionic Conductivity and Its Dependence on Structural Disorder in Halogenated Argyrodites $\text{Li}_6\text{PS}_5\text{X}$ ($\text{X} = \text{Br}, \text{Cl}, \text{I}$), *Chemistry of Materials*. **2019**, *31*, pp. 8673–8678.
- [20] H.-J. Deiseroth, S.-T. Kong, H. Eckert, J. Vannahme, C. Reiner, T. Zaiß, M. Schlosser, $\text{Li}_6\text{PS}_5\text{X}$: A Class of Crystalline Li-Rich Solids With an Unusually High Li^+ Mobility, *Angewandte Chemie International Edition*. **2008**, *47*, pp. 755–758.

- [21] R.P. Rao, S. Adams, Studies of lithium argyrodite solid electrolytes for all-solid-state batteries, *Physica Status Solidi (a)*. **2011**, *208*, pp. 1804–1807.
- [22] P.R. Rayavarapu, N. Sharma, V.K. Peterson, S. Adams, Variation in structure and Li⁺-ion migration in argyrodite-type Li₆PS₅X (X = Cl, Br, I) solid electrolytes, *Journal of Solid State Electrochemistry*. **2012**, *16*, pp. 1807–1813.
- [23] M.A. Kraft, S.P. Culver, M. Calderon, F. Böcher, T. Krauskopf, A. Senyshyn, C. Dietrich, A. Zevalkink, J. Janek, W.G. Zeier, Influence of Lattice Polarizability on the Ionic Conductivity in the Lithium Superionic Argyrodites Li₆PS₅X (X = Cl, Br, I), *J Am Chem Soc*. **2017**, *139*, pp. 10909–10918.
- [24] Z. Ma, H.-G. Xue, S.-P. Guo, Recent achievements on sulfide-type solid electrolytes: crystal structures and electrochemical performance, *J Mater Sci*. **2018**, *53*, pp. 3927–3938.
- [25] C. Yu, F. Zhao, J. Luo, L. Zhang, X. Sun, Recent development of lithium argyrodite solid-state electrolytes for solid-state batteries: Synthesis, structure, stability and dynamics, *Nano Energy*. **2021**, *83*, 105858.
- [26] R. Matsuda, E. Hirabara, N.H.H. Phuc, H. Muto, A. Matsuda, Composite Cathode of NCM Particles and Li₃PS₄-LiI Electrolytes Prepared using the SEED Method for All-Solid-State Lithium Batteries, *IOP Conf Ser Mater Sci Eng*. **2018**, *429*, 012033.
- [27] A. Banerjee, X. Wang, C. Fang, E.A. Wu, Y.S. Meng, Interfaces and Interphases in All-Solid-State Batteries with Inorganic Solid Electrolytes, *Chem Rev*. **2020**, *120*, pp. 6878–6933.
- [28] R. Matsuda, H. Muto, A. Matsuda, Air-Stable Li₃SbS₄-LiI Electrolytes Synthesized via an Aqueous Ion-Exchange Process and the Unique Temperature Dependence of Conductivity, *ACS Appl Mater Interfaces*. **2022**, *14*, pp. 52440–52447.
- [29] H.M. Chen, C. Maohua, S. Adams, Stability and ionic mobility in argyrodite-related lithium-ion solid electrolytes, *Physical Chemistry Chemical Physics*. **2015**, *17*, pp. 16494–16506.
- [30] Z. Wang, G. Shao, Theoretical design of solid electrolytes with superb ionic conductivity: alloying effect on Li⁺ transportation in cubic Li₆PA₅X chalcogenides, *J. Mater. Chem. A*. **2017**, *5*, pp. 21846–21857.

- [31] Z. Deng, Z. Zhu, I.-H. Chu, S.P. Ong, Data-Driven First-Principles Methods for the Study and Design of Alkali Superionic Conductors, *Chemistry of Materials*. **2017**, *29*, pp. 281–288.
- [32] R. Song, R. Xu, Z. Wang, M. Yang, X. Yan, C. Yu, L. Zhang, Oxide doping improving interface performance for $\text{Li}_7\text{P}_3\text{S}_{11}$ solid electrolytes, *J Alloys Compd.* **2022**, *921*, 166125.
- [33] N.H.H. Phuc, T. Maeda, T. Yamamoto, H. Muto, A. Matsuda, Preparation of $\text{Li}_3\text{PS}_4\text{-Li}_3\text{PO}_4$ Solid Electrolytes by Liquid-Phase Shaking for All-Solid-State Batteries, *Electronic Materials*. **2021**, *2*, pp. 39–48.
- [34] R.F. Indrawan, T. Yamamoto, H.H.P. Nguyen, H. Muto, A. Matsuda, Liquid-phase synthesis of $100\text{Li}_3\text{PS}_4\text{-}50\text{LiI-xLi}_3\text{PO}_4$ solid electrolytes, *Solid State Ion*. **2020**, *345*, 115184.
- [35] K. Hikima, H.J. Ler, R.F. Indrawan, H. Muto, A. Matsuda, Li_4SiO_4 Doped- $\text{Li}_7\text{P}_2\text{S}_8\text{I}$ solid electrolytes with high lithium stability synthesised using liquid-phase shaking, *RSC Adv*. **2022**, *12*, pp. 7469–7474.
- [36] Z. Sun, Y. Lai, N. lv, Y. Hu, B. Li, L. Jiang, J. Wang, S. Yin, K. Li, F. Liu, Insights on the Properties of the O-Doped Argyrodite Sulfide Solid Electrolytes ($\text{Li}_6\text{PS}_5\text{-}_x\text{ClO}_x, x=0\text{-}1$), *ACS Appl Mater Interfaces*. **2021**, *13*, pp. 54924–54935.
- [37] L. Peng, S. Chen, C. Yu, C. Wei, C. Liao, Z. Wu, H.-L. Wang, S. Cheng, J. Xie, Enhancing Moisture and Electrochemical Stability of the $\text{Li}_{5.5}\text{PS}_{4.5}\text{Cl}_{1.5}$ Electrolyte by Oxygen Doping, *ACS Appl Mater Interfaces*. **2022**, *14*, pp. 4179–4185.
- [38] Z. Zhang, L. Zhang, X. Yan, H. Wang, Y. Liu, C. Yu, X. Cao, L. van Eijck, B. Wen, All-in-one improvement toward $\text{Li}_6\text{PS}_5\text{Br}$ -Based solid electrolytes triggered by compositional tune, *J Power Sources*. **2019**, *410–411*, pp. 162–170.
- [39] M. Wu, G. Liu, X. Yao, Oxygen doped argyrodite electrolyte for all-solid-state lithium batteries, *Appl Phys Lett*. **2022**, *121*, 203904.
- [40] T. Chen, D. Zeng, L. Zhang, M. Yang, D. Song, X. Yan, C. Yu, Sn-O dual-doped Li-argyrodite electrolytes with enhanced electrochemical performance, *Journal of Energy Chemistry*. **2021**, *59*, pp. 530–537.
- [41] T. Hwang, Y.-J. Lee, S.R. Lee, Y.-C. Ha, M. Cho, S.-M. Lee, K. Cho, The crucial role of oxygen substitution in argyrodite solid electrolytes from the bulk to the

- surface under atmospheric conditions, *J Mater Chem A Mater.* **2022**, *10*, pp. 16908–16919.
- [42] T. Chen, L. Zhang, Z. Zhang, P. Li, H. Wang, C. Yu, X. Yan, L. Wang, B. Xu, Argyrodite Solid Electrolyte with a Stable Interface and Superior Dendrite Suppression Capability Realized by ZnO Co-Doping, *ACS Appl Mater Interfaces.* **2019**, *11*, pp. 40808–40816.
- [43] A. Miura, N.C. Rosero-Navarro, A. Sakuda, K. Tadanaga, N.H.H. Phuc, A. Matsuda, N. Machida, A. Hayashi, M. Tatsumisago, Liquid-phase syntheses of sulfide electrolytes for all-solid-state lithium battery, *Nat Rev Chem.* **2019**, *3*, pp. 189–198.
- [44] A. MATSUDA, H. MUTO, N. H.H. PHUC, Preparation of Li₃PS₄ Solid Electrolyte by Liquid-Phase Shaking Using Organic Solvents with Carbonyl Group as Complex Forming Medium, *Journal of the Japan Society of Powder and Powder Metallurgy.* **2016**, *63*, pp. 976–980.
- [45] H. Gamo, J. Nishida, A. Nagai, K. Hikima, A. Matsuda, Solution Processing via Dynamic Sulfide Radical Anions for Sulfide Solid Electrolytes, *Advanced Energy and Sustainability Research.* **2022**, *3*, 2200019.
- [46] J. Ruhl, L.M. Riegger, M. Ghidui, W.G. Zeier, Impact of Solvent Treatment of the Superionic Argyrodite Li₆PS₅Cl on Solid-State Battery Performance, *Advanced Energy and Sustainability Research.* **2021**, *2*, 2000077.
- [47] L. Zhou, K.-H. Park, X. Sun, F. Lalère, T. Adermann, P. Hartmann, L.F. Nazar, Solvent-Engineered Design of Argyrodite Li₆PS₅X (X = Cl, Br, I) Solid Electrolytes with High Ionic Conductivity, *ACS Energy Lett.* **2019**, *4*, pp. 265–270.
- [48] Y. Subramanian, R. Rajagopal, K.-S. Ryu, High ionic-conducting Li-argyrodites synthesized using a simple and economic liquid-phase approach and their application in all solid-state-lithium batteries, *Scr Mater.* **2021**, *204*, 114129.
- [49] J.E. Lee, K. Park, J.C. Kim, T. Wi, A.R. Ha, Y.B. Song, D.Y. Oh, J. Woo, S.H. Kweon, S.J. Yeom, W. Cho, K. Kim, H. Lee, S.K. Kwak, Y.S. Jung, Universal Solution Synthesis of Sulfide Solid Electrolytes Using Alkahest for All-Solid-State Batteries, *Advanced Materials.* **2022**, *34*, 2200083.
- [50] M. Wada, G.J. Kwon, Y. Nishiyama, Structure and Thermal Behavior of a Cellulose I–Ethylenediamine Complex, *Biomacromolecules.* **2008**, *9*, pp. 2898–2904.

- [51] Y.-J. Zhu, X.-L. Hu, Microwave-assisted polythiol reduction method: a new solid–liquid route to fast preparation of silver nanowires, *Mater Lett.* **2004**, *58*, pp. 1517–1519.
- [52] R.F. Indrawan, H. Gamo, A. Nagai, A. Matsuda, Chemically Understanding the Liquid-Phase Synthesis of Argyrodite Solid Electrolyte $\text{Li}_6\text{PS}_5\text{Cl}$ with the Highest Ionic Conductivity for All-Solid-State Batteries, *Chemistry of Materials.* **2023**, *35*, pp. 2549–2558.
- [53] M. Rahm, P. Erhart, R. Cammi, Relating atomic energy, radius and electronegativity through compression, *Chem Sci.* **2021**, *12*, pp. 2397–2403.
- [54] Z. Zhang, Y. Sun, X. Duan, L. Peng, H. Jia, Y. Zhang, B. Shan, J. Xie, Design and synthesis of room temperature stable Li-argyrodite superionic conductors *via* cation doping, *J Mater Chem A Mater.* **2019**, *7*, pp. 2717–2722.
- [55] M.A. Reddy, M. Fichtner, Ionic Conductivity of Nanocrystalline Metal Fluorides, in: Photonic and Electronic Properties of Fluoride Materials, *Elsevier*, **2016**: pp. 449–463.
- [56] K. Minami, A. Hayashi, M. Tatsumisago, Electrical and electrochemical properties of the $70\text{Li}_2\text{S}\cdot(30-x)\text{P}_2\text{S}_5\cdot x\text{P}_2\text{O}_5$ glass-ceramic electrolytes, *Solid State Ion.* **2008**, *179*, pp. 1282–1285.
- [57] T. Swamy, X. Chen, Y.-M. Chiang, Electrochemical Redox Behavior of Li Ion Conducting Sulfide Solid Electrolytes, *Chemistry of Materials.* **2019**, *31*, pp. 707–713.
- [58] K. Minami, A. Hayashi, S. Ujiie, M. Tatsumisago, Electrical and electrochemical properties of glass–ceramic electrolytes in the systems $\text{Li}_2\text{S}-\text{P}_2\text{S}_5-\text{P}_2\text{S}_3$ and $\text{Li}_2\text{S}-\text{P}_2\text{S}_5-\text{P}_2\text{O}_5$, *Solid State Ion.* **2011**, *192*, pp. 122–125.
- [59] K. Takada, M. Osada, N. Ohta, T. Inada, A. Kajiyama, H. Sasaki, S. Kondo, M. Watanabe, T. Sasaki, Lithium ion conductive oxysulfide, $\text{Li}_3\text{PO}_4-\text{Li}_3\text{PS}_4$, *Solid State Ion.* **2005**, *176*, pp. 2355–2359.
- [60] D. Xie, S. Chen, Z. Zhang, J. Ren, L. Yao, L. Wu, X. Yao, X. Xu, High ion conductive Sb_2O_5 -doped $\beta\text{-Li}_3\text{PS}_4$ with excellent stability against Li for all-solid-state lithium batteries, *J Power Sources.* **2018**, *389*, pp. 140–147.

- [61] A. KATO, M. NAGAO, A. SAKUDA, A. HAYASHI, M. TATSUMISAGO, Evaluation of Young's modulus of $\text{Li}_2\text{S-P}_2\text{S}_5\text{-P}_2\text{O}_5$ oxysulfide glass solid electrolytes, *Journal of the Ceramic Society of Japan*. **2014**, *122*, pp. 552–555.
- [62] H.M. Chen, C. Maohua, S. Adams, Stability and ionic mobility in argyrodite-related lithium-ion solid electrolytes, *Physical Chemistry Chemical Physics*. **2015**, *17*, 16494–16506.
- [63] J. Zhang, X. Gu, Hydrolysis mechanism of Li-argyrodite $\text{Li}_6\text{PS}_5\text{Cl}$ in air, *Rare Metals*. **2023**, *42*, pp. 47–55.
- [64] T. Hwang, Y.-J. Lee, S.R. Lee, Y.-C. Ha, M. Cho, S.-M. Lee, K. Cho, The crucial role of oxygen substitution in argyrodite solid electrolytes from the bulk to the surface under atmospheric conditions, *J Mater Chem A Mater*. **2022**, *10*, pp. 16908–16919.

Chapter 5

General Conclusion and Future Works Possibility

This dissertation focused on the synthesis and performance evaluation of two types of solid electrolytes: the $100\text{Li}_3\text{PS}_4\text{-}50\text{Li-xLi}_3\text{PO}_4$ SE and the oxygen-doped argyrodite SEs. In the first part of the dissertation, the $100\text{Li}_3\text{PS}_4\text{-}50\text{Li-xLi}_3\text{PO}_4$ SE was successfully synthesized using a low-pressure heat treatment process with ethyl propionate as the solvent. The addition of Li_3PO_4 resulted in significant improvements in ionic conductivity and stability compared to the SE without Li_3PO_4 . The sample $100\text{Li}_3\text{PS}_4\text{-}50\text{Li-}10\text{Li}_3\text{PO}_4$, heat treated at $130\text{ }^\circ\text{C}$ for 2 hours, exhibited a high ionic conductivity of $8.5 \times 10^{-4}\text{ S cm}^{-1}$ at room temperature. This finding demonstrated the effectiveness of incorporating Li_3PO_4 in enhancing the electrochemical performance of the SE.

In the second part of this dissertation, the focus was on the scalable liquid phase synthesis of oxygen-doped argyrodite solid electrolytes, specifically $\text{Li}_6\text{PS}_5\text{Cl}$. The use of ACN and PTH as solvents allowed for the synthesis of $\text{Li}_6\text{PS}_5\text{Cl}$ without any Li_3PO_4 impurity, resulting in enhanced ionic conductivity and improved Li metal anode stability. The absence of Li_3PO_4 impurity in $\text{Li}_6\text{PS}_5\text{Cl}$ led to better Li dendrite growth suppression and improved battery cycle performance. This dissertation also highlighted the importance of solvent selection in achieving high electrochemical performance without impurities.

Additionally, the dissertation investigated the oxygen doping of argyrodite SEs, such as $\text{Li}_6\text{PS}_{4.875}\text{O}_{0.125}\text{Cl}$ ($x=0.05$) and $\text{Li}_6\text{PS}_{4.75}\text{O}_{0.25}\text{Cl}$ ($x=0.10$). Oxygen doping enhanced the stability of the SEs by incorporating the POS_3^{3-} anion, inhibiting chemical reactions at the SE surface. $\text{Li}_6\text{PS}_{4.875}\text{O}_{0.125}\text{Cl}$ demonstrated excellent electrochemical stability, high capacity retention, and reversibility, with an impressive capacity retention of 99.8% over cycling. This indicated minimal capacity loss and showcased the exceptional long-term stability of the SEs with oxygen doping.

To be exact, the addition of Li_3PO_4 into the $\text{Li}_3\text{PS}_4\text{-LiI}$ system and P_2O_5 into $\text{Li}_6\text{PS}_5\text{Cl}$ results in the formation of oxysulfide units, which play a crucial role in improving the electrochemical stability at the interface of the solid electrolyte. Among these oxysulfides, POS_3^{3-} stands out as it is theoretically predicted to have the highest stability compared to the

others. This enhanced stability of the oxysulfide, particularly POS_0^{3-} , contributes significantly to the overall performance and reliability of the solid electrolyte in various electrochemical applications. The incorporation of these oxysulfide units opens up new possibilities for the design and development of advanced solid-state batteries with improved safety and performance characteristics.

In summary, this dissertation successfully demonstrated the synthesis of enhanced solid electrolytes through the incorporation of Li_3PO_4 and oxygen doping. These electrolytes showed improvements in ionic conductivity, stability, compatibility with Li metal anodes, and battery cycle performance. The findings presented in this dissertation have significant implications for the development of high-performance solid-state batteries with improved electrochemical properties and long-term stability. The presence of the oxysulfide structure from the PO_xS_y anion contributes to the enhancement of the electrochemical interface of the sulfide solid electrolyte. Further research focusing on increasing the intensity of these anions will help to further enhance the stability.

The promising findings from this research open up various possibilities for further exploration and development. One potential avenue is to investigate the coating of cathode active materials with the oxygen-doped argyrodite solid electrolytes. Coating the cathode materials with SEs can improve the surface contact area between the electrodes and electrolytes, leading to enhanced ion transport and overall battery performance. This approach could contribute to the development of more efficient and stable battery systems.

Furthermore, exploring the incorporation of other doping materials, such as nitrogen sources, into the sulfide-based solid electrolytes is another interesting direction. This could be aimed at enhancing the air stability of the electrolytes, as sulfide-based materials can be sensitive to moisture and oxygen exposure. By incorporating nitrogen-based dopants, the stability of the SEs could be further improved, enabling their use in more demanding environments and applications.

Moreover, the impact of this research extends beyond the field of energy storage. The scalability of the liquid phase synthesis method holds significant potential for low-cost production of all-solid-state Li-ion batteries with enhanced safety features. This could lead to the widespread adoption of ASSLiBs, contributing to the advancement of renewable energy technologies, electric vehicles, and portable electronic devices. The societal and environmental

benefits of such advancements are substantial, including reduced reliance on fossil fuels, decreased greenhouse gas emissions, and improved energy storage solutions.

List of Publications

The following publications cover part of the work presented in this dissertation.

- [1] Radian Febi Indrawan, Tokoharu Yamamoto, Huu Huy Phuc Nguyen, Hiroyuki Muto, Atsunori Matsuda, “Liquid-phase synthesis of $100\text{Li}_3\text{PS}_4\text{-}50\text{LiI-xLi}_3\text{PO}_4$ solid electrolytes”, *Solid State Ionics*, **345**, 115184, 2020.
- [2] Radian Febi Indrawan, Hirotada Gamo, Atsushi Nagai, and Atsunori Matsuda, “Chemically Understanding the Liquid-Phase Synthesis of Argyrodite Solid Electrolyte $\text{Li}_6\text{PS}_5\text{Cl}$ with the Highest Ionic Conductivity for All-Solid-State Batteries”, *ACS Chemistry of Materials*, **35** (6), 2549-2558, 2023.
- [3] Radian Febi Indrawan, Reiko Matsuda, Kazuhiro Hikima, and Atsunori Matsuda, “Enhanced Electrochemistry Stability of Oxygen Doped $\text{Li}_6\text{PS}_5\text{Cl}$ Argyrodite Solid Electrolyte by Liquid-Phase Synthesis”, *Solid State Ionics*, 4 September 2023 (Accepted)

Acknowledgements

I would like to express my deepest gratitude and appreciation to everyone who directly or indirectly contributed to the completion of this dissertation and study.

I would like to express my deepest gratitude and thankfulness to the almighty God, Allah SWT, for guiding me on this path and allowing me to reach this point. I am truly grateful and humbled by His blessings and say "Alhamdulillah" for His guidance and support throughout my journey.

I would like to express my sincere and profound gratitude to my supervisor, Professor Atsunori Matsuda from Toyohashi University of Technology. Professor Matsuda served as the leader of Matsuda's Laboratory, where I conducted my research and experimental work. His invaluable guidance and unwavering support as my supervisor have been instrumental in the successful completion of this study. I am deeply grateful for his insightful comments and suggestions, which have significantly contributed to the development and progress of my research. Furthermore, I extend my heartfelt appreciation to Professor Atsunori Matsuda for his assistance beyond the scope of research. He has played a crucial role in facilitating my academic journey at Toyohashi University of Technology. Without his initial permission and support, I would not have been able to embark on this academic pursuit at such a prestigious institution. I am truly indebted to Professor Atsunori Matsuda for his mentorship, kindness, and unwavering support throughout this transformative journey.

I would like to express my deep gratitude to Professor Hiroyuki Muto and Professor Inada Ryoji from Toyohashi University of Technology for their invaluable contributions as the reviewers and examiners of my dissertation defense. Their expertise and knowledge in the field have greatly enriched my understanding of the subject matter. I am truly grateful for their rigorous evaluation, constructive feedback, and insightful suggestions, which have undoubtedly expanded my knowledge and enhanced the quality of my research.

I would like to express my sincere gratitude to Assistant Professor Dr. Kazuhiro Hikima from Matsuda's Laboratory, Toyohashi University of Technology, for his invaluable guidance and support. Throughout my study, his assistance and input have been tremendously beneficial

to me. His expertise and mentorship have made significant contributions to my academic and research endeavors. I am truly grateful for his unwavering support.

I sincerely want to express my gratitude to Dr. Nguyen Huu Huy Phuc from Hochiminh City University of Technology, who was previously a part of Matsuda's Laboratory. I am grateful for his guidance and support since the beginning of my Master's program. From the start, he has been by my side, teaching and assisting me throughout my journey. I would also like to congratulate him on his new position at the new university.

I would like to express my heartfelt gratitude to Tokoharu Yamamoto, who graduated from Toyohashi University of Technology which also was a part of Matsuda's Laboratory member and my lab mentor. During my Master's studies in Matsuda's Laboratory, his guidance and support were invaluable to me. He played a pivotal role in teaching me the fundamentals of conducting experiments and using laboratory equipment. I am truly grateful for his expertise and mentorship throughout my research journey.

I would like to express my deepest appreciation and heartfelt thanks to my wife, Dr. Irine Yunhafita Malya, who is currently working alongside me in Matsuda's Laboratory at Toyohashi University of Technology. Her unwavering support and constant presence throughout my doctoral journey have been invaluable. Her encouragement and companionship have played a vital role in helping me successfully complete my doctoral course. I am truly grateful for her understanding, patience, and unwavering belief in my abilities. Dr. Irine Yunhafita Malya, thank you for being my rock and the source of my strength throughout this challenging academic endeavor.

I would like to extend my sincere gratitude to Dr. Keiichiro Maegawa, who graduated from Matsuda's Laboratory at Toyohashi University of Technology. Dr. Maegawa has been not only my mentor but also a dear friend. He has consistently provided support and guidance, not only in my research activities but also in navigating life as a foreigner in Japan. I am deeply appreciative of his willingness to assist me in various aspects and for sharing his knowledge and experiences. I consider myself truly fortunate to have Dr. Keiichiro Maegawa as a friend and mentor, and I want to express my heartfelt thanks for his unwavering support throughout my journey.

I would like to express my heartfelt gratitude to my esteemed colleague, Dr. Hirotada Gamo, who also obtained his degree from Matsuda's Laboratory at Toyohashi University of Technology. I am deeply grateful for his invaluable assistance and support in my research and

laboratory activities. Dr. Gamo has been an exceptional mentor, generously sharing his extensive knowledge and expertise in the field of electrochemistry. His remarkable skills in academia have significantly contributed to my academic growth. I am truly thankful for his guidance and contributions, and I want to sincerely thank Dr. Hirotada Gamo for his unwavering support and collaboration throughout our academic journey together.

I would like to express my sincere gratitude to my fellow researchers, Mrs. Reiko Matsuda, Mrs. Takahashi Masayo, and Mrs. Kusaba Ikuyo, from Matsuda's Laboratory, Toyohashi University of Technology. Their invaluable guidance and teachings throughout our research activities have been instrumental in the progress and success of our work. Their expertise and support have greatly enhanced the research process, making it more engaging and enriching.

I am deeply grateful to Dr. Atsushi Nagai from ENSEMBLE3, Poland, who was also a former member of Matsuda's Laboratory, Toyohashi University of Technology. I would like to express my sincere appreciation for his valuable guidance and direct assistance in my research activities. Dr. Nagai's willingness to share his vision and extensive knowledge in organic chemistry has greatly contributed to my growth as a researcher. I am truly thankful for his mentorship, which has allowed me to enhance my understanding and research skills.

I would like to express my sincere gratitude to Dr. Tan Wai Kian and Dr. Go Kawamura from Toyohashi University of Technology for their invaluable support throughout my academic journey.

I would like to extend my heartfelt gratitude to all of Matsuda's laboratory members, colleagues, friends, and all those who have provided guidance, assistance, and support throughout the completion of this dissertation.

I would like to express my heartfelt gratitude to all the members of the Li-ion Batteries team from Matsuda's Laboratory, Toyohashi University of Technology. Their cheerful demeanor and kindness have created an uplifting atmosphere during our research activities.

Lastly, I would like to express my heartfelt gratitude to my family in Indonesia. To my mother, Netty Kurniati, and my sisters Dr. Sari Dewi Kurniasih and Nilamsari Kurniasih, thank you for your unwavering support and endless prayers for my success. I would also like to extend my appreciation to my grandparents, aunts, uncles, and cousins for their love and

encouragement throughout my journey. Your support has been instrumental in my achievements, and I am truly grateful for having such a wonderful and caring family.

July, 2023

Radian Febi Indrawan

